Nanometer Probing of Operating Nano-Photonic Devices

by

Rudra Sankar Dhar

A thesis
presented to the University of Waterloo
in fulfillment of the
thesis requirement for the degree of
Doctor Philosophy
in
Electrical and Computer Engineering

Waterloo, Ontario, Canada, 2014

© Rudra Sankar Dhar 2014

I hereby declare that I am the sole author of this thesis. This is a true copy of the thesis, including any required final revisions, as accepted by my examiners.

I understand that my thesis may be made electronically available to the public.

ABSTRACT

The external performance of quantum optoelectronic devices is governed by the three-dimensional profiles of electric potentials determined by the distribution of charge carriers (electrons and holes) within the active regions of the devices. Charge carrier dynamics play a vital role in active photonic quantum/nano devices, such as electrically-pumped semiconductor lasers. As an example, in quantum cascade lasers (QCLs) the Electric Field Domain (EFD) hypothesis posits that the potential distribution might be simultaneously spatially non-uniform and temporally unstable. Until now, there are no experimental means of probing the inner potential profile directly and as a result the mechanisms responsible for sub-par device performance of QCLs remain the subject of speculation. Another example is interband cascade lasers (ICLs), in which the distribution of gain-providing charge carrier governs the operation and performance of the devices, but has not been experimentally measured prior to this study.

This work presents a systematic experimental study of gain-providing charge carrier distribution in a lasing interband cascade laser and electric potential distribution in THz QCLs. The unique charge carrier distribution profile in the quantum-well active region is quantitatively measured at nanometer scales by using the non-invasive scanning voltage microscopy (SVM) technique. Experimental results clearly confirm the accumulation and spatial segregation of holes and electrons in the core of the ICL device. The measurement also shows that the charge carrier density is essentially clamped in the presence of stimulated emission in ICLs, thus conclusively differentiating the lasing from non-lasing devices. The SVM technique has been applied to lasing THz QCLs to verify the hypothesis of electric field domains in semiconductor quantum structures. The experimental results reveal that the multi-quantum-well active region is divided into multiple sections having distinctly different electric fields. The electric field across these serially-stacked quantum cascade modules are observed not to continuously increase in proportion to the gradual increase of the applied device bias, but rather jumps between discrete values related to tunneling resonances. Also in the THz QCLs the progression of the observed EFDs are carefully probed. Experimental evidences reveal that an incremental change in device bias leads to a hopping-style shift in the EFD boundary – the higher electric field domain expands at least one module each step at the expense of the lower field domain within the active region. The SVM findings in THz QCLs indicate the importance of quantum active region design for intrinsically more uniform and stable electric field profiles.

The two showcase study examples demonstrate that the cryogenic-temperature SVM is an enabling technique, being able to measure and resolve nanometer scale features non-destructively on operating devices. This experimental approach allows directly mapping the electric field distribution as well as the charge carrier distribution inside operating semiconductor quantum devices at nanometer scales, thus connecting the inner workings with the external measures of the devices. The experimental approach is expected to facilitate a deeper understanding of fundamental processes that are governing the operation and performance of a wide range of nanoelectronic and nanophotonic devices.

Acknowledgements

I would like to thank my supervisor Prof. Dayan Ban for his encouragement, knowledge, patience and never ending enthusiasm throughout my PhD studies. I want to express my gratitude to the members of my PhD committee: Prof. Karin Hinzer, Prof. Yuning Li, Prof. C.R. (Selva) Selvakumar, and Prof. Zbigniew Wasilewski, for reading my thesis and helpful discussions.

I am grateful to many members of the Reverse Engineering department of Chipworks for active collaborative support. In particular, I would thank Dr. Sinjin Dixon-Warren, Mr. Jeff Campbell, Mr. Mohamed Kawaliye and Mr. Mike Green for their generous support. I would thanks Dr. Jianzhao Li of University of Toronto for his immense support and advice at my initials stages of my research. I would like to express my thanks to our collaborators at University of Oklahoma, and National Research Council of Canada from where I would especially thank Prof. R. Q. Yang, and Dr. Emmanuel Dupont, respectively, for providing designed and fabricated devices for the research project. This work would not have been possible without the help and support of their devices. I would like to also thank Dr. Ghasem Razavipour who also helped me through this project.

I would like to express my thanks to my colleagues Saeed Fathololoumi, Jun Chen, Ghasem Razavipour, Guocheng Liu, Chao Xu, Mark Ferguson, and Xueren Wang for interesting discussions and talks.

I also want to express my gratitude to all my friends who supported me, including but not limited to Kalikinkar, Sudipto, Ripon and Debolina. I really enjoyed their company and help during the time spent with them.

Last but not the least; I would like to acknowledge the endless love and support from my family.

Dedication

To my beloved wife, *Baishakhi*,

my mother

and

to the memory of my father.

Table of Contents

Abstract.. iii
Acknowledgement.. v
Table of Contents.. vii
List of Tables.. x
List of Figures.. xi
List of Abbreviations.. xxiii
List of Publications.. xxiv

CHAPTER 1: Introduction.. 1
1.1 Motivation for the Work.. 1
1.2 Research Objectives.. 4
1.3 Organization of the Thesis.. 5

CHAPTER 2: Literature and Instrument Review.. 7
2.1 Introduction to Atomic Force Microscope (AFM).. 8
2.2 AFM Measurement.. 9
2.2.1 Contact Mode.. 9
2.2.2 Non-contact Mode.. 11
2.2.3 Tapping Mode.. 11
2.3 Advancement in contact mode AFM measurement.. 12
2.3.1 Principle for major contact mode AFM profiles.. 12
2.3.2 Dopant and Charge carrier profiling and analysis.. 14
2.3.2.1 Scanning spreading resistance microscopy (SSRM).. 15
2.3.2.2 Scanning capacitance microscopy (SCM).. 18
2.3.2.3 Scanning voltage microscopy (SVM).. 21
2.4 Measurement Tool: AFM.. 24
2.4.1 Digital Instruments Dimension 3100.. 24
2.4.2 Attocube Cryogenic Temperature AFM.. 28
2.5 Summary.. 30

CHAPTER 3: Two-Dimensional Dopant Profiling of Terahertz (THz) Quantum Cascade Laser (QCL) Devices.. 31
3.1 Introduction to SSRM and SCM on THz QCL.. 32
3.2 Experimental Procedure for scanning THz QCL devices.. 35

3.3 Nanosurface Profiling of Carriers and Discussion……………..…..… 38
3.3.1 Carrier profiling using SSRM Measurements…..…....………... 38
3.3.2 Carrier profiling using SCM Measurements…………………...... 45
3.3.3 Calibration Results……………………………………….......... 49
3.4 Summary………………………………………………………….............. 50

CHAPTER 4: Nanoscopic Probing for Determining Charge Density in Mid-IR Interband Cascade Lasers (ICLs)……………. 51
4.1 Introduction to SVM on ICL………………..…..…………………. 52
4.2 Experimental Procedure……………………………..……………… 55
4.2.1 SVM Technique on AFM….……….. 55
4.2.1.1 Room Temperature SVM setup…………..……................ 56
4.2.1.2 Cryogenic Temperature SVM setup……........................... 59
4.2.2 Mid-IR ICL Device Structure and Performances……...….…… 61
4.3 Nanosurface profiling of ICLs …………………………….................. 64
4.3.1 Non-uniform Electric Field Measurement………...……….…... 64
4.3.2 Quantitative Analysis and Discussion……….......................... 70
4.4 Summary………………………………………………….............. 83

CHAPTER 5: Direct Observation and Determination of the Evolution of Electric Field Domains (EFDs) in THz QCL Devices…….…... 84
5.1 Introduction to SVM on THz QCL…………………………………. 85
5.2 Experimental Procedures…………………………………….…….. 87
5.2.1 Cryogenic Temperature SVM Technique.................................. 88
5.2.2 THz QCL Devices, Structures and Performances.……………. 89
5.3 Nanosurface Profiling and Mapping of Carriers in THz QCLs…. 93
5.3.1 Observation of EFDs in non-lasing and lasing THz QCLs…..… 94
5.3.2 Direct Observation and Imaging of EFDs in lasing THz QCLs.. 105
5.3.3 Determination and Evolution of EFD in Operating THz QCLs.. 115
5.4 Summary………………………………………………….............. 125

CHAPTER 6: Conclusion and Future Work…………………..….. 127
6.1 Summary and Conclusion…………………………………............. 127
6.2 Future Work……………………….……….………………….. 130

Appendices A: THz QCL Device Fabrication and Performance Measurement.. 131
A.1 THz QCL Device Fabrication……………..……………………..…. 131

A.1.1 Metal-Metal Waveguide………………………………………… 131
A.1.2 Semi Insulating Surface Plasmon Waveguide………………… 135
A.2 External Performance on THz QCL Devices……………………… 137
A.2.1 Experimental set up and Measurements……………………... 137
A.2.2 Device Design and Simulation………………………………… 140

References…………………………………………………………… 144

List of Tables

CHAPTER 3

Table 3.1. SSRM resistance across the active region of THz QCL device at DC tip bias voltages of 1.0, 1.5, 2.5 and 3.5V for V843 and V775 samples.

Table 3.2. Comparison of average doping concentration derived from calibrated SSRM and SCM measurements and the average designed doping concentration values of the active region of the THz QCL device for different DC tip bias voltages.

CHAPTER 4

Table 4.1. For R090, the measured internal average electric field (F), the experimental charge carrier sheet density (σ_i, i=1, 2, 3, 4, 5), the total hole sheet density ($\sigma_h = \sigma_1+\sigma_3+\sigma_5$), the total electron sheet density ($\sigma_e = \sigma_2+\sigma_4$), and the theoretical modeling sheet carrier density (σ_m) by using Equation (5.3).). m_r^*= 0.0355 me is used in the calculation, where me is the free electron mass. The device is forward-biased at 77 K with a threshold voltage of 3.4 V. The uncertainty of the experimental charge carrier sheet density is estimated to be ±10%. The modeling results are in good agreement with the experimental data (red fonts).

CHAPTER 5

Table 5.1. SVM measured electric field in each observed electric field domain for V843. The electric field values are obtained by linearly fitting the different sections of the voltage curves. The small variation is attributed to small system errors.

Table 5.2. SVM measured electric field in each observed electric field domain for V962. The electric field values are obtained by linearly fitting the different sections of the voltage curves. The small variation is attributed to small system errors.

List of Figures

CHAPTER 1

Figure 1.1. Schematic of the THz QCL structure.

CHAPTER 2

Figure 2.1. Schematic of AFM measurement set up for contact mode profiling.

Figure 2.2. A comparison of the experimental and simulated results showing SSRM resistance profiles for $n^{++}p$ structure.

Figure 2.3. SSRM image of InP based laser (a) the mesa of the structure resolved closely, (b) both line 1 and line 2 shown in (a) are plotted as analysis graphs, (c) 5 µm mesa.

Figure 2.4. (a) 5 µm SSRM scan image of a multiple quantum well buried heterostructure laser sample. (b) SSRM resistance profile at three different DC bias conditions of the p-n-p-n current blocking structure.

Figure 2.5. SCM image contrast variation showed schematically.

Figure 2.6. (a) SCM image of the APD structure. (b) SCM dC/dV profiles for a variety of DC biases.

Figure 2.7. SCM image of the InP Buried Heterostructure multiple quantum well structure.

Figure 2.8. SCM scan of 2T-cell (a) dC/dV Amplitude mode image for 20 µm scan (b) dC/dV Phase mode image for 20µm scan (c) dC/dV Phase mode image for 5µm scan showing the “1” and “0” bit contrast difference and (d) SCM line scanning profile.

Figure 2.9. (a) SVM scan image of RWG laser device with inset showing a schematic structure of the device. (b) SVM lateral cross section voltage profile displaying non uniform voltage distribution for n-InAlAs layer.

Figure 2.10. Atomic Force Microscope, DI 3100 ready for scanning at room temperature.

Figure 2.11. (a) SSRM/ SCM module that are attached onto the DI 3100 AFM to measure spreading resistance/ dC/dV signal respectively (b) Cantilever probe holder with a Universal Connector for application of bias onto the sample. The electrical probe connection from (b) is plugged into the (a) for SSRM/SCM connection.

Figure 2.12. Schematic block diagram of the SVM circuitry connection.

Figure 2.13. Cryogenic Atomic Force Microscope from Attocube. 1. AFM Stand with the ferrule, 2. AFM stick that already holds the AFM stand in 1, 3. AFM Controller Electronics.

CHAPTER 3

Figure 3.1. Schematic diagram of the cross section of fabricated THz QCLs with metal-metal waveguide. The quantum well-barrier (QW) active region of the device is based on four well cascade module design that is repeated 276 times forming 276 modules. The thickness of the active region is 10 µm. The semiconductor active region is sandwiched between the two metal cladding layers at the top and the bottom. One of the module is zoomed to show the QW layer structure consisting of $GaAs/Al_{0.25}Ga_{0.75}As$ material for the thicknesses as mentioned. The injector barrier layer in each module has a 44 Å thick Si based delta-doping layer with doping concentration of 3.25×10^{10} cm^{-2}.

Figure 3.2. SSRM image of the THz QCL sample V843 in cross section with dc tip bias of 1 V. (a) Scanning was done at a scan rate of 0.5 Hz for a 5 x 12 µm area. The n-type GaAs/AlGaAs 10 µm four-well structure quantum well-barrier active region is seen to form a metal-semiconductor junction with the top metal of the device. (b) Scanning was done at a scan rate of 0.5 Hz for a 4 x 4 µm area.

Figure 3.3. SSRM image of the active region of the sample V843 THz QCL device for a 1 x 0.5 µm scan area at scan rate of 0.25 Hz showing 14 modules of delta doped layers. Individual module can be resolved with ~36 nm thickness.

Figure 3.4. SSRM image of the active region of the sample V843 THz QCL device for a 1 x 0.35 µm scan area at scan rate of 0.25 Hz showing 8 modules of delta doped layers. Individual module can be resolved with ~44 nm thickness.

Figure 3.5. Resistance profile measured by SSRM across the THz QCL active region for DC tip bias voltages of 1.0, 1.5, 2.5 and 3.5 V to a lateral distance of 500 nm from the top metal of the device. (a) for V843 sample (b) for V775 sample..

Figure 3.6. SSRM resistance vs SIMS doping concentration for Si-doped GaAs epitaxial layers separated by undoped GaAs and grown by MBE on an n^+-GaAs substrate. Calibration measurements performed at dc tip biases of 1.0 V, 1.5 V, 2.5 V, and 3.5 V.

Figure 3.7. Typical SCM image obtained on the cross-section of the THz QCL. Scanning was done at open-loop amplitude mode for a scan for an area of 5 x 12 μm, with AC bias of 1.0 V and scan rate of 0.5 Hz. The active region of the device is seen to be clearly delineated from the metal layers at either edge.

Figure 3.8. SCM image of the active region THz QCL for a 1 x 0.5 μm scan area at scan rate of 0.25 Hz showing 14 modules of delta doped layers. Individual modules with ~36 nm thickness can be resolved.

Figure 3.9. SCM signal (dC/dV) vs the SIMS doping concentration extracted from an n-type GaAs standard staircase sample. The correlation curves were obtained at each of the following ac bias voltages: 0.5, 0.75, 1.0, 1.25 and 2.0 V.

CHAPTER 4

Figure 4.1. Schematic of room temperature scanning voltage microscopy measurement setup. The device sample is biased using an Avtech power supply. The injected voltage along with the measured current on top of the device is monitored by the oscilloscope. The AFM probe scans the cross-section of the sample surface and sends the measured data via the ADC2 panel of the AFM system to the AFM controller.

Figure 4.2. A schematic diagram to show the synchronization between SVM sampling and applied device bias pulse train. The device pulse repetition rate is f (= $1/\Delta t$), the AFM probe scan distance is d, and the sampling number of each line scan is N. Then the probe scan speed is set at $v_p = df/(N-1)$ to satisfy the synchronization condition.

Figure 4.3. Schematic of the cryogenic temperature scanning voltage microscopy (SVM) set-up. A cascade laser sample under test is mounted on the AFM system that is biased in pulsed mode using an Avtech pulse generator. The applied bias pulses

are monitored using an oscilloscope to ensure good pulse shape. The voltage signal picked up by the AFM probe is fed directly into the AFM data acquisition system through a built-in analog-digital-converter (ADC) panel 2. In the SVM experiments, the scan range is set as desired for the measurement purpose. The scan speed is set accordingly to synchronize the SVM voltage reading at each sampling point with the device bias pulses.

Figure 4.4. (a) Schematic layer structure for R094 interband cascade laser. (b) Schematic layer structure for R084 interband cascade laser.

Figure 4.5. (a) LIV characteristics for R090 interband cascade laser showing the lasing threshold at 77 K at 3.4 V. (b) LIV characteristics for R084 interband cascade laser with the lasing threshold of 2.7 V at 77 K and 2.5 V at room temperature (300 K). The light current measurements for the devices were performed at different temperature varied from 20 K to the highest lasing temperature of the device.

Figure 4.6. Scanning voltage microscopy image across the R090 ICL device at cryogenic temperature of 77 K. (a) SVM scan 2D voltage profile for 3 μm × 3 μm^2 scan area from the top metal to the bottom contact layer across the device at an applied bias of 3.0 V on top of the device. Different sections of the device as per the structure are clearly viewed from the SVM image. (b) 1D section analysis of the SVM voltage profiles for biases 0.5 V – 5.0 V in step of 0.5. Most of the voltage drops across the ~386 nm interband cascade region of the device while drop is also observed at the heterojunction of the undoped InAs confinement layer to the n$^+$ InAs layer forming a depletion region. (c) The voltage drop (ΔV) and the depletion width at the InAs n$^+$-undoped n heterojunction near the top metal contact is achieved for different applied biases from the 1D voltage profile scans in (b), and the calculated depletion width at no-bias is ~157.2 nm.

Figure 4.7. (a) 1D section analysis of the SVM measured voltage profiles for R094 at cryogenic temperature of 77 K. The voltage profiles acquired clearly indicate the potential drop to mostly occur in the active region of ~954 nm before the bottom contact layer. (b) 1D SVM voltage profile of R084 across the 3 μm distance

from the top contact indicates most of the voltage to drop across the ~362 nm thick interband cascade region.

Figure 4.8. (a) A 512 nm scanned voltage profile of R090 focussing the active region portion at 77 K at an applied bias of 3.0 V. 8 clear pairs of voltage dips each ~9 nm wide is observed and denoted with a dotted line at every ~48 nm resolving 8 modules in the active region that accurately corresponds to the device design. (b) SVM voltage profile of 512 nm on the active region portion at 77 K at an applied bias of 2.8 V for R084. 8 clear voltage dips of ~5 nm wide observed at every ~45 nm resolving 8 modules in the active region as per the device design. Unlike R090, the voltage dips are single dips that evidently designate one GaInSb layer in the device design. (c) Voltage drop across R094 is observed in the active region portion from the scanned image measured at an applied bias of 3.5 V. 7 clear pairs of voltage dips each ~13 nm wide is observed and denoted with a dotted line at every ~63 nm resolving 7 modules in the active region.

Figure 4.9. Non-uniform electric field observed across each module that are periodic among the modules. (a) High resolution 1D SVM scanned voltage profile of 512 nm on the active region portion of the device at 77 K. The dotted lines indicate the 8 dips in the voltage across the ~386 nm active region. (b) 1D voltage profile of 512 nm scan at an applied bias of 3.5 V with corresponding electric field (-dV/dx) distribution across the region. 8 pairs of spikes at every ~48 nm in the active region observed resolving 8 modules in the device.

Figure 4.10. Identification of accumulation of dynamic charge carriers at 77 K from zoomed-in voltage profile in ICL devices at the start of the active region. Two pairs of voltage dips observed for R090 on the 63 nm scanned voltage profile at 3.5 V on top of the device, which correspond to two pairs of spikes in electric field at a distance of 48 nm with each pair covering 9 nm. The adjudged d^2V/dx^2 profile is calculated from voltage and electric field distribution and compared with the ideal schematic conduction band (CB) and valence band (VB) energy level band diagram under no bias condition for the module region. Each pair of zig-zag in d^2V/dx^2 profile has two charge carrier dips and two peaks signifying electron

concentration in InAs layers and hole concentration in GaInSb layers, respectively, at GaInSb/InAs/GaInSb/InAs/AlSb interface that is clearly imaged.

Figure 4.11. Accumulation of dynamic charge carriers in the active region of ICL. 84 nm scanned voltage profile of R094 at 3.5 V on top of the device resolves two pairs of dips in voltage with two pairs of corresponding spikes in the electric field each ~13 nm wide, at a distance of 63 nm. The adjudged d^2V/dx^2 profile is compared with the schematic CB and VB energy band diagram at no bias for the module region. A pair of zig-zag consisting of two dips for electron concentration in InAs layer and two peaks representing hole concentration are observed at InAs/GaInSb/InAs/GaInSb/InAs/AlSb interface, signifying electron-hole transfer and interaction across the CB and VB energy states.

Figure 4.12. Identification of accumulation of dynamic charge carriers at 77 K from zoomed-in voltage profile in ICL devices at the start of the active region. 61 nm scanned voltage profile of R084 device at 2.8 V on top of the device resolves two dips in voltage with two corresponding spikes in the electric field each ~5 nm wide, at a distance of 45 nm. The adjudged d^2V/dx^2 profile is compared with the CB and VB energy band diagram under ideal no bias condition for the module region. Unlike for R090 and R094 ICLS in Figure 4.10 and Figure 4.11, a spike consisting of a dip for electron concentration in InAs layer and two peak representing hole concentration are observed at InAs/GaInSb/InAs/AlSb interface, where electron-hole transfer and interaction takes place across the CB and VB energy states. Voltage dips suggest existence of internal electric field at the GaInSb/InAs junction in each module due to electron-hole transfer and interaction across the conduction band and valence band energy states.

Figure 4.13. Clamping and non-clamping of charge carrier density for R090 ICL device. (a) The experimental sheet charge carrier densities (σ_i, i=1, 2, 3, 4, 5) as a function of device bias at 77 K at which temperature the device lases at 3.4 V. (b) the experimental sheet charge carrier densities (σ_i, i=1, 2, 3, 4, 5) as a function of device bias at room temperature (300 K), at which temperature the device does not lase.

Figure 4.14. Clamping of charge carrier density for R084 ICL device. (a) The experimental sheet charge carrier densities (σ_i, i=1, 2, 3, 4, 5) as a function of device bias at 77 K at which temperature the device lases at 2.7 V. (b) the experimental sheet charge carrier densities (σ_i, i=1, 2, 3, 4, 5) as a function of device bias at 300 K, at which temperature the device lases at 2.5 V.

Figure 4.15. For R090 ICL device, the experimental total electron density (σ_2 + σ_4) as a function of the internal average electric field. The solid line is a linear fitting curve based on Equation 5.3.

Figure 4.16. Temperature dependence of charge carrier density. The active-region charge carrier sheet densities (σ_h and σ_e) are measured at 3.8 V for different temperatures from 77 K to room temperature. Both increases linearly but slowly with temperature until the maximum lasing temperature (T_{max}). After T_{max}, σ_h and σ_e increases rapidly with temperature. The experimental threshold current is also plotted over the same temperature range for comparison, which shows much strong temperature dependence.

CHAPTER 5

Figure 5.1. Schematic diagram of the cross section of fabricated THz QCLs with metal-metal waveguide. (a) f-25 non-lasing device showing three well cascade module design with 219 times forming 219 modules in the quantum well-barrier (QW) active region of the device. (b) f-30 lasing device showing 222 modules in the quantum well-barrier (QW) active region of the device. The thickness of the active region is 10 µm and the active region is sandwiched between the two metal cladding layers at the top and the bottom for both devices. One of the modules is zoomed for both devices to show the QW layer structure consisting of GaAs/$Al_{0.25}Ga_{0.75}As$ material for the thicknesses as mentioned. The phonon well in each module has a homogeneous Si doping of 50 Å thick in the middle of the layer.

Figure 5.2. (a) Experimental current density – device bias (J-V) of the non-lasing f-25 device at 77 K. (b) Experimental current density – device bias (J-V) for lasing f-

30 device at 77 K along with and light – current density (L-J) curves at 77 K and several other temperatures (10, 100, 130 and 150 K).

Figure 5.3. (a) Experimental current density – device bias (J-V) and simulated current density –nominal active-region electric field (J-F) curves of the V843 device at 77 K, and light – current density (L-J) curves at 77 K and several other temperatures (10, 100 and 130 K). The threshold electric field is 19.6 kV/cm at 77 K. (b) Experimental current density – device bias (J-V) and simulated current density –electric field (J-F) curves of the V962 device along with and light – current density (L-J) curves at 77 K and several other temperatures (10, 50, 100 and 130 K). For all the images the nominal active-region electric field is calculated using $(V- \Phi)/d$, V is the applied device bias, Φ is the Schottky contact drop (~0.8 V) and d is the active region thickness (~10 μm).

Figure 5.4. Cryogenic temperature SVM performed on f-series devices. (a) Evolution of EFD observed in non-lasing f-25 at 12 V bias from the 2D 11×11 μm^2 voltage profile image. (b) The voltage profile image on lasing f-30 at 11 V resolve the EFD from the 11×11 μm^2 scan across the device.

Figure 5.5. (a) 1D voltage profile section analysis of the SVM voltage profiles across the active region for the applied biases covering from 2 V – 18 V for non-lasing f-25. (b) 1D voltage profile section analysis for the lasing f-30 THz QCL with applied biases spanning from 2 V - 18 V. The measurement at 12.5 V is performed at the lasing region of the device which is linear while both at current plateau and the NDR region SVMs show two EFDs.

Figure 5.6. The SVM measured electric field across individual cascade modules in the active region of operating THz QCL device as a function of applied device bias. (a) For f-25 the two EFDs coexist in bias ranges of 9-15 V. (b) For f-30 the two EFDs coexist in bias ranges of 10-12 V and from 13-17 V. Shown together are the partition number of the cascade modules in each EFD. Discrete symbols (Measured n_k, k = 1, 2, 3, 4) are calculated from the first approach ($n_k = l_k/d$) based on the SVM measurement results of EFD length (l_k) in (Figure 5.4 (a) and (b)). Solid lines (Calculated n_k, k = 1, 2, 3, 4) are calculated from the second

approach (see text for details). The sum (Measured total) of the SVM measured module numbers ($n_1 + n_2$, or $n_3 + n_4$).

Figure 5.7. (a) High resolution SVM scan executed across 512 x 512 nm^2 area from top metal into the active region at 12 V applied bias on f-25 THz QCL device. (b) Zoomed-in 1D voltage profile across the active region portion is plotted along with the absolute value of electric field (|dV/dx|).

Figure 5.8. (a) 2D SVM scan at the EFD boundary position in the active region distinctly resolves two electric field slope magnitudes F_1= 7.763 kV/cm and F_2 = 14.588 kV/cm. (b) Zoomed-in 1D voltage profile across the EFD position along with the |dV/dx|. Voltage drop dips of ~5 nm width are resolved in all images in the active region portion at every ~45.4 nm and the EFD boundary exists at the center of the doping layer.

Figure 5.9. (a) 2D SVM scan at the EFD boundary position in the active region distinctly resolves two electric field slope magnitudes F_1= 8.791 kV/cm and F_2 = 11.282 kV/cm at an applied bias of 12 V on top of f-30. (b) Zoomed-in 1D voltage profile across the EFD position along with the |dV/dx|. Voltage drop dips are clearly resolved in all images in the active region portion that occurs at every ~40 nm, which are ~5 nm wide. Dotted lines in (b) mark these drops. The EFD position exists at the center of the doping layer.

Figure 5.10. Formation and evolution of electric field domains in operating THz QCL. (a) The SVM measured 2D voltage profile across the active region of a THz QCL (device V843, cooled at 77 K) under a forward bias of 12 V. It shows two electric field domains (F_1 and F_2) across the ~10 μm thick multi-quantum-well active region. The inset of the figure displays a 2D AFM topology image simultaneously acquired over the same area. (b) 2D SVM measured voltage distribution profile at an applied device bias of 10 V for THz QCL device V962. The EFDs (F_1 and F_2) across the ~10 μm thick active region is clearly revealed [140]. For both (a) and (b) the devices were biased in pulsed mode (3.5 μs pulse width, 100 Hz repetition rate).

Figure 5.11. (a) One dimensional (1D) section analysis of the SVM voltage profile across the active region of the device at applied device biases spanning 2V – 23.5V for

V843. (b) 1D voltage profile curves at higher biases (20 V to 25 V) with a smaller device bias step (0.5 V) between the SVM scans so as to present more detailed EFD evolution in the NDR region for V843. The formation and evolution of two electric field domains over the multi-quantum-well active region is clearly observed in device bias ranges spanning 10 – 17 V and 22– 25 V in (a) and (b). (c) 1D voltage distribution SVM voltage profile across the active region of the V962 device at applied device biases spanning 2V – 24V.

Figure 5.12. The SVM measured electric field across individual cascade modules in the active region of operating V843 device as a function of applied device bias. The electric field increases in direct proportion with the applied device biases over ranges of 2 – 9 V and 18 – 21 V. Two EFDs coexist in bias ranges of 10-17 V and 22 - 25 V. Shown together is the partition number of the cascade modules in each EFD. Discrete symbols (Measured n_k, k = 1, 2, 3, 4) are calculated from the first approach ($n_k = l_k/d$) based on the SVM measurement results of EFD length (l_k) in (Figure 5.11 (a) and (b)). Solid lines (Calculated n_k, k = 1, 2, 3, 4) are calculated from the second approach (see text for details). The sum (Measured total) of the SVM measured module numbers ($n_1+ n_2$, or $n_3+ n_4$) is ~276.

Figure 5.13. Rough and high-resolution SVM scans. (a) The 1D SVM voltage curve cross the active region of the V843 device at a bias of 15 V and at T = 77 K. The rough scan (dashed line) spans 11 μm from the top metal layer to the bottom metal layer, clearly showing the co-existence of two electric field domains. It also shows that the voltage curve is straight and smooth in each section. The three zoomed-in scans (one close to the top metal layer, one at the EFD boundary, one close to the bottom metal layer) spans 500 nm each (solid curves in the insets). (b), (c), (d), The corresponding further zoomed-in curves that show the small voltage dips at the delta-doped injection barriers. The bottom curve in each figure (b, c, d) is the first order derivative ($|dV/dx|$) of each corresponding voltage profile curve, for the purpose of identifying the exact location of the voltage dips.

Figure 5.14. High-resolution 2D SVM image near the top metal/semiconductor interface. The 2D SVM voltage image over a 500 × 500 nm^2 scan area starting from the top

metal into the active region of the V843 device at 15 V and 77 K. It clearly resolves the top metal layer, the top GaAs contact layer, and 8 quantum cascade modules, which are separated by small voltage dips in this 2D voltage profile. The period of each individual cascade module is measured from the figure to be ~36.1 nm.

Figure 5.15. Resolution of individual quantum cascade modules and the boundary of EFDs. (a) The 2D SVM voltage image over a 500 × 500 nm^2 scan area near the EFD boundary on the V843 device at 15 V and 77 K. It clearly reveals two electric fields over a span of 14 cascade modules. The period of each individual cascade module is measured from the figure to be ~36.1 ± 0.1 nm. (b) A 1D zoomed-in view of three consecutive modules near the EFD boundary. The EFD boundary, in other words the turning point of the electric field, locates at ~12 nm ± 0.5 nm (due to 1 nm observable resolution limit of SVM) to the upstream of the delta-doped injection barrier layer of one module.

Figure 5.16. Resolution of charge shifting by hopping of EFD boundary. 1D SVM voltage profile curves at a series of device biases with a small incremental bias step (~10 ± 1 mV increase each time). The EFD boundary does not shift if the device bias increase is less than ~30 mV. When it does, the EFD boundary is observed to hop at least one module each time (a phenomenon being termed as *EFD boundary hopping*). All curves (except the one at 15.001 V) are accumulatively shifted by 0.01V vertically for clarity in the figure.

Figure 5.17. Simulation of the EFD boundary. Self-consistently solving the coupled Schrödinger-Poisson equations yields the simulation results of electron wavefunction and band diagram across the EFD boundary, confirming the EFD boundary is ~12.3 nm away from the delta-doped injection barrier in the transitional module. The delta-doped dopants are assumed to exponentially diffuse (by 48 Ang/decade) to the upstream direction of electron flux due to Si segregation during the molecular beam epitaxy of the QCL structure. The line running at GaAs conduction band edge (in gray and white) is the potential curve V(z) that the SVM tries to measure. The two curves on the top show the simulated charge density profile and electric field profile, respectively. The simulation is performed at a device bias of 12 V.

APPENDICES

Figure A.1. Schematic of the Metal-Metal fabrication process steps for the THz QCL device.

Figure A.2. SEM micrograph for fabricated (a) 200 µm and (b) 30 µm QCL after cleaving, and (c) image of packaged devices.

Figure A.3. Schematic of fabrication for the SISP THz QCL with metal-metal structure.

Figure A.4. SEM image of a fabricated SISP THz QCL.

Figure A.5. Schematic of the LIV measurement set up for THz QCL and ICL devices.

Figure A.6. LIV Measurement of THz QCL for sample V843.

Figure A.7. LIV Measurement of THz QCL for sample V775.

Figure A.8. Three electron tunneling resonances. Band diagram of cascade modules of the THz QCL (V843) active region with the moduli squared of the main electron wave functions. The cascade module of the THz QCL consists of four GaAs (Wells) and four $Al_{0.25}Ga_{0.75}As$ (barriers) layers. The energy separation between the upper (*2*) and lower (*1*) lasing states is ~13 meV at 77 K at an electric field of 21 kV/cm, corresponding to a lasing frequency of ~3.2 THz. It shows that at F = ~4.4 kV/cm **(a)**, the extraction level (*e*) aligns with the lower lasing level (*1*), at F = ~8.7 kV/cm **(b)**, the extraction level (*e*) aligns with the upper lasing level (*2*), and at F = ~21 kV/cm **(c)**, the extraction level (*e*) aligns with the injection level (*i*). The energy levels (*e*, *1*, *2*, *i*) are named in ascending energy order at threshold. Note that the level *2* may not be always higher than the level *1* even though it is conventionally named as the upper lasing state.

Figure A.9. Light-current density-voltage (*L-J-V*) characteristics of the THz QCL (V843). The *J-V* curve in (a) is measured at 10 K. At V_1 = ~5.5 V, the *J-V* curve shows a shoulder, corresponding to the *e-1*tunneling resonance. At V_2 = ~9.4 V, the *J-V* curve shows another shoulder, corresponding to the *e-2* tunneling resonance. At V_3 = ~21.8 V, the *J-V* curve shows negative differential resistance (NDR), corresponding to the misalignment of the *e-i* tunneling resonance. The device lases up to 138 K in pulsed mode. The pulse width is 250 ns and the pulse repetition rate is 1 kHz in the measurements. No perceptible difference on device performance is observed before and after the SVM scans.

List of Abbreviations

AFM	Atomic force microscope
C-V	Capacitance-voltage
DI	Digital Instruments
EFD	Electric field domain
ICL	Interband cascade laser
IR	Infrared
LIV	Light-current-voltage
MBE	Molecular beam epitaxy
MM	Metal-metal
MQW	Multiple quantum well
NDR	Negative differential resistance
NSOM	Near-field optical scanning microscopy
QCL	Quantum cascade laser
QW	Quantum well
RW	Ridge waveguide
SCM	Scanning capacitance microscopy
SEM	Scanning electron microscope
SKPM	Scanning kelvin probe microscopy
SISP	Semi insulating surface plasmon
SIMS	Secondary ion mass spectroscopy
SPM	Scanning probe microscope
SSRM	Scanning spreading resistance microscopy
SVM	Scanning voltage microscopy
TEM	Transmission electron microscope
THz	Terahertz

List of Publications

Referred Journals

1. R. S. Dhar, L. Li, H. Ye, X. Wang, R.Q. Yang, and D. Ban "Nanoscopic Resolving of Dynamic Charge Carrier Distribution in operating Interband Cascade Laser", Optics Express, submitted August 2014.
2. R. S. Dhar, S. G. Razavipour, E. Dupont, C. Xu, S. Laframboise, Z. Wasilewski, Q. Hu and D. Ban, "Direct Nanoscale Imaging of Evolving Electric Field Domains in Quantum Structures", Nature Communication, submitted April 2014.
3. R. S. Dhar, and D. Ban "Two-dimensional profiling of carriers in terahertz quantum cascade lasers using calibrated scanning spreading resistance microscopy and scanning capacitance microscopy", Journal of Microscopy, Vol. 251, No.1, pp.35-44, July 2013.

Referred Conferences

1. R. S. Dhar, S. G. Razavipour, E. Dupont, C. Xu, S. Laframboise, Z. Wasilewski, Q. Hu, and D. Ban, "Direct Observation of Electric Field Domain in the Active Region of Terahertz Quantum Cascade Laser", IQCLSW 2014 Conference, Italy, September, 2014.
2. R. S. Dhar, C. Xu, D. Ban, L. Li, H. Ye, R.Q. Yang, M.B. Johnson, T.D. Mishima and M.B. Santos, "Direct Observation of Non-uniform Electric Field in the Active Regions of an Interband Cascade Laser", CLEO 2014 Conference, San Jose, USA, June 8-13, 2014.
3. R. S. Dhar, Z. R. Wasilewski, and D. Ban, "Cryogenic Temperature Voltage Profiling of Operating Laser Devices", TechnConnect World 2014 Conference, USA, June15-19, 2014.
4. R. S. Dhar, and D. Ban, "SSRM and SCM study for doping concentration of THZ QCL devices", Photonics North 2012 Conference, Montreal, Canada, June 6-8, 2012, Proc. of SPIE, Vol. 8412, September 2012.

Chapter 1: Introduction

The emergent field of nanotechnology has evolved new areas of applications, such as nanoelectronics, nanomechanics, nanophotonics and nanomagnetics [1-3]. In nanophotonics, recent achievements to date include are one-, two-, and three-dimensional photonic crystals, transverse near-field structures, micro-ring photonic wire lasers, and quantum cascade lasers [4, 5,]. Because of the small size and high efficiency of these devices, high density integration is feasible, leading to very large scale integration (VLSI) photonics [6]. Room temperature luminescent silicon [7] may feature in one path to the integration of nanoelectronic and nanophotonic devices [8] into a unified system.

The advancement in nanoscale science and engineering characterisation bloomed with the invention of the Scanning Tunneling Microscope (STM) in 1982 [9] and then the subsequent invention of the Atomic Force Microscope (AFM) in 1986 [10], though TEM imaging technique was commercially available since 1939. The AFM and STM along with TEM became the most sophisticated tools for nanoscopic investigation and thus enhanced study in the area of nanoscience to characterize and understand the surface morphologies and electronic structure of material surfaces being used in nanoscale devices. These imaging techniques can be used to gain insight into the inner workings of quantum structures in nanophotonic devices. The functionality of the quantum structures relates to quantum confinement in the nanoscale regime is the prime focus of this thesis.

1.1 Motivation for the work

In today's era of nanophotonic devices, terahertz (THz) quantum cascade lasers (QCLs) are among the advanced high performance devices that will be used in future optical communication systems and also in various other fields like astronomy, sensing, security and medicine [5]. THz

QCL devices have been used in research for over a decade since their invention by Kohler et al. [11] in 2002. A schematic of a THz QCL device is shown in Figure 1.1. At present, these advanced THz QCL devices work at low temperature and perform best at liquid helium temperatures, down to ~10 K. The THz QCLs lasing temperature is one of the major handicaps, as it is well below room temperature and this is the biggest obstacle on the path of commercialization. This stands as the biggest disadvantage for this device to be operated commercially. THz QCL research has shown that the device lases when biased at high currents and voltages, where only a small amount of injected current contributes to output power, while the rest becomes thermally induced leakage current [12]. This leakage grows substantially at higher temperatures due to optical phonon scattering taking place in the active region of the device [12, 13].

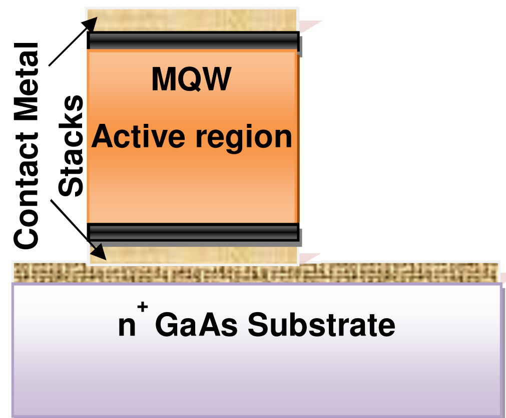

Figure 1.1. Schematic of the THz QCL structure.

The THz QCL device active region is around 10 μm thick, and depending on the design, the number of quantum well-barrier modules in the region vary from 200-300 [13-16]. Each of the modules consists of a highly doped layer. The total active region growth takes an extended time when using MBE growth tools, leading to potential instabilities of a few factors in the growth process. These are summarized as the inconsistency in layer thickness and the variation of doping concentration between the first and the last module grown, the layer composition shift along the growth process, and more general variability of the whole process from the start to the end. These issues stand as some of the key factors leading to nonlinearities in electric field distribution and high-field domain formation in operating devices, which may significantly degrade device performance and/or renders devices inoperable [17]. This may

impede THz QCL device operation at higher temperature, which is a challenge that needs to be countered. A hypothesis posits of the existence of at least 1-2 electric field domains (EFDs) in the current plateau and negative differential resistance (NDR) regions of operation for THz QCL devices as observed from light-current-voltage (LIV), external device performance, measurements [18]. This hypothesis is attained from the analytical study of supperlattice structures that revealed high field domain formation in the device [19-21]. Measuring and confirming the active region structural parameters and their uniformity after material epitaxial growth and device fabrication is of utmost importance.

The internal dynamics, particularly the electric field distribution and formation of EFDs in the active region of the device, is the major issue that possibly debilitates high temperature performance. In-depth research is needed to understand the device structure from a device growth point of view by imaging the quantum well-barrier module structure before device characterization and estimating the doping concentration of the active region of the device by 2D carrier profiling. This is an important aspect that needs to be studied and experimentally analyzed, and these findings can be accommodated for in new device design.

The core of this thesis is the desire to directly probe, measure, image, and observe the internal behaviour and dynamics (relating fundamental physical parameters such as potential, electric field, charge carriers) of operating THz QCLs, interband cascade lasers (ICL) and other quantum/nano devices. This is possible by establishing a connection and relating the internal mechanisms with external measures of these devices. For this purpose, demonstration and evaluation of enabling tools are required for research and development in quantum nanoscopic physics. No technique perhaps has yet been testified that can, without destroying the device, experimentally relate external measures to direct carrier profiling and mapping of carrier concentration in 2D structures. With the establishment of enabling tools or techniques, the key inner workings of operating nanodevices – voltage profiles, carrier densities, EFDs – can be measured at the nanometer scale. Further, research is needed to confirm the delta-doping profile and uniformity of the quantum cascade modules in fabricated THz QCLs, as both the doping and uniformity remains important to correlate the structural parameters to external device performance.

Visualizing EFD and extracting the inner dynamic profiles of the devices resolve the fundamental device parameters that may limit best performance. This present work explores

quantum optoelectronic devices under lasing conditions and opens up new possibilities for engineering novel materials and devices with unparalleled properties. Thus, establishing and developing a tool that can relate the inner workings to external measures of the device, which can bring forth some fundamental properties that may be able to solve the major concerns about THz QCL devices of low lasing temperature is desirable.

1.2 Research Objectives

Scanning electron microscope (SEM) images have been employed to show device structure [16], but detailed structural information (such as individual quantum cascade modules that are made of ultra-thin GaAs and AlGaAs layers) cannot be resolved due to the SEM's limited spatial resolution. Transmission electron microscopy (TEM) was used to resolve fine structures, including nanometer thick individual quantum wells and barrier layers, but it is a destructive process – semiconductor wafers/devices cannot be used after TEM inspection [16]. Secondary ion mass spectroscopy (SIMS) can be used to measure the dopant concentration profile in semiconductor wafers, but it is also a destructive process, and in some cases, it is not quite suitable, for example, for probing delta-doping dopant profiles [17].

AFM-based techniques are the alternative for performing non-destructive carrier measurement on nano regime quantum devices. Scanning spreading resistance microscopy (SSRM) [22, 23] and scanning capacitance microscopy (SCM) [24, 25] are the two enabling techniques for 2D dopant profiling and mapping of dopant concentration for nanometer regime devices. Scanning voltage microscopy (SVM) is another AFM-based contact mode measurement technique used to characterize and measure optoelectronic based semiconductor laser devices. SVM is the most advanced technique based on the nature and diversity of its usage that can scan operating nanophotonic devices. These SCM, SSRM and SVM techniques have been branded noteworthy, being able to measure and resolve nanometer scale features non-destructively on operating devices.

In this thesis the focus is to answer critically important questions regarding the internal device dynamics (electric potential, electric field and dynamic charge carriers) for operating optoelectronic devices such as THz QCLs and ICLs. The active region of the THz QCL is to be visualized, imaged, and its carriers profiled to determine the electric field variations that significantly enhance the nonlinearity and initiates in high field domain formation under

operating conditions. For this purpose SVM is developed and established to operate in cryogenic temperature condition (THz QCLs lases at low temperatures) and measure the internal dynamics of the devices. The objectives of this research are to develop and focus on significantly original contributions that establish a compelling connection between the external measurement of nanophotonic devices and the fundamental internal device physics while finally proving and demonstrating with the AFM instrument as a tool with advanced SVM techniques that can characterize nanometer scale features nanoscopically.

SVM was meant to be initially employed on mid-infrared (IR) ICL devices to directly probe and measure the voltage distribution across the depth of the device. Potential profiles are to be generated and the measurement can quantitatively estimate the charge density at the nanometer scale of the device. Cryogenic temperature SVM measurements on THz QCL devices are to be performed, which will track evolution of the EFDs if any. The voltage profiles, carrier densities, and EFDs that constitute the key inner workings of operating nano-devices will thus be measured at the nanometer scale. This experimental verification and analysis is necessary for new and improved device designs. Thus, the internal mechanisms of quantum nanophotonic devices under operation are to be explored.

1.3 Organization of the Thesis

The thesis is organized into seven chapters.

In Chapter 2, *Literature and Instrument Review*, a detailed introduction to the AFM instrument is presented, detailing different modes of operation and a view of the techniques in contact mode measurement used in the later chapters for the project. A review of previous works on the three different scanning probe microscopy techniques - SCM, SSRM and SVM - is provided. The findings of the literature led to the formulation of the challenges pursued in the remainder of the work. A brief review of the instruments that will be used in the rest of the research is presented.

Chapter 3, *Two-Dimensional Dopant Profiling of Terahertz (THz) Quantum Cascade Laser (QCL) Devices*, exhibits the nanosurface 2D profiling of the device. SSRM- and SCM-based AFM techniques are applied to two types of THz QCL devices. The module thickness in the active region layer is identified due to charges in the delta-doping layers. The heavily doped delta-doping layers present in the injector barrier of each quantum cascade module are resolved

for the first time indicating uniformity of the MBE device growth. The nominal doping concentration of the active region of the THz QCL device is semi-quantitatively determined and estimated signifying the localization of static charge carriers present in the device.

In Chapter 4, *Nanoscopic Probing for Determining Charge Density in Mid-IR Interband Cascade Lasers (ICLs)*, a novel cryogenic-temperature scanning voltage microscopy (SVM) technique based on the AFM system is developed, established and applied to probe the inner workings of an operating interband cascade laser (ICL). High precision and high resolution SVM measurements revealed the voltage profile and in turn the electric field distribution in nanometer regime across the active region of the device. SVM performed on operating ICL devices at cryogenic temperature down to 77 K and at room temperature of 300 K. The substantial variation of electric field over the active region in each cascade stages are detected, which suggests considerable charge transfer and accumulation with type-II QW layers, resulting in some strong internal electric field in the region. Spatial segregation of electrons and holes due to the unique type-II band-gap alignment in the device are observed leading to direct observations of the inner workings of the operating nano-optoelectronic device.

In Chapter 5, *Direct Observation and Determination of the Evolution of Electric Field Domains (EFDs) in THz QCL Devices*, evolution and formation of the electric field domains (EFDs) are directly observed and determined with the help of cryogenic-temperature SVM technique probed in nanometer scale on operating THz QCL devices. Nanosurface profiling on both non-lasing and lasing THz QCLs resolved the EFD boundary position along with its evolution. The two-dimensional voltage profile achieved from SVM provide clear evidence of the existence of two slopes to exist in the active region of THz QCL under operation, indicating evolution of EFD at the transfer of the slope. The EFD boundary exist where the maximum amount of dynamic charge carriers accumulate in the module, thus resulting in the EFD boundary to hop from one module to the next with increase in applied device bias when the required charge accretion overcomes the bias. The electric potentials profile across quantum cascade modules and the charge carriers that perhaps instigate the evolution of EFDs are directly and experimentally resolved from operating THz QCL devices.

Chapter 6, *Conclusion and Future Work*, summarizes the advances made during the course of this work. The main conclusion and original contributions are highlighted. An outlook is given on future directions and application of the experimental methods pioneered herein.

Chapter 2: Literature and Instrument Review

This chapter introduces the atomic force microscope (AFM) as an instrument that has the ability to perform nanosurface profiling of carriers in the atomic scale (nanometer regime) by imaging the sample surface. The instrument has a cantilever bearing a tip with a radius on the order of ~20 nm which scans the sample surface using some implied force with the help of the AFM controller. Some important uses of AFM measurement are discussed based on contact mode scanning on application of DC or AC biases to the tip or by applying bias to the sample to characterise. The benefit of the instrument stands as it can scan semiconductor samples presenting miniature features and in-depth details of a sample's operating characteristics without the damage that is typical with the use of instruments like secondary ion mass spectroscopy (SIMS) or transmission electron microscopy (TEM).

This chapter also outlines the two different types of AFM used for this project, the Dimension DI3100 AFM and the Attocube AFM, providing a detailed description of both. The experimental procedures and initial set-up of these instruments for particular measurements are discussed. The room temperature AFM was set up for contact mode measurement such as scanning spreading resistance microscopy (SSRM), scanning capacitance microscopy (SCM) and scanning voltage microscopy (SVM) on semiconductor devices. SSRM and SCM scanning procedures in the devices have also been discussed. For low temperature measurement of the THz QCL devices, the setup of the Attocube AFM to measure the voltage distribution and profile the nonlinearity effect of the electric field has also been described.

2.1 Introduction to Atomic Force Microscope (AFM)

AFM is a type of scanning probe microscopy (SPM) with very high-resolution on the order of fractions of a nanometer, more than a thousand times smaller than the optical diffraction limit. In 1982, Gerd Binnig and Heinrich Rohrer [9] made the first scanning tunneling microscope (STM), a precursor to the AFM, earning them the Nobel Prize for Physics in 1986 [26]. In 1986, Binnig, Quate and Gerber invented the first AFM, which became commercially available in 1989 [10]. The AFM became one of the foremost tools for imaging, measuring, and manipulating matter at the nanoscale regime. A mechanical probe is used to collect the information by "feeling" the surface. The very precise scanning is enabled by the piezoelectric elements that execute tiny but exact movements on command. Sometimes conducting cantilevers are used with some variations and the electric potentials are scanned. The electrical conductivity or transport is probed to the underlying surface, in more advanced versions of the AFM, where the currents pass through the tip, though with reports of inconsistent data this is eventually much more challenging [31].

The surface of a rigid material is analyzed by the AFM technique all the way down to the atomic level. A mechanical probe tip is used by the AFM to magnify surface features up to 10^8 times, producing a 3-D image of the surface. The technique is based on the STM, but electrical conduction not required in the AFM. AFM is used to study the surface roughness analyze the 2-D and 3-D profiles, image the device structure, dopant profiling, perform transverse cross-section analysis, and also understand materials problems in many areas. AFM is advantageous compared to the conventional microscopy techniques. The sample is probed on the AFM for measurements in *x, y,* and *z* (normal to the sample surface), so that three-dimensional images of a sample surface is obtainable [26]. In the fields of materials science, chemistry, biology, physics, and the specialized field of semiconductor physics, AFM has proven significant with these useful options. The continuing development of AFM technology provides scientists with a powerful tool to characterize a variety of sample surfaces under different conditions. AFM is an extremely versatile and useful form of microscopy particularly for its ability to image nonconducting specimens at, in some cases, the atomic scale. AFM can be used in room temperature and more recently at low temperatures even down to 4K as cryogenic AFM for near-field optical scanning microscopy (NSOM), STM and confocal microscopy (CFM).

AFM has been commercially available for years and different types of AFM are used for different applications. The well-known general purpose AFM from Digital Instruments is the Dimension series AFM, built for scanning at room temperature. The Attocube AFM is built for both room temperature and cryogenic use down to 4K. Both these systems can scan the sample surface under different conditions and different modes of operation. The AFM measurements achieve scanned images from the sample surface and also the topographic views [26]. The surface morphology and profile of the scanned surface can be acquired, detecting even features of nanometer orders.

2.2 AFM Measurement

A tip (probe) is mounted at the end of a cantilever on the AFM and is used to scan the specimen surface. The cantilever tip is normally made of silicon or silicon nitride with a radius of curvature in the order of nanometers. The tip is brought close onto the sample surface resulting in force to the tip, deflecting the cantilever according to Hooke's law. If the tip was scanned at a constant height the tip might collide with the surface due to its roughness, causing damage. Hence, to adjust the tip-to-sample distance and to maintain a constant force between the tip and the sample, in most cases, a feedback mechanism is employed. The sample needs to be able to move in the z direction for maintaining a constant force, and in the x and y directions for positioning the sample for scanning, and so it is mounted on a piezoelectric tube. In modern AFMs the tip is mounted on a vertical piezo scanner while the sample is being scanned in X and Y using another piezo block. The topography of the sample is represented as a resulting map of the area $z = f(x,y)$. Depending on the application, the AFM can operate in a number of modes. In general, the possible imaging modes are contact mode, non-contact and tapping modes where the cantilever is vibrated.

2.2.1 Contact Mode

In contact mode AFM, also known as static mode of operation, the cantilever is “hauled” across the sample surface and the delineations of the surface are measured directly using the cantilever deflection. In this mode of operation, the cantilever tip deflection is used as a feedback signal. On the cantilever, an extremely low force of ~10^{-9} N is maintained, thereby pushing the tip against the sample [26]. Low stiffness cantilevers are used to boost the deflection signal,

reducing the noise and drift at the time of scanning. Strong attractive forces exist close to the sample surface, causing the tip to "snap-in", and so the force between the tip and surface is kept constant. The actual tip deflection between the tip and sample is recorded and then converted into an analogue image of the sample surface as demonstrated in the schematic of Figure 2.1. In order to start scanning, the AFM tip is manually brought close to the surface of the sample, and then the adjustment in tip–sample distance is made by the scanner based on the user-determined set point. The tip then scans the sample under the action of a piezoelectric actuator, by moving the sample or the tip relative to the other [26]. A constant tip–sample separation is maintained by moving the scanner in the *z* direction in the feedback loop, shown in Figure 2.1, and the set point deflection is retained.

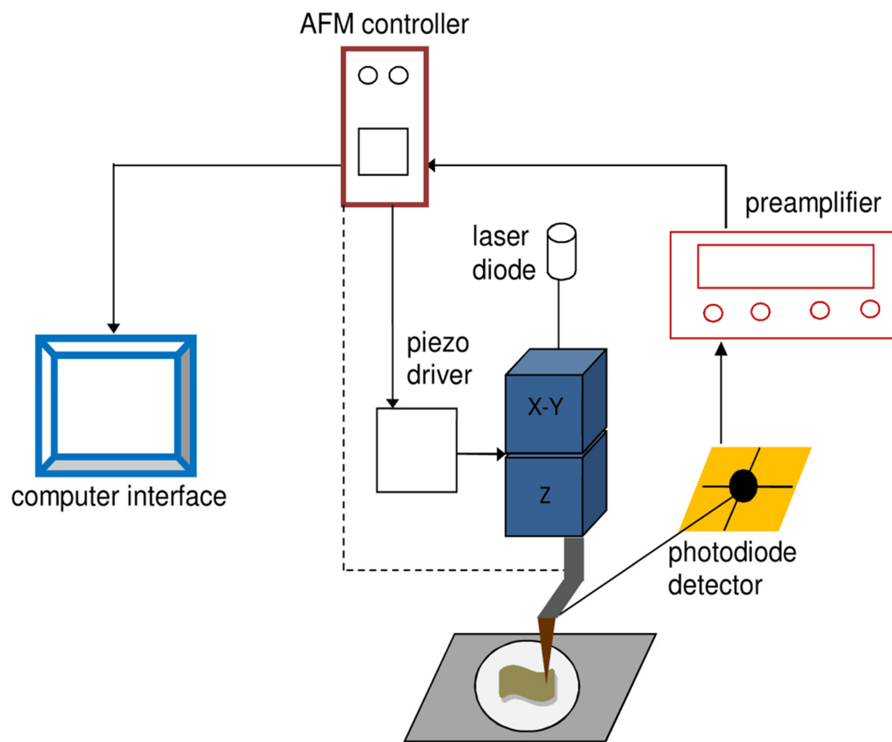

Figure 2.1. Schematic of AFM measurement set up for contact mode profiling [27].

In contact mode operation, the AFM measurement is performed for several types of useful applications, all with different measurement profiling options. Electrical measurements are one of the most important contact mode applications. For this type of measurement with the AFM system an electrical (AC and or DC) bias is applied to the probe tip or to the sample surface at the time of scanning by the AFM controller. This type of bias application for AFM

measurement results in measuring the resistance, current, voltage or capacitance change on the sample surface from one point to the other as the tip scans across the region. This type of scanning basically injects the bias to the surface through the tip and reads the change giving a cross sectional analysis of the device and a view of its behaviour for resistance, capacitance and voltages. The tips used for this type of measurements are generally conductive tips made of PtIr, magnetic- or diamond-coated depending on the device to be scanned. This type of profile measurements are known as scanning spreading resistance microscopy (SSRM), scanning capacitance microscopy (SCM), and scanning voltage microscopy (SVM).

2.2.2 Non-contact mode

In the non-contact or dynamic mode, the cantilever is made to oscillate slightly above its resonant frequency where the amplitude of oscillation is typically a few nanometers (<10 nm). The tip-sample interaction force modifies the oscillation amplitude, phase and resonance frequency. The sample's characteristic is thus studied on the basis of these changes with respect to the external reference oscillation. The scanning software constructs a topographic image of the sample surface as the tip-to-sample distance at each data point (x,y) is measured. In this mode of measurement the tip or sample degradation effects do not occur. Frequency modulation is one of the schemes for dynamic mode operation. As the frequency is measured, the frequency modulation mode allows use of very stiff cantilevers providing stability close to the surface [27].

2.2.3 Tapping mode

The tapping mode, also known as intermittent contact mode, is a developed version of the dynamic contact mode AFM [28]. This came into being when the non-contact dynamic mode measurements posed a major problem. Many samples develop a liquid meniscus layer in ambient conditions, and so keeping the probe tip close to the sample for short-range forces to become detectable while preventing sticking to the surface pose is a major problem. Tapping mode operation is similar to non-contact mode where the cantilever is made to oscillate at or slightly below its resonance frequency with amplitudes between 20 to 100 nm [28]. This “tapping” method lessens the damage done to the surface and tip compared to that done in contact mode and is gentle enough even for the visualization of supported lipid bilayers or adsorbed single polymer molecules under a liquid media.

2.3 Advancement in contact mode AFM measurement

The AFM measurement under contact mode is one of the foremost forms of AFM scanning. As discussed previously, here the tip scans the surface of the sample in close contact with force applied to the tip, also sometimes known as force microscopy. While scanning the cantilever is pushed against the sample surface and the cantilever deflection is sensed, which is compared to the desired value of deflection. If the measured deflection is different a voltage is applied to the piezo to restore the desired value of deflection, thus measuring the height of features on the sample surface. For measuring semiconductor device samples contact mode allows trapped electrostatic charge (partially dissipated) to contribute to attractive forces. A minimum force is controllably applied by the probe to the sample, creating a substantial frictional force while the probe scans the sample. In some cases these forces may be strong and far more destructive than the normal force, sufficient to damage the sample or blunt the cantilever probe, in turn distorting the resulting data. Controlling the force to some extent and scanning the sample without causing damaging while getting meaningful data is of prime importance. The contact mode measurement can thus be worked under some different profiles.

2.3.1 Principle for major contact mode AFM profiles

There are different profiles/varieties of contact mode AFM, including SSRM, SCM and SVM. All these types of measurement strategies require application of force to the tip at the time of scanning for better resolution and detection of the change in the device from layer to layer. But this force needs to be controlled carefully while measuring so as not to damage the sample or the probe.

The first concept of SSRM came from Vandervost et al. [29, 30]. The technique used high force, so the measured resistance is dominated by spreading resistance and not the contact resistance. The objective of SSRM is able to directly measure the two-dimensional carrier profile and the sample cross-section [31]. A DC bias is applied between the tip and the sample backside when scanned using a hard probe, while the current is measured using a logarithmic current amplifier in the range of 10 pA to 0.1 mA. Due to application of high force on the tip the preferred probes for SSRM measurement are made of silicon coated with doped diamond [32, 33]. The resistivity is linked theoretically to the measured resistance of the sample under the probe by the equation:

$R = \rho/4a$ (2.1)

where ρ is the resistivity of the sample and "a" is the electrical radius of the probe. This is a simplistic approach which is, not fully satisfactory as a range of inaccuracies and additional concerns exist, resulting from the density of surface states and their energy distribution, the shape of the probe, and the applied force. Calibration sample measurements should therefore be performed, and the ideal curve deviation is expressed with a barrier resistance component $R_{barrier}$ as proposed by De Wolf et al. [23]:

$R = \rho/4a + R_{barrier}(\rho)$ (2)

A direct link to the carrier distribution information is offered by the SSRM technique and the possibility of realizing first-order quantification of measurements [34] is achieved, with advantages being spatial resolution and dopant gradient resolution combined with adequate reproducibility [31, 34]. SSRM benefits from a large dynamic range and the conductivity of the diamond probe, and is measured in series with the spreading resistance.

The SCM technology dates back to 1985 when Matey and Blanc described the instrument to measure capacitance [35-37]. Slinkman et al. [38] patented SCM based on AFM in 1991. In this the AFM controlled the tip position while the capacitance measurement was independent. In 1995, Digital Instruments, Inc. commercialized a combination of the AFMs and the capacitance sensors to form SCM [24, 39, 40]. For SCM the tip needs to be highly electrically conductive and, while scanning the sample, it has to be in electrical contact with both the capacitance sensor and the sample. The spatial resolution of the scanned image is determined by the tip radius. In SCM the sensor is used to measure the capacitance using a driven LCR resonant circuit incorporated in series as part of the circuit, while the oscillation amplitude provides the capacitance measurement [24]. Due to the voltage-dependent capacitance between the conductive SCM tip and a semiconductor sample, a contrast appears in the SCM image. The SCM electronics measure the difference in capacitance between the tip and the sample. SCM operates in two different modes: constant ΔV mode or the open-loop mode; and the constant ΔC mode or the closed-loop mode. In open loop mode a sinusoidal AC voltage is applied between tip and the sample. In the closed-loop mode a feedback loop is added onto the SCM to adjust the magnitude of AC bias keeping ΔC constant.

Scanning voltage microscopy or nanopotentiometry is a recent development of the AFM system. This technology has been employed to study the 2-D profiles of the electrical potential within the device when under operation, thus presenting a clear understanding of the device functionalities with nanometer spatial resolution [41]. The progress of this expertise concentrates mostly on the optical and laser devices. The core challenges of probing the internal voltage profiles directly and quantitatively, and establishing the free doping concentration within the quantum-well lasers have been tackled well by this method [41]. For SVM there should be no DC offset, and no inversion of voltage data referencing the *n*-type contact to ground as part of the experimental configuration. The ground loop noise is removed as the grounds of the current source and voltmeter are connected. The probe noise is also abridged as the cable shield is connected to the common ground point. Very high input impedance voltmeter usage is crucial to measure the voltage difference between the AFM probe contact point and the reference point while minimizing the disruption due to the device operation. The device is scanned by a diamond-coated conductive tip due to its high force constant and resonance frequency. SVM measures the voltage variation across the multiple-quantum well layers for laser diodes under operation in the nanometer regime to give a 3-D analysis of the presence of free carriers present. The method works when the conductive AFM tip is placed on a semiconductor material not in electronic equilibrium and the floating potential is established between probe and bulk semiconductor [42]. The probe scans the sample surface while interacting with electrons and holes in the active region of the device. The net current between probe and the device is kept at zero, adjusting the Fermi level position on the probe side with help of the high impedance amplifier circuit in the feedback loop. The potential difference is measured as a function of distance, as the AFM probe scans across the lateral distance of the active region of the device.

2.3.2 Dopant and Charge carrier profiling and analysis

There has been much work done in the development of the SSRM and the SCM technologies based on the AFM systems [22-25, 31, 32, 34, 35]. Presently both these technologies are quite established methods for profiling the free carrier concentration in devices. The expertise has been initially applied on silicon-based devices for study and was later employed on optical laser diodes based on III-V semiconductors by detecting a change in resistance and the change in dC/dV due to variations in capacitance for SSRM and SCM, respectively. SSRM and SCM

modules are available commercially [24, 32, 35] along with the AFM systems that can directly observe and record the determined data and feed it to the AFM controller while scanning is performed on the device surface. SVM, compared to SSRM and SCM, is a newer technology that establishes the dopant profiling of the device while giving a clear understanding of the change in voltage taking place between different layers at the time of scanning. A brief review of the work done to present in these areas are described below.

2.3.2.1 Scanning spreading resistance microscopy (SSRM)

SSRM measurements were performed on the cross section of the device structures. Eyben et. al. [31] performed SSRM on $n^{++}p$ that was As-doped to a level $>10^{20}$ at/cm^3 with a p-type Si substrate of 2×10^{15} at/cm^3 and compared these readings with simulation results as shown in Figure 2.2. The absence of the junction peak is clearly indicated while a slow increase of the resistance with depth was observed; this is due to the induction of the inversion layer along the cross section. A large depletion layer is formed, due to the low doping level in the bulk, so the conduction band electrons become majority carriers, leading to band bending near the surface to form the inversion layer [31].

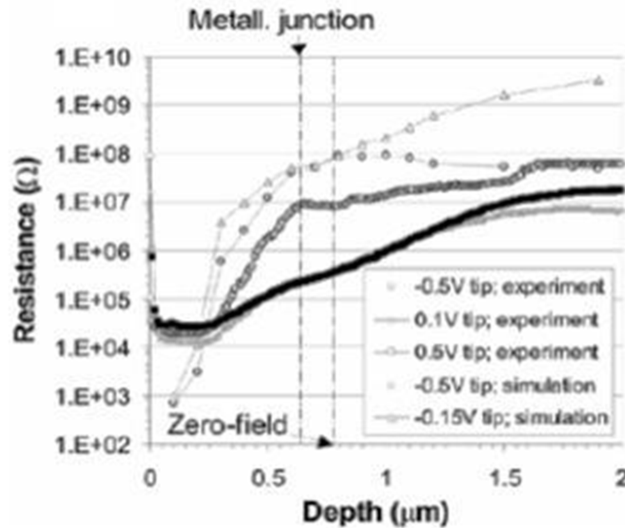

Figure 2.2. A comparison of the experimental and simulated results showing SSRM resistance profiles for $n^{++}p$ structure. [31].

The quantification of the SSRM data is done by using equation (1) from section 2.3.1 which depends on the tip radius "a", but, due to the influence of the nanocontact nature

(Schottky), between the surface and the conductive probe resistance, straight-line dependence is not pragmatic. More practically, the approach of using a look-up procedure based on calibration curves on the standard data of known samples provides high-reproducibility estimation for an assurance quantification accuracy of around 20–30%. InP is an essential material for optoelectronics due to the intrinsic material properties for the laser diodes and SSRM has been applied to study the 2D features for the complex device structures that are critical for reliability. A high-quality interface needs to be formed with the InP layers to provide both current and optical confinement. The parasitic capacitance of the total laser structure is reduced by the highly resistive blocking layer, either semi-insulating (SI) layers or reversed p/n junctions, significant for high-speed applications [31, 43]. This leads to a complicated and unpredictable 2D dopant/carrier distribution. Here, SSRM offers a unique capability without device destruction: providing a detailed 2D analysis of the structure [44].

A SSRM image of an InP laser is shown in Figure 2.3 (a) [31] with two semi-insulating (SI) layers. The non-homogeneous, ultrathin, SI-2 layer has been resolved and measured, clearly as viewed in Figure 2.3 (c). The line analysis of Figure 2.3 (a) has been undergone, and both Line 1 and Line 2 resistance variation with device depth is presented in graphically in Figure 2.3 (b). The two conductive slices next to the mesa are seen to be linked with the p-type cap layer, when Line 2 crosses the mesa and the gap is the extension of SI-2, giving a high SSRM resistance up to 10^9 Ω [31]. Thus exceptionally complicated structures are revealed from this analysis by SSRM. As the growth rate and the dopant/carrier profiles are of a 2D nature, so conventional 1D profiling techniques (e.g. SIMS, etc.) or 2D metrology techniques (e.g., SEM, etc.) are not capable of this type of analysis [17, 31, 45]. SSRM measurements were also carried out on quantum well structures of III-V based semiconductor materials for a vertical cavity surface emitting laser (VCSEL) sample [46]. The VCSEL structure had two Distributed Bragg Reflectors (DBRs), with three InGaAs quantum wells in between the GaAs regions, on top of bulk GaAs. Four different scan images for different implantation doses “a” 7 x 10^{13} cm^{-2}, “b” 2 x 10^{14} cm^{-2}, “c” 8 x 10^{14} cm^{-2}, and “d” 1 x 10^{15} cm^{-2} were performed [46]. The quantum well GaAs region between the upper and lower DBRs of each picture was aligned vertically with the middle GaAs region [46]. From the SSRM image, resistance lines were drawn and a detailed view of changes in resistivity magnitude due to the implantation was achieved. Thus, SSRM can detect

nanometer range features like quantum wells and also indicate the resistivity change taking place in the region, giving a qualitative measure of the doping concentration of the sample.

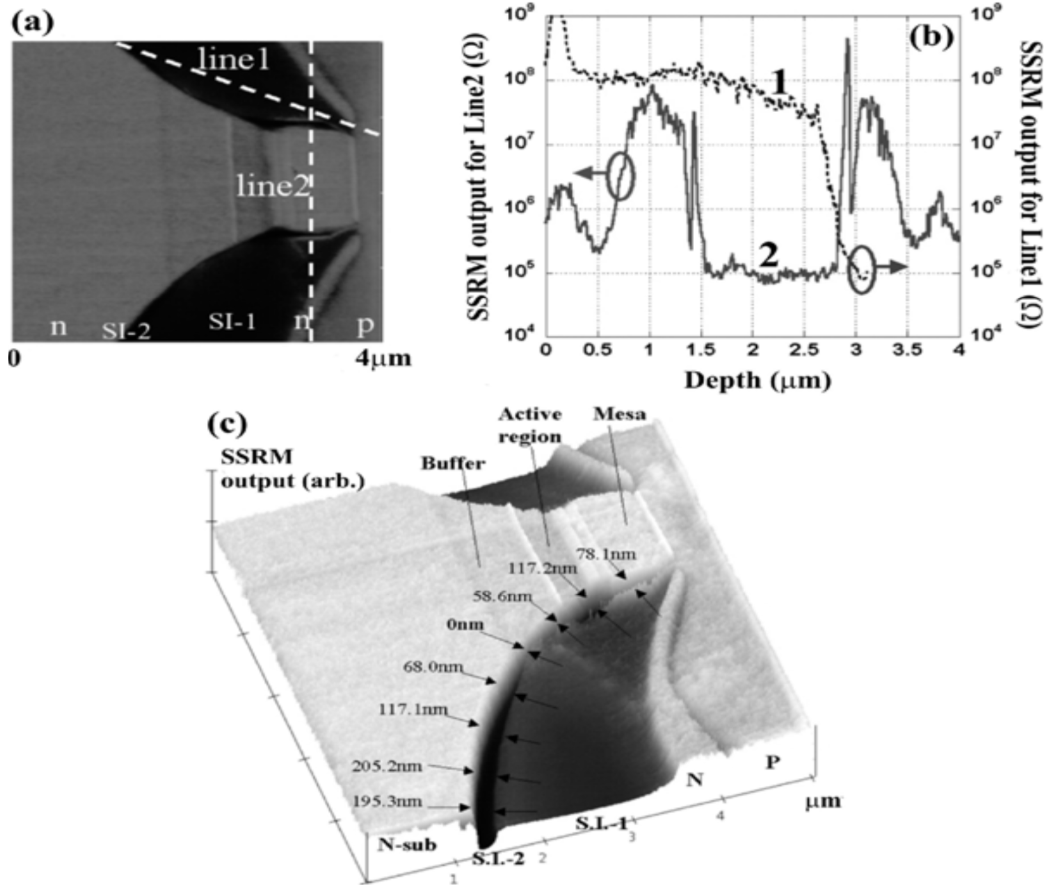

Figure 2.3. SSRM image of InP based laser (a) the mesa of the structure resolved closely, (b) both line 1 and line 2 shown in (a) are plotted as analysis graphs, (c) 5 μm mesa. [31]

Ban et al. [33] employed SSRM to study the buried heterostructure (BH) multiple quantum well (MQW) laser. The measurement was performed by a Digital Instruments DI 3100 AFM using a conductive diamond probe. SSRM imaging gave the cross section view of the structure as shown in Figure 2.4 (a), obtained from a freshly cleaved facet of the device [33]. At the bottom of the image the n-substrate appeared as a bright region while the mesa structure, though buried, is clearly resolved in the SSRM image. The narrow MQW active region, grown by MOCVD, was resolved as a bright ribbon near the center of the image clad by p-and n-doped layers above and below [32, 33]. The p-n-p-n current blocking structure of the laser appears symmetrically on either sides of the active region. Figure 2.4 (b) shows the averaged spreading

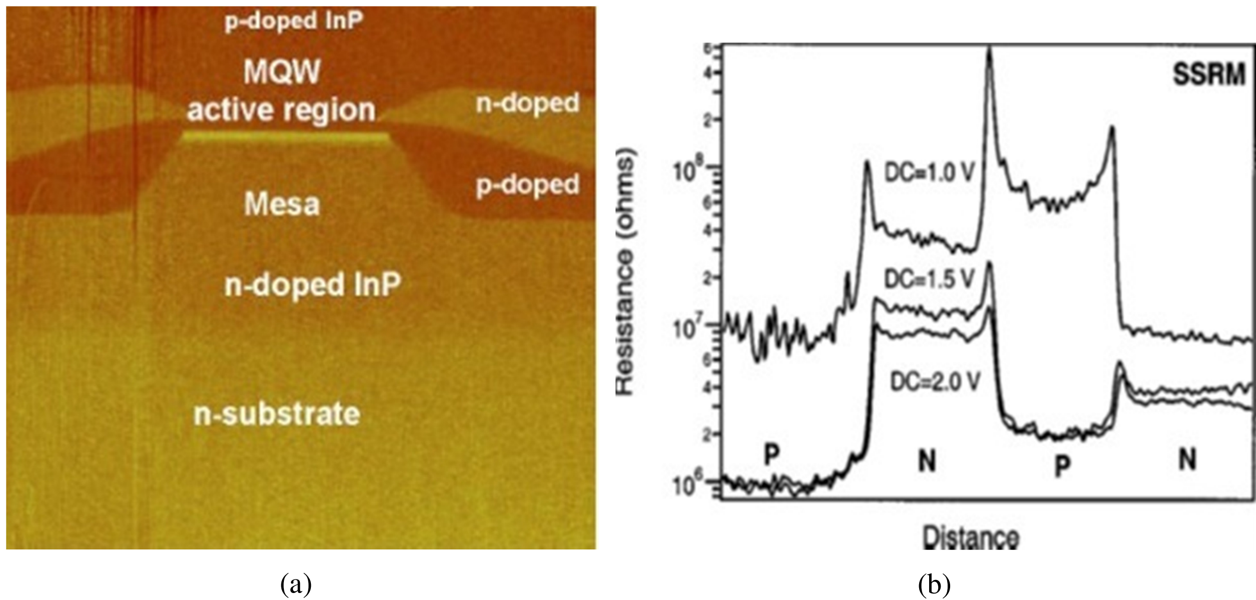

(a) (b)

Figure 2.4. (a) 5 µm SSRM scan image of a multiple quantum well buried heterostructure laser sample [33]. (b) SSRM resistance profile at three different DC bias conditions of the p-n-p-n current blocking structure [33].

resistance across the distance of the device for the p-n-p-n structure scanned at different DC biases [33]. An increase in DC bias on the AFM tip shows a decrease in the resistance, providing an observation of SSRM dependence. The carrier concentration of the p-n-p-n structure has been estimated based from a known GaAs staircase sample [33]. SSRM measurement was then used to profile the dopant concentration in the device structure, establishing a good correlation between the nominal doping density and the SSRM dopant density [33]. Thus, SSRM imaging achieves spatial resolution in the nanometer regime, resolving the pn junctions to give a clear view and the understanding required for a complicated BH MQW laser device.

2.3.2.2 Scanning capacitance microscopy (SCM)

SCM measurement is based on the theory of metal-oxide-semiconductor (MOS) capacitance. In Figure 2.5 the capacitance is demonstrated to vary with applied tip-sample bias for the MOS structure, depicting the SCM contrast mechanism [24]. An AC bias voltage V_{ac} is applied to induce a change in the tip-sample capacitance, ΔC, which varies the C-V curve between the tip and the semiconductor. As the tip scans a highly doped semiconductor, V_{ac} changes with small

ΔC, and as the tip shifts over a low carrier concentration region, Vac induces large ΔC [24]. The SCM scanning is performed on the cross section of the device and is quite similar to SSRM, resolving contrast between different layers of varied doping concentration. SCM, is a nanosurface profiling and qualitative analysis tool that has been used many a times [24, 32] for failure analysis and to measure 2D carrier profiling. Quantitative 2D dopant profiles are also obtainable from SCM images [24, 32]. The quantification of the SCM data is done on the basis of the slope of the C-V curve and calculating the dC/dV values from the measurement. While

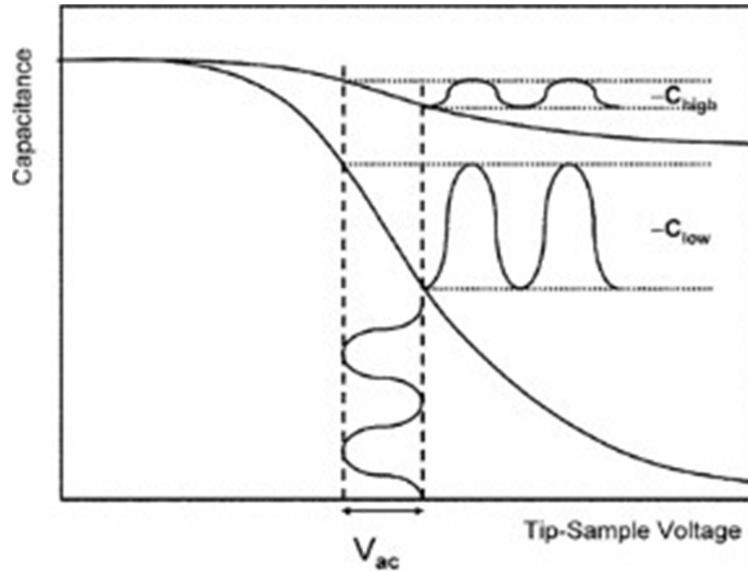

Figure 2.5. SCM image contrast variation showed schematically [24].

SCM scan is performed on the device, it needs to have a thin layer of oxide all over the device surface so as to form the MOS capacitance between the conductive probe and the surface. The approach of using a look-up procedure based on calibration curves on the standard data of known samples provides quantification accuracy of around 10–20% [24]. SCM has been used for 2D dopant profiling in III-V based semiconductor devices. SCM has been applied on laser diodes to study the 2D features of complex device structures critical for performance and device reliability [24, 32, 39, 42]. SCM technology has also been used to study the stored charge carriers that is to read previously stored data, present in the floating gates in non-volatile memory (NVM) devices, a proposed method to measure on-site charges in flash electrically erasable programmable read only memory (EEPROMs) [47]. These charges are said to be in either an ON/OFF state in the form of binary bits such as "1b" and "0b" [47, 48].

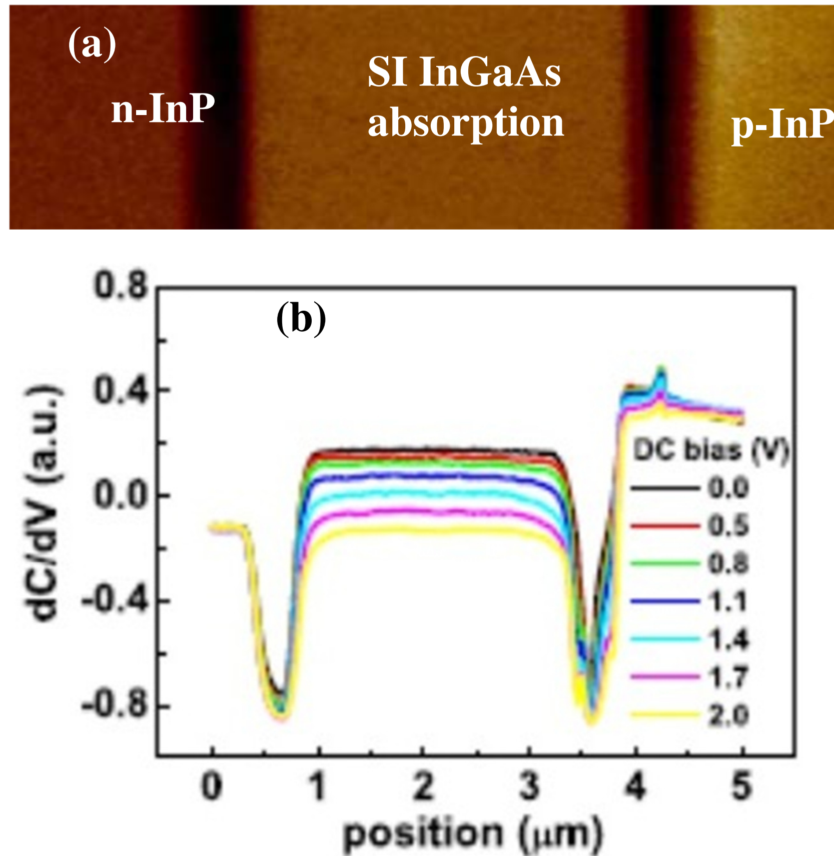

Figure 2.6. (a) SCM image of the APD structure. (b) SCM dC/dV profiles for a variety of DC biases [25].

SCM measurements have been carried out on the cross section of the avalanche photodiode (APD) by Yin et al. [25] at 1 V modulation voltage and dC/dV measured as shown in Figure 2.6. The metal organic vapour-phase epitaxy (MOVPE)-grown InGaAs/InP APD structure had a n-InP substrate followed by a 200 nm Si-doped n-InP buffer layer, a 2.8 μm semi-insulating (SI) InGaAs absorption layer, a 70 nm Si-doped n-InGaAsP grading layer, a 170 nm Si-doped n-InP charge layer, a ~500 nm semi-insulating (SI) InP multiplication layer and a ~2.0 μm Zn-diffused p-InP layer [25]. The layers of the sample were resolved in Figure 2.6 (a), showing the disparity depending on the doping concentration for each layer and a noticeable variance of the SCM signal is observed in the InGaAs absorption layer. The DC bias is applied between the tip and the sample, modulating the surface band bending during SCM measurement to study the surface potential from the dC/dV signal. The SCM profile across the device structure under varied DC tip bias is shown in Figure 2.6 (b). With the increasing DC bias in InGaAs

absorption layer, the dC/dV signal is found to shift from positive to negative [25], illustrating the clear nature of the APD device.

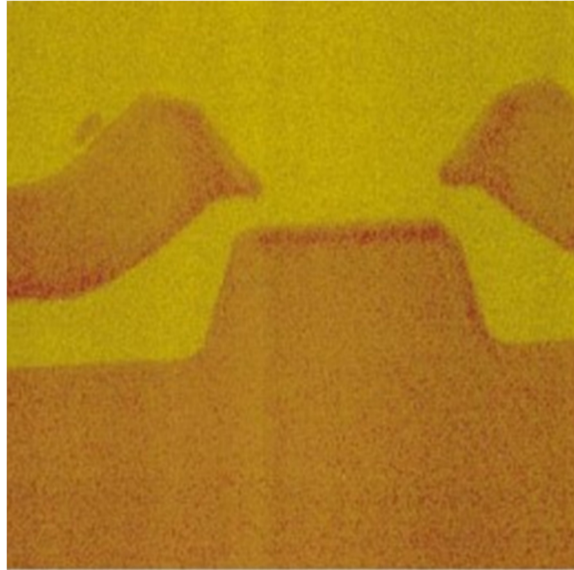

Figure 2.7. SCM image of the InP Buried Heterostructure multiple quantum well structure [33].

Ban et al. [33] employed SCM for the BH MQW laser as for SSRM to present a comparative study using the same AFM set up and the cross section image in Figure 2.7. The n-p-n-p layers were clearly resolved showing the MQW bright at the center. The 1D line scanning of the image resulted in the dC/dV signals that were then calibrated using a standard staircase InP sample of known doping concentration to determine the carrier concentration of the sample. SCM measurement was used to profile the dopant concentration in the device structure to present a good correlation between the nominal doping density and the SCM measured dopant density [33]. The SCM scan confirming a complicated BH MQW laser device's doping concentration, thereby resolving the quantum wells in the mesa, is considered as a demonstration of one of the most useful tools to understand the device structure and operation without damaging the device.

SCM has also been used to directly probe and therefore measure stored charges in Flash EEPROM devices with its high spatial resolution of ~15 nm. Nardi et al. [48] presented a study of the stored charges for a 1 Mbit NOR Flash from Atmel with a 5 V power supply on a 0.35 μm CMOS technology node. The device has two NMOS transistors (2T) with one Access Transistor (AT) and one Floating Gate Transistor (FGT). The SCM scanned image is shown in Figure 2.8 (a) the dC/dV Amplitude (b) the dC/dV Phase for 20 μm image (c) the dC/dV Phase for 5 μm

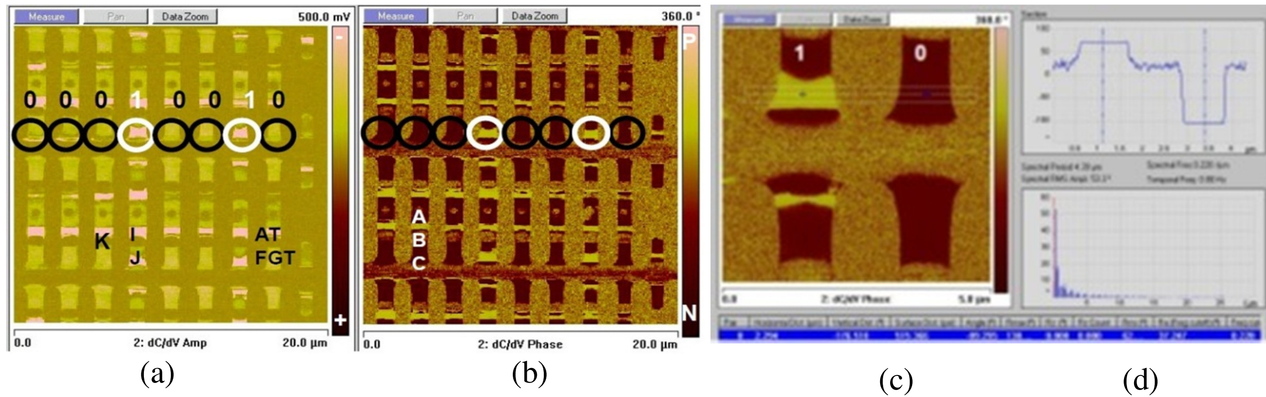

(a) (b) (c) (d)

Figure 2.8. SCM scan of 2T-cell (a) dC/dV Amplitude mode image for 20µm scan (b) dC/dV Phase mode image for 20µm scan (c) dC/dV Phase mode image for 5µm scan showing the "1" and "0" bit contrast difference and (d) SCM line scanning profile [48].

image and in (d) the SCM section analysis profile [48]. The 2T-Cell Flash was previously programmed with "12h"= "00010010" and after electrical descrambling, a backside de-processing was performed before the SCM scan. The information about the carrier concentration is presented in Figure 2.8 (a) and (b) with strong signals in low doped substrate regions marked as I and J and weak signals for high doped regions labeled as cell drains A, S/D regions B and cell sources C respectively [48]. The programmed data "12h" is well represented with clear contrast in both images. Figure 2.8 (c) resolves the stored charge as "1b" and "0b", while Figure 2.8 (d) represents the peaks due to the presence and absence of charges. SCM technology presents higher carrier sensitivity, up to a single electron [48], due to the capacitance resonator. This approach of stored charge calibration for future flash memories, storing less charge onto their floating-gate-transistor's (FGT's) than the ~1000 electrons used in 90 nm-node negative AND gate (NAND) Flash is of utmost importance [48]. SCM is considered to be a 2D profiling technique that helps in understanding structure and operation while the device still remains intact for operation.

2.3.2.3 Scanning voltage microscopy (SVM)

The concept of SVM was introduced by Ban et al. [49] by directly imaging the depletion region of an InP p-n junction diode under operation. This technique supplied insight to the electrical characteristics of the device under different operating conditions, delineating in 2D the voltage on the cross section of the device [49, 50]. The measured SVM signal engages in the single-

particle electrostatic potential and the local carrier concentration present in the device under operation, which are linked together to establish a correlation for the SVM measurement process [49, 51]. The InP diode was imaged under forward and reverse bias operation conditions using SVM on AFM. The change with and without applied bias in the electrostatic potential and the variation in dopant concentration was determined from the voltage as the AFM probe scanned the sample surface [49]. SVM has been used for analysis of InP/InGaAsP-based lasers such as the BH MQW laser and the ridge waveguide (RW) MQW laser. The efficiency and optical output power of the laser device is directly related to the optical gain based on the spatial overlap of electrons and holes in the MQW active region.

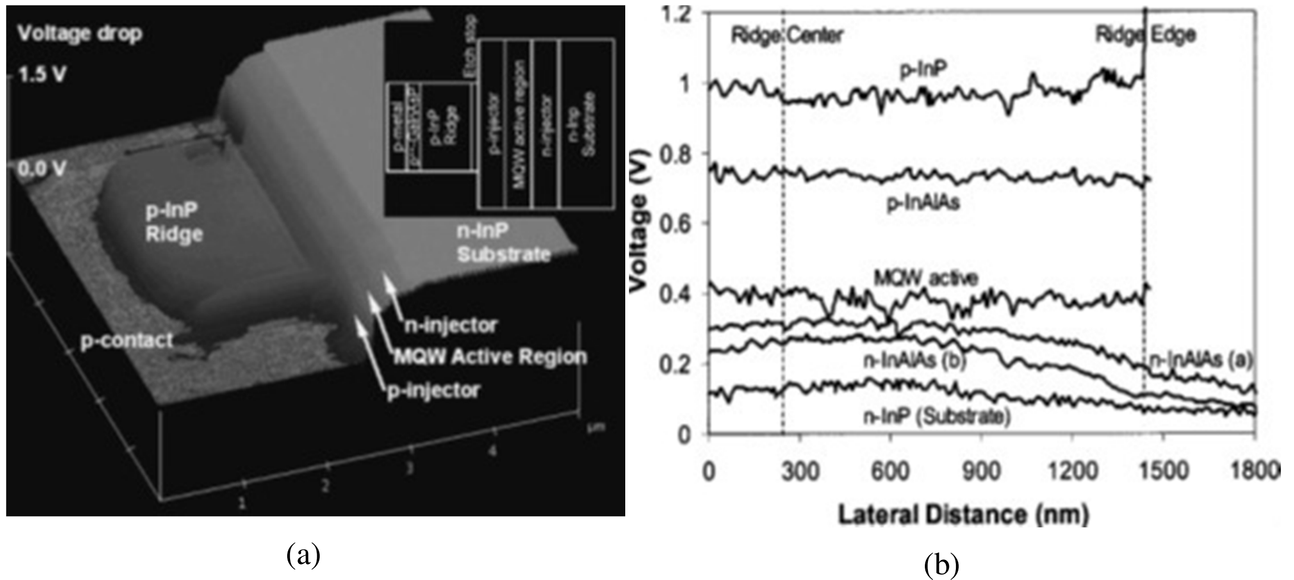

(a) (b)

Figure 2.9. (a) SVM scan image of RWG laser device with inset showing a schematic structure of the device [53]. (b) SVM lateral cross section voltage profile displaying non uniform voltage distribution for n-InAlAs layer [52].

Ridge wave-guide (RWG) lasers mainly used in optical communication systems provide low threshold current in lateral transverse mode operation, emitting nearly circular optical far field patterns. A 2D image of the SVM transverse cross-section of RWG MQW is presented in Figure 2.9 (a) is biased under a forward current injection of 100 mA, resolving the ridge structure with the etch stop layer, the MQW active region, the n- and p-cladding layers and the *n*-substrate [41, 42, 52, 53]. The figure also shows in the inset the schematic of the RWG. The voltage profile in the SVM image within the n-cladding layer, is not uniform across the ridge, and this

non-uniformity is clearly observed in Figure 2.9 (b) showing a flat voltage within the p-InAlAs ridge and MQW active region [52]. A 75 mV lateral voltage difference at 100 mA and around 200 mV at 150 mA is measured from Figure 2.9 (b) in the n-InAlAs layer below the ridge. This inconsistency of lateral voltage distribution was observed to be directly associated with lateral current profiles with in-depth investigation [52]. Thus, from the SVM image and voltage profile of the operating MQW RWG lasers on the nanometer scale, the 2D carrier transport via experimental means was investigated quantitatively. The local current density at the edge was 40% smaller than at the center under 150 mA forward bias [52]. Thus SVM was used to provide quantitative 2D internal voltage distribution with high spatial resolution.

SVM techniques can differentiate the dominant energy transfer mechanism by resolving the device structure. The spatial resolution is sufficient to characterize sizes of individual nanocrystals and outfits by using AFM to address individual nanocrystals [53]. To date SVM has thus been used as a failure analysis tool to be able to pinpoint causes of device failure; as a quantitative diagnostic tool capable of identifying sources of suboptimal performance; it is a reverse-engineering tool that can illuminate device structure and active behavior [52] for laser devices operating at room temperature.

2.4 Measurement Tool: AFM

The AFM is known for its ability to image and measure in nanoscale regime been demonstrated to resolve features of fractions of nanometer without damaging the device. A sharp tip hangs on the cantilever of the AFM to scan the sample surface [54]. Force between the tip and the sample, when the tip is in close proximity with the sample's surface. Along with force, additional quantities such as spreading resistance, capacitance, and voltage variation can be simultaneously measured through the use of specialized types of conductive probes under contact mode measurement. Two types of commercially available AFMs have been employed for this project: the Digital Instruments Dimension 3100 and the Attocube AFM.

2.4.1 Digital Instruments Dimension 3100

The commercially available Digital Instruments Dimension 3100 AFM has been utilised for the measurement of spreading resistance, capacitance and voltage variation across the sample surface. This AFM consists of four major parts: the AFM head along with the cantilever, the

optical microscope unit, the electronics with a computer system, and the video image capture unit. The instrument scans the sample surface and produces high resolution, three-dimensional images. Near the top of the microscope hangs a rod-shaped piezoelectric tube which has a flexible cantilever mounted on one end, which holds the tip. On the piezoelectric tube, voltages applied to the X and Y electrodes deflects it horizontally, producing a detailed scan over the sample surface while the vertical height of the tip is controlled by the voltage applied to the Z electrode on the piezo [54]. Figure 2.10 shows the Dimension 3100 AFM.

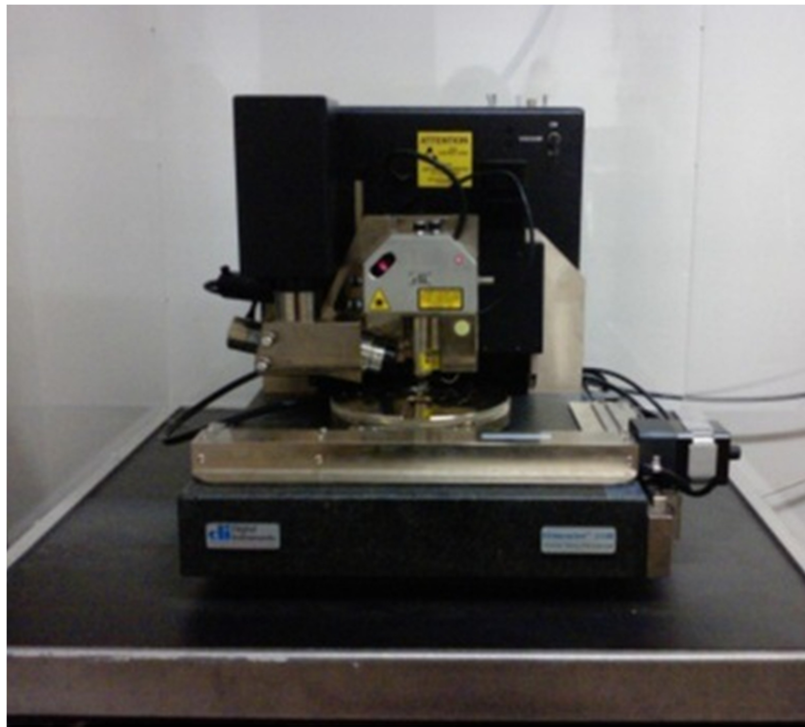

Figure 2.10. Atomic Force Microscope, DI 3100 ready for scanning at room temperature. [54]

The Dimension 3100 AFM has been used for contact mode measurement using a conductive tip that is commercially available, either boron-doped diamond coated tips or with PtIr coating. For measurement of resistance and capacitance variation on the sample surface, SSRM and SCM modules have been used, respectively. Figure 2.11 (a) shows the SSRM or SCM module. The module is screwed onto the AFM head and a connection jack is attached to the AFM electronics that is directly connected to the controller. The module also has a connection point at the bottom, by which it passes the applied bias to the probe hanging on the cantilever. The cantilever tip holder used for SSRM and SCM measurement is shown in Figure

2.11 (b). It has a probe holder clamp and a Universal Connector wire with clamp that connects to the module. The bias DC and or AC, depending on whether the operation is SSRM or SCM, is entered on the software and is applied to the tip through this connector at the time of scanning. The probe mounted on the cantilever hangs from the AFM head, and the cantilever connector connects the module and is set for scanning as shown in Figure 2.10. For better resolution and detection of different layers for miniature features, these measurements require an application of force onto the tip at the time of scanning. SSRM requires a higher amount of force than does SCM measurement as in SSRM spreading resistance is measured at the tip to sample surface contact while in SCM the measurement is performed based on the oxide layer interface between the tip and sample forming a MOS capacitance [32, 34, 35]. Diamond-coated tips are considered to be more reliable.

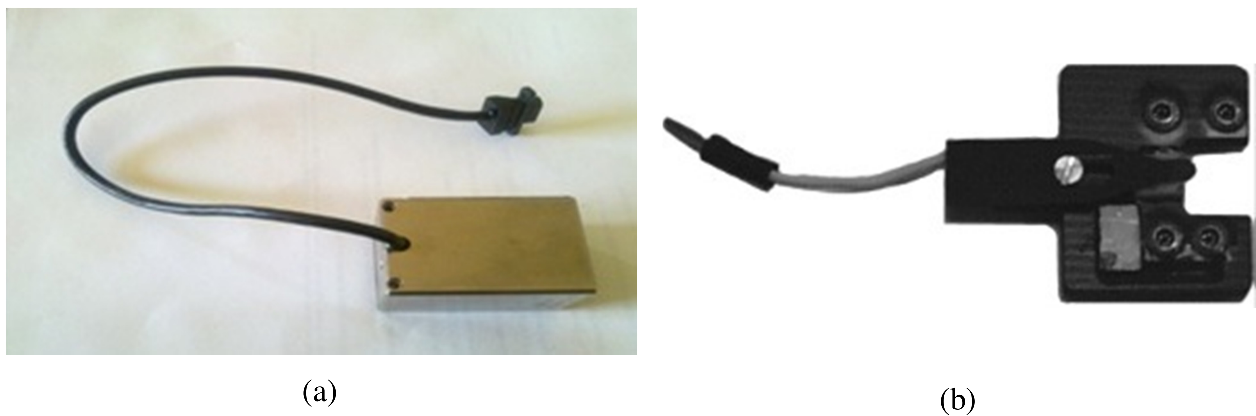

(a) (b)

Figure 2.11. (a) SSRM/ SCM module that are attached onto the DI 3100 AFM to measure spreading resistance/ dC/dV signal respectively (b) Cantilever probe holder with a Universal Connector for application of bias onto the sample. The electrical probe connection from (b) is plugged into the (a) for SSRM/SCM connection.

An SSRM module has been used to measure the resistance, on application of DC bias through the tip, while scanning and simultaneously imaging the surface morphology of the device. This technique presents a 2D mapping of electrical carriers in the device. The spreading resistance value derived from the measured electrical current is a function of the local carrier concentration at the surface surrounding the probe. A logarithmic current amplifier with a range of 10 pA to 0.1 mA senses the current, I, passing through the sample. Resistance is calculated on the basis of Ohm's Law: $R = V_{DC}/I$. Material resistivity is defined as resistance times the cross-

sectional area divided by the length of the conducting path. Constant force between tip and sample is maintained, and current images are generated, enabling direct correlation of local topography with electrical properties [54]. In SSRM, when the tip scans the sample, the sample needs to be grounded to the AFM system ground to avoid electrical distortions. SCM measures small capacitance variations with high spatial resolution, imaging 2D carrier profiles in semiconductor devices [54]. The tip forms a parallel plate capacitor with the semiconductor sample and the dC/dV signal is measured. Selectable AC and DC biases are applied between the sample and the tip, with the tip acting as a virtual ground.

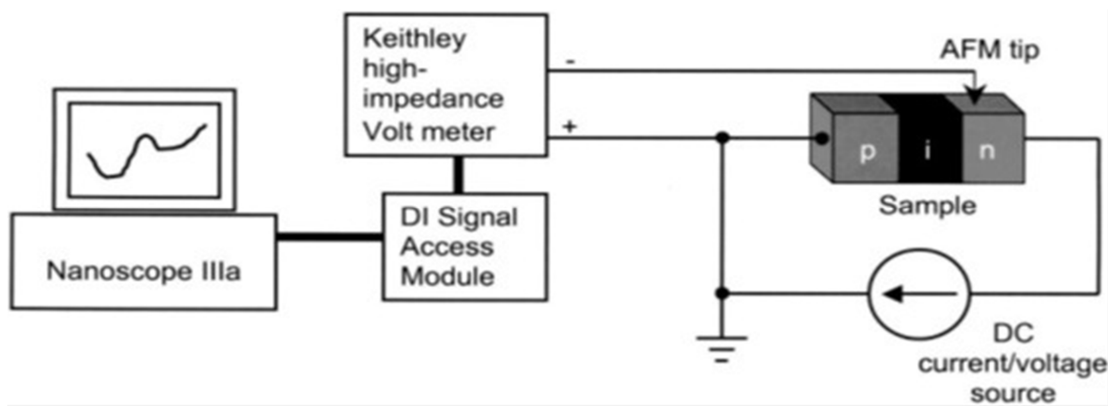

Figure 2.12. Schematic block diagram of the SVM circuitry connection [49].

SVM is an AFM-based technique, capable of measuring precisely with high spatial resolution the voltage distribution through a fully operating device. Due to its nanometer spatial resolution, SVM is particularly well-suited to analyse nanoelectronic devices (such as transistors or diodes) or quantum electronic devices (such as quantum well diode lasers) directly. Usually tips of only a few nanometers in width are used as a conductive probe for the measurement, and it is placed in full contact with an operational electronic/optoelectronic sample under test [33, 49]. The schematic circuitry of the SVM measurement set up is shown in Figure 2.12. The sample under test is biased and made to operate. The probe is connected to a high-impedance voltmeter that collects the voltage variations measured while scanning the sample surface. This is then fed to the Signal Access module (SAM) and in turn sent to the AFM controller. The measured voltage will determine the changes in the electrostatic potential and the carrier concentration at the SVM tip at different bias conditions. This determination is applicable to many local properties such as carrier concentration, band positions, carrier profiling on the

surface and the nonlinearity of the electric field for THz QCL devices. SVM directly elucidates the electrical characteristics of the devices under a variety of operating conditions, thus providing a close view into the behavior of device operation. SVM is the only known non-destructive technique that can be used for measuring the variation and profiling nonlinearities across the layers in an operating device. If the input impedance of the voltmeter is sufficiently large the SVM probe should not perturb the operation of the operational sample [33, 52]. SVM has so far been used to study devices operating at room temperature. This technique needs to be developed for low temperature operation at liquid helium (4 K) or liquid nitrogen (77 K) as these are the operating temperatures for the THz QCL devices. For this purpose a cryogenic AFM is needed which is discussed in the following section.

2.4.2 Attocube Cryogenic Temperature AFM

Commercially available Attocube cryogenic AFM has been used for the contact mode AFM measurement. The system is capable of measuring spreading resistance, capacitance and voltage drop variations while scanning across the sample surface. Other scanning probe microscopy techniques can be used on this system. This AFM consists of few major parts: the AFM stand, the AFM stick with CCD camera and the LED and the AFM controller electronics. The AFM stand has the x, y and z piezos for scanning and positioning the sample placed on it. There is a sample holder plate on the stand and samples of different kinds can be placed for scanning. The sample holder has a probe connected for temperature measurement. The x, y and z piezo for positioning the sample are used with help of the AFM electronics and the same is case for scanning adjustments. These adjustments help the sample to be positioned and the portion to be scanned is selected. The attocube AFM system is shown in Figure 2.13 [55].

This AFM stand is attached to the long AFM sticks after loading the sample on the stand. The AFM stick holds the cantilever head, the multimode fiber connection for passing infrared laser light and collecting the interference signal and the CCD camera [55]. Similar to the DI 3100 instrument the diamond-coated conductive probe is loaded on the cantilever head. The fiber connection is made using a small ferrule. Initially a visible light laser is used to center the light through the ferrule on the probe and then the infrared laser is used while the interference signal is monitored on the AFM electronics and the ferrule is brought as close as possible to the probe, to ~10 μm [55]. A dither spectroscopy is performed to view the peak to peak laser voltage

of ~0.3V. The LED system is then used to view the sample image using the CCD camera on the AFM stick. The controller electronics is used to perform auto-approach so that the sample shifts in z-direction towards the probe and achieves contact with the tip. The system is ready for contact mode AFM measurements. The z-spectroscopy is then checked to see the point of contact the tip makes with the sample and the sample is scanned in contact mode. While scanning the AFM system can be modified for SSRM or SCM measurements by applying DC and/or AC biases to the tip by the controller electronics of the AFM.

Figure 2.13. Cryogenic Atomic Force Microscope from Attocube. 1. AFM Stand with the ferrule, 2. AFM stick that already holds the AFM stand in 1, 3. AFM Controller Electronics. [55]

The 2D voltage profiling SVM technique developed on DI 3100 can also be applied on this attocube AFM. The cleaved facet of the sample has to be placed on the system under contact mode to scan the surface while the sample is under operation. This AFM system already has a high-impedance voltmeter that can record the data directly to the controller electronics, which will collect the scanned image, the profiling features and the voltage drop profiles at different

junctions. The voltage drop measured at each junction in the device will be able to provide an assessment about the uniformity of the voltage drop across the region, giving a measure of how the device is expected to behave. The attocube AFM is thus expected to be modified and updated with this SVM capacity. The system can then be developed to work at low temperature for cryogenic SVM capability.

2.5 Summary

This chapter presents a background to and the purpose and advantages of the AFM system. A detailed review of work on the AFM and its utilization for the study of different aspects of devices like MOSFETs, lasers and photodiodes has been summarized. The nanoscopic probing technique based on such different aspects as SSRM, SCM and SVM applied on the AFM has also been studied. These probing techniques carried on other devices revealed interesting physics in operating devices. The two different types of AFM instruments (Digital Instruments 3100 and the Cryogenic Attocube AFM) have been discussed, and the setup that will be used later in the project has been described. All the measurement profiles were under contact mode AFM. The SCM and SSRM modules have been used on DI 3100, while a circuitry arrangement had been set up for the SVM. As THz QCL devices operate in cryogenic temperature the cryogenic Attocube AFM and its setup has also been summarized.

Chapter 3: Two-dimensional dopant profiling of terahertz (THz) quantum cascade laser (QCL) devices

This chapter presents the two-dimensional (2D) dopant profiling of the active region of THz QCL devices with the help of atomic force microscopy (AFM). Scanning spreading resistance microscopy (SSRM) and scanning capacitance microscopy (SCM) has been shown as the two promising AFM techniques for 2D dopant profiling and mapping of dopant concentration for the sub-nanometer regime devices.

The distribution of charge carriers inside the active region of a THz QCL is measured for the first time using SSRM and SCM measurement technique. Scanning is performed on the cross section of the THz QCL structure with scan speed varying from 0.25 Hz to 1 Hz. Two different THz QCL samples V843 (double phonon based four-well design) and V775 (resonant phonon based three-well design) are employed to compare the results. Individual quantum well–barrier modules of 35.7 nm and 44.4 nm module thicknesses in the active region of the V843 and V775 samples, respectively, are resolved for the first time using high-resolution SSRM and SCM techniques at room temperature.

SSRM and SCM measurements on the quantum well-barrier structure were calibrated utilizing known GaAs dopant carrier staircase samples measured and confirmed by SIMS. Doping concentrations derived from SSRM and SCM measurements were found to be in quantitative agreement with the designed average doping values of the n-type active region in the THz QCL. The secondary ion mass spectroscopy (SIMS) provides a partial picture of internal device parameters, and results were used to demonstrate the efficacy of uniting calibrated SSRM and SCM to delineate qualitatively and quantitatively the transverse cross-sectional structure of

complex two-dimensional THz QCL devices as was performed by Ban eta et al [32] for buried heterostructrue devices.

3.1 Introduction to SSRM and SCM on THz QCL

There has been considerable progress made in various terahertz (THz) technologies including the developments of THz QCLs [11, 12, 14, 56-60]. The focus in this area of research mainly comprised of improving the steady state device performance [12]. Engineering the band structure of the multiple-quantum-well active region of the THz QCL, maximum lasing temperature of up to 199.5 K (pulsed) and 117 K (CW) has been achieved [15, 61]. The THz QCL devices lase when biased at high currents and voltages, where only a small amount of injected current contributes to the output power while the rest becomes thermally induced leakage current that exaggerates substantially at higher temperatures due to optical phonon scattering taking place in the active region of the device [12, 60]. The active region of the THz QCL devices in general is around 10 μm thick, with the number of quantum well-barrier modules varying between 200 and 300 depending on the design [14-16, 60]. The quantum well-barrier layers present in the active region of the device consist of un-doped material with each module consisting of a delta-doped layer in the injector barrier that is highly doped with Si dopant. The active region growth period is prolonged, leading to uncertainty in several factors of the process. This uncertainty can be summarized as the discrepancy in layer thickness (~10 nm variations) between the first module and the last module grown, and the variation of doping concentration between the initial stage and the end stage. These issues stand as some of the key factors leading to nonlinearity in electric field distribution and high-field domain formation in an operating device, and significantly degrade device performance and/or even render a device inoperable. Therefore, measuring and confirming the active region's structural parameters and their uniformity after material epitaxial growth and device fabrication is of utmost importance. This can be achieved by imaging the position and width of the modules/quantum layers through the cross section in the active region accurately enough and also calculating the variance in concentration over the structure.

Scanning electron microscopy (SEM) images have been looked upon to show how the device looks like [16], but detailed structural information (such as individual quantum cascade modules that are made of ultra-thin GaAs and AlGaAs layers) can't be resolved due to SEM limited spatial resolution. Transmission electron microscopy (TEM) was used to resolve fine

structures including nanometer thick individual quantum wells and barrier layers, but it is a destructive process – semiconductor wafers/devices can't be used after the TEM inspection [16]. The dopant concentration profile in semiconductor wafers can also be measured by secondary ion mass spectroscopy (SIMS), but it is also a destructive process, and in some cases, it is not quite suitable, for example, for probing delta-doping dopant profiles. There have been studies of the influence and effect of doping concentration on THz QCL devices, by Liu et al. [62] Ajili et al. [63] and Benz et al. [64], specifying how the device operation changes with change in doping concentration. The studies showed the free carrier absorption leading to waveguide loss [64], due to significant dependence on the wavelength as was suggested by Höfling et al. [65], and Mujagic et al. [66], and also a linear dependency of the threshold current density on doping was observed [62]. In addition to the waveguide loss some studies [62, 64] have also been carried out on electron density, which has in particular a notable influence on the carrier dynamics, via the injector doping density in the QCLs. The end result is an increased dynamic range of lasing [67]. To this point, no report, without destroying the devices, has experimentally shown direct carrier profiling and mapping of carrier concentration in two dimensional (2D) structures resolving the different modules in the device. Confirmation is also needed of the delta-doping profile and uniformity of the quantum cascade modules in fabricated terahertz quantum cascade lasers, as uniformity is important in correlating the structural parameters to device performance. Previously, a microprobe technique has also been used that gave direct access to the electrons and lattice temperature in the active region for mid-IR (infrared) and THz QCL devices [68, 69]. This technique was suitably used to reveal the local parameters for electron dynamics simulation, but there has been no such method to probe and determine the overall doping concentration of the device's active region. Scanning spreading resistance microscopy (SSRM) [22, 23, 70] and scanning capacitance microscopy (SCM) [24, 25] are the two enabling techniques for two-dimensional (2D) dopant profiling and mapping of dopant concentration for nanometer regime devices. Both SSRM and SCM employ procedures that are done on atomic force microscopy (AFM) using a conductive tip that is kept in direct contact with the sample surface, resulting in semi-quantitative measurement of the spatial distribution of free-carriers for the sample under test [32, 33, 52]. Although employing SSRM is associated with some surface scratching during scanning, as the measurements are performed on the cross section, this scratching does not

hamper the device in its suitability of operation. Thus, the device can emit identical THz light signals (its major purpose) before and after performing SSRM.

The SSRM technique was first conceived by Vandervorst prior to its implantation at IMEC in 1994 [29, 30]. A DC voltage bias is applied to the tip and the resulting current is measured through the sample in SSRM as a function of the tip position on the surface using a six-decade logarithmic amplifier. The current is proportional to the product of the local free-carrier concentration (n) and the carrier mobility (μ) near the point of contact and is also inversely proportional to the spreading resistance in the vicinity of the tip [32, 52], though the variations due to the tip–surface contact resistance must also be considered [42, 71]. This contact resistance is found to contribute negligibly to overall spreading resistance [42, 71].

The first AFM-based SCM technique was patented by IBM in 1991 and is quite similar to the ones used today [38]. The basis of the capacitance detection in SCM is formed by the ultra-high-frequency (UHF) resonant capacitance sensor, where the conductive probe tip is connected to the resonator via a transmission line [32, 42]. AC voltage bias is applied to the tip resulting in alternating electric field between the semiconductor surface and the conductive AFM tip, the sample surface carriers are attracted to or repelled from the tip to form depletion or accumulation of carriers underneath the tip contact point, which induces capacitance variation between the AFM tip and the sample surface. This change in capacitance is recorded and displayed as the darker and brighter regions on the sample image, corresponding to n- and p-doped regions or higher and lower doped regions. As the AFM tip scans the semiconductor surface the SCM dC/dV signal is acquired, and its magnitude can be translated to the local carrier concentration in the sample [32, 33, 42, 52].

From previous chapter it is known that the SSRM and SCM techniques were originally developed focusing on silicon based structures and devices [49, 72-74]. Recently, a number of reports have explored III-V compound structures for SSRM and SCM [32, 46, 75-77]. The limit of spatial resolution typically depends on the order of tip radius, but also depends on factors like the scan rate and the sample surface. Ban et al. [32, 53] have performed SSRM measurements on III-V based buried heterostructure laser devices and were able to resolve single quantum wells with a well width of 6 nm. In these measurements, the limit of spatial resolution was credited to several factors: a sharp tip, very slow scanning of the sample surface thus removal of the signal to noise ratio (SNR), and also to a freshly-prepared sample surface that was scanned to minimize

the native oxide effect. Both SSRM and SCM have been used to determine the dopant profiles in various semiconductor structures with spatial resolution in the order of tip radius (20 nm) [32, 76]. The dopant levels have been determined quantitatively by using GaAs and InP doping staircase structures as suitable standard samples for calibration [32, 71]. The mid-IR and THz QCLs have module thicknesses varying between 30 to 50 nm, well within the limits of the spatial resolution of the tip. Thus, the 2D profiling of carriers and quantitative calculation of the dopant concentration for both the mid-IR and the THz QCLs can be achieved. Both of these SSRM and SCM measurement techniques can be employed not only to achieve a qualitative mapping of the sample surface being scanned but also to quantitatively calculate the conductance/dopant density of the sample as has been previously done by Ban et al. [32]. This concept was successfully employed and in 1972 a capacitance electronic disc (CED) as an original application of the scc-technique in the SelectaVision was branded as RCA videodisk player [78].

In this chapter, for the first time the calibrated SSRM and SCM measurements on the active region of the THz QCL sample resolving the individual quantum well-barrier modules has been reported. The delta-doped layers present in each module appear as distinctive lines and in turn differentiates the modules, undoubtedly determining the module thickness. The carrier concentrations have also been derived for the n-type quantum well-barrier active region structure of the THz QCL device, utilizing data extracted from SIMS for n-type standard GaAs based staircase sample and calibrating with the SSRM and SCM measurements.

3.2 Experimental Procedure for scanning THz QCL devices

A commercially available atomic force microscope system (Digital Instruments Dimension 3100) has been employed for doing the SSRM and SCM experiments. Boron-doped diamond-coated cantilever tips (Digital Instruments) with a spring constant = 42 N/m, model no. DDESP-10, were used in SSRM and SCM measurements in ambient conditions. The scanning was done on the cross section of the active region of a THz QCL device comprised of the III-V semiconductor compound material, to entice a quantitative correlation between the SSRM, SCM measurements and SIMS results.

Contact-mode AFM was engaged for the SSRM measurements of the THz QCL devices that have 10 µm thick active region. The tip was kept at virtual ground and DC tip bias was selected and applied between the sample and the conductive tip. The electric current flowing

from the tip through the sample and to the sample chuck as a function of the AFM tip position was measured implementing a sensitive six-decade (1mA – 1nA) logarithmic amplifier [32, 49]. The tip was scanned at 0.25–2 µm/s speed and the sample bias voltage was varied from +1.0 to 3.5 V DC.

The open-loop SCM operation is defined mainly by four parameters: the AC bias modulation voltage, the modulation frequency, the DC offset voltage, and the capacitor sensor probing voltage. The closed-loop operation is defined by another extra parameter, the capacitance feedback set-point voltage [32, 33, 52]. SCM operation induces capacitance variation in the sample near the tip on application of bias through the tip as a thin native oxide layer is formed on the sample surface resulting in a parallel plate capacitor with the oxide layer being the dielectric. Some charges get trapped in this dielectric layer, leading to variation in the Fermi-level [32]. Thus, a flat-band shift occurs in the C-V curve that is well compensated for the DC offset voltage [32, 33]. The differential capacitance signal is changed to maximize (maximum C–V curve slope) by adjusting the DC voltage [32, 33]. For the open-loop method, data were acquired in ‘‘dC/dV,’’ in which, for a given voltage modulation on the sample, either the amplitude or the phase of the capacitance variation is obtained; and for the closed-loop method, data were acquired in ‘‘feedback,’’ wherein the AC voltage is adjusted to maintain a constant capacitance throughout the image. For SCM, the tip was scanned in contact mode at a speed of 0.25–2 µm/s, but without contact force. The sample bias voltage was varied from 0.5 to 2.0 V_{ac} [32].

SSRM and SCM measurements were carried out on the cross section of the active region of the THz QCL devices, which were grown by molecular beam epitaxy (MBE) method. The THz QCL devices employed for SSRM and SCM measurements were V843 [79] and V775 [15] samples. Both the devices have the active region thicknesses of 10 µm. The active region design of the V843 sample consists of a four-well (GaAs/AlGaAs quantum well-barrier) structure with a delta-doping layer present in the injector barrier of each module making up to a total of 276 modules [79] as shown in Figure 3.1. In this growth process, the n-type material used had an average designed doping concentration of 9.0 x 10^{15} cm^{-3}. In Figure 3.1, the module structure has been clearly shown giving the detailed thickness of each material layers. The injector barrier present in each module of the active region constitutes of a two-dimensional (2D) delta doped layer with Si dopant at a sheet concentration of 3.25 x 10^{10} cm^{-2}. The whole active

region is sandwiched between the two metal cladding layers at the top and the bottom as shown in Figure 3.1. The active region design of the V775 sample consists of a three-well (GaAs/AlGaAs quantum well-barrier) structure making up to a total of 227 modules in the 10 µm thick region [15]. In this growth process, the n-type material used had an average designed doping concentration of 9.0 x 10^{15} cm^{-3}. The injector barrier in each module of the active region comprises of a two-dimensional (2D) delta doped layer with Si dopant at a sheet concentration of 3.96 x 10^{10} cm^{-2}.

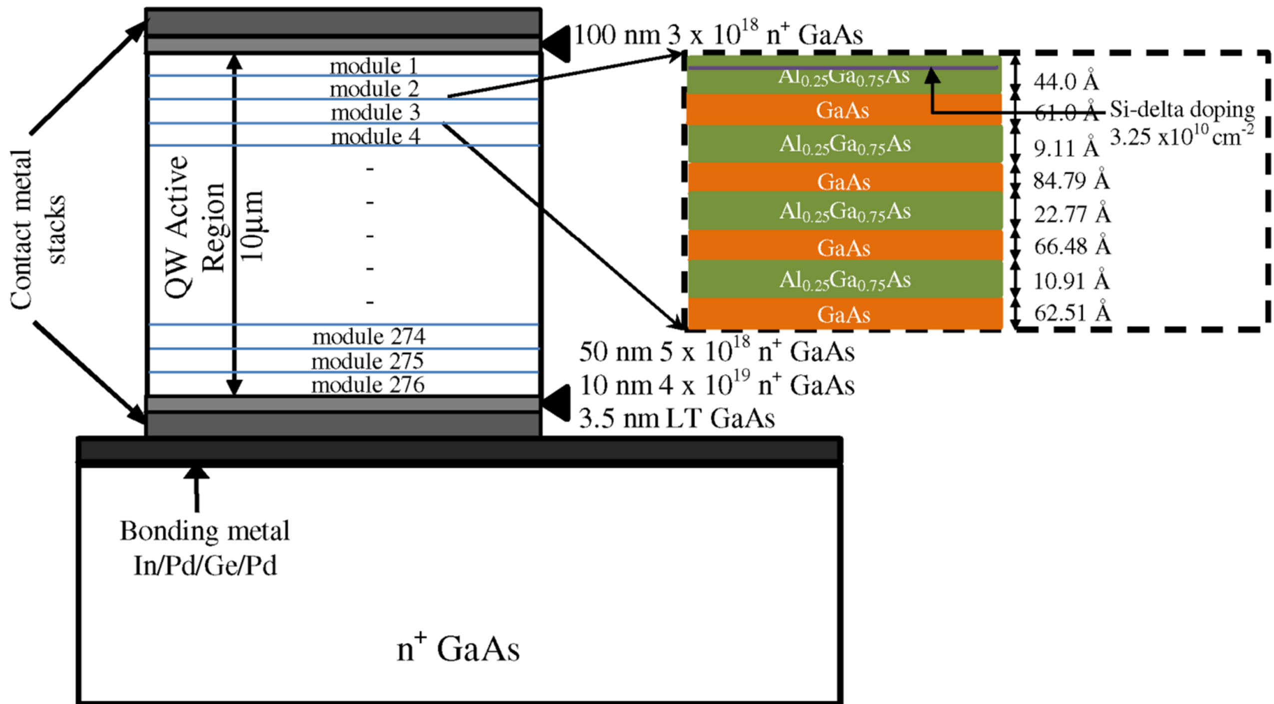

Figure 3.1. Schematic diagram of the cross section of fabricated THz QCLs with metal-metal waveguide. The quantum well-barrier (QW) active region of the device is based on four well cascade module design that is repeated 276 times forming 276 modules. The thickness of the active region is 10 µm. The semiconductor active region is sandwiched between the two metal cladding layers at the top and the bottom. One of the module is zoomed to show the QW layer structure consisting of $GaAs/Al_{0.25}Ga_{0.75}As$ material for the thicknesses as mentioned. The injector barrier layer in each module has a 44 Å thick Si based delta-doping layer with doping concentration of 3.25 x 10^{10} cm^{-2} [17].

In order to calibrate SSRM and SCM, a GaAs sample with multiple n-doped layers and a staircase doping profile (ranging from 10^{15} to 10^{19} cm^{-3}) was grown by MBE. The cross sections of all the samples were cleaved and exposed for SSRM and SCM measurements. It is to

be noted that this sample cleaving causes no complications in the operation and functionality of the device, and thus, the device can emit identical THz light signals (the major purpose of the device) before and after. Samples were then mounted with the cleaved edge facing upward in a metal clamp for scanning.

3.3 Nanosurface Profiling of Carriers and Discussion

3.3.1 Carrier Profiling using SSRM Measurements

The cross section of the active region structure of the THz QCL device was examined first by SSRM. A typical SSRM current image was obtained from the uncoated facet of the laser device as shown in Figure 3.2 for the sample V843. The scan was performed at a DC tip bias voltage of1V and at a scan rate was 0.5 Hz for Figure 3.2 (a) and (b). Figure 3.2 (a) presents a scan area of 5×12 μm^2, starting at the right, a very dark area is viewed that is the outside edge that leads to the topmetal of the device. The top n-metal is seen to be ~300 nm thick, adjacent to the 10 μm thick active region of the device. At the left end in Figure 3.2 (a), the bottom metal of the device appears as a dark layer. Figure 3.2 (b) shows the SSRM scanned image of 4×4 μm in a 3-D view giving a clear contrast between the top n-metal to the active region of the device The active region, comprising the quantum well-barrier layers appears as one flat surface, and no individual

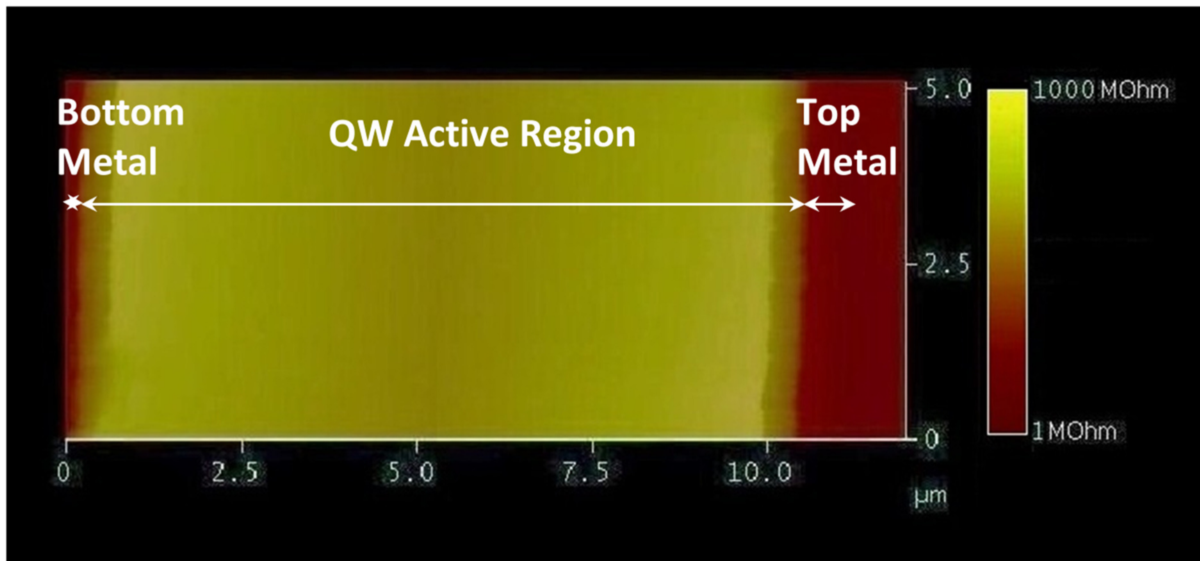

(a)

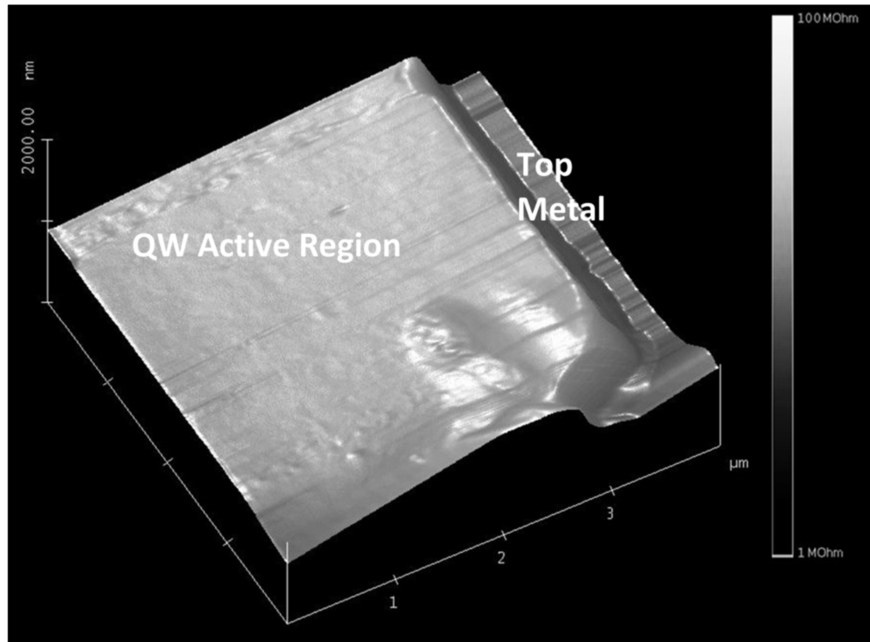

(b)

Figure 3.2. SSRM image of the THz QCL sample V843 in cross section with dc tip bias of 1 V. (a) Scanning was done at a scan rate of 0.5 Hz for a 5 × 12 µm area. The n-type GaAs/AlGaAs 10 µm four-well structure quantum well-barrier active region is seen to form a metal-semiconductor junction with the top metal of the device [17]. (b) Scanning was done at a scan rate of 0.5 Hz for a 4 × 4 µm area [45].

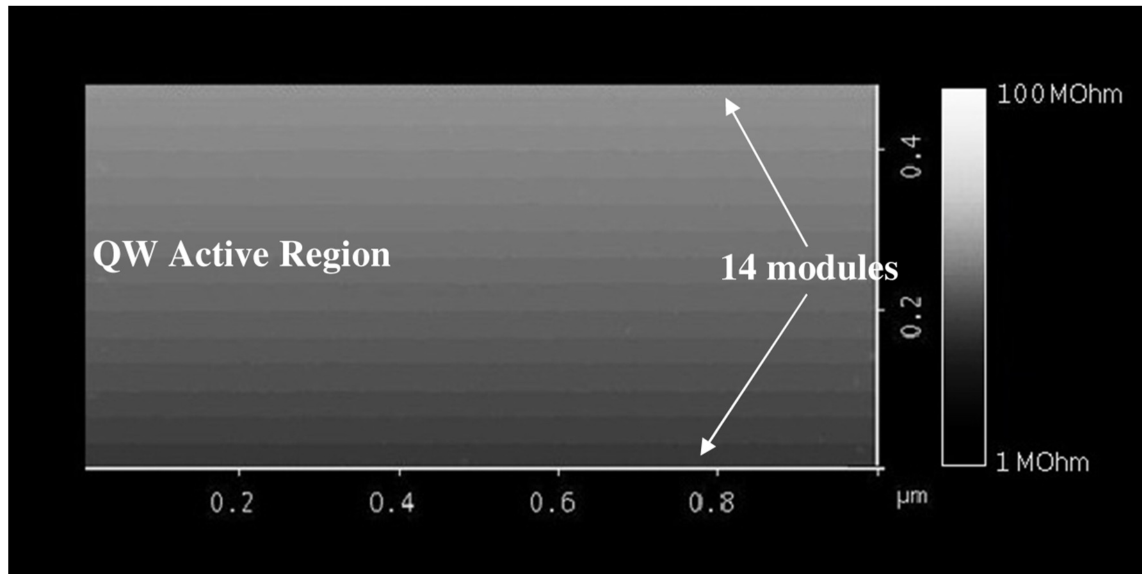

Figure 3.3. SSRM image of the active region of the sample V843 THz QCL device for a 1 x 0.5 µm scan area at scan rate of 0.25 Hz showing 14 modules of delta doped layers. Individual module can be resolved with ~36 nm thickness [17].

quantum wells (GaAs) and barrier layers ($Al_{0.25}Ga_{0.75}As$) are resolved, because the average doping concentration profile throughout the region of GaAs/AlGaAs based material structure is even.

The 10 μm active region of the device comprises of 276 modules [79], which corresponds to 13.8 modules over a lateral distance of 0.5 μm. Each module of the device has 4 quantum well-barrier layers, with the injection barrier having the delta doping layer in all the modules, as shown schematically in Figure 3.1. SSRM scanning was conducted over a zoomed-in area of 1 x 0.5 μm^2 at a tip bias of 1 V and a scan rate of 0.25 Hz to illustrate the active region of the device. As shown in Figure 3.3, 14 thin lines can easily be observed and the SSRM signal contrast comes from the delta doping profile in each quantum cascade module. As a result, the 14 thin lines in return delineate 14 individual modules. The width of each module was directly measured to be 35.7 nm, which is very close to the design value (36.2 nm). The small discrepancy is likely due to experimental calibration error in SSRM scans. The high resolution SSRM image in Figure 3.3 undoubtedly detects the delta-doped layer in each module and hence signifies them as bright contrast lines that are equally spaced from each other, giving a clear delineation of individual quantum cascade modules as well as directly determining the module thickness. Nevertheless individual GaAs (quantum wells) and AlGaAs (barriers) layers in one cascade module can't be resolved, this is due to the limited spatial resolution (~20 nm, on the same order of the radius of the AFM tip) and small material contrast between GaAs and $Al_{0.25}Ga_{0.75}As$ (small Al composition).

SSRM was also performed on V775 THz QCL device. The THz QCL sample V775 is a three-well quantum cascade design with 227 modules present in the 10 μm active region [15], which relates to approximately 8 modules being present in the distance of 0.35 μm. A high resolution SSRM scanned image of the active region of the device is presented in Figure 3.4, for a scan area of 1 x 0.35 μm^2 at a tip bias of 1.5 V with scan rate of 0.25 Hz. The 8 lines of delta-doped layers have been resolved demonstrating 8 modules present in the 0.35 μm lateral distance. From the image in Figure 3.4 the width of each module has been calculated to be exactly 44.4 nm which is very close to the 44.1 nm width of each module as per the design of sample V775. So from the high resolution SSRM images in Figure 3.3 and Figure 3.4, undoubtedly the delta-doped layer in each module has been detected and hence signifies them as bright contrast lines that are equally spaced from each other giving a clear assessment of the

individual modules, in turn determining the module thickness. For different tip biases with the scan rate of 0.25 Hz individual quantum well-barrier modules are thus resolved from the SSRM image.

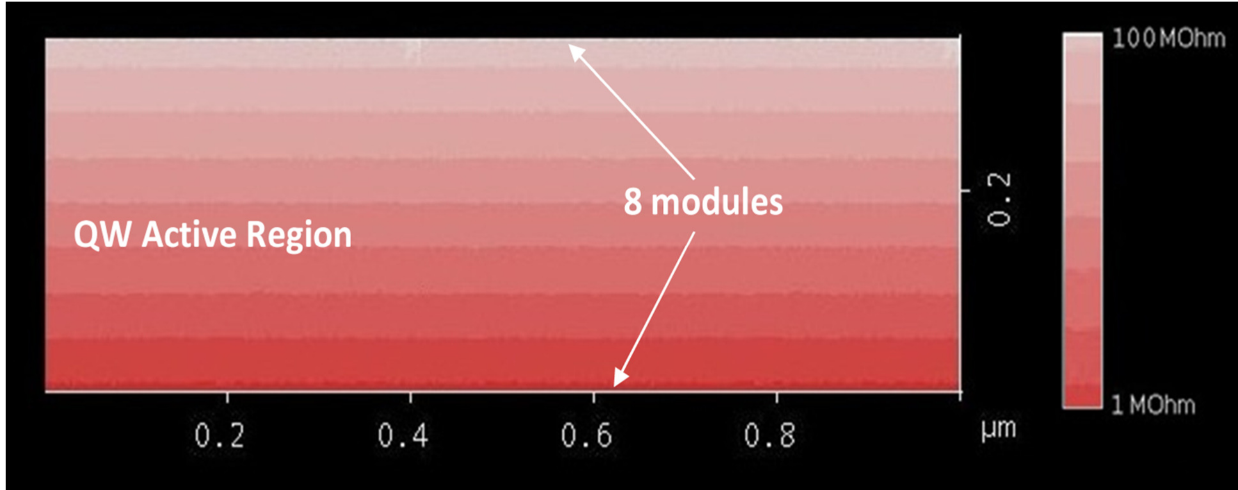

Figure 3.4. SSRM image of the active region of the sample V843 THz QCL device for a 1 × 0.35 µm scan area at scan rate of 0.25 Hz showing 8 modules of delta doped layers. Individual module can be resolved with ~44 nm thickness.

Figure 3.5 shows the averaged spreading resistance as a function of lateral distance from the top metal contact of the device surface to the active region for the THz QCL device. The plot shows the SSRM resistance profile measured at four different DC bias voltages. The resistance of the active region is seen to decrease with increase in DC bias on the tip of 1.0, 1.5, 2.5 and 3.5V, indicating existence of bias dependence on the SSRM resistance. This bias dependence is attributed to the diamond tip used for scanning having a resistance in the order of kilo ohms, and also due to the establishment of a Schottky-like contact between the probe tip and sample surface [32, 42, 49, 52, 71, 72]. Thus, the scan results as presented in Figure 3.5, shows resistance variation in the semiconductor as well as on the top metal. The metal layer being at a lower signal value is quite significant at the left edge of the graph and the active region seen to have started from a lateral distance of 250 nm and maintains the same stature as the spreading resistance, varying between 6.1 – 3.2 MΩ for different tip bias voltages, as shown in Figure 3.5 (a) and (b). The active region of the device comprises of un-doped material (GaAs/AlGaAs) for the quantum well-barrier structure, except for a delta-doped layer embedded in the injection

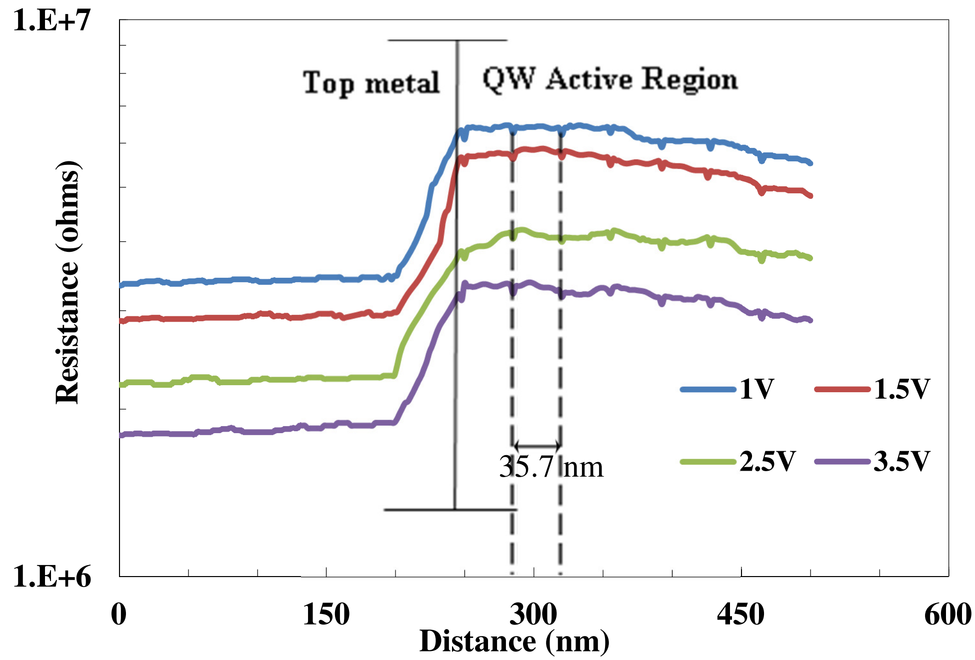

(a)

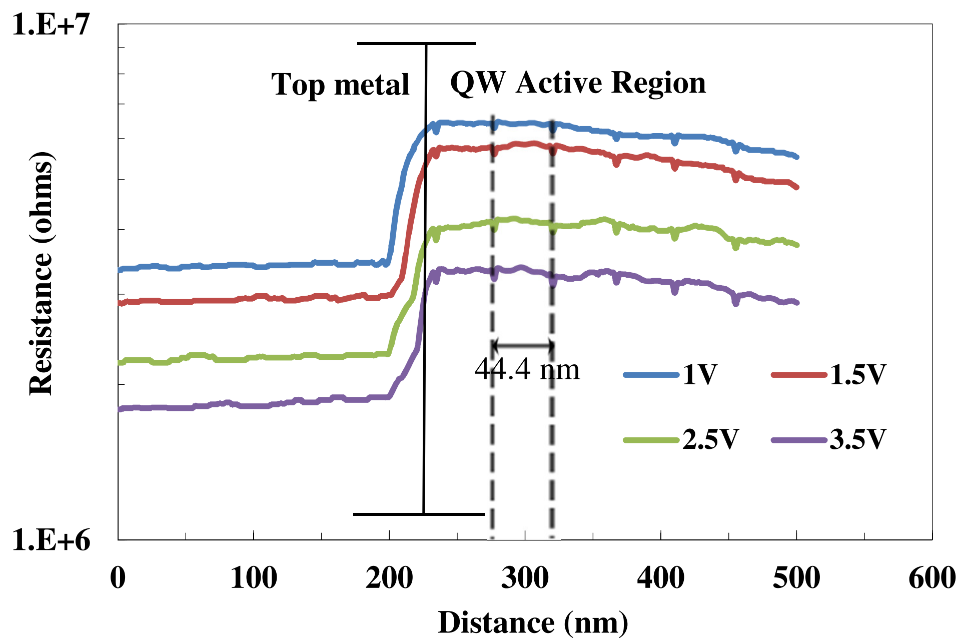

(b)

Figure 3.5. Resistance profile measured by SSRM across the THz QCL active region for DC tip bias voltages of 1.0, 1.5, 2.5 and 3.5 V to a lateral distance of 500 nm from the top metal of the device. (a) for V843 sample [17] (b) for V775 sample.

barrier in each module. The delta-doped layer is a 2D layer that is heavily doped with Si dopant having a sheet doping concentration of 3.25×10^{10} cm^{-2} and 3.96×10^{10} cm^{-2} for samples V843 and V775, respectively. [1]Considering the delta-doped layer and un-doped layers, the average doping concentration of the whole active region has been estimated to be 9.0×10^{15} cm^{-3}. As shown in Figure 3.5 the variation of resistance along the active region is negligible, although a small negative slope is observed, attributed to the nearby conducting boundary (top metal), which is an example of the SSRM current spreading distribution modelled by Wolf et al. [23]. From Figure 3.5 (a) and (b) the down peak (dips) in the spreading resistance at every lateral distance of 35.7 nm and 44.4 nm, respectively, shows the position of delta-doped layers. The dips are significant due to the very high contrast between the delta-doped layers, which have a high sheet doping concentration, and the un-doped quantum well-barrier region. This difference in contrast due to doping concentration is quite similar to contrast reversal observed by Stephenson et al. [80], while performing SCM between n and p-type materials. This contrast was later also detected by Lu et al. [71] and by Ban et al. [32, 52]. Here this effect of contrast difference is observed, as the tip used for scanning the device is under positive DC bias. As the tip scans the device, in each module, the highly doped ions present in the delta-doped layer are attracted, while the individual quantum well-barriers, being un-doped, have no effect, resulting in dips, (Figure 3.5). Thus, although, the spatial resolution is in order of tip diameter ~20 nm, one can visualize the effect of delta doping dips due to the high contrast difference between heavily doped and un-doped layers, and is viewed at every 35.7 nm and 44.4 nm distances, respectively. The delta doped layer in each module of the active region is significantly observed on the resistance curve, indicating more carrier concentration, due to the contrast existing between the undoped active region and the highly doped delta-doped layer. Figure 3.5 (a) and (b) confirms again the thickness of the modules that is resolved from Figure 3.3 and Figure 3.4, respectively.

Table 3.1 presents the averaged SSRM resistance for the n-type GaAs/AlGaAs based quantum well-barrier structure in the active region of the THz QCL device, taken from the mean value of the resistance curve for each of the different DC biases of Figure 3.5 (a) and (b). The mean calculation is based on the region of last 250 nm that distinguishably constitutes only the active region of the device. For both the V843 and the V775 THz QCL samples the average

---

[1] In V843, active region 10 μm with 276 modules, each module 36.16 nm. 2D doping in each module is $3.25\text{x}10^{10}$ cm^{-2}. Whole active region doping is $(3.25\text{x}10^{10})/(36.16\text{x}10^{-7}) \approx 9\text{x}10^{15}$ cm^{-2}

measured resistance ranges from 6.1 x 10^6 to 3.2 x 10^6 Ω, depending on the DC bias voltage. These values, in conjunction with the calibration curves discussed below, were used to derive and estimate the average doping concentration of the n-type layered active region of the structure.

Table 3.1. SSRM resistance across the active region of THz QCL device at DC tip bias voltages of 1.0, 1.5, 2.5 and 3.5V for V843 and V775 samples [17].

Dc tip bias	1.0V	1.5V	2.5V	3.5V
n-type active region, sample V843	6.14 x 10^6Ω	5.48 x 10^6Ω	3.99 x 10^6Ω	3.18 x 10^6Ω
n-type active region, sample V775	6.12 x 10^6Ω	5.48 x 10^6Ω	4.01 x 10^6Ω	3.18 x 10^6Ω

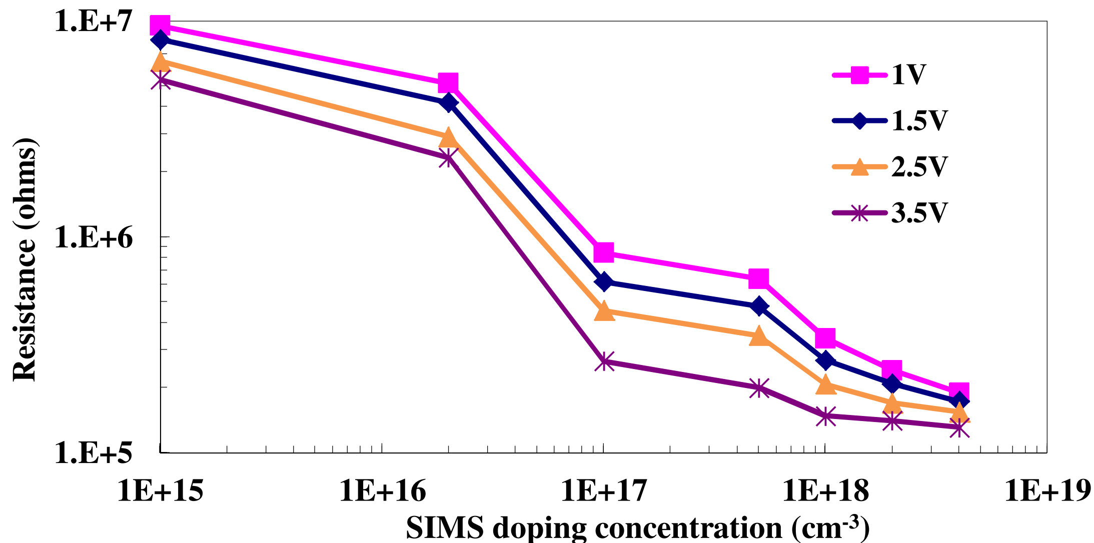

Figure 3.6. SSRM resistance vs SIMS doping concentration for Si-doped GaAs epitaxial layers separated by undoped GaAs and grown by MBE on an n^+-GaAs substrate. Calibration measurements performed at dc tip biases of 1.0 V, 1.5 V, 2.5 V, and 3.5 V [17].

A standard n-type GaAs sample with staircase doping profile structures are employed to do the SSRM calibration measurements using identical diamond tip, contact force and bias voltages as was performed by Lu et al. [71] and Ban et al. [32].. The SSRM measurements of the calibration samples and the unknown structures have been shown to be carried out under

identical experimental conditions. SIMS was employed to determine the doping concentrations in the calibration GaAs staircase sample. The SSRM measured resistance is plotted against the dopant concentration as determined by SIMS to build up calibration curves – the SSRM resistance monotonically decreases as the doping concentration increases. Figure 3.6 shows four calibration curves, obtained under DC tip bias voltages of 1.0, 1.5, 2.5, and 3.5 V, respectively. The curves presented for each measurement were plotted with x (±10%) and y (±5%) error bars indicating measurement variation, both for the SIMS doping concentration and SSRM spreading resistance of ±10% and ±5%, respectively. These curves are used to extract the average carrier concentrations in the active region of the THz QCL device from the SSRM data. For the n-type GaAs standard sample, the four calibration curves obtained at different DC biases from SSRM measurements tend to converge at high doping concentration, over 2×10^{18} cm^{-3}. Thus, at low doping concentration levels ($1 \times 10^{15} – 1 \times 10^{18}$ cm^{-3}), the bias dependence of SSRM resistance is much more significant than that at high doping levels (above 2×10^{18} cm^{-3}). Thus, the SSRM resistance depends on the applied DC tip bias, as is clearly indicated in Figure 3.6. The GaAs sample used has a staircase doping concentration structure; hence the calibration curves for SSRM resistance are seen to vary non-linearly. This variation occurs because the SSRM resistance is known to change with doping concentration on the semiconductor sample [32, 41, 72]. The contact resistance between the probe tip and the sample surface clearly plays a major role for samples that have low free carrier concentration, as the total resistance measured by the SSRM technique is a sum of the number of terms, including the tip–surface contact resistance, the spreading resistance, the back-contact resistance, and other instrumental terms [32, 71]. From the curves, it has been observed that the range of the dopant levels over which SSRM is operational depends on the DC bias applied to the AFM probe tip, typically in the range of about 10^{15}–10^{19} cm^{-3}. As it is known that the tips wear out in contact mode SSRM and SCM measurements, the THz QCL was scanned again after the calibration sample scanning and was found to give similar resistance results with a negligible variation of only 2-3 %, thus, confirming the suitability of the calibration measurements.

3.3.2 Carrier profiling using SCM Measurements

SCM measurement was also employed to examine the cross section of the THz QCL lasers. Due to the weak force being applied by the AFM probe onto the sample surface, SCM introduces

much less scratching to the sample surface during the scans [32, 33, 52, 73]. Figure 3.7 shows a typical SCM image that was obtained from the cleaved facet of the THz QCL device (sample V843) in dC/dV open-loop amplitude mode. The open-loop mode scanning was performed at an AC bias voltage of 1.0 V at a scan rate of 0.5 Hz. The SCM image shows the basic cross-sectional features of the THz QCL active region, although the spatial resolution is not very high in this 5 x 12 μm^2 scanning area compared to that of the SSRM image. The lateral distribution of the quantum well layers in the active region of the device underneath the probe contact point is contingent upon the spatial resolution of the SCM image. This difference in resolution occurs because the spatial resolution in the SSRM image is mostly determined by the radius of the probe tip, while the spatial resolution of an SCM image depends more on the lateral distribution of the depletion region in the semiconductor underneath the probe contact point.

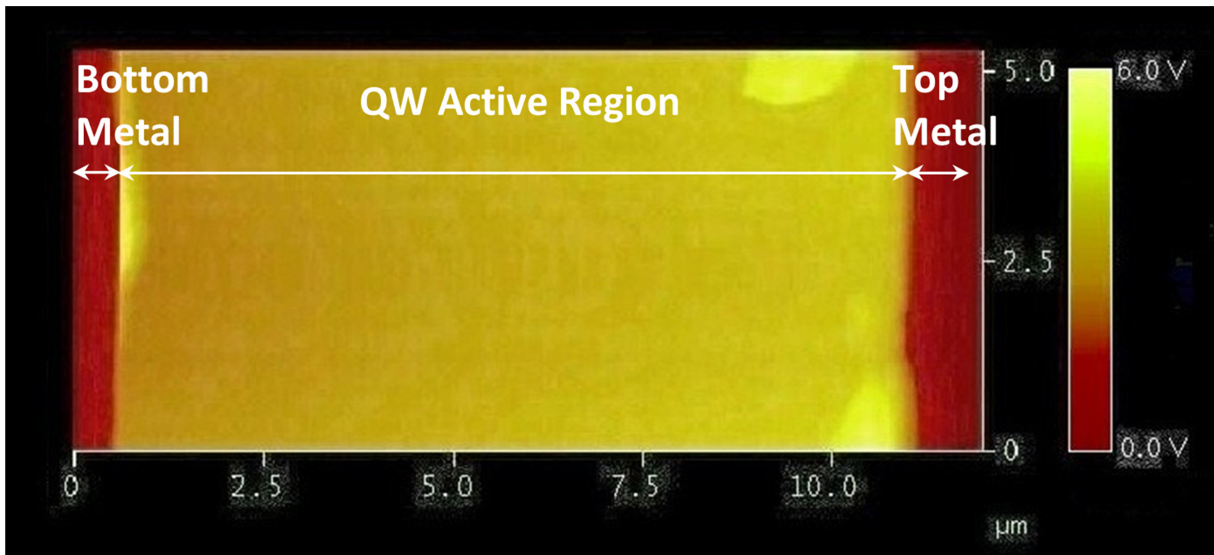

Figure 3.7. Typical SCM image obtained on the cross-section of the THz QCL. Scanning was done at open-loop amplitude mode for a scan for an area of 5 × 12 µm, with AC bias of 1.0 V and scan rate of 0.5 Hz. The active region of the device is seen to be clearly delineated from the metal layers at either edge [17].

The open-loop image in Figure 3.7 shows the top metal layer as a dark region on the right edge of the image. Then onwards, the brighter region is the semiconductor based quantum well-barrier active region consisting of the quantum well-barriers covering a lateral distance of 10 µm, and again at the left end, the bottom metal layer is viewed as a darker region. The active region appears to be quite bright compared to the metal layers on either side. Due to low

resolution of the SCM, only a clear delineation between the metal and the semiconductor layers is visible.

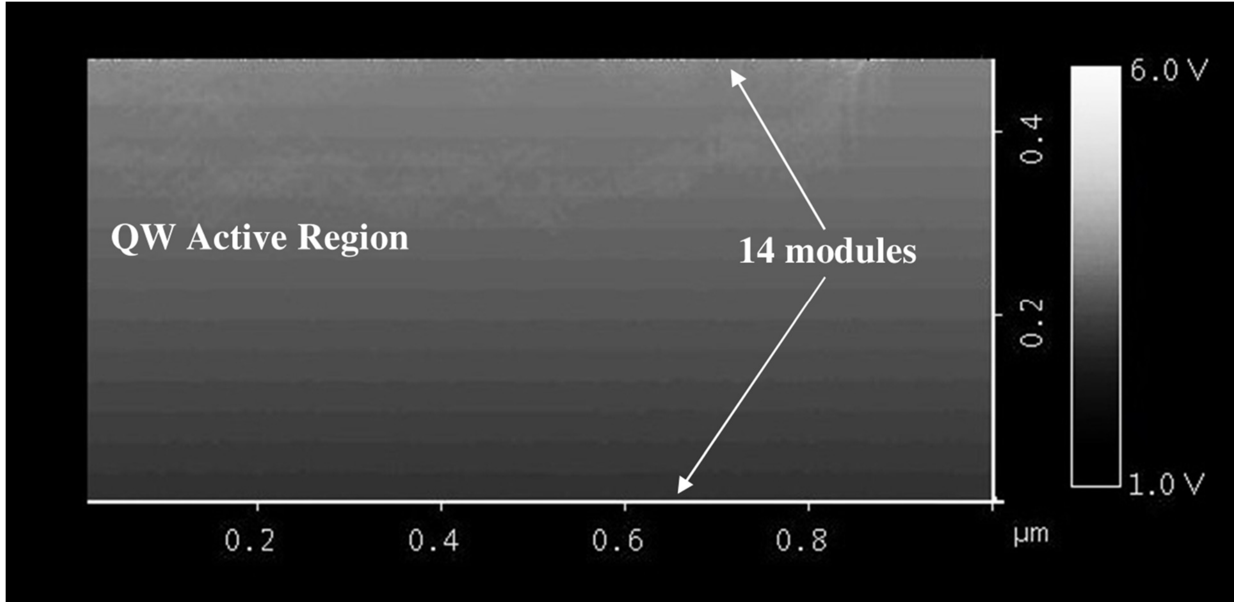

Figure 3.8. SCM image of the active region THz QCL for a 1 × 0.5 µm scan area at scan rate of 0.25 Hz showing 14 modules of delta doped layers. Individual modules with ~36 nm thickness can be resolved [17].

A zoomed-in SCM image over a smaller scan area (1 × 0.5 μm^2) of the active region is presented in Figure 3.8. The scanning was done at a scan rate of 0.25 Hz with 1.0 V AC bias under open-loop amplitude mode. The delta doped layers present in each module of the active region of the device can be resolved in Figure 3.8, although the visibility is less clear than the one in the high resolution SSRM image, due to lower spatial resolution of the SCM. Similar to the SSRM image in Figure 3.3, individual GaAs (quantum wells) and $Al_{0.25}Ga_{0.75}As$ (the barrier layers) cannot be resolved in the SCM image due to low contrast in material composition, and doping concentration as well as the poorer spatial resolution of SCM. In Figure 3.8, 14 thin lines can be observed over a 0.5 µm wide active region in Figure 3.8, corresponding to the delta doped layers of the 14 cascade modules. The thickness of each module was therefore measured to be 35.7 nm, identical to what was obtained from the SSRM image and very close to the design value (36.2 nm).

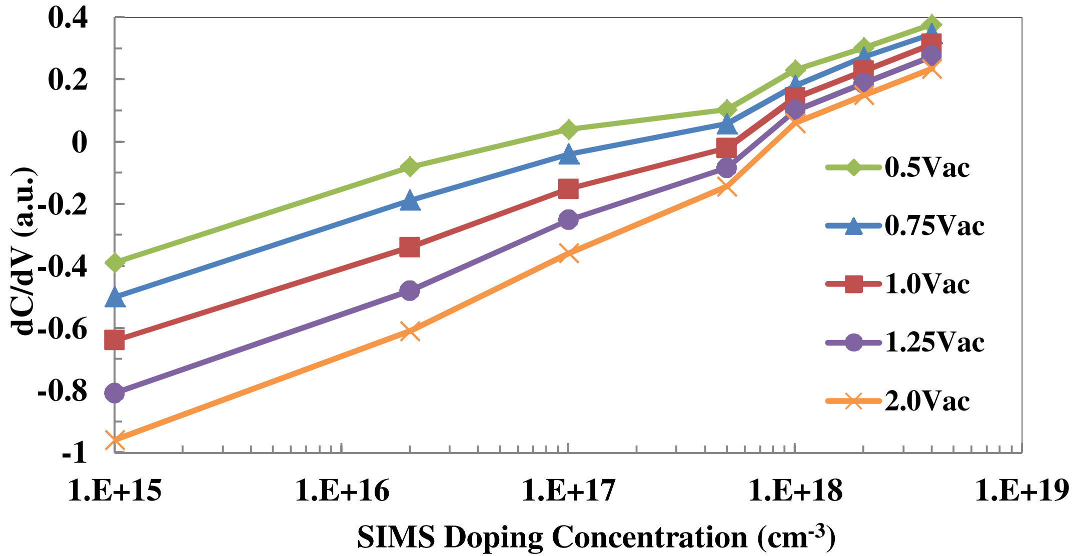

Figure 3.9. SCM signal (dC/dV) vs the SIMS doping concentration extracted from an n-type GaAs standard staircase sample. The correlation curves were obtained at each of the following ac bias voltages: 0.5, 0.75, 1.0, 1.25 and 2.0 V [17].

In semiconductors, previous investigations have been sought to attain a direct correlation between the SCM signal and doping concentration [81]. The quantitative correlation requires either that the dopant profile and doping concentration be extracted only over a narrow range [82], or that the dopant density be known at one measured position [42, 72, 73, 83]. As there is no well-established model or algorithm for direct translation of SCM signals to doping concentrations, standard samples with staircase doping profiles were employed, as we did for the SSRM measurement.

Five calibration curves were generated from the open-loop SCM measurements and compared with the SIMS depth profile for the n-type GaAs staircase doping profile structure, under different AC bias voltages and plotted in Figure 3.9. The SCM signal (dC/dV) at different AC biases escalates with increase in doping concentration for the full dynamic range of the graph from $1 \times 10^{15} - 4 \times 10^{18}$ cm^{-3}. However, at doping concentration above 5×10^{17} cm^{-3}, the SCM signal for different biases tends to merge but still maintains a decent dependence on the carrier concentration. Similarly, as explained earlier for Figure 3.6 for SSRM, the graph in Figure 3.9 shows a non-linear variation of dC/dV SCM signal to the doping concentration. We now use these calibration curves from Figure 3.9, combined with the SCM values acquired from the

quantum well-barrier active region structure of the THz QCL, to derive the average doping concentration of the n-type active region of the device.

3.3.3 Calibration Results

With the calibration curves achieved through SSRM measurement in Section 3.3.1, the doping concentration of the quantum well-barrier structure in the active region of the THz QCL device was obtained and listed in Table 3.2. Additionally, the designed average values of the dopant concentration in the active region are provided. A reasonably consistent agreement exists between the SSRM-determined dopant concentrations and the average designed dopant density (within 25%). In both the SSRM resistance and the SCM signal measurements random noise exists and is considered to be the measurement uncertainty [32, 72, 80]. This uncertainty is approximated on the basis of the mismatch errors achieved considering the SSRM resistance measured data from both the THz QCL device and the GaAs staircase sample and is considered and estimated to be around ±10% due to instrumental error [24, 32, 71]. The actual average designed dopant concentration is consistently greater than the SSRM resistance values determined from each of the four DC biases for the n-type active region of the device. The tip-sample contact induces nonlinear behaviour, which can be explained by the physical model based on a Schottky energy-band structure [71]. This nonlinear behaviour builds up an inaccuracy in the measurement data, and this may be considered as systematic error [24, 32, 71].

Table 3.2. Comparison of average doping concentration derived from calibrated SSRM and SCM measurements and the average designed doping concentration values of the active region of the THz QCL device for different dc tip bias voltages [17].

THz QCL Structure	Nominal Average doping Conc. ($x10^{15}$)	SSRM dc =1.0V (x 10^{15})	SSRM dc =1.5V (x 10^{15})	SSRM dc =2.5V (x 10^{15})	SSRM dc =3.5V (x 10^{15})	SCM ac =0.5V (x 10^{15})	SCM ac =0.75V (x 10^{15})	SCM ac =1.0V (x 10^{15})	SCM ac =1.25V (x 10^{15})	SCM ac =2.0V (x 10^{15})
n-type active region	9.00 (±10%)	8.00 (±10%)	6.80 (±10%)	6.00 (±10%)	6.80 (±10%)	8.10 (±10%)	9.70 (±10%)	10.20 (±10%)	10.00 (±10%)	9.50 (±10%)

The SCM calibration curves were utilized and the doping concentration in the active region structure of the THz QCL were obtained and listed in Table 3.2 as well. The average doping concentration corresponding to the different AC biases agrees with the average designed doping concentration of the active region within 15%, as derived from the calibrated curves of SCM data. The SCM-determined dopant concentrations for the n-type layers exhibit reasonably consistent agreement, with around 10% deviation from the average doping density due to instrumental error [24, 32, 71].

3.4 Summary

SSRM and SCM have been used for the two-dimensional dopant carrier profiling of the carriers across the active region of the THz QCL device under ambient conditions. Good correlation was demonstrated between the average designed and the SSRM measured dopant density of the device. High resolution SSRM images for the active region of the device have been able to reveal the quantum well-barrier modules due to the delta doped layer present in each module, yielding individual module thickness of 35.7 nm for sample V843 and 44.4 nm for sample V775. Due to the DC tip bias while measuring SSRM resistance, the module features have been viewed with each module thickness confirmed. SSRM and SCM measurements were calibrated with MBE-grown GaAs staircase-doped structures. The calibrated SSRM and SCM measurement results of dopant concentration in an n-type active region are in good agreement with the average designed doping concentration of the device. The experimental results show that SSRM and SCM are tools that enable measurement of 2D low doping concentration profiles in III-V quantum semiconductor structures and that allow fine features to be delineated at nanometer scales.

Chapter 4: Nanoscopic Probing for Determining Charge Density in Mid-IR Interband Cascade Lasers (ICLs)

This chapter resolves some of the fundamental properties that play a pivotal role in active nano-photonic devices, by determining dynamic charge carrier density and their transport along with the potential energy profile across cascade stages that governs the external performance of lasing quantum devices such as in ICLs under an external bias. The inner potential profiles are to be directly probed experimentally to reveal the uniformity of electric field and determine the carrier density in the region. Here an experimental nanoscopic probing technique is employed to investigate the gain-providing charge carrier distribution in lasing ICLs by imaging, observing and mapping charge carriers; while the electric field and dynamic charge carrier accumulation in the active region with nanometer resolution is projected.

The unique charge carrier distribution profile in the quantum-well active region is quantitatively measured at nanometer scales by using non-invasive scanning voltage microscopy (SVM) technique based on the AFM system. SVM is known to be the most advanced contact mode AFM technique that presents high spatial resolution images while mapping and profiling the surface of the sample in nanoscale. SVM is developed and established for the first time at cryogenic temperature to achieve potential profile across the device operating (lasing) under pulse bias. The details of the circuitry arrangements and the measurement conditions are illustrated. A two-dimensional profile image (electric potential and carrier profile) of the sample resolves the inner workings of the device, when the sample under operation.

Experimental results clearly confirm accumulation and segregation of holes and electrons in the device as in ICLs, carrier transport involves both conduction band (CB) and valence band (VB) of different material combination. The measurement also shows and

quantifies charge carrier density that is clamped in the presence of stimulated emission determining non-uniformity of electric field in the active region. The findings with nanoscopic probing is of utmost importance for evaluating potential performance of the device indicating future improvements by giving a clear opinion about the structure and behavior of charge carrier density and their transport in the potential energy profile across the cascade stages under an external bias in the device. The experimental approach leads to a deeper understanding of fundamental processes that govern the operation and performance of numerous nanoelectronic devices, quantum devices and optoelectronic devices.

4.1 Introduction to SVM on ICL

Electrically-pumped semiconductor lasers have been employed for many ubiquitous applications such as telecommunication, gas sensing, optical disc drivers, to name a few [84-89]. For designing and fabricating high-performance semiconductor lasers, optical gain-providing charge carriers need to be efficiently injected into the desired energy states in the active region, from which photons are generated leading to light being emanated [57, 15]. QCL are perhaps the most well-known unipolar lasers [90, 91], while conventional diode lasers with multiple quantum wells (MQWs) connected in parallel is a good example of the bipolar lasers [92]. ICLs exploit the cascading mechanism for achieving high voltage efficiency and quantum efficiency, are actually bipolar devices in which equal numbers of electrons and holes are generated from an internal semimetallic interface, with electron injection to one direction and hole injection to the opposite direction [93, 94]. The advantages of an ICL over a conventional MQW diode laser include uniform injection of carriers to each active region module, which is ensured by the series connection in the structure, and lower carrier concentration for lasing threshold [95]. As such, ICLs have become one important coherent light source that covers mid-infrared wavelength range (e.g., 3-6 μm) [96-100].

The charge carrier distribution inside the MQW active region plays a critical role in device functionality and performance. In ICLs the carrier transport is via interband tunneling in type-II heterostructures. The type-II band-edge alignment along with the large conduction band offset in the nearly lattice-matched InAs/GaSb/AlSb III-V material system is used in ICL devices, which leads to achieve excellent carrier confinement allowing the emission wavelengths of the device to be tailored from mid-IR range to far-IR [95]. Hence, these ICL devices with

reduced threshold current density have proved to be promising and practically energy-efficient semiconductor laser sources covering a wide mid-IR wavelength spectrum. Though, intensive theoretical models were developed to calculate charge carrier distribution profile in semiconductor quantum structures [101-104] in ICL devices, the simulation results have rarely been experimentally verified in a direct manner due to lack of enabling experimental tools. Internal phenomena and external performance measures were seldom linked through compelling experimental observation. Many failures and degradation of device operation remain puzzling as a result. For example, modeling suggests that a single hole injector quantum well (QW) would suffice in an ICL, nevertheless, empirical studies have found improvement when the second GaSb QW is included to make the tunneling barrier quite thick [93]. The R084 [95] a broad-area laser device lased in pulsed mode at a wavelength near 5 μm, above room temperature (to 320 K) with a threshold current density less than 600 A/cm^2 at 300 K. Quantification of charge density in the type-II band edge of the ICLs active region can assess the external performance of the lasing device. Recently, record-breaking device performance improvement of ICLs was reported and was attributed to rebalancing of electrons and holes in the active region, but the carrier density profile was only modeled and input/output behaviors of the device were measured [96]. Apparently, quantitative and direct measurements of inner workings such as charge carrier density profile would greatly facilitate in-depth understanding of underlying physics in ICLs, leading to technology advancement and innovation.

Although significant progress has been made in the development of ICLs [95, 96], experimental verification of some of the major fundamental properties that relates to the potential energy profile are unknown such as charge carrier density and their transport, effect of electric field on lasing ICLs and voltage distribution across individual cascade stages under an external bias. The ICLs are known to involve in interband (CB and VB) carrier transport phenomenon across different material layers, so modeling or even experimentally determining charge carrier density in the active region has been quite difficult. Vurgaftman et al.[99] presented some estimation based on calculated quasi-equilibrium carrier density across the modules. Experimentally quantifying and estimating the charge density that affects the possible device performance will be evaluated indicating the effect of electric field and dynamic charge carrier accumulation. These are some of the major physical parameters and in some devices they are known to act as detrimental issues to devices, such as in terahertz quantum cascade lasers

where they form electric field domains, and degrade device performance [18]. These high field domain formations were also observed in supperlattice structures [19-21]. For enhanced performance of future ICLs, experimental quantification of charge density and dynamic carrier distribution in each module of the active region is of utmost significance. Also the variation of charge carriers with change in temperature needs to be estimated for an analysis of how the carrier concentration change as device transits from lasing to non-lasing operating temperature.

Scanning voltage microscopy (SVM), also called nanopotentiometry, is a tool based on the AFM system that can directly measure voltage change or electric field distribution, with high spatial resolution from the cross section of a fully operating device [33, 49, 50, 52, 53]. This is a nanoscopic probing measurement technique in which the AFM probe is used to measure the potential of each data point inside a given semiconductor resulting in internal potential distribution as a form of voltage mapping of the scanned area. This technique was successfully used on III-V material based laser devices working under DC bias in room temperature [33, 49, 52, 53]. This mapping reveals the local potential properties, such as electric field distribution due to dynamic carrier concentration from which the estimation of charge density in the operating semiconductor device is acquired. Due to high resolution of the AFM probe (~20 nm), the structural layers can also be resolved accurately from the voltage profiling of the mapped image. This technique has few advantages over other related measurement methods as: (a) it does not significantly perturb the device under test [33]; (b) it allows measuring and characterization of operating and lasing devices; (c) it resolves 2D transverse cross section of devices; (d) it presents 1D voltage profile across the distance; and (e) it is a nondestructive technique to the device under test [33].

In this chapter the first experimental measurements of internal charge carrier density profile of actively-biased ICLs from 77 K up to room temperature by using SVM technology are performed. The electron and hole segregation spatially in the undoped multiple quantum well active region are revealed, nevertheless, maintaining the overall balance in total charges, directly confirming the hypothesis of rebalancing of electrons and holes by heavily n-doping the electron injection layers [99]. The experimental results unambiguously show that the charge carrier density at the type-II band-edge in the MQW active region is essentially clamped in the presence of stimulated emission and is determined quantitatively while monotonically increases with device bias otherwise. In contrast to the exponential temperature dependence of the threshold

current, the clamped charge carrier density of the ICL sample is found to slowly increase with temperature from 77 K to its maximum lasing temperature (~248 K) for ICL sample R090, indicating a fairly weak temperature dependence of the threshold gain. The voltage profiling of the device leading to directly imaging and mapping of carriers resolving the nanoscopic structure also present the effect and distribution of dynamic charge carrier concentration along the active region of the operating device under lasing and non-lasing conditions.

4.2 Experimental Procedure

This section details the scanning voltage microscopy (SVM) technique based on the AFM system. The SVM circuitry along with its arrangement to perform the measurement is covered, specifying the conditions and challenges needed to overcome and finally establish the setup. The devices measured were pulse biased so a synchronization of the AFM probe scanning the voltage peak was established to achieve data accuracy. Also the mid-IR ICL device structure and its external characterization is studied which is later employed for SVM measurement. As the mid-IR ICL lases both at room temperature and cryogenic temperature, to verify and establish the cryogenic temperature SVM and determine the unknowing truth of the mid-IR ICL device structure.

4.2.1 SVM Technique on AFM

A commercially available atomic force microscope system (Attocube AFM) is employed for performing SVM measurements. This AFM system can work both at room temperature as well as in cryogenic temperature of liquid nitrogen (77K) or liquid helium (4K). A boron-doped diamond-coated conductive cantilever probe from Bruker with a spring constant = 42 N/m, model no. DDESP-10, is used for the SVM measurements in both conditions. The sample is mounted in the AFM system with the facet of the laser device facing the cantilever probe to implement contact mode SVM scanning. The whole AFM microscope head along with the mounted sample is inserted in the AFM metallic tube which in turn is vacuumed and purged with Helium gas and then this tube with the AFM system is placed inside a suspension chamber for room temperature measurement otherwise placed in a cryogenic chamber for low temperature measurement. In either case, the sample mounted on the system is connected to external circuitry for the system to perform SVM measurements while the cantilever probe detects the voltage

signals from the top of the sample surface at the time of scanning that is directly fed back into the acquisition system and is recorded. The external circuitry applies pulsed bias to the sample, the frequency and pulse width depends on the sample to be measured (f = 100 Hz, w = 5 μs for mid-IR ICL device), while the applied bias and current on the sample is monitored on the oscilloscope. Both the AFM topology and the voltage profile across the sample are acquired simultaneously by the AFM controller. Details of the experimental techniques are outlined in the following subsections.

4.2.1.1 Room Temperature SVM setup

The AFM based SVM measurement is a contact mode measurement technique in which the AFM probe scans the sample surface. The nanoscopic surface profiling based SVM is a high resolution imaging technique that maps and profiles voltage distribution (as device is under operation) across the sample as the conductive probe scans the sample surface. To achieve a high resolution image the probe tip is made to have a deep contact into the sample surface while the scanning is performed, for this purpose the force on the tip is made to be quite high (~2-5 μN) which accounts for the risk of the tip wearing out very fast and sometimes breaking while also causing scratches on the surface making it inoperable. But care needs to be taken so that neither the tip breaks nor the sample becomes inoperable which remains a big challenge in SVM. Along with the optimization of force (based on the resolution of the scanned image), the scan speed, pixel size of the scan, and scan frequency needs to be adjusted precisely for high accuracy mapping. Otherwise, the scanned image may not be mapped properly, the resolution will be degraded and also the tip may break. The tip used for the measurement has a radius of ~20 nm while the scanned image resolves details within ~6-10 nm variations. A careful execution, calibration and synchronization of all these factors are accomplished to produce a high spatial resolution scanned image with perfect mapping of carriers from the surface.

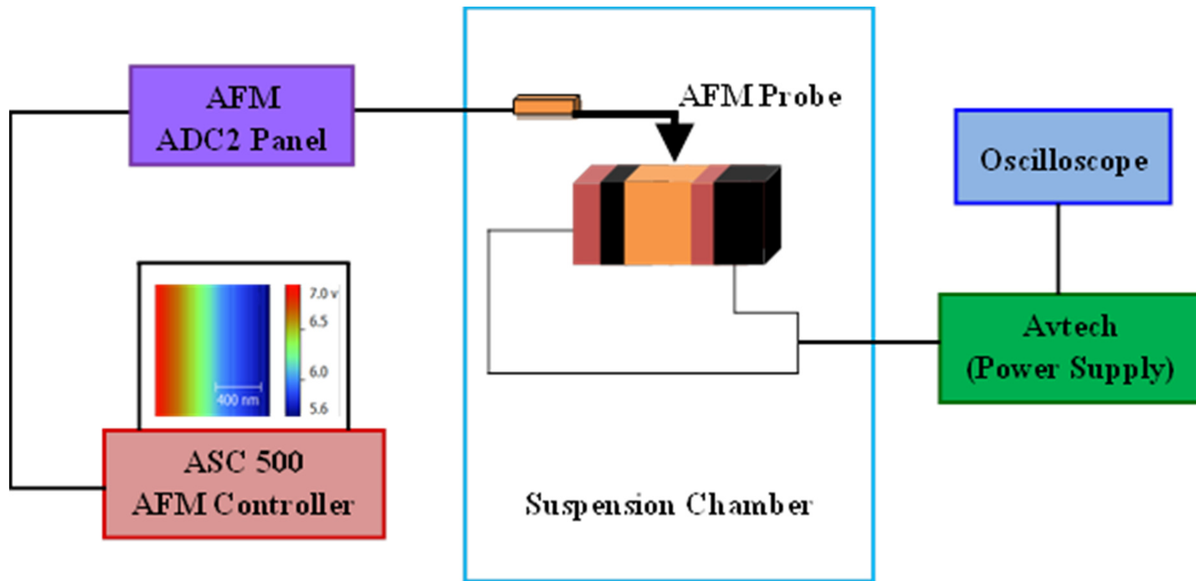

Figure 4.1. Schematic of room temperature scanning voltage microscopy measurement setup. The device sample is biased using an Avtech power supply. The injected voltage along with the measured current on top of the device is monitored by the oscilloscope. The AFM probe scans the cross-section of the sample surface and sends the measured data via the ADC2 panel of the AFM system to the AFM controller.

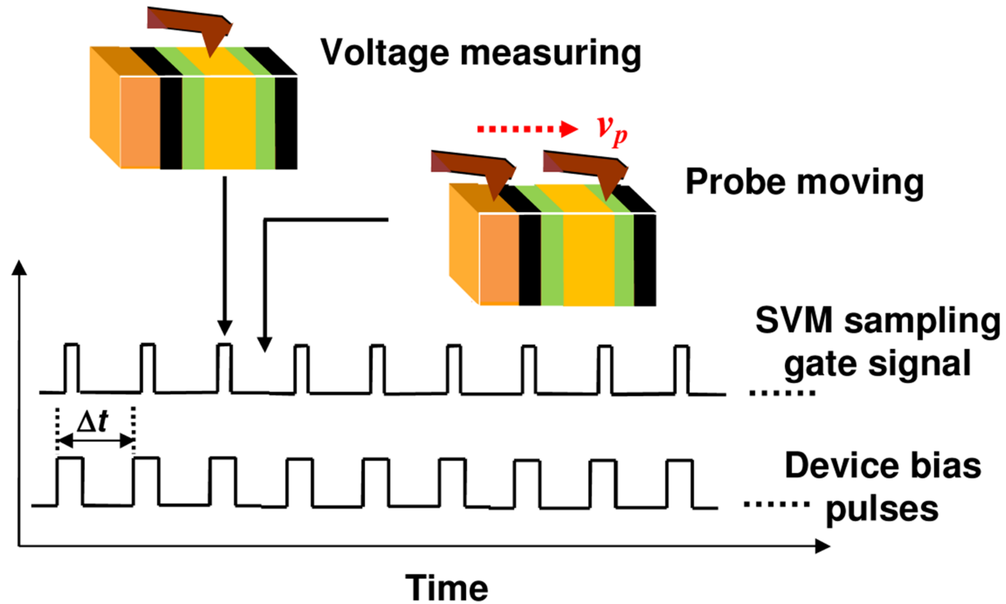

Figure 4.2. A schematic diagram to show the synchronization between SVM sampling and applied device bias pulse train. The device pulse repetition rate is f (= $1/\Delta t$), the AFM probe scan distance is d, and the sampling number of each line scan is N. Then the probe scan speed is set at $v_p = df/(N\text{-}1)$ to satisfy the synchronization condition.

In the SVM measurement the sample to be measured is biased externally so the device is in operation or in lasing condition. The probe is made to scan the surface while the bias passes through the device and every point of contact with the sample and the probe is grabbed by the probe and mapped, so a voltage data profiling is performed. Figure 4.1 shows the schematic experimental setup of the SVM measurement at room temperature. As mentioned earlier the attocube AFM is used for the measurement purpose. The sample is mounted on a sample holder with its facet facing the AFM probe. The whole system is placed in the suspension chamber to avoid any vibration and external disturbances at the time of measurement. The SVM experimental setup is quite similar to the setup used by Ban et al. [33, 49, 52] for voltage profiling of buried heterostructure (BH) laser devices; except that the AFM system itself is different as the measurement for the thesis also needs to be performed at cryogenic condition. The schematic of the whole SVM setup is shown in Figure 4.1. The sample to be scanned is connected externally and a pulse biased is applied via avtech (model no. AVR-3HF-B-PN-UWA) at a frequency of 100 Hz and pulse width 5 μs for mid-IR ICL device, while the applied bias and current on the sample is monitored on the oscilloscope. The bias on the device is varied from 0 V up to 3.3 V. The AFM nanoscopic probe scans the sample in contact mode and reads and senses the voltage data for 512 pixel points across the device for whatever area the measurement is required generating a nanoscopic profile image of the scanned region at each applied sample bias. This voltage data is then measured by the probe and directly acquired through the ADC2 panel of the ASC500 AFM controller of the AFM system itself as a nanosurface profile map is achieved. The SVM voltage sampling is synchronized with the electric pulses applied to the device under test in the time domain as observed in Figure 4.2 and is detailed below. A 1D voltage profile is achieved for each scan across the sample surface presenting a voltage variation. The frequency and width of the applied pulse bias are well synchronized with probe scanning speed, pixel points and scan frequency. This coordination is the most difficult and utmost challenging part of the measurement, as this determines how well the data is collected from the peak of the pulse bias. To achieve best result one pulse must be synchronized with one data measurement point. This synchronization along with the SVM measurement objective is only fulfilled following the calculation based on the equation $v_p = df/(N-1)$ as shown in Figure 4.2 where v_p is the probe velocity, N is the number of line scans, d is total scanned distance and f is the frequency of pulse bias.

4.2.1.2 *Cryogenic Temperature SVM setup*

The cryogenic temperature AFM measurement based on scanning probe microscopy system has been previously used [105]. Here the cryogenic AFM system is used along with the room temperature SVM setup on the AFM system for the purpose of developing cryogenic SVM. The schematic of the cryogenic temperature SVM setup is shown in Figure 4.3. In the measurement sample, a cascade laser device, is mounted on a sample holder (heat-sink) also known as cold finger which in turn is mounted to the piezoelectric stage inside the AFM microscope head. The microscope head is then sealed in a vacuum tube (pumped down to 1×10^{-3} mbar), which is

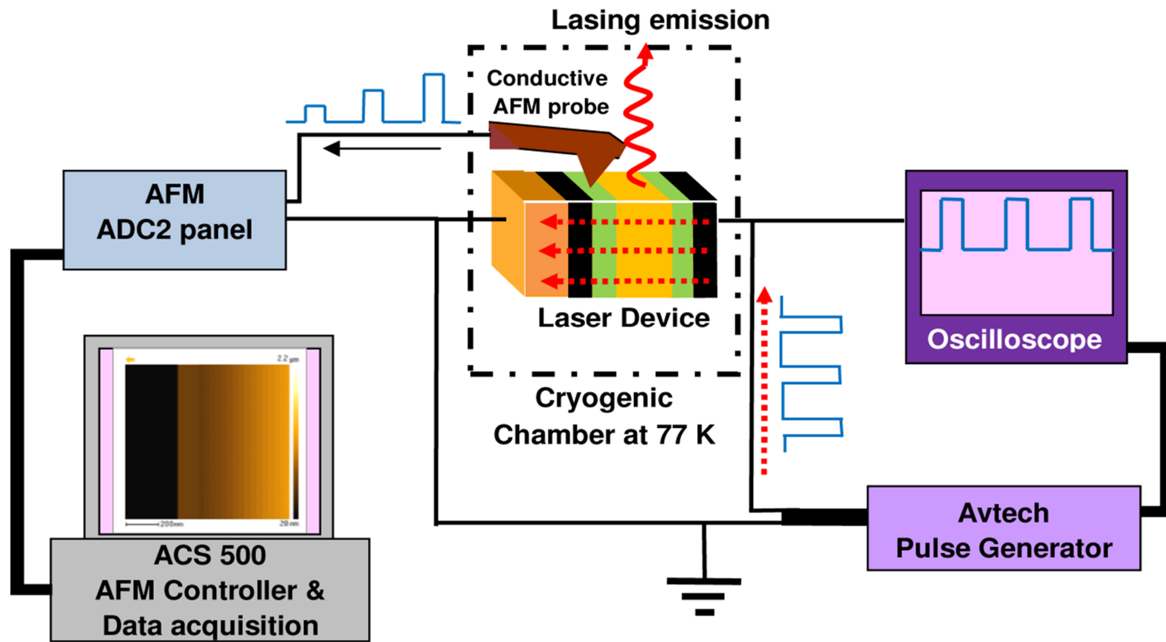

Figure 4.3. Schematic of the cryogenic temperature scanning voltage microscopy (SVM) set-up. A cascade laser sample under test is mounted on the AFM system that is biased in pulsed mode using an Avtech pulse generator. The applied bias pulses are monitored using an oscilloscope to ensure good pulse shape. The voltage signal picked up by the AFM probe is fed directly into the AFM data acquisition system through a built-in analog-digital-converter (ADC) panel 2. In the SVM experiments, the scan range is set as desired for the measurement purpose. The scan speed is set accordingly to synchronize the SVM voltage reading at each sampling point with the device bias pulses.

submerged into a chamber (cryogenic chamber) full of liquid nitrogen. A small amount of helium gas is purged into the vacuum tube to an internal pressure of 200 mbar, enabling sufficient heat exchange between the heat-sink and the tube wall. The device (heat-sink)

temperature is monitored and kept at 77 K during the SVM scans. A conductive AFM probe (Diamond-coated, Boron-doped Si cantilever probe, spring constant 42 N/m, radius of probe tip ~20 nm) scans in contact mode over the transverse cross-section, cleaved laser facet (uncoated), of the device to access the voltage signal from sample surface. The device is actively biased in pulse mode as was the case of the room temperature SVM set up and the bottom electrical contact is set as a voltage reference. Voltage signals from the AFM probe are directly fed back to and recorded by the AFM data acquisition system through a built-in ADC channel (voltage resolution 1 mV). The scanning is executed at low frequencies with a slow scan speed of 100 – 500 nm/s. The applied force to the SVM cantilever probe is in the range of 2 – 5 μN, depending on measurement requirements. The contact force is set high enough to ensure the probe is able to penetrate mechanically into the native oxide layer on the semiconductor so as to establish a good electric contact non-destructively, although special care is taken to avoid damaging the laser emission facet. This may result in some scratching on the sample surface but it is negligibly small (~20 nm tip diameter) compared to the width of the facet (~150 μm), hence not affecting device performance. Each 2D SVM image consists of 512 line scans and each line scan consists of 512 sampling points.

The major features that emphasize the novelty of the SVM method are: (1) Non-destructive in-situ measurements – different from conventional input-output characterizations in which a mid-IR ICL device is actively biased, but no nanoscopic information is revealed, or conventional static structure characterizations in which nanoscopic structure details are retrieved but the device is not in operation and is often destructive, this SVM probes nanoscopic information while the device is under lasing operation. It visualizes for the first time the formation and evolution of non-uniform electric field inside the multi-quantum-well active region of an operating mid-IR ICL. SVM also precisely quantifies the charge transfer and accumulation with type-II quantum well layers, resulting in some internal electric field in the region and other important parameters such as the ohmic contact voltage drop and the depletion region width in the top semiconductor contact layer. As such, nanoscopic origins and macroscopic behaviors are linked for the first time in mid-IR ICLs. (2) High spatial resolution – the high-resolution SVM scans are demonstrated to resolve individual interband cascade modules and identify the exact position of non-uniformity, which is an important information for investigating the impact to further the understanding and development of ICLs performance. (3)

Highly sensitive in voltage measurement – the high-resolution and high-precision SVM has clearly revealed a small voltage dip resulting from the potential alteration associated with the electron-hole interactions in the device, which has been till date neglected in ICL theoretical modeling because of its relatively small value ~18 mV compared to the total potential drop per module of ~300 mV.

4.2.2 Mid-IR ICL Device Structure and Performances

The mid-IR ICL devices employed for the purpose of the thesis are R090, R094 and R084 samples grown and reported by Yang et al. [95, 96]. The details of the growth and device structure along with the performance measurements (light-current-voltage) are presented here.

The mid-IR ICL devices are plasmon waveguide structures grown on n^+-type InAs (001) epi-ready substrates that have advantages such as improved thermal dissipation, less demanding material growth and increased flexibility in the design resulting from reduced optical losses [106]. A Gen-II MBE system is used for the purpose of the sample growth [95, 96]. The R090, R094 and R084 ICL devices consist of 8, 15, and 8 cascade stages or modules, respectively, in the active region of the device. The number of modules varies from device to device depending of the lasing wavelength for which the device is meant for. The modules in the active region of the three devices comprise of asymmetric AlSb/GaInSb/InAs/GaInSb/InAs/AlSb, AlSb/InAs/GaInSb/InAs/GaInSb/InAs/AlSb and AlSb/InAs/GaInSb/InAs/AlSb coupled quantum wells (QWs), similar to a "W" structure, respectively [93, 95, 99, 107]. The QW layer thicknesses are adjusted for tailoring the lasing wavelength. The cascade modules in the active region of the device form the waveguide core that is sandwiched between the top (~1.5 μm thick) and bottom (~1.2 μm thick) *n*-InAs (slightly doped or undoped) separate confinement layers. The waveguide core along with the confinement layers for these devices (R090, R094 and R084) are again sandwiched between an n^+-InAs top and bottom cladding layer (doped with Si at ~ 1×10^{19} cm^{-3}) and a thin n^+-InAs top contact layer [106, 107]. The bottom cladding layer for all the devices is 1.6 μm while the top cladding layer is 35 nm. The absence of a thick top plasmon InAs cladding layer for the ICL devices is to cause some optical loss associated with the metallization on the top contact layer; however the loss is not sufficient to prevent lasing at lower temperatures. A schematic of the R094 and R084 layer structure for the ICL is outlined in Figure 4.4 (a) and (b), respectively. It is also noted that the

Layer	Doping	Thickness
InAs	~ 1.0×10^{19} cm^{-3}	0.035 μm
InAs	~ 1.5×10^{17} cm^{-3}	0.020 μm
InAs	undoped	1.35 μm
Active region (15 modules) Active section/electron injector/hole injector		0.9559 μm
AlAs(3)/AlSb	undoped	0.0019 μm
InAs	undoped	1.0 μm
InAs	~ 1.5×10^{17} cm^{-3}	0.020 μm
InAs	~ 1.0×10^{19} cm^{-3}	1.6 μm
InAs	n-type	substrate

(a)

Layer	Doping	Thickness
InAs	~ 1.0×10^{19} cm^{-3}	0.035 μm
InAs	~ 4.3×10^{18} cm^{-3}	0.010 μm
InAs	undoped	1.5 μm
Active region (8 modules) Active section/electron injector/hole injector		0.3624 μm
AlAs(3)/AlSb	undoped	0.0021 μm
InAs	undoped	1.2 μm
InAs	~ 4.3×10^{18} cm^{-3}	0.010 μm
InAs	~ 1.0×10^{19} cm^{-3}	1.6 μm
InAs	n-type	substrate

(b)

Figure 4.4. (a) Schematic layer structure for R094 interband cascade laser. (b) Schematic layer structure for R084 interband cascade laser.

optical loss from the metal layer is less in interband lasers with TE polarized modes compared to TM polarized modes in quantum cascade lasers [95]. This loss in the interband lasers are significantly reduced with the insertion of a dielectric layer (*e.g.* SiO_2) between the top metal layer and the majority of top central ridge, where this dielectric layer fundamentally acts as the top optical cladding role and the current is injected through narrow metal contacts [95]. There have been few studies on different top waveguide cladding configurations [108] that clearly indicated the replacing of top InAs-plasmon waveguide cladding with a dielectric-metal hybrid cladding, the device performance is comparable or slightly superior to that with two sided plasmon cladding layers, in good agreement with the theoretical modelling published for the ICL devices by Yang et al. [95]. At the time of device fabrication, a SiO_2 layer is usually employed for insulation that serves as the top cladding, but is occasionally omitted in broad-area lasers for

quick examination. Recent InAs-based ICL devices have enhanced hole injectors with two or three QWs and smaller electron injectors, compared to initial IC lasers [106, 109]; this development aids in suppressing the leakage current [93].

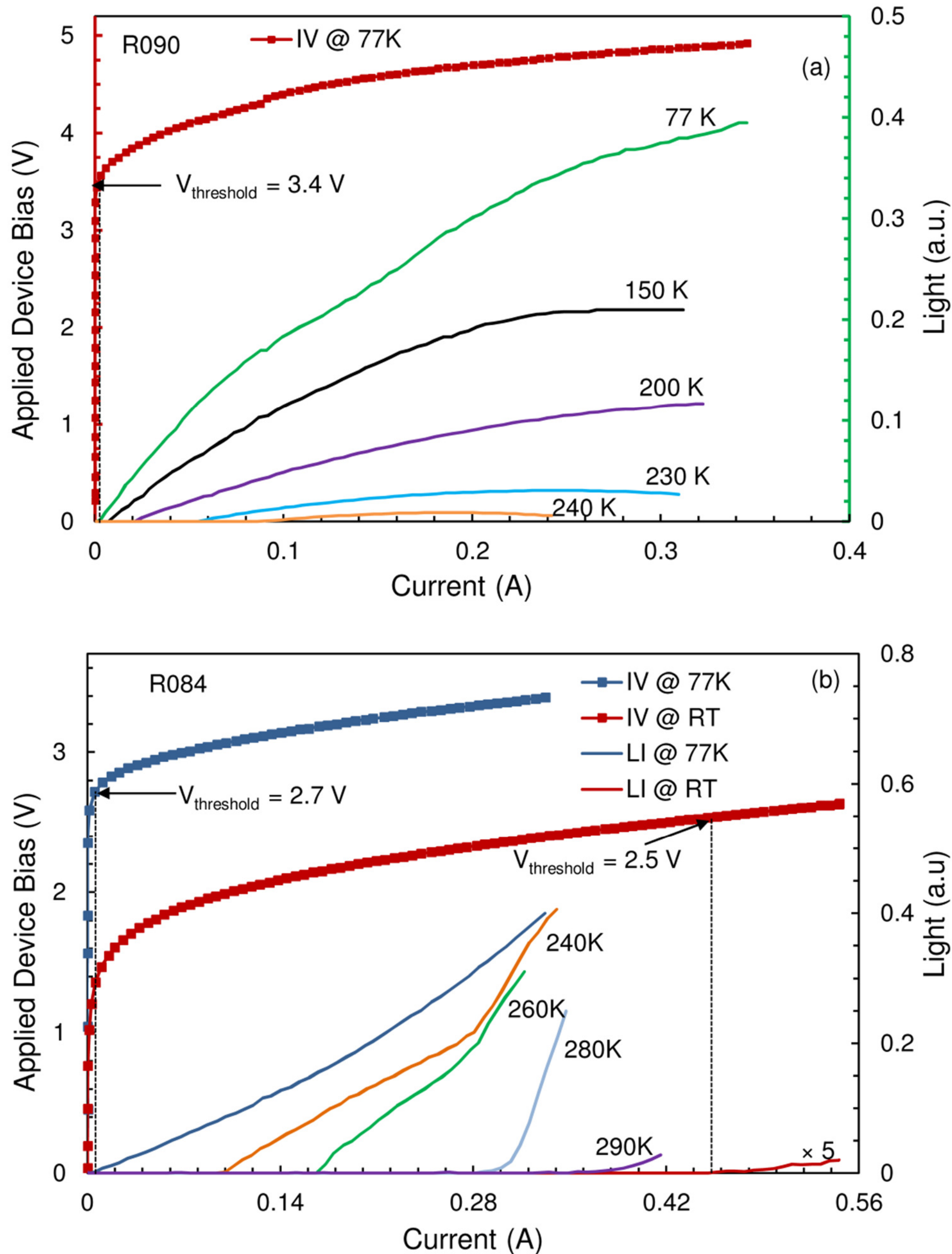

Figure 4.5. (a) LIV characteristics for R090 interband cascade laser showing the lasing threshold at 77 K at 3.4 V. (b) LIV characteristics for R084 interband cascade laser with the lasing threshold of 2.7 V at 77 K and 2.5 V at room temperature (300 K). The light current measurements for the devices were performed at different temperature varied from 20 K to the highest lasing temperature of the device.

The three devices R090, R094 and R084 were designed with 8, 15 and 8 cascade stages respectively by Yang et al. [95, 96], as mentioned earlier for the devices to lase at different wavelengths. Only R084 is ICL device that lases even at room temperature of 320 K at ~5 μm. Light-current-voltage (LIV) measurements under pulsed bias using avtech and oscilloscope with temperatures varying from 20 K to highest lasing temperature of the device was performed for R090 and R084 ICL devices and the LIV measurements for the devices are presented in Figure 4.5 (a) and (b).

4.3 Nanosurface profiling of ICLs

4.3.1 Non-uniform Electric Field Measurement

The ICL samples under test consists of eight (R090 and R084) and fifteen (R094) periods of active and injection sections with a peak emission wavelength of ~4.3 μm for R090 at 77 K and ~5 μm for R084 at 320 K. Each period of the active section (where radiative recombination occurs) has two InAs electron quantum wells and two GaInSb hole quantum wells for R090; three InAs electron quantum wells and two GaInSb hole quantum wells for R094; and two InAs electron quantum wells and one GaInSb hole quantum wells for R084. The electron injection section is made of InAs/AlSb(As) digitally graded quantum wells. The eight cascade modules are sandwiched by the top and bottom micrometer-thick undoped InAs separate confinement layers (SCLs). The detailed device structures are outlined in section 4.2.2. Figure 4.6 (a) illustrates a two-dimensional voltage profile across the R090 device active region that is obtained by scanning a conductive cantilever probe over a transverse cross section area (3×3 μm^2) on the front emission facet [33, 52, 53]. The device is biased at 3.0 V in pulsed mode at 77 K. The measured voltage, drops monotonically from the top metal (positively biased at 3.0 V), across the intermediate layers, to the grounded bottom SCL/contact layers (at 0 V). Four sections are clearly resolved due to their contrast in electric potential – the top metal layer, the top SCL layer (undoped InAs), the interband cascade region layer (eight cascade modules) and part of the bottom SCL/contact layer. As expected, most of the voltage drop occurs over the 386 nanometer thick interband cascade region of the R090 ICL device. The topology image obtained simultaneously from the atomic force microscopy scans confirms that the cross section of the front emission facet is almost atomically flat.

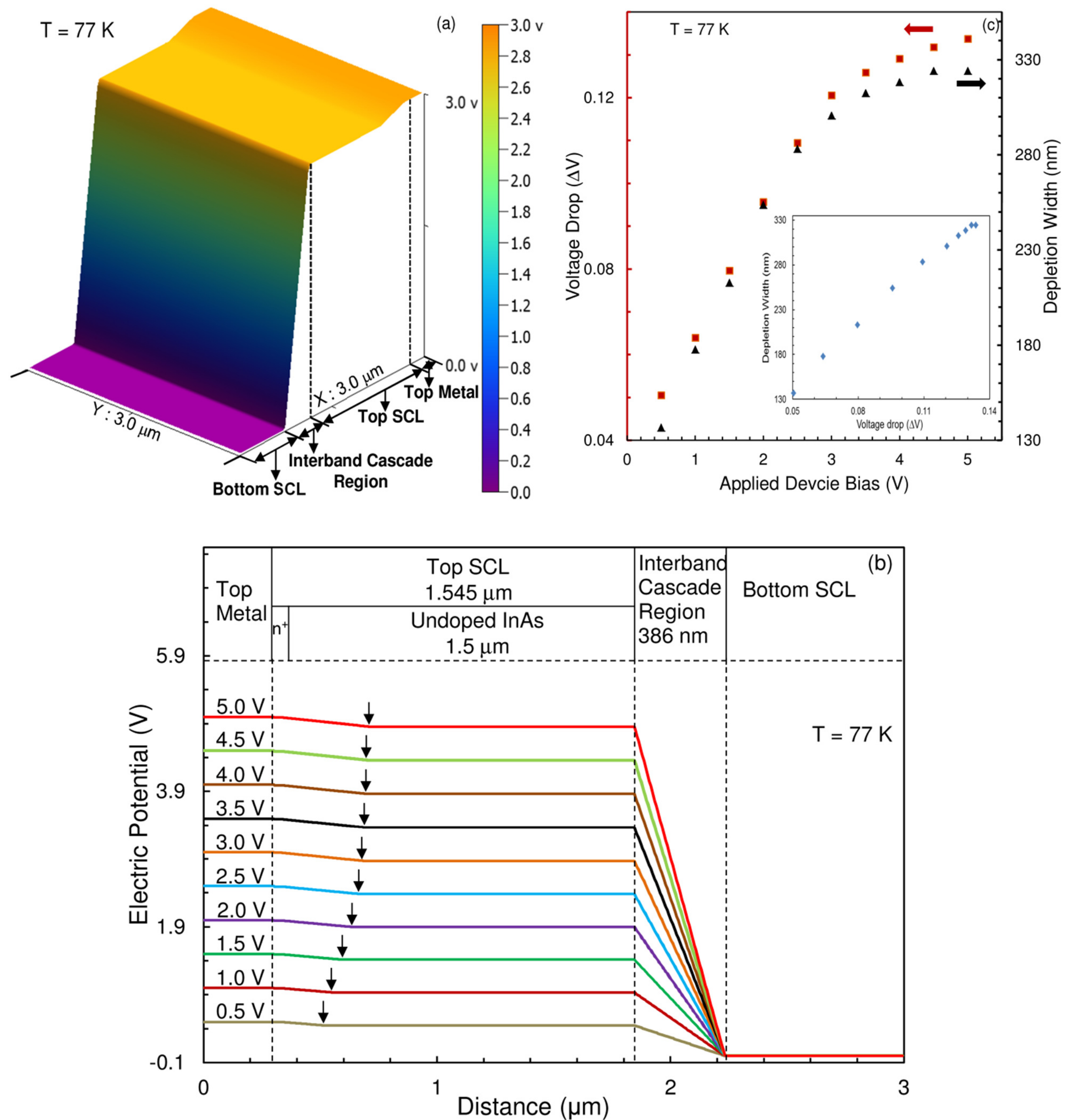

Figure 4.6. Scanning voltage microscopy image across the R090 ICL device at cryogenic temperature of 77 K. (a) SVM scan 2D voltage profile for 3 µm × 3 µm^2 scan area from the top metal to the bottom contact layer across the device at an applied bias of 3.0 V on top of the device. Different sections of the device as per the structure are clearly viewed from the SVM image. (b) 1D section analysis of the SVM voltage profiles for biases 0.5 V – 5.0 V in step of 0.5. Most of the voltage drops across the ~386 nm interband cascade region of the device while drop is also observed at the heterojunction of the undoped InAs confinement layer to the n$^+$ InAs layer forming a depletion region. (c) The voltage drop (ΔV) and the

depletion width at the InAs n⁺-undoped n heterojunction near the top metal contact is achieved for different applied biases from the 1D voltage profile scans in (b), and the calculated depletion width at no-bias is ~157.2 nm.

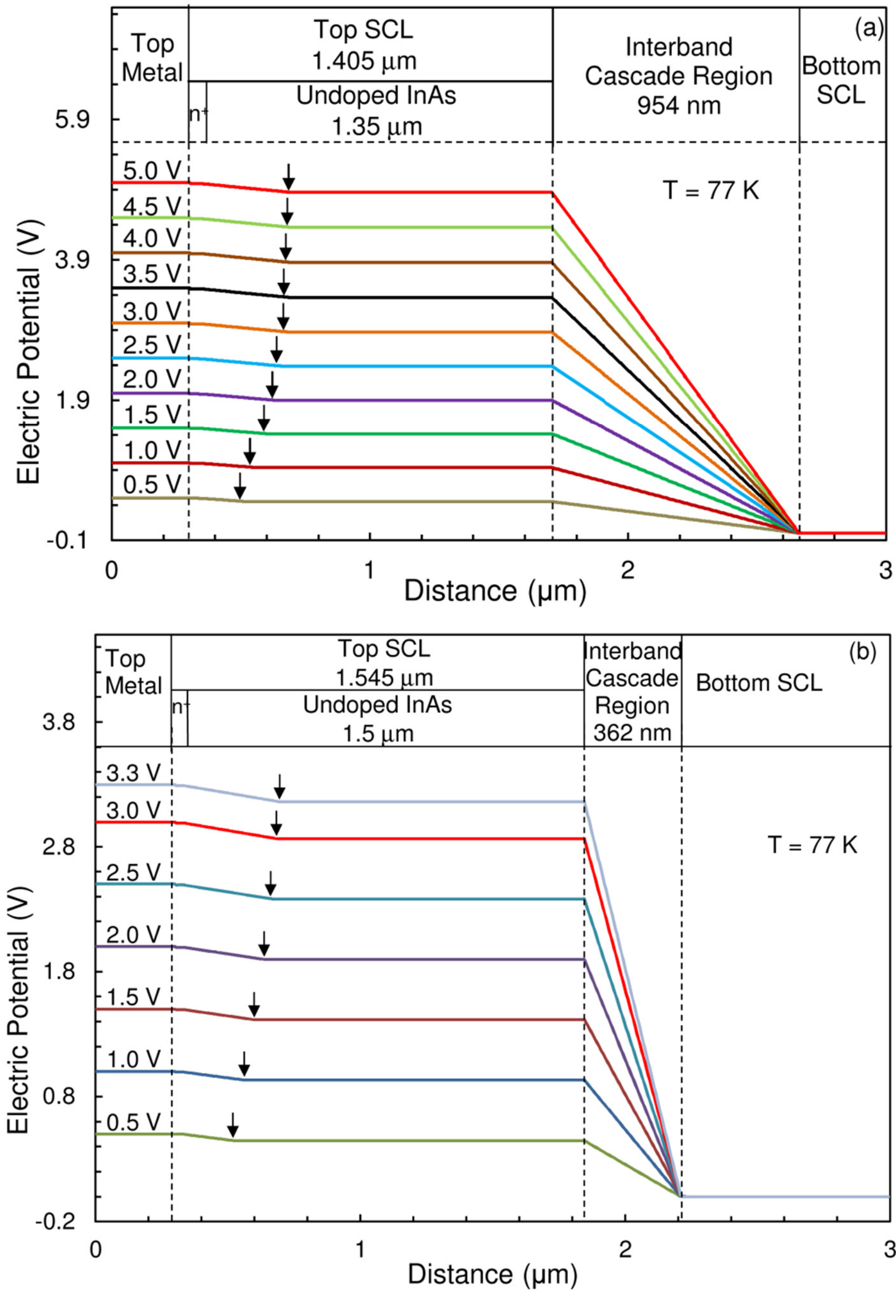

Figure 4.7. (a) 1D section analysis of the SVM measured voltage profiles for R094 at cryogenic temperature of 77 K. The voltage profiles acquired clearly indicate the potential drop to mostly occur in the active region of ~954 nm before the bottom contact layer. (b) 1D SVM voltage profile of R084 across the 3 µm distance from the top contact indicates most of the voltage to drop across the ~362 nm thick interband cascade region [110].

Similar SVM scans are performed at different applied device biases from 0.5 V up to 5.0 V with a step of 0.5 or 0.3 V at 77 K for R090, R094 and R084 devices. By averaging cross-section line scans that make up a two-dimensional (2D) SVM image similar to the one shown in Figure 4.6 (a), one-dimensional SVM measured voltage profile curves are obtained as a function of the distance from the top metal layer and presented in Figure 4.6 (b) and Figure 4.7 (a), (b) [110] for R090, R094 and R084, respectively. The interband cascade region widths consisting of the active sections are distinctly observed experimentally using SVM technique to be 386 nm, 954 nm and 362 nm as per the design structure of R090, R094 and R084 devices, respectively. The slope of the voltage profile curve is almost uniform over the interband cascade region (thus indicating a constant electric field) and increases proportionally with the increase of the applied device bias. A slight voltage drop is observable at the top contact layer/top SCL layer interface, which is likely attributed to the junction between the n^+ InAs contact layer (n-doped ~1×10^{19} cm^{-3}) and the nominally undoped InAs SCL (which might have background n-type doping ~1×10^{16} cm^{-3}) near the interface for all the device measurements. The different concentration in these two layers generates a discontinuity of ~45 meV in the quasi-Fermi energy from the analytical calculations of the n^+ - n semiconductor hetrojunction. When the device is under forward bias, the current flows from the top contact into the top SCL layer, meaning a reverse bias junction is formed. The measured voltage drop over this junction and the depletion width are plotted in Figure 4.6 (c) for R090 ICL device. Both the voltage drop and the depletion width increase almost linearly with the applied device bias at the beginning and then gradually saturates at higher biases. This undesired voltage drop is only 0.13 V at a device bias of 5.0 V, confirming the high voltage efficiency ((5-0.13)/5×100%=97.4%) in the ICL devices.

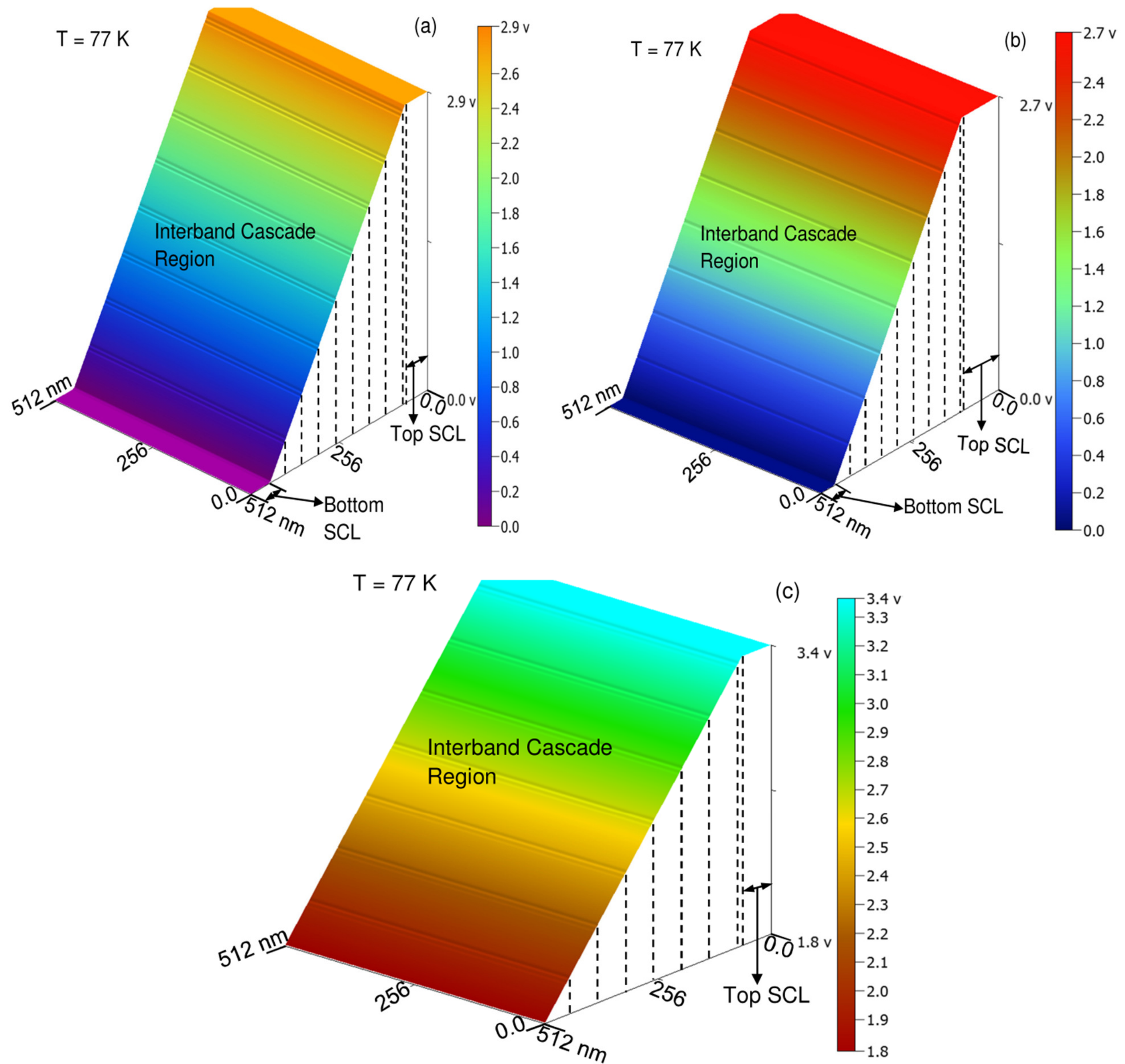

Figure 4.8. (a) A 512 nm scanned voltage profile of R090 focussing the active region portion at 77 K at an applied bias of 3.0 V. 8 clear pairs of voltage dips each ~9 nm wide is observed and denoted with a dotted line at every ~48 nm resolving 8 modules in the active region that accurately corresponds to the device design. (b) SVM voltage profile of 512 nm on the active region portion at 77 K at an applied bias of 2.8 V for R084. 8 clear voltage dips of ~5 nm wide observed at every ~45 nm resolving 8 modules in the active region as per the device design. Unlike R090, the voltage dips are single dips that evidently designate one GaInSb layer in the device design [110]. (c) Voltage drop across R094 is observed in the active region portion from the scanned image measured at an applied bias of 3.5 V. 7 clear pairs of voltage dips each ~13 nm wide is observed and denoted with a dotted line at every ~63 nm resolving 7 modules in the active region.

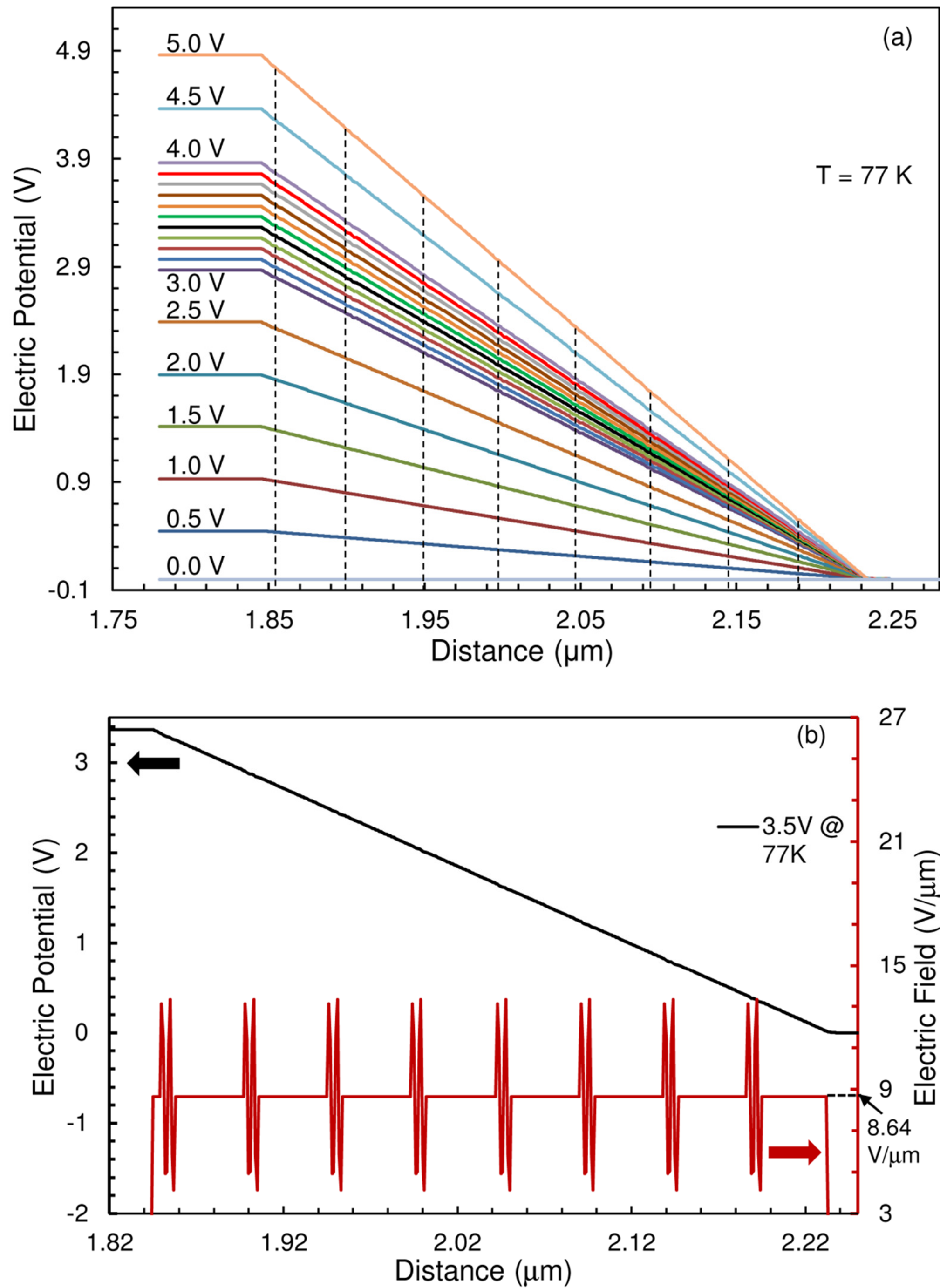

Figure 4.9. Non-uniform electric field observed across each module that are periodic among the modules. (a) High resolution 1D SVM scanned voltage profile of 512 nm on the active region portion of the device at 77 K. The dotted lines indicate the 8 dips in the voltage across the ~386 nm active region. (b) 1D voltage profile of 512 nm scan at an applied bias of 3.5 V with corresponding electric field (-dV/dx) distribution across the region. 8 pairs of spikes at every ~48 nm in the active region observed resolving 8 modules in the device.

Individual cascade modules are resolved in high-resolution SVM scans by reducing the scan range. Figure 4.8 (a) (b) [110] and (c) shows such two-dimensional voltage profiles over a smaller area of 512 × 512 nm^2 for R090, R084 and R094, respectively. It is revealed that every ~48 nm and ~63 nm in distance for R090 (Figure 4.7 (a)) and R094 (Figure 4.7 (c)), respectively, a pair of voltage dips, while at every ~45 nm a voltage dip for R094 (Figure 4.7 (b)), is observed, and is denoted by dashed lines. There are in total eight such pairs of voltage dips for R090 and eight single voltage dips in R084 over the interband cascade region, corresponding to the eight cascade modules in the devices. The measured 48 nm, 45 nm and 63 nm periods for R090, R084 and R094, respectively, agrees well with the design module thickness (386 nm/8 = 48.25 nm; 954 nm/15 = 63.6 nm; and 362 nm/8 = 45.25 nm). Such voltage dips are measured at all device biases from zero bias to 5 V at step of 0.5 V or 0.1 V for R090 and the 1D section analysis of the SVM profile images are presented in Figure 4.9 (a). The magnitude of the voltage dips depend on the applied device bias (increase in applied bias increases number of carriers, hence voltage dip magnitude increases) and are in the range of micro-volts up to a few mV. The internal electric field (F) inside the MQW active region can be obtained by calculating the first order derivative of voltage against distance ($F = -dV/dx$), which are plotted in Figure 4.9 (b), clearly delineate the exact location of the pair of voltage dips. At a device bias of 3.5 V, the average electric field across the MQW active region is F = 8.64 V/μm. Over each of the eight voltage dip pair regions, the electric field spikes are observed, yielding two peaks and two valleys. As will be discussed in more detail shortly, the nonuniform electric field is a direct sign of the expected spatial segregation of electrons and holes in the unique type-II quantum wells in the active sections of this ICL device. The SVM measurements for all these devices were performed several times on a same sample and data acquired is found to be repeatable indicating good reliability of the SVM measurements.

4.3.2 Quantitative Charge Density Analysis and Discussion

The voltage dip pairs become more perceivable by further zooming in the voltage profile curve. As shown in Figure 4.10, each voltage dip pair spans a distance of ~9 nm and the magnitude of the voltage dips is around 7 mV at the device bias of 3.5 V for R090. The first voltage dip pairs are located at 5 nm away from the interface of the undoped InAs top SCL layer and the interband

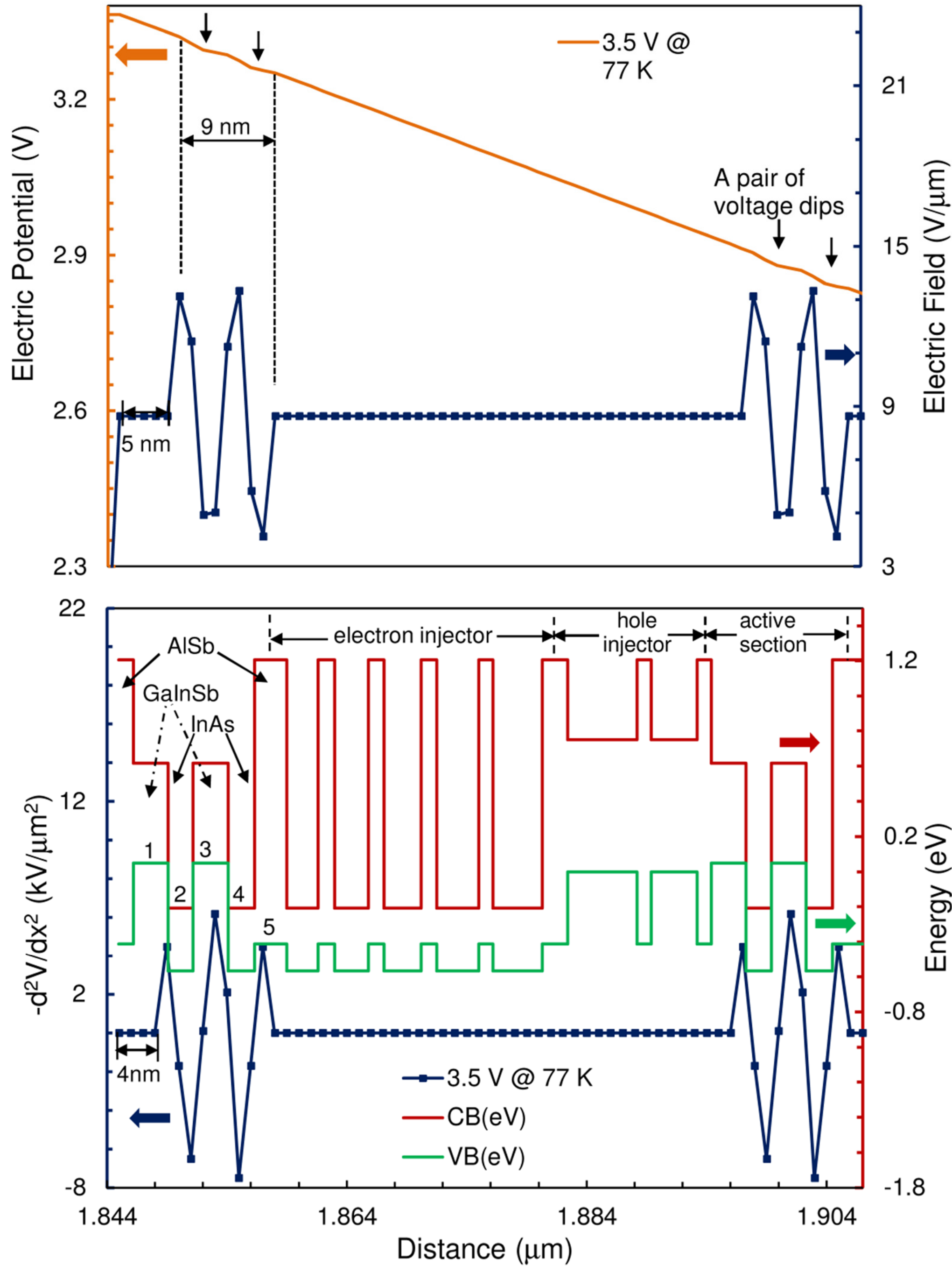

Figure 4.10. Identification of accumulation of dynamic charge carriers at 77 K from zoomed-in voltage profile in ICL devices at the start of the active region. Two pairs of voltage dips observed for R090 on the 63 nm scanned voltage profile at 3.5 V on top of the device, which correspond to two pairs of spikes in electric field at a distance of 48 nm with each pair covering 9 nm. The adjudged d^2V/dx^2 profile is calculated from voltage and electric field distribution and compared with the ideal schematic conduction band (CB) and valence band (VB) energy level band diagram under no bias condition for the module

region. Each pair of zig-zag in d^2V/dx^2 profile has two charge carrier dips and two peaks signifying electron concentration in InAs layers and hole concentration in GaInSb layers, respectively, at GaInSb/InAs/GaInSb/InAs/AlSb interface that is clearly imaged.

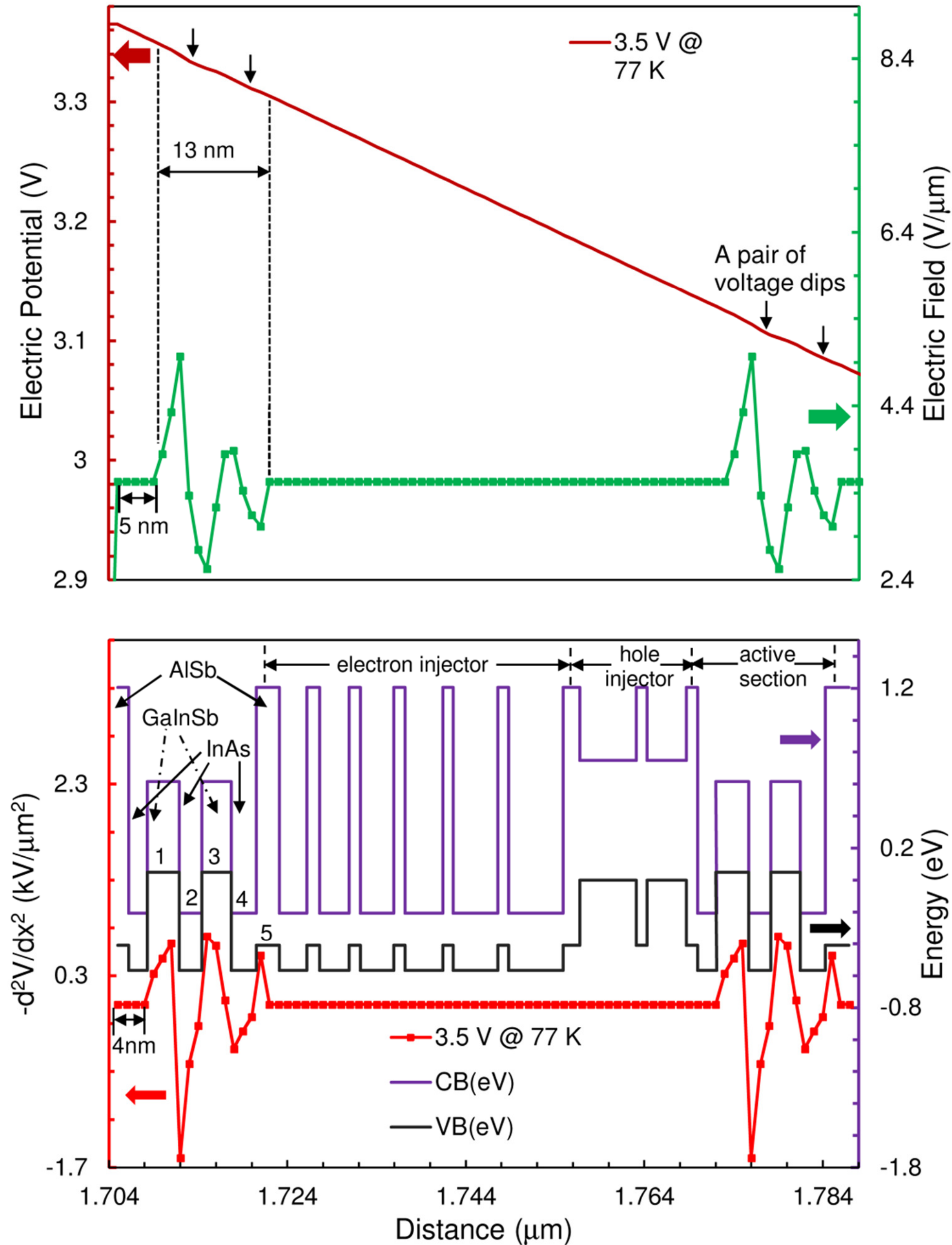

Figure 4.11. Accumulation of dynamic charge carriers in the active region of ICL. 84 nm scanned voltage profile of R094 at 3.5 V on top of the device resolves two pairs of dips in voltage with two pairs of corresponding spikes in the electric field each ~13 nm wide, at a distance of 63 nm. The adjudged d^2V/dx^2 profile is compared with the schematic of the CB and VB energy band diagram at no bias for the module

region. A pair of zig-zag consisting of two dips for electron concentration in InAs layer and two peaks representing hole concentration are observed at InAs/GaInSb/InAs/GaInSb/InAs/AlSb interface, signifying electron-hole transfer and interaction across the CB and VB energy states.

cascade region, corresponding to the nominal coordinates of the InAs/GaInSb MQW active section of the first cascade module (see adjudged Figure 4.10). Similar voltage peak and dips are observed for R094 and R084 ICLs in Figure 4.11 and Figure 4.12, respectively. SVM measurement is conducted left to right as well as from right to left thus asserting repeatability of the measured data and the measurements for all these devices were performed several times and the voltage dips are observed to occur repeatedly at the same location indicating reliability and repeatability of the SVM measurements. This repeatability also confirms and localizes the voltage dips. From the voltage profiles for the devices R090, R094 and R084 the voltage dips are observed at regular intervals of 48 nm, 63 nm and 45 nm, respectively, resolving individual modules in repeated SVM measurements; and this module thickness matches with the design structure. The electric field (-dV/dx) and d^2V/dx^2 profiles in Figure 4.10, 4.11 and 4.12 are acquired from averaging 512 line scans voltage profiles for each data point in all SVM measurements, thus indicating accuracy and reliability of the measured parameters. All the line scans resolved identical voltage dips that relates to spikes in electric field. The spikes are observed for voltage dips in every module for all the devices indicating accuracy and reliability of the dV/dx and d^2V/dx^2 distributions. The dips are observed for the entire device consisting of 8 or 15 modules as per the device structure and the voltage dips match accurately with the electric field and carrier density profiles which in turn match the schematic energy band diagram across the modules in Figure 4.10, 4.11 and 4.12. Thus, based on the accuracy and reliability of the SVM measurements and repeatable data acquisition the electric field and carrier profiles are imaged. The voltage dip pairs in R094 spans for ~13 nm while for R084 the voltage dip extents for ~5 nm. For R090, the rest of the voltage dip pairs repeat every ~48 nm; for R094 therepetition is every ~63 nm; and for R084, the voltage dip occurs at every ~45 nm, they therefore coincide to the InAs/GaInSb MQW active section of the corresponding modules, respectively. The top part of the images in Figure 4.10, 4.11 and 4.12 shows more detailed features of the electric field distribution profile, which are almost identical in each of the eight or fifteen cascade modules (the figure only shows the first two) depending of the device. The

identical electric field distribution profile among the eight cascade modules for R090 represents uniform carrier injection and distribution in each of the modules, ensured by the aforementioned series connection in the structure [94]. Perhaps more strikingly, from the voltage distribution profile, one can derive the net charge carrier density profile (n(x)) by calculating the second order derivative of V(x) as [111]

$$n(x) = -\frac{\varepsilon_0 \varepsilon_r}{q}\frac{d^2V(x)}{dx^2} \qquad (4.1)$$

where ε_0 is the vacuum permittivity, ε_r the relative permittivity and q the electron charge assuming that the work done is only electric work relating to local electric charge carrier density [111]. The calculated $-d^2V/dx^2$ results are plotted in the adjudged (below) images of Figure 4.10, 4.11 and 4.12, for R090, R094 and R084, respectively, together with the band diagram of the active and injection sections at zero bias. It is to be noted that there exists no voltage variations in the SVM measurements especially in the electron and hole injector parts though there exist a hetero interface, this is directly attributed to no net charge existing in the portion across the structure. Nevertheless, it shows that the net charge density is zero in the hole injector and most of the electron injector section for all the devices, while negative net charges accumulate in the InAs conduction-band quantum wells of the active section and positive net charges accumulate in the GaInSb valence-band quantum wells of the active section as well as the first AlSb valence-band quantum well of the electron injector section for all the three devices. Apparently electrons and holes are injected into the active section for radiative recombination, but they spatially segregate from each other due to the unique band alignments in the type-II antimonide system [93]. It is to be noted that this SVM result marks a direct and to the best of knowledge, these are the first-ever published observations of charge carrier distribution while the semiconductor quantum laser is in operation, illustrating the great potential for SVM techniques to advance ICL research and development. Theoretical modelling has already disclosed substantial electron accumulation in the electron injector quantum wells by heavy n-doping [93, 99]. Such electron density distribution is however not observed in the injector section in the SVM measurements, which might likely be attributed to the negative charges of the accumulated electrons that are mostly neutralized by the positive charges of the ionized n-type dopants in the same region, while the SVM is only sensitive to net electric charges. The carrier density acquired from these

carrier profiles achieved from SVM measurements are observed to be at par with the simulated carrier density values acquired by Vurgaftman et al. [93, 99].

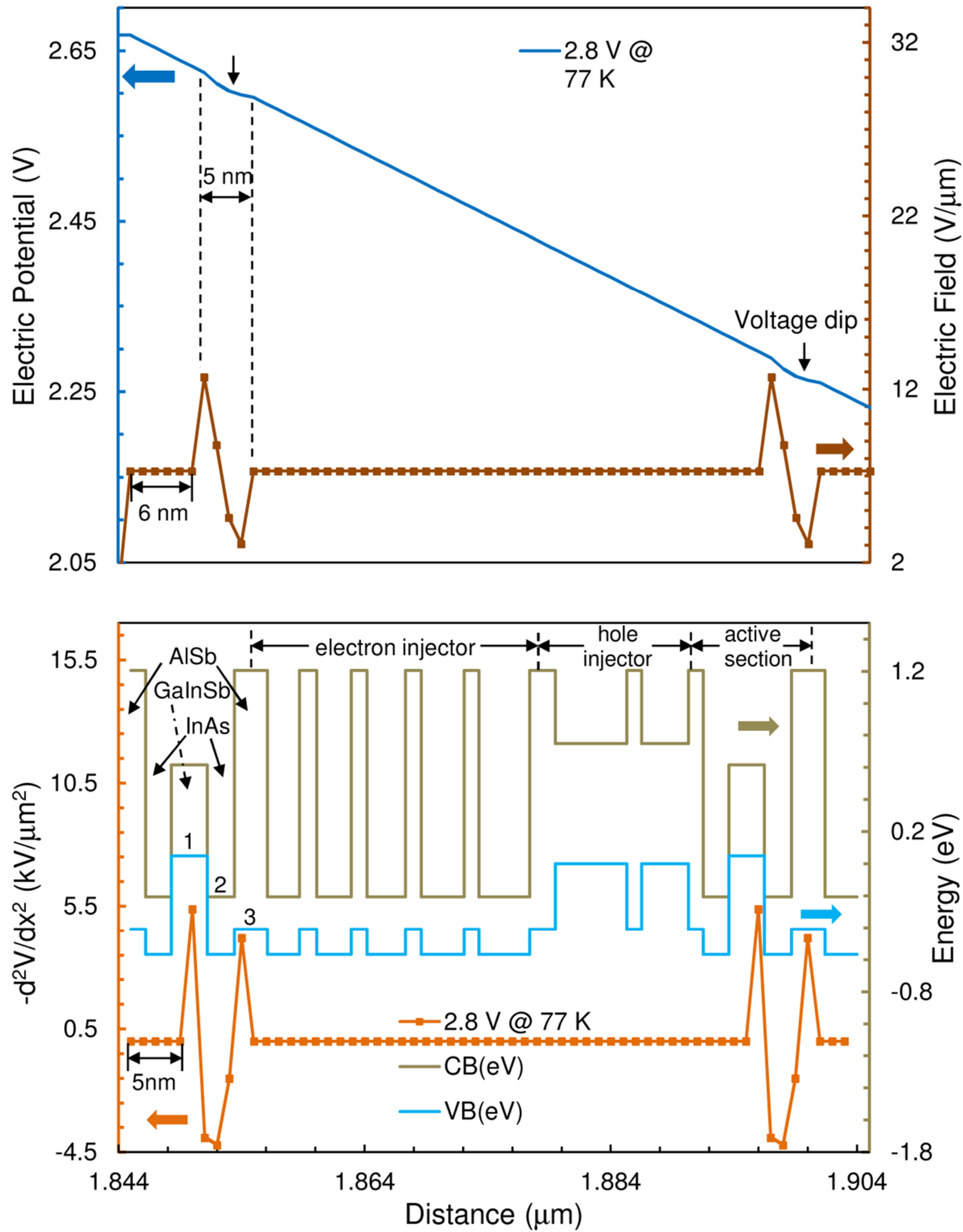

Figure 4.12. Identification of accumulation of dynamic charge carriers at 77 K from zoomed-in voltage profile in ICL devices at the start of the active region. 61 nm scanned voltage profile of R084 device at 2.8 V on top of the device resolves two dips in voltage with two corresponding spikes in the electric field each ~5 nm wide, at a distance of 45 nm. The adjudged d^2V/dx^2 profile is compared with the CB and VB energy band diagram under ideal no bias condition for the module region. Unlike for R090 and R094

ICLs in Figure 4.10 and Figure 4.11, a spike consisting of a dip for electron concentration in InAs layer and two peak representing hole concentration are observed at InAs/GaInSb/InAs/AlSb interface, where electron-hole transfer and interaction takes place across the CB and VB energy states. Voltage dips suggest existence of internal electric field at the GaInSb/InAs junction in each module due to electron-hole transfer and interaction across the conduction band and valence band energy states.

The charge carrier sheet density in each of the quantum wells of the active section can be calculated by integrating n(x) as

$$\sigma_i = \int_i n(x)dx \qquad (4.2)$$

where σ_i is the charge carrier sheet density in the i-th quantum well of the active section and n(x) is the net charge carrier density profile obtained earlier. The symbol i = 1, 2, 3, 4, 5, corresponds to the first GaInSb hole well, the first InAs electron well, the second GaInSb hole well, the second InAs electron well and the first AlSb hole well in the electron injector section, for R090 and R094 in the order from left to right in adjudged Figure 4.10 and Figure 4.11, respectively; while in R084, i = 1, 2, 3, correspond to the GaInSb hole well, the InAs electron well and the first AlSb hole well in the electron injector section in Figure 4.12. The experimental charge carrier sheet densities (σ_i) are achieved by performing the integration using Equation (4.2) and are plotted as a function of the applied device bias at 77 K for R090 and R084 ICLs in Figure 4.13 and Figure 4.14. The carrier sheet density for 77 K for both the devices first increases quickly with the device bias, and gradually saturates at higher biases as seen in Figure 4.13 (a) and 4.14 (a). The dashed line denotes the threshold voltage 3.4 V and 2.7 V of the R090 and R084 ICLs sample at 77 K (Figure 4.5 (a) and (c)). As expected, the carrier density in the active section is essentially clamped when the device starts lasing – all additional injected carriers are consumed by stimulated emission [84]. Similar measurements and calculations are repeated at room temperature (300 K) for comparison, at which temperature the R090 ICL sample does not lase, but the R084 sample lases at a threshold voltage of 2.5 V. The experimental sheet charge carrier densities (σ_i) at room temperature are plotted in Figure 4.13 (b) and 4.14 (b) for R090 and R084, respectively. For R090, a monotonic increase for the whole device bias range from zero to 4 V is observed as the devices is non-lasing at 300 K, while clamping and saturation of charge carriers are observed for R084 due to its lasing condition. In the absence of stimulated emission, the carrier density in the active section is not clamped for R090.

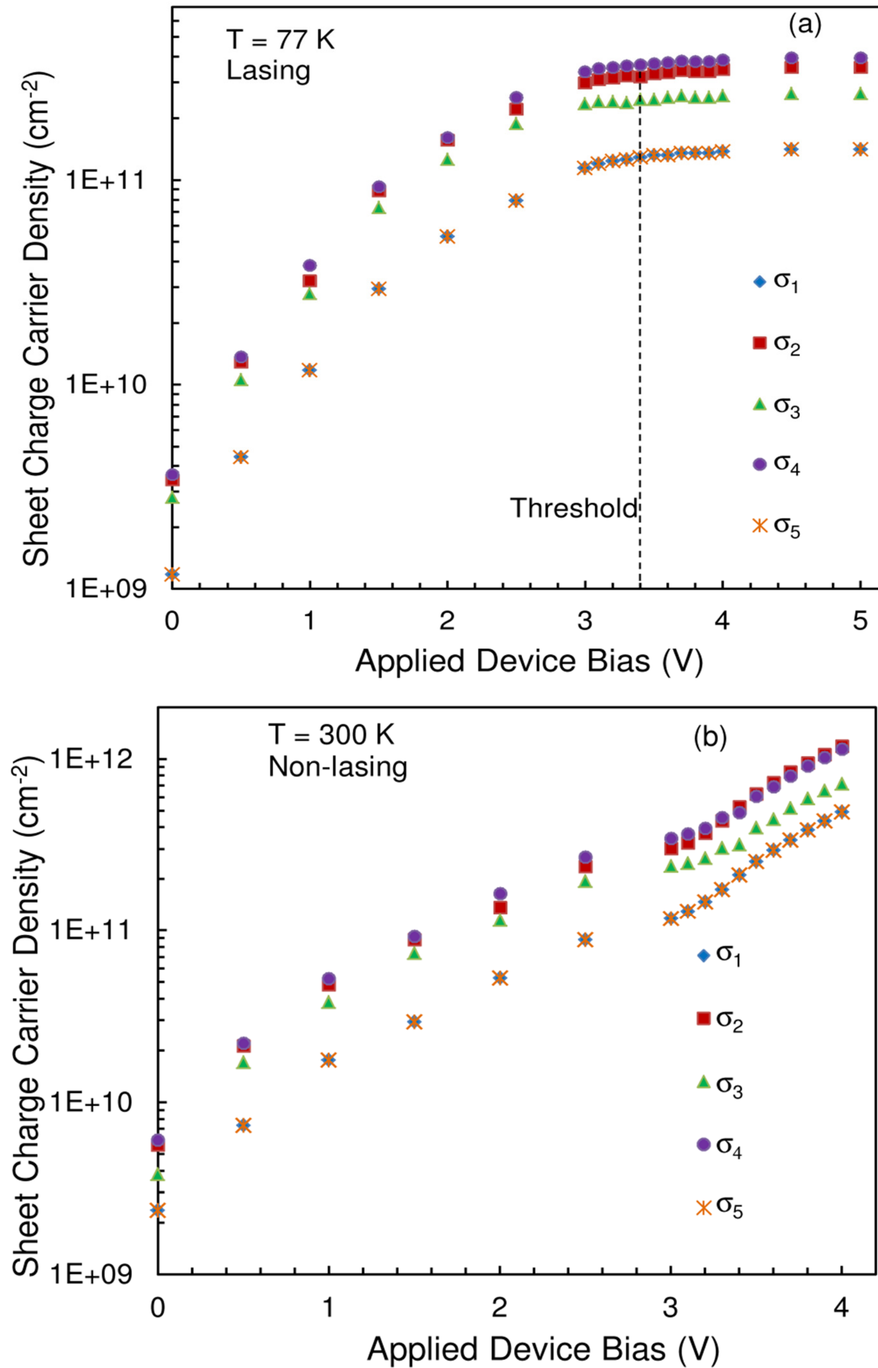

Figure 4.13. Clamping and non-clamping of charge carrier density for R090 ICL device. (a) The experimental sheet charge carrier densities (σ_i, i=1, 2, 3, 4, 5) as a function of device bias at 77 K at which temperature the device lases at 3.4 V. (b) the experimental sheet charge carrier densities (σ_i, i=1, 2, 3, 4, 5) as a function of device bias at room temperature (300 K), at which temperature the device does not lase.

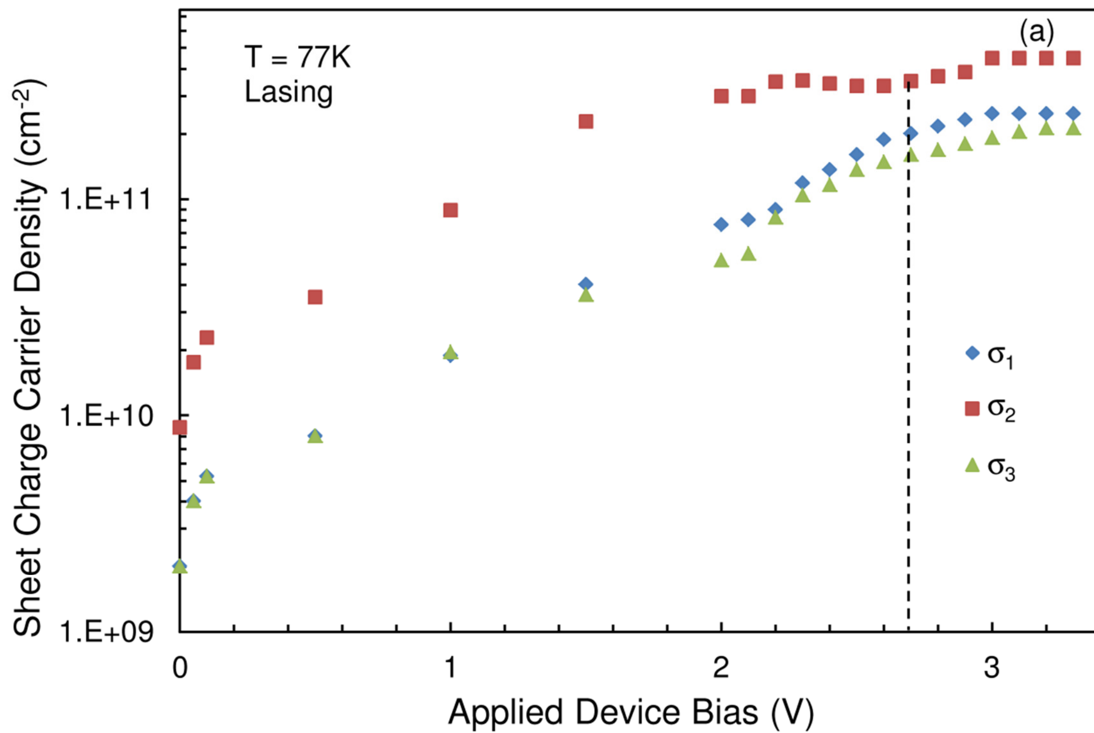

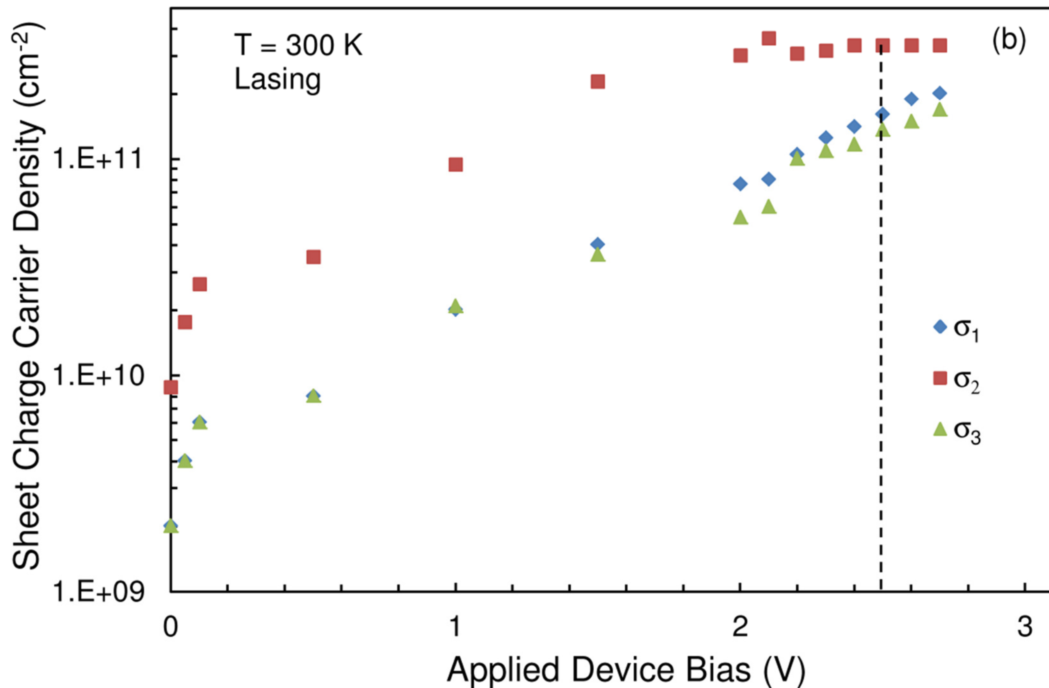

Figure 4.14. Clamping of charge carrier density for R084 ICL device. (a) The experimental sheet charge carrier densities (σ_i, i=1, 2, 3, 4, 5) as a function of device bias at 77 K at which temperature the device lases at 2.7 V. (b) the experimental sheet charge carrier densities (σ_i, i=1, 2, 3, 4, 5) as a function of device bias at 300 K, at which temperature the device lases at 2.5 V.

Table 4.1. For R090, the measured internal average electric field (F), the experimental charge carrier sheet density (σ_i, i=1, 2, 3, 4, 5), the total hole sheet density ($\sigma_h = \sigma_1+\sigma_3+\sigma_5$), the total electron sheet density ($\sigma_e = \sigma_2+\sigma_4$), and the theoretical modeling sheet carrier density (σ_m) by using Equation (4.3). m_r^*= 0.0355 m_e is used in the calculation, where m_e is the free electron mass [93]. The device is forward-biased at 77 K with a threshold voltage of 3.4 V. The uncertainty of the experimental charge carrier sheet density is estimated to be ±10% based on calculations. The modeling results are in good agreement with the experimental data (red fonts) which is also presented in Figure 4.15.

Device Bias (V)	F ($\times 10^6$ V/m)	σ_1 ($\times 10^9$ cm^{-2})	σ_2 ($\times 10^9$ cm^{-2})	σ_3 ($\times 10^9$ cm^{-2})	σ_4 ($\times 10^9$ cm^{-2})	σ_5 ($\times 10^9$ cm^{-2})	σ_h ($\times 10^9$ cm^{-2})	σ_e ($\times 10^9$ cm^{-2})	σ_m ($\times 10^9$ cm^{-2})
0	0	1.18	3.43	2.8	3.63	1.18	5.16	7.07	-
0.5	1.150	4.43	1.29E+1	1.59E+1	1.37E+1	4.43	2.48E+1	2.66E+1	-
1.0	2.399	1.18E+1	3.23E+1	4.2E+1	3.84E+1	1.18E+1	6.56E+1	**7.07E+1**	**5.54E+1**
1.5	3.631	2.95E+1	8.88E+1	1.11E+2	9.29E+1	2.95E+1	1.7E+2	**1.82E+2**	**1.95E+2**
2.0	4.869	5.31E+1	1.57E+2	1.9E+2	1.62E+2	5.31E+1	2.96E+2	**3.19E+2**	**3.35E+2**
2.5	6.117	7.97E+1	2.22E+2	2.83E+2	2.54E+2	7.97E+1	4.43E+2	**4.76E+2**	**4.76E+2**
3.0	7.372	1.15E+2	2.99E+2	3.54E+2	3.39E+2	1.15E+2	5.84E+2	**6.38E+2**	**6.18E+2**
3.3	8.133	1.27E+2	3.23E+2	3.58E+2	3.63E+2	1.27E+2	6.12E+2	**6.86E+2**	**7.04E+2**
3.5	8.638	1.33E+2	3.31E+2	3.72E+2	3.71E+2	1.33E+2	6.37E+2	7.03E+2	7.56E+2
4.0	9.924	1.39E+2	3.47E+2	3.89E+2	3.88E+2	1.39E+2	6.67E+2	7.35E+2	8.92E+2
4.5	11.21	1.42E+2	3.55E+2	3.98E+2	3.96E+2	1.42E+2	6.81E+2	7.51E+2	1.03E+2
5.0	12.50	1.42E+2	3.55E+2	3.98E+2	3.96E+2	1.42E+2	6.81E+2	7.51E+2	1.16E+3

Table 4.1 summarizes some of the experimental data of the charge carrier sheet densities. It can be noticed that the charge carrier sheet density in the active section (σ_e and σ_h) is small but definitely not zero when the device is at zero bias. This could be attributed mainly to charge transfer across InAs/GaInSb interfaces because InAs and GaInSb have very different affinities with type-II hetero-interface. As electrons and holes are generated in pair at the InAs/GaInSb type II interface, charge neutrality should be maintained inside the device. However, the total hole sheet density (σ_h) is not exactly matching to the total electron sheet density (σ_e), instead a relative difference of ~10% (up to ~27% difference for zero bias) is observed over the bias range. This quantitative discrepancy is mainly caused by the inaccuracy in numerical manipulations of the SVM data (such as differentiation and integration) while using Equations 4.1 and 4.2 for

modeling calculations presented in Figure 4.15. Nevertheless, the average internal electric field remains constant throughout the eight cascade modules (as shown in Figure 4.9 (b)), which ultimately confirms the preservation of exact charge neutrality in each of the eight active sections.

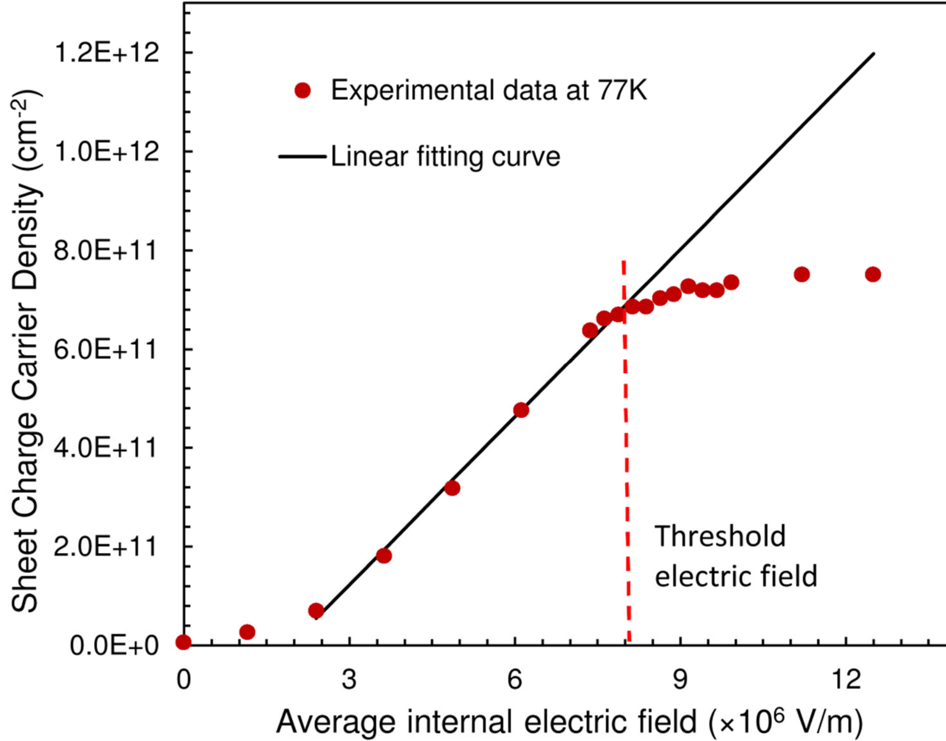

Figure 4.15. For R090 ICL device, the experimental total electron density ($\sigma_2 + \sigma_4$) as a function of the internal average electric field. The solid line is a linear fitting curve based on Equation 4.3.

A simple model has been developed to estimate the quasi-equilibrium charge carrier sheet density [96]. Assuming that equal electron and hole concentration is generated by the overlap (E_{SM}) of the conduction and valence bands at the type II semi-metallic interface with parabolic bands, and assuming $E_{SM} >> k_{B}T$ and two-dimensional densities of states, the charge carrier sheet densities are given by [93]

$$\sigma_h = \sigma_e \approx m_r^* \frac{E_{SM}}{\pi\hbar^2} \quad (4.3)$$

where m_r^* is the reduced effective mass, ħ is the reduced Planck constant and E_{SM} is the overlap energy. E_{SM} depends on electric field (F) as $E_{SM} = qF \times \Delta d - E_i$, where Δd is the center-of-mass

distance of the electron and hole wavefunction distributions across the type II interface. The spatially indirect bandgap (E_i) could vary drastically in growth and is believed difficult to be precisely calculated from modeling. Equation (4.3) clearly shows that when the assumption conditions are satisfied, the charge carrier sheet densities would exhibit an approximately linear dependence on the internal electric field. It is to be noted that Δd varies with the electric field, but such a variation is relatively small in type-II heterostructures compared to their already substantial separation at zero bias. Δd is thus set as a constant fitting parameter in the data analysis. In Figure 4.15 the experimental electron sheet density at 77 K is plotted as a function of the average internal average electric field, together with a linear fitting based on Equation (4.3). Over the electric field range of 2.399×10^6 V/m to 8.133×10^6 V/m (corresponding to applied device biases from 1.0 V to 3.3 V), the linear fitting curve matches well to experimental data. The fitting yields Δd to be 7.6 nm, somewhat larger as expected than the separated value of 7.4 nm at zero bias from wavefunction calculations [93]. The spatially indirect bandgap (E_i) is derived to be 14.6 meV. Above the threshold electric field, the electron sheet density is essentially clamped and thus deviates from the linear fitting curve. For smaller electric fields (below 2.399×10^6 V/m), Equation (4.3) does not apply accurately, as there is no energy overlap at the type II interface.

The SVM technique provides a direct experimental means to investigate the temperature dependence of the threshold carrier sheet density. As observed from the LIV curve for R090 in Figure 4.5 (a), the threshold current and the threshold voltage increase with temperature. The ICL sample lases up to 248 K (T_{max}), at which temperature the threshold voltage is 3.8 V. A series of SVM scans are therefore performed at a bias of 3.8 V at different temperatures from 77 K to room temperature (300 K). For any given temperature lower than T_{max}, the threshold voltage is lower than 3.8 V. Since the charge carrier sheet density is clamped above the threshold voltage, the carrier density measured at 3.8 V should equal to its threshold value at this given temperature. As such, the consistence in comparing the threshold carrier sheet density for all temperatures lower than 248 K is ensured by choosing 3.8 V as the device bias in these series SVM measurements. Figure 4.16 presents the measured data of the total electron sheet density(σ_e) and the total hole sheet density (σ_h) in the active section as a function of temperature, showing together is the measured threshold current of the device. The threshold current slowly increases with temperature from 60 K to 170 K, then increases rapidly till T_{max}. In contrast, the

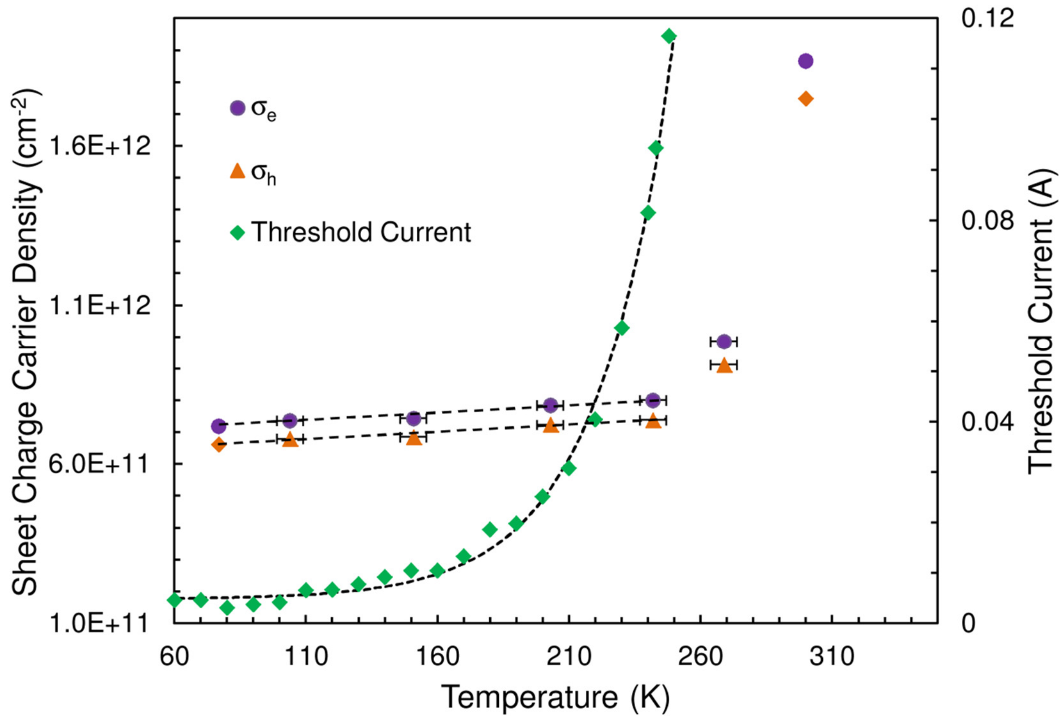

Figure 4.16. Temperature dependence of charge carrier density. The active-region charge carrier sheet densities (σ_h and σ_e) are measured at 3.8 V for different temperatures from 77 K to room temperature. Both increases linearly but slowly with temperature until the maximum lasing temperature (T_{max}). After T_{max}, σ_h and σ_e increases rapidly with temperature. The experimental threshold current is also plotted over the same temperature range for comparison, which shows much strong temperature dependence.

threshold charge carrier density exhibits an almost linear but slow increase with temperature from 77 K to 240 K. At temperatures above T_{max}, the total charge carrier sheet density is not clamped any more due to the absence of stimulated emission and therefore increases rapidly. In particular, the measured carrier density at room temperature is more than two times the value at 240 K. The optical gain in the active section in the device is typically proportional to the population inversion, namely the charge carrier density. The SVM results suggest the optical gain may not change substantially over the temperature range of 77 K to 240 K. Nevertheless, the strong temperature dependence of the threshold current (characteristics temperature T_0 = ~29 K) indicates that the carrier lifetime of the lasing states experience fast decrease at temperatures above 170 K. The mechanism for such a fast reduction of carrier lifetime, as being pointed out earlier [112], could be likely attributed to the non-radiative Auger recombination process, which

may increase by a factor of 64 when temperature increases from 77 K to 270 K [113]. The SVM data reveals substantial hole accumulation in the first AlSb hole well in the electron injector section, which may induce considerable electron-hole non-radiative recombination, leading to another potential carrier leakage channel. It is unclear how big a role this leakage channel may play in the reduction of carrier lifetime, which merits further research efforts.

4.4 Summary

In summary, a novel cryogenic-temperature scanning voltage microscopy technique is developed and applied to probing the inner workings of an operating interband cascade laser. The voltage distribution profile across the cascade modules of the devices are measured at different device biases and temperatures at nanometer scales with high accuracy. The SVM results clearly reveal nonuniform internal electric field distribution in the active sections of the devices, confirming the spatial segregation of electrons and holes due to the unique type-II band-gap alignment in the device. The charge carrier sheet density is derived from the SVM data, which is essentially clamped in the presence of stimulated emission. The temperature-dependent measurements indicate that the Auger recombination process may be a major carrier relaxation mechanism at high temperatures, through which threshold current is significantly increased. The understanding of such a process and other potential leakage mechanisms would help to improve the device performance at high temperatures. The results obtained from the nanoscopic voltage measurements on a lasing mid-IR ICL device provide the first experimental evidence by resolving internal device dynamics that the electric field across the active regions of an ICL is not uniform. The substantial variation of electric field over the active region in each cascade stage suggests considerable charge transfer and accumulation with type-II QW layers, resulting in some strong internal electric field in the region. Hence, a non-uniform electric field is detected locally as a net effect in the active regions of the ICL. Nevertheless, the demonstration of resolving dynamic charge carrier density distribution in an operating optoelectronic laser device is unprecedented as the carrier densities achieved are validated to match the modelled carrier accumulations acquired by Vurgaftman et al. [93, 99]; and could open the door to many future applications in probing the underlying mechanisms for many puzzling sub-par performance and degradations in nanoelectronic devices, quantum devices and optoelectronic devices.

Chapter 5: Direct Observation and Determination of the Evolution of Electric Field Domains (EFDs) in THz QCL Devices

This Chapter employs cryogenic temperature scanning voltage microscopy (SVM) technique based on the AFM system developed and as described in Chapter 4. The THz QCL devices are directly probed using this SVM measurement setup, and internal device structures and mechanism are observed that relate to the evolution of the EFDs. As a result, the EFDs that may be responsible for sub-par QCL device performance and which have been the subject of speculation [18] thus far are observed and determined to exist in the devices.

SVM is the most advanced contact mode AFM technique that presents high spatial resolution images while mapping and profiling the surface of the sample in nanometer scale. The SVM measurement is performed when the sample is under operation. A two-dimensional nanosurface profile of the sample is generated that evidently resolves the inner workings of the device structure and presents its underlying physics. The profile image achieved, presents a detailed voltage distribution profile across the scanned sample area, thus instigating the change in the physical structure and device physics when the sample is under operation.

The external performance of quantum optoelectronic devices is governed by the spatial profiles of electrons and potentials within the active regions of THz QCL devices [88]. For example, in QCLs, the EFD hypothesis posits that the potential distribution might be simultaneously spatially nonuniform and temporally unstable. Unfortunately, there exists no prior means of probing the inner potential profile directly. As a result, the mechanisms responsible for sub-par device performance of QCLs remain the subject of speculation. The nanoscale electric potential distribution inside operating QCLs is measured by using scanning voltage microscopy at cryogenic temperature. As per the EFD hypothesis, it is observed in this

chapter that the multi-quantum-well active region is indeed divided into multiple sections having distinctly different electric fields. The electric field across these serially-stacked quantum cascade modules does not continuously increase proportionally to the gradual increase in the applied device bias, but is observed to rather hop between discrete values that are related to tunneling resonances. The evolution of EFDs, indicate that an incremental change in device bias leads to a hopping-style shift in the EFD boundary – the higher electric field domain expands at least one module each step at the expense of the lower field domain within the active region. The findings indicate the importance of quantum active region design for intrinsically more uniform and stable electric field profiles.

5.1 Introduction to SVM on THz QCL

The THz QCLs had their inception in scientific research in 2002 [11], and the past decade has witnessed significant progress in the development of compact semiconductor THz coherent sources [59, 114]. Based on diverse quantum active region designs, several different THz QCL devices have been demonstrated, including chirped superlattice (CSL), bound-to-continuum (BTC), resonant-phonon (RP) and indirect-pumping (IDP) schemes [59, 79, 115]. Substantial effort has been placed on improving device performance, not only through optimized active region design, but also high-quality molecular beam epitaxy growth, advanced device fabrication techniques and innovative waveguide engineering. In the absence of a magnetic field, lasing frequencies ranging from 1.2 to 5.2 THz [116, 117] were measured from THz QCLs. Broadband lasing [118] and continuously-tunable lasing [119] of THz QCLs were also demonstrated. The maximum lasing temperature of THz QCLs has significantly improved [15, 61, 120-123] over the last decade, and output power has now reached 470 mW in pulsed mode [124]. Mode-locked THz QCLs [125], THz QCLs with large wall plug efficiency [126], photonic crystal THz QCLs [90], THz QCLs with low divergence emission beams [127, 128] have been realized. More recently, broadly-tunable terahertz generation based on different frequency generation in the cavity of a mid-infrared quantum cascade laser was reported [129]. Nevertheless, despite the aforementioned rapid advances, all reported terahertz quantum cascade lasers lase only at cryogenic temperatures. The reason why room temperature operation is not yet possible eludes the community [130].

Thus far, fabricated THz QCLs have typically been characterized using conventional electrical and optical techniques, such as pulsed and/or DC light-current-voltage [12, 61], lasing spectrum and far-field pattern measurements [13]. The THz time-domain spectroscopy technique was successfully applied to probe actively-biased THz QCLs, enabling direct measurement of the optical gain/loss of the active region [131, 132]. The intrinsic linewidth of THz QCLs was also experimentally investigated [133]. By contrast, transmission electron microscopy (TEM) and scanning electron microscopy (SEM) were employed to obtain static microscopic structure information, such as direct measurement of the interface roughness in QCL materials [134] or visual illustration of QCL laser emission facets [124]. Until recently, THz QCL characterization techniques were limited to either input/output behaviors or static structural information. Recently, SCM and SSRM based AFM techniques have also been applied on the THz QCLs [17], as mentioned in Chapter 3 of this thesis, and the two-dimensional (2D) dopant profiling and mapping of carriers have been determined. The high-resolution images presented a 2D view of the active region of the device and identified the delta-doped layers present in each module due to charge carrier accumulation in the regions [17]. Internal nanoscopic origins and external macroscopic performance measures are seldom linked through compelling experimental observation. As a result, very little direct evidence has been observed and determined to clarify of why many devices fail or perform poorly. In particular, there is an inability to directly and quantitatively profile electric potentials across quantum cascade modules, preventing conclusive identification of the underlying mechanisms that lead to insufficient optical gain for lasing operation at higher temperature.

Voltage distribution plays a key role in governing device performance, especially for THz QCLs; it dictates how efficiently electrons are injected into desired states to achieve sufficient population inversion – a prerequisite for lasing. It is therefore critically important to measure the voltage distribution within an actively-driven laser directly. Scanning voltage microscopy (SVM) is an enabling tool to quantitatively probe the voltage distribution and has sufficient spatial resolution to even resolve individual quantum wells [53, 135]. This capability could disclose important experimental evidence for the formation and evolution of electric field domains in semiconductor quantum structures that are based on electron resonant tunneling. These domains have long been hypothesized and only verified indirectly through the observation

of sawtooth-like current-voltage (I-V) or light-voltage (L-V) curves or the measurements of active-region photoluminescence spectra [19–21, 136].

Conventional SVM has found limited application to lasing THz QCLs because SVM measurements can only be performed at room temperature [53, 135], while current THz QCLs can only be operated at cryogenic temperatures. Furthermore, many interesting quantum dynamics (such as optical and electrical instability and formation of electric field domains) can only be observed at low temperatures [18]. Rapidly increasing progress in the design and fabrication of THz QCLs with improved performance may help overcome this barrier. For example, THz QCLs that can lase up to ~200 K have already been demonstrated [15]. In addition, cryogenic temperature SVM apparatus that can be operated at liquid helium or liquid nitrogen temperatures with a nanometer resolution have been successfully developed in chapter 4 of this thesis for research utilization, and are readily accessible using modern scanning probe microscope technology. The external performance of these quantum optoelectronic devices are governed by the spatial profiles of electrons and potentials within the active regions of these devices [88]. For example, in QCLs, the EFD hypothesis posits that the potential distribution might be simultaneously spatially nonuniform and temporally unstable. As yet, unfortunately, there exist no means of probing the inner potential profile directly. As a result, the mechanisms responsible for sub-par device performance of QCLs remain the subject of speculation. Here, the nanoscale measured electric potential distribution inside operating QCLs, by using scanning voltage microscopy [49] at a cryogenic temperature is reported. In this chapter, for the first time, it is confirmed that as per the EFD hypothesis, the multi-quantum-well active region is indeed divided into multiple sections having distinctly different electric fields for THz QCLs.

5.2 Experimental Procedure

The cryogenic temperature SVM technique established for the AFM system in Chapter 4 is briefly discussed in this section. Here the cryogenic SVM is utilized to observe and determine the voltage distribution profile while mapping the carriers and studying the effect of dynamic carriers in THz QCLs. This has long been hypothesized to nonlinearity indicating formation of EFD in the active region of the device. This chapter focuses to map voltage distribution and image inner workings that lead to understanding of the device physics of lasing nanophotonic devices. This section also discusses the structures of THz QCLs for two different designs

(resonant-phonon [59, 15, 122] and indirect-pumping [79]). The f-series devices (f-25 and f-30) are resonant-phonon (RP) design THz QCLs [15, 18], while V843 and V962 are indirect-pumping (IDP) THz QCLs [79, 137]. The detail active region structures of these devices are presented here.

5.2.1 Cryogenic Temperature SVM Technique

A commercially available atomic force microscope system (Attocube AFM) is employed for performing SVM measurements. The THz QCL device operates at cryogenic temperature, so the SVM setup employed in this chapter is the cryogenic temperature SVM already discussed in Chapter 4. The cryogenic temperature SVM was carried out in liquid nitrogen at a temperature of 77 K. A boron-doped diamond-coated conductive cantilever probe from Bruker, with a spring constant = 42 N/m, model no. DDESP-10, with a spatial resolution of ~20 nm is used for the measurements at 77 K. As detailed in Chapter 4, the sample is mounted in the AFM system with the facet of the laser device facing the cantilever probe to implement contact mode SVM scanning. The AFM microscope head, along with the mounted sample, is inserted in the AFM metallic tube, which in turn is vacuumed and purged with Helium gas. This tube with the AFM system is then placed inside the cryogenic chamber for low temperature measurement. The sample on the system is connected to external circuitry to perform SVM measurements while the cantilever probe detects the voltage distribution as the probe scans the sample surface The external circuitry applies pulsed bias to the sample, with the frequency f = 100 Hz and pulse width w = 3 μs for THz QCL device. The applied bias and current on the device are monitored on the oscilloscope. The SVM measured voltage profile across the sample is acquired by the AFM controller. The frequency and width of the applied pulse bias are well synchronized with the probe scanning rate, pixel points and scan frequency. Synchronization is made so that the probe at each pixel point of the scan reads and collects data from the peak of one pulse bias at that point of contact. The SVM scan rate and the pulse bias are synchronized to achieve high resolution mapping of the sample surface.

The SVM setup is as described in detail in Chapter 4. The bias applied on top of the device is varied from 2 V up to 18 V for f-series devices, and from 2 V to 25 V for IDP devices as the operating region of the devices vary. The scanning is executed at low frequencies with a slow scan speed of 100 – 500 nm/s. The force applied to the SVM cantilever probe is in the

range of 2 – 5 μN, depending on measurement requirements. The contact force is set high enough to ensure the probe is able to penetrate mechanically into the native oxide layer on the semiconductor so as to establish a good electric contact non-destructively, although special care is taken to avoid damaging the emission facet of the laser. From each of the SVM scans, a 2D high resolution image is generated that clearly presents the voltage distribution across the device.

5.2.2 THz QCL Devices, Structures and Performances

The THz QCL devices that are used for the SVM measurements were grown by MBE, and all these devices are metal-metal (MM) waveguide based devices. The details of the growth and fabrication procedure for MM devices are discussed in Appendix A.1.1 and are quite similar for all devices except for the active region portion. The active region of these laser devices is ~10 μm thick and sandwiched between the top and bottom metal contact. The active region is comprised of GaAs/AlGaAs quantum well-barrier modules that vary between 200-300 depending on the structure, design and function of the device. Based on the design structure, the devices with RP (f-series devices f-25 and f-30) [18] and IDP (V843 and V962) [79, 137] designs are employed for cryogenic temperature SVM measurements.

The active region design of the f-series devices consists of a three-well GaAs/AlGaAs quantum well-barrier structure with the phonon well ~158 Å thick just after the injector barrier in each module of the device. The f-25 and f-30 devices have a Si-doped homogeneous doping concentration of 6×10^{16} cm^{-3} of 5 nm at the centre of the phonon well, as shown in Figures 5.1 (a) and (b), respectively. Both f-25 and f-30 devices have design specifics of 219 and 222 modules in the 10 μm thick active region, with each module 45.66 nm and 45.05 nm thick, respectively [18]. The average device doping concentrations calculated as per the design for f-25 and f-30 are 6.57×10^{15} cm^{-3} and 6.66×10^{15} cm^{-3}, respectively. The external performances of the f-series devices are presented in Figure 5.2. The f-25 device used for the SVM measurement is a non-lasing device, and the current density-device bias (J-V) characteristics are presented in Figure 5.2 (a), while the light-current density-device bias (L-J-V) of the lasing f-30 is shown in Figure 5.2 (b). For both the devices in Figure 5.2 (a) and (b), the nominal active-region electric field is calculated using $(V- \Phi)/d$, V is the device bias, Φ is the Schottky contact drop (~0.8 V), and d is the active region thickness (~10 μm). A comparative study of the lasing and non-lasing

THz QCL devices is made to directly observe the EFD and determine the voltage distribution in the change when under bias.

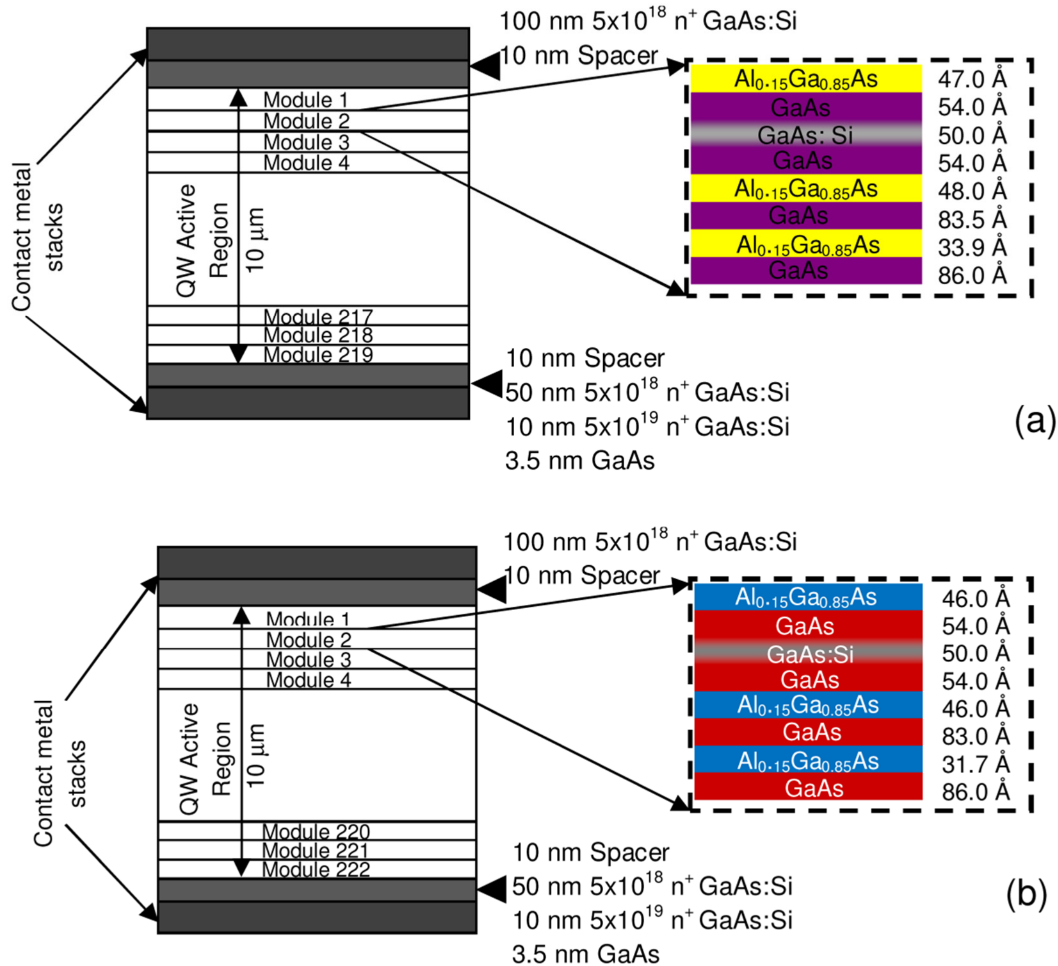

Figure 5.1. Schematic diagram of the cross section of fabricated THz QCLs with metal-metal waveguide. (a) f-25 non-lasing device showing three well cascade module design with 219 times forming 219 modules in the quantum well-barrier (QW) active region of the device. (b) f-30 lasing device showing 222 modules in the quantum well-barrier (QW) active region of the device. The thickness of the active region is 10 µm and the active region is sandwiched between the two metal cladding layers at the top and the bottom for both devices. One of the modules is zoomed for both devices to show the QW layer structure consisting of GaAs/$Al_{0.25}Ga_{0.75}As$ material for the thicknesses as mentioned. The phonon well in each module has a homogeneous Si doping of 50 Å thick in the middle of the layer.

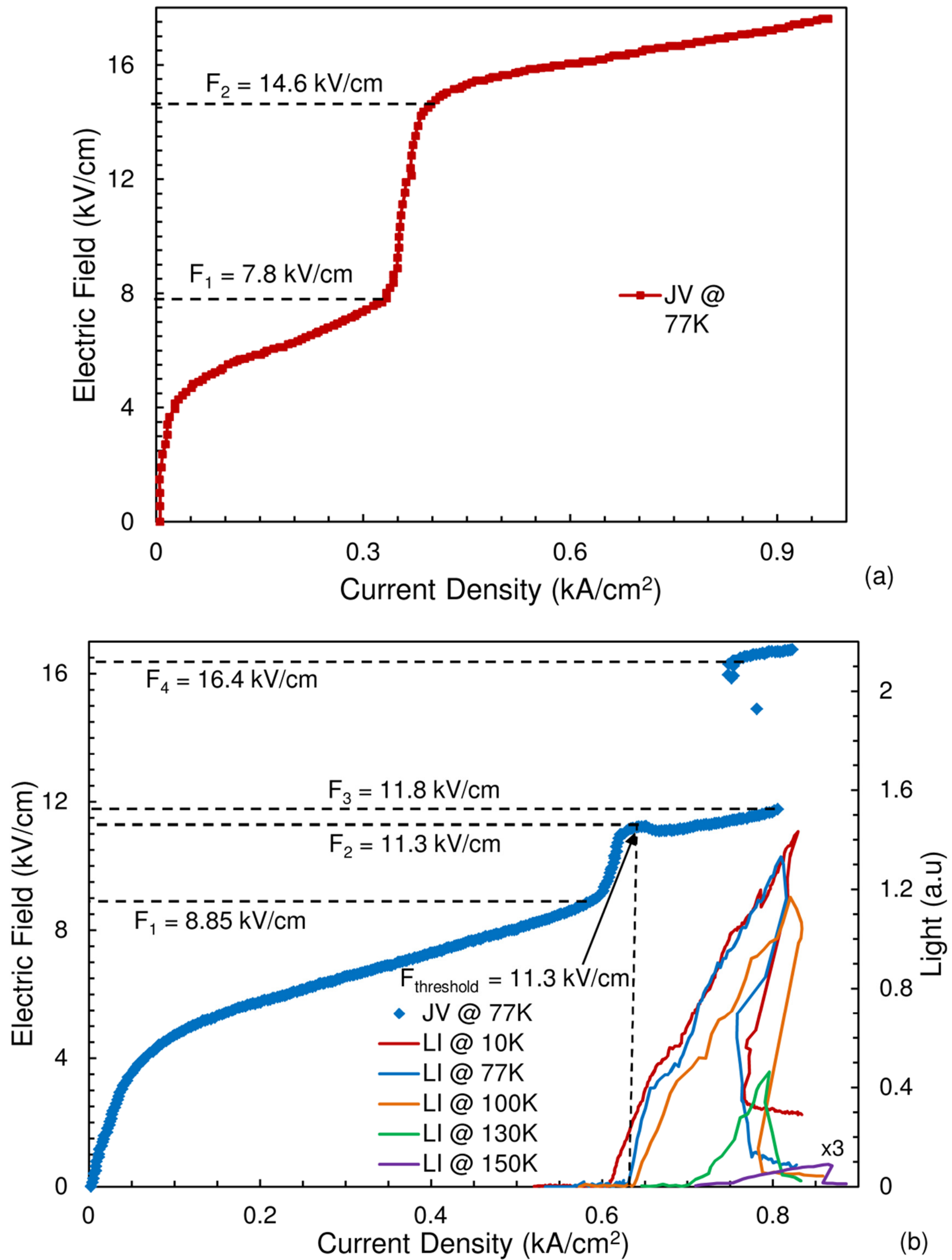

Figure 5.2. (a) Experimental current density – device bias (J-V) of the non-lasing f-25 device at 77 K. (b) Experimental current density – device bias (J-V) for lasing f-30 device at 77 K along with and light – current density (L-J) curves at 77 K and several other temperatures (10, 100, 130 and 150 K).

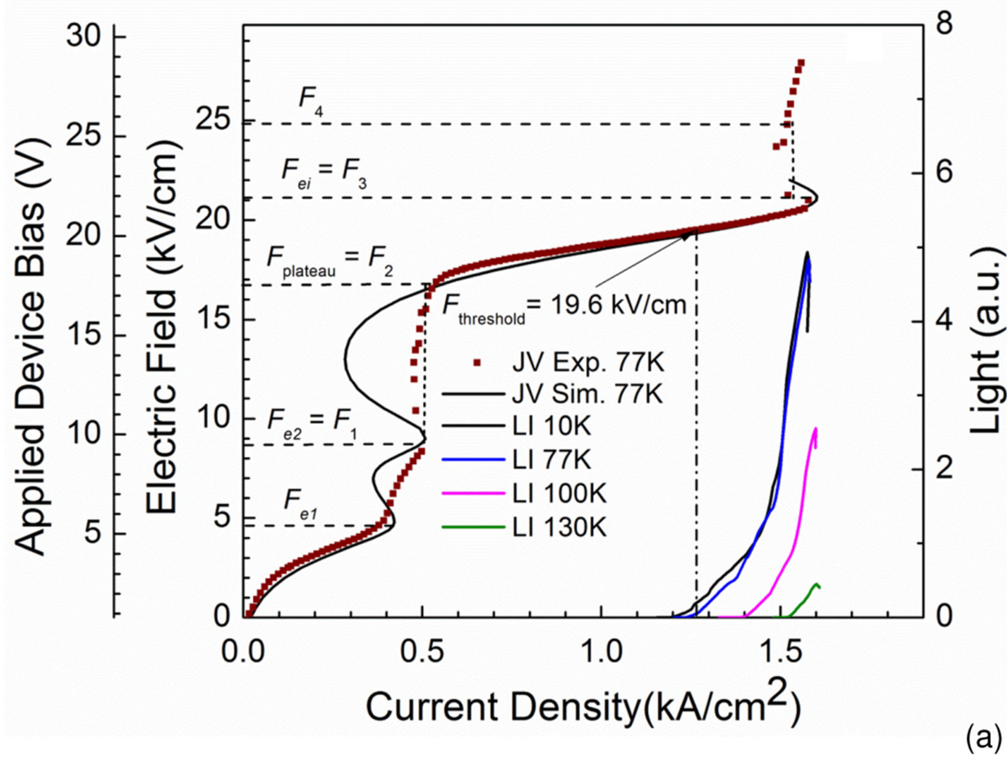

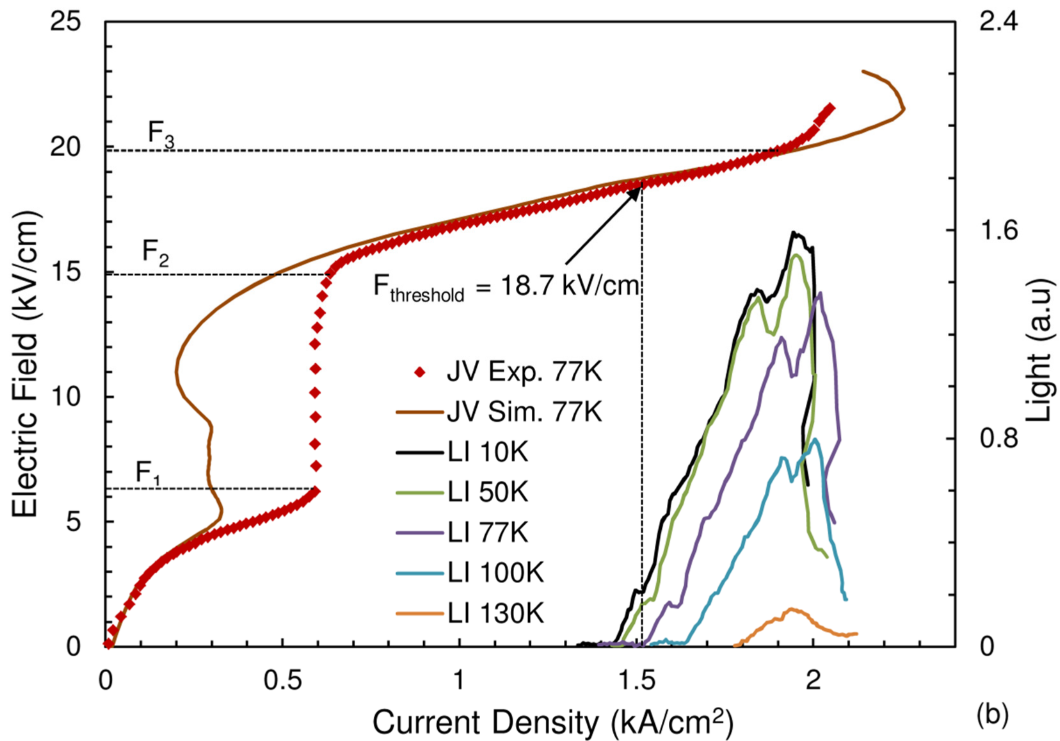

Figure 5.3. (a) Experimental current density – device bias (J-V) and simulated current density [79] – nominal active-region electric field (J-F) curves of the V843 device at 77 K, and light – current density (L-J) curves at 77 K and several other temperatures (10, 100 and 130 K). The threshold electric field is

19.6 kV/cm at 77 K. (b) Experimental current density – device bias (J-V) and simulated current density [137] –electric field (J-F) curves of the V962 device along with and light – current density (L-J) curves at 77 K and several other temperatures (10, 50, 100 and 130 K). For all the images the nominal active-region electric field is calculated using $(V- \Phi)/d$, V is the applied device bias, Φ is the Schottky contact drop (~0.8 V) and d is the active region thickness (~10 μm).

The active region structures for the indirect-pumping scheme designed devices V843 and V962 are quite different from each other with respect to the number of quantum well-barriers in each module and also in the operation of the devices. The V843 sample consists of a four-well quantum well-barrier structure with a delta-doping layer present in the injector barrier of each module, making up a total of 276 modules [79] in the active region, as shown in Figure 3.1. Thus, the module thickness is 36.16 nm. The average designed doping concentration of the device is 9.0×10^{15} cm^{-3}, while the delta-doped layer with Si dopant has a sheet concentration of 3.25×10^{10} cm^{-2} as per the design [17, 79]. The active region design of V962 sample comprises a five-well-barrier structure in the 10 μm thick active region [137]. In the growth process of this V962 device, the n-type material used has an average designed doping concentration of 9.0×10^{15} cm^{-3}, while the Si-doped delta-doped layer has a sheet doping concentration of 3.0×10^{10} cm^{-2}, which is present in the injector barrier of each module of the active region. The device consists of 253 modules with a module thickness of 39.45 nm as per the design of the device [137]. The external performances (light-current density-electric field) of lasing IDP V843 and V962 devices are presented in Figures 5.3 (a) and (b). It is to be noted that the simulated IV curve does not match the experimental IV, especially in the current plateau region of operation, as the effect of EFD is not considered in the simulation for the Figure 5.3 (a) and (b). All the different sections, such as the current plateau, the lasing and the negative differential resistance (NDR) regions due to injection and extraction of carriers in both the f-series and IDP devices, are clearly indicated in the L-J-V curves in Figure 5.3.

5.3 Nanosurface Profiling and Mapping of Carriers in THz QCLs

With the cryogenic temperature SVM set-up described in section 5.2.2, the voltage profile across the transverse cross section of the active region of a lasing THz QCL at 77 K is directly measured, resolving individual quantum cascade modules. The electric field distribution profile

is an essential parameter and must be known while studying QCL technologies in which the energy level alignment across modules plays a critical role in overall device performance. The electric current is maximized when the two quantum levels are aligned as per the quantum mechanical description of resonant tunneling. Afterwards, this tunneling current begins to drop as the bias further increases, thus generating a negative differential resistance (NDR) region [138]. Most of the THz QCL device modelling [104, 139-141] simulate only one cascade module in principle, although the active region of the device typically consists of up to 200-300 of nominally-identical cascade modules. Such modeling is based on an inherent and significant assumption that the electric field is uniform across the entire quantum structure so that each module experiences the same bias condition [101, 104, 137, 139]. It is therefore alleged that the collective current density–voltage (J-V) behavior of the entire active region can be represented by the individual J-V of a single quantum cascade module [79, 104, 137]. The present detection schemes have directly and compellingly revealed that the quantum cascade modules in a THz QCL active region could be operating under distinctly different bias conditions (different electric fields), which are observed both below and above the lasing threshold over a wide range of applied device biases.

5.3.1 Observation of EFDs in non-lasing and lasing THz QCLs

The probable existence of electric field domain in operating THz QCLs has been hypothesized by Fathololoumi et al. [18] from the external L-J-V measurements. These measurements and hypothesis of the EFD were presented on f-series THz QCL devices. But no internal device dynamic measurement to confirm this hypothesis has yet been performed to directly resolve the EFDs. The EFDs are expected to exist both in non-lasing and lasing THz QCL devices in the current plateau region of operation as indicated by Fathololoumi et al. [18] as per the J-V curve. The cryogenic SVM measurement technique that is capable of performing voltage profile analysis on operating devices is employed for the purpose. This measurement technique can image and observe the effect of dynamic charge carriers in the THz QCLs while they perform voltage profiling and mapping of carriers across the device. The f-series THz QCL devices under test are the non-lasing f-25 and the lasing f-30. For the non-lasing f-25 device, as there is no lasing threshold, the current plateau region combines with the NDR region [18] and is observed to vary from F_1 = 7.8 kV/cm to F_2 = 14.6 kV/cm, according to the J-V curve in Figure 5.2 (a).

While, for the lasing f-30 THz QCL, the current plateau and the NDR regions are separate regions of operation and vary from F_1 = 8.85 kV/cm to F_2 = 11.3 kV/cm and from F_3 = 11.8 kV/cm to F_4 = 16.4 kV/cm, respectively, as observed in Figure 5.2 (b).

Cryogenic temperature SVM is carried out using a conductive cantilever probe to scan across both f-25 and f-30 device active regions. Two-dimensional voltage profiles are obtained for the 11 × 11 μm^2 area at 77 K from the emission facet on application of 12 V and 11 V biases on top of the devices presented in Figure 5.4 (a) and (b), respectively. A continuous drop in voltage from the top metal through the active region to the bottom metal of the device is noticed, while a sharp drop of ~0.7-0.8 V is observed at the Schottky-like junction between the top metal and the top n^+ GaAs contact layer in both the devices. The images in Figure 5.4 envisage two EFDs across the ~10 μm thick active region at that bias, one close to the top metal layer, with a higher electric field (nearly equal in magnitude to F_2), and one close to the bottom metal layer, with a lower electric field (nearly equal in magnitude to F_1). Analogous SVM scans are performed at different applied biases ranging from 2 V up to 18 V for the devices with steps of 2, 1 or 0.5 V. For f-25, as the current plateau and the NDR regions combine, biases of 16 V and above exceed the NDR region of the device, while for f-30, the NDR region starts from 13 V onwards. On averaging the line scans from the 2D image similar to Figure 5.4 (a) and (b), one-dimensional (1D) voltage profile curves are obtained as a function of the distance from the top metal and presented in Figure 5.5 (a) and (b) for f-25 and f-30 devices, respectively. At low biases, 2 V – 8V for f-25 and 2 V – 9V for f-30, the electric field across the active region is quite uniform which presents a single slope that increases with an increase in applied bias on top of the device. From 9 V – 15 V for f-25, and from 10 V – 12 V, and again from 13 V – 17 V for f-30, two slopes in the active region portion of the voltage profile are observed from the SVM scans in Figure 5.5. The two slopes in each of these bias ranges remain almost identical, while the boundary between the high and low electric field domains steadily shifts from the top metal to the bottom metal layer. At higher biases, from 16 V – 18 V for f-25, only one slope is observed in Figure 5.5 (a) as this bias range is above the NDR region of the device as per the J-V curve in Figure 5.2 (a). The lasing threshold is 11.3 kV/cm or 12.1 V for f-30 from Figure 5.2 (b), so the SVM measurement at 12.5 V applied bias shows a linear drop across the active region. Thereafter, at higher voltages from 13 V – 17 V, the f-30 transits to the NDR region of the operation, and again, two slopes in the active region portion of the voltage profile are observed in

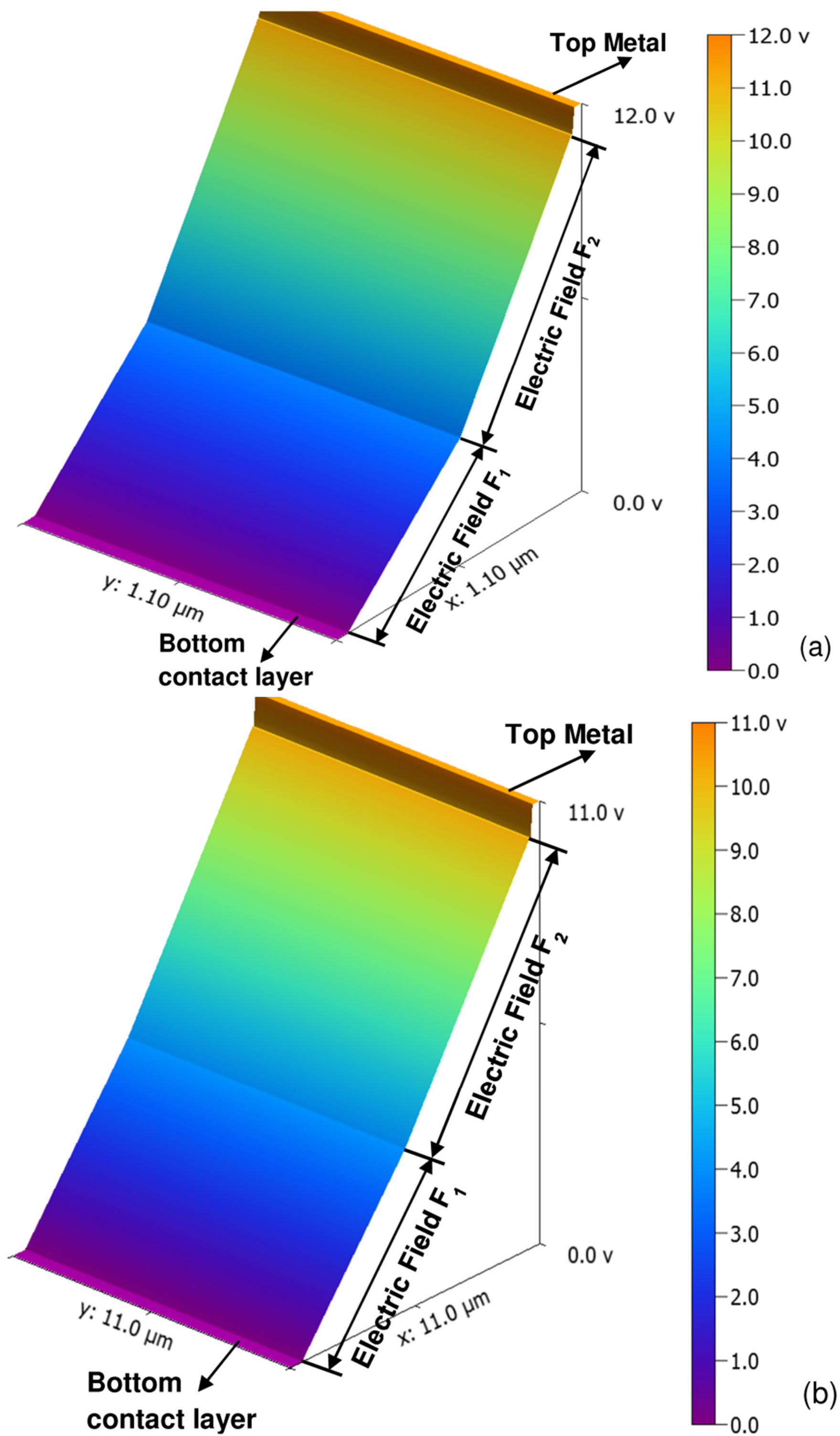

Figure 5.4. Cryogenic temperature SVM performed on f-series devices. (a) Evolution of EFD observed in non-lasing f-25 at 12 V bias from the 2D 11×11 μm^2 voltage profile image. (b) The voltage profile image on lasing f-30 at 11 V resolve the EFD from the 11×11 μm^2 scan across the device.

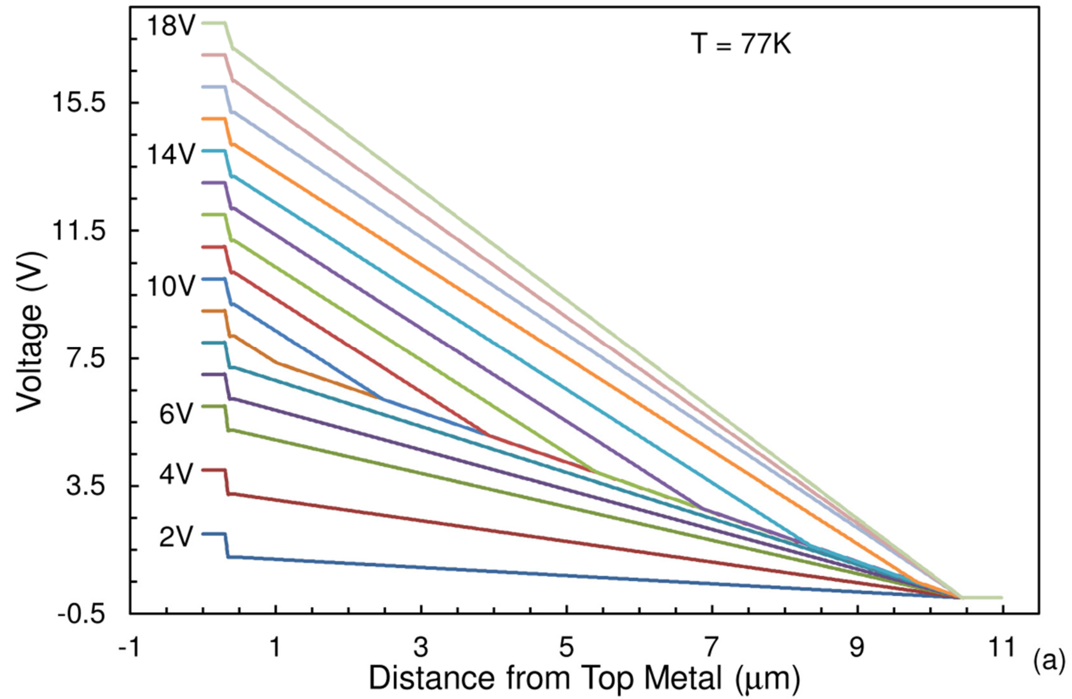

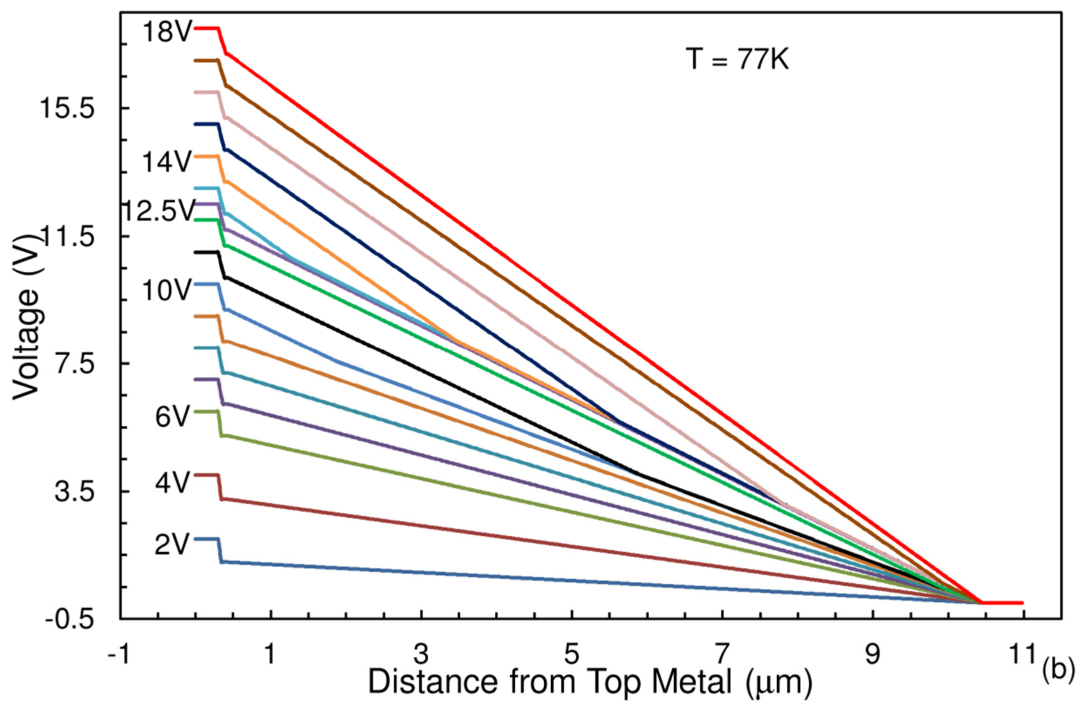

Figure 5.5. (a) 1D voltage profile section analysis of the SVM voltage profiles across the active region for the applied biases covering from 2 V – 18 V for non-lasing f-25. (b) 1D voltage profile section analysis for the lasing f-30 THz QCL with applied biases spanning from 2 V - 18 V. The measurement at 12.5 V is performed at the lasing region of the device which is linear while both at current plateau and the NDR region SVMs show two EFDs.

Figure 5.5 (b). From here, it is thus observed that both lasing and non-lasing THz QCL devices pursue a region where EFDs are evolved and distinctly detected experimentally. Also, both these devices show linear drops at biases above the NDR region of operation, the EFDs are observed to be formed and developed in the NDR and current plateau regions of operation.

This SVM measurement presents a precise quantitative analysis from the slopes of the voltage profile curves as F = average of ($\Delta V/\Delta d$) quantifying the electric field (F) within the observed EFDs in Figure 5.5 (a) and (b). Two distinct electric fields, F_1 and F_2, are observed at biases 9 V – 15 V, with an average of 7.76 kV/cm and 14.59 kV/cm, respectively, for f-25 THz QCL device. For f-30, the F_1 and F_2 are observed at biases between 10 V – 12 V, with an average of 8.79 kV/cm and 11.29 kV/cm, respectively. Two additional electric fields, F_3 and F_4, are observed in the NDR region of operation at biases between 13 V – 17 V, with an average of 11.74 kV/cm and 16.39 kV/cm, respectively. The process of being able to resolve and quantitatively measure different EFDs when THz QCL is under operation and thus quantifying the effect of dynamic charge carrier transport across the EFD Boundary in the device marks as a major advancement. The length (l_k) of each EFD section for f-25 and f-30 THz QCLs are measured directly from the SVM voltage profile curves in Figure 5.5 (a) and (b), respectively. As one cascade module period is d = 45.6 nm and d = 45.1 nm in thickness for f-25 and f-30, the number (n_k) of the cascade modules in each EFD section can be obtained from $n_k = l_k/d$ (k = 1, 2). These numbers can also be calculated through a second approach that assumes a linear partition of the cascade modules between the two EFDs (F_1 and F_2) that comply with the total applied device bias (V), which yields

$$n_1 + n_2 = N \tag{5.1}$$

$$n_1 F_1 d + n_2 F_2 d + \Phi = V \tag{5.2}$$

where Φ is the voltage drop across the Schottky-like junction at the interface of the top metal layer and the top n^+ GaAs contact layer, N is the total number of modules, and V is the applied device bias. The numbers of quantum cascade modules in each EFD are obtained through these two approaches (SVM measured and theoretically calculated), exhibiting very good agreement, as presented in Figure 5.6 (a) and (b) for f-25 and f-30, respectively. This finding confirms that the boundary of the electric field domains linearly shifts from the top to the bottom contact layer (opposite to the electron flux direction) as device bias increases. A similar analysis is applied to another high field domain transition observed between F_3 and F_4 for f-30 device. At 12 V applied

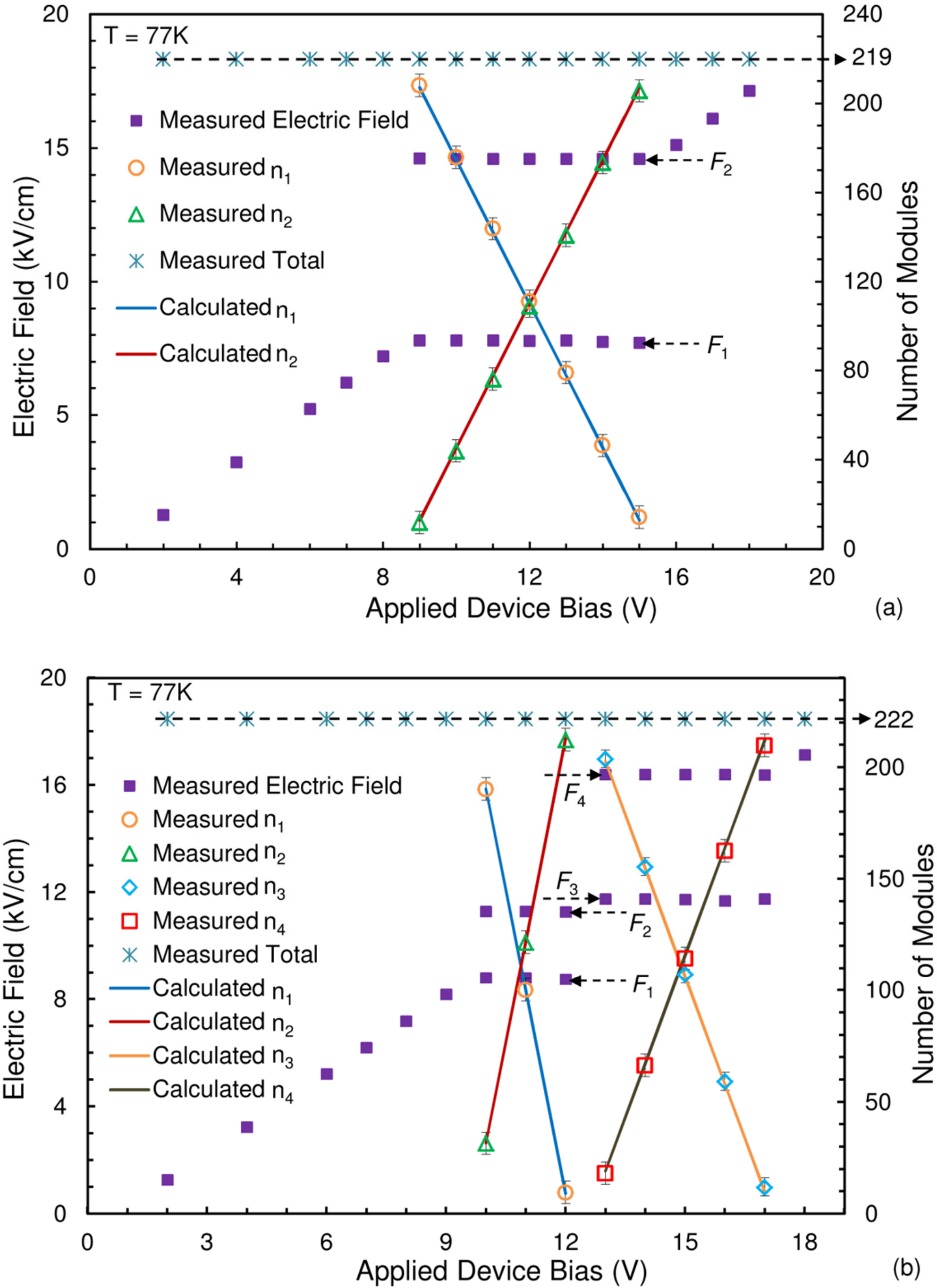

Figure 5.6. The SVM measured electric field across individual cascade modules in the active region of operating THz QCL device as a function of applied device bias. (a) For f-25 the two EFDs coexist in bias ranges of 9-15 V. (b) For f-30 the two EFDs coexist in bias ranges of 10-12 V and from 13-17 V. Shown together is the partition number of the cascade modules in each EFD. Discrete symbols (Measured n_k, k = 1, 2, 3, 4) are calculated from the first approach ($n_k = l_k/d$) based on the SVM measurement results of EFD length (l_k) in (Figure 5.4 (a) and (b)). Solid lines (Calculated n_k, k = 1, 2, 3, 4) are calculated from

the second approach (see text for details). The sum (Measured total) of the SVM measured module numbers (n_1+ n_2, or n_3+ n_4).

bias on top of f-30 lasing starts as observed from Figure 5.2 (b), so a minimum of ~212 number of modules are required as per Figure 5.6 (b) to exist at electric field F_2, for the start of lasing operation at 77 K. The lasing continues in the NDR region that has electric fields F_3 and F_4 and after, thus indicating the evolution of F_3 and F_4 may limit the lasing power. Looking at the SVM-measured electric field across individual cascade modules as a function of applied device bias, the two gaps are clearly noticed, over which the electric field hops directly from F_1 to F_2 and from F_3 to F_4, respectively in Figure 5.6 (b) for f-30 THz QCL.

High resolution SVM scanning is performed by reducing the scan area to 512×512 nm^2 on the THz QCL devices. Individual quantum cascade modules are resolved from these compact area scans. The measurements are performed close to the top metal/semiconductor interface into the active region and another close to the EFD boundary for the non-lasing f-25 device at an applied bias of 12 V on top of the device. The 2D voltage profiles and their corresponding 1D profiles along with the absolute value of electric field (|dV/dx|) calculation in the active region portion, are presented in Figure 5.7 (a), (b) and Figure 5.8 (a), (b). The voltage profiles and the electric field distribution across the scanned device section are clearly resolved in Figure 5.7 and Figure 5.8, this SVM resolution is achieved with one data point per nanometer, thus presenting nanometer scale features. Though the tip radius is ~20 nm the spatially observed data is ~1 nm. This SVM measurement is justifiable and accurate enough as the measurement was performed on several samples with each sample presenting similar voltage drops at the doping layer (this is clearly observed due of contrast between undoped active regions to highly doped 5 nm layer in phonon well). Also SVM was carried out on each sample many times presenting identical data thus indicating repeatable, hence reliable. From the f-25 SVM scan images in Figure 5.7 and Figure 5.8, it is revealed that at every ~45.6 nm in the multiple-quantum-well active region, a voltage drop exists, which is ~5 nm wide, exactly equivalent to the homogeneous doping in the phonon well according to the f-25 structure presented in Figure 5.1 (a). The first drop in voltage due to this doping layer is observed in Figure 5.7 (a) and (b) to be ~10 nm from the start of the active region, which is very close to 10.1 nm, the exact doping position as per the f-25 THz QCL device structure. Six dips of voltage drop are detected at ~290 nm distance of the active region in

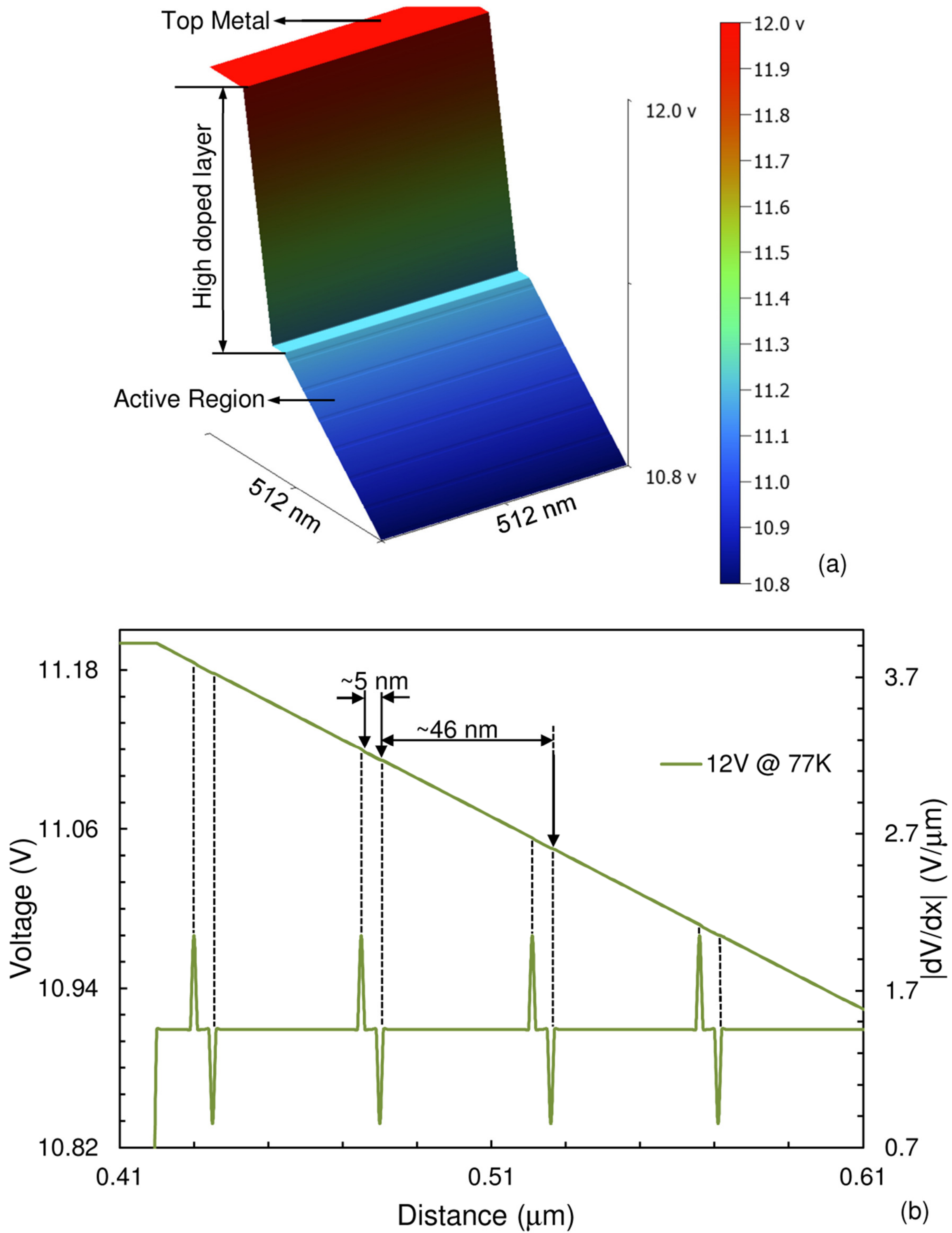

Figure 5.7. (a) High resolution SVM scan executed across 512 x 512 nm^2 area from top metal into the active region at 12 V applied bias on f-25 THz QCL device. (b) Zoomed-in 1D voltage profile across the active region portion is plotted along with absolute value of electric field (|dV/dx|).

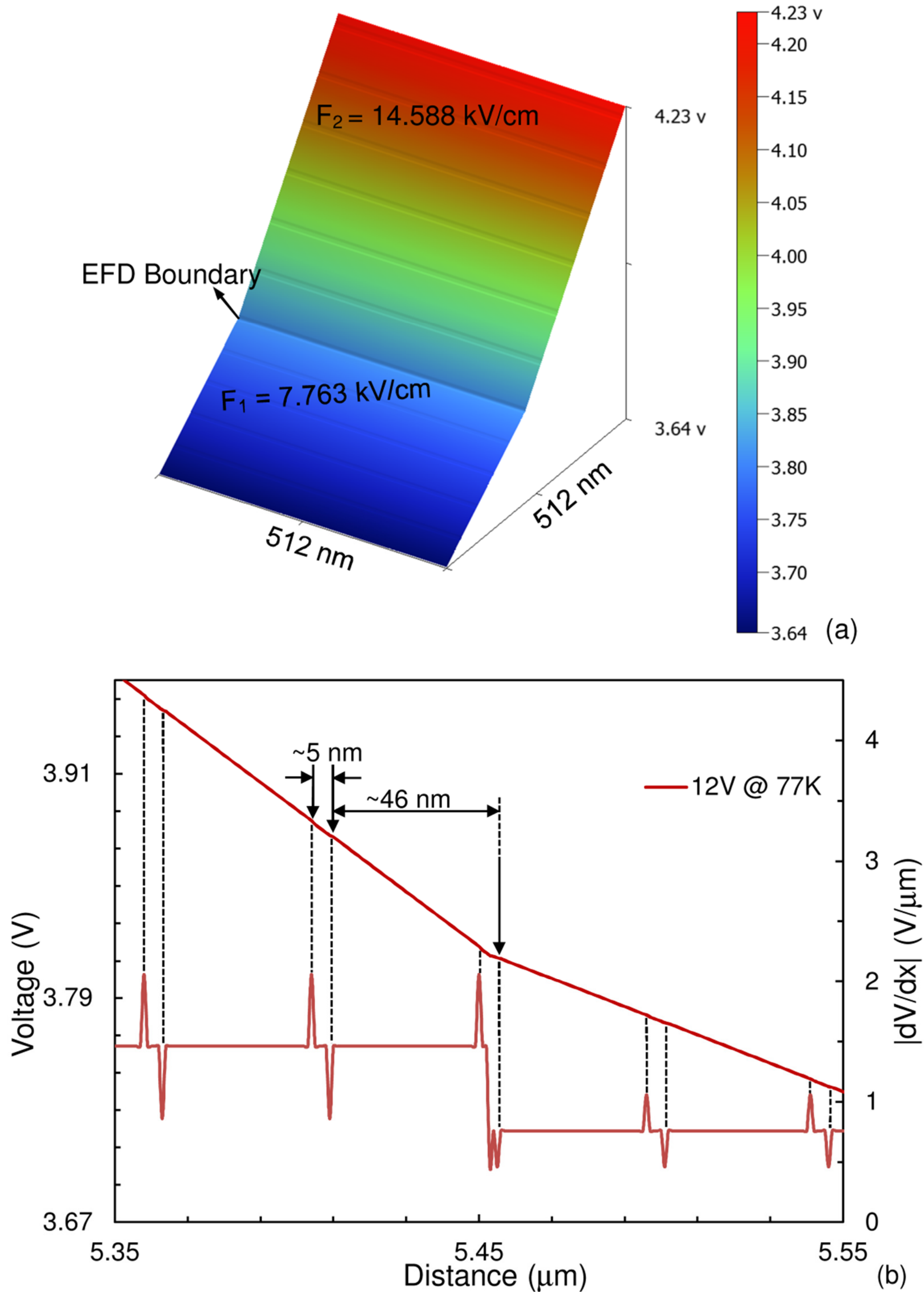

Figure 5.8. (a) 2D SVM scan at the EFD boundary position in the active region distinctly resolves two electric field slope magnitudes F_1= 7.763 kV/cm and F_2 = 14.588 kV/cm. (b) Zoomed-in 1D voltage profile across the EFD position along with the |dV/dx|. Voltage drop dips of ~5 nm width are resolved in all images in the active region portion at every ~45.6 nm and the EFD boundary exists at the center of the doping layer.

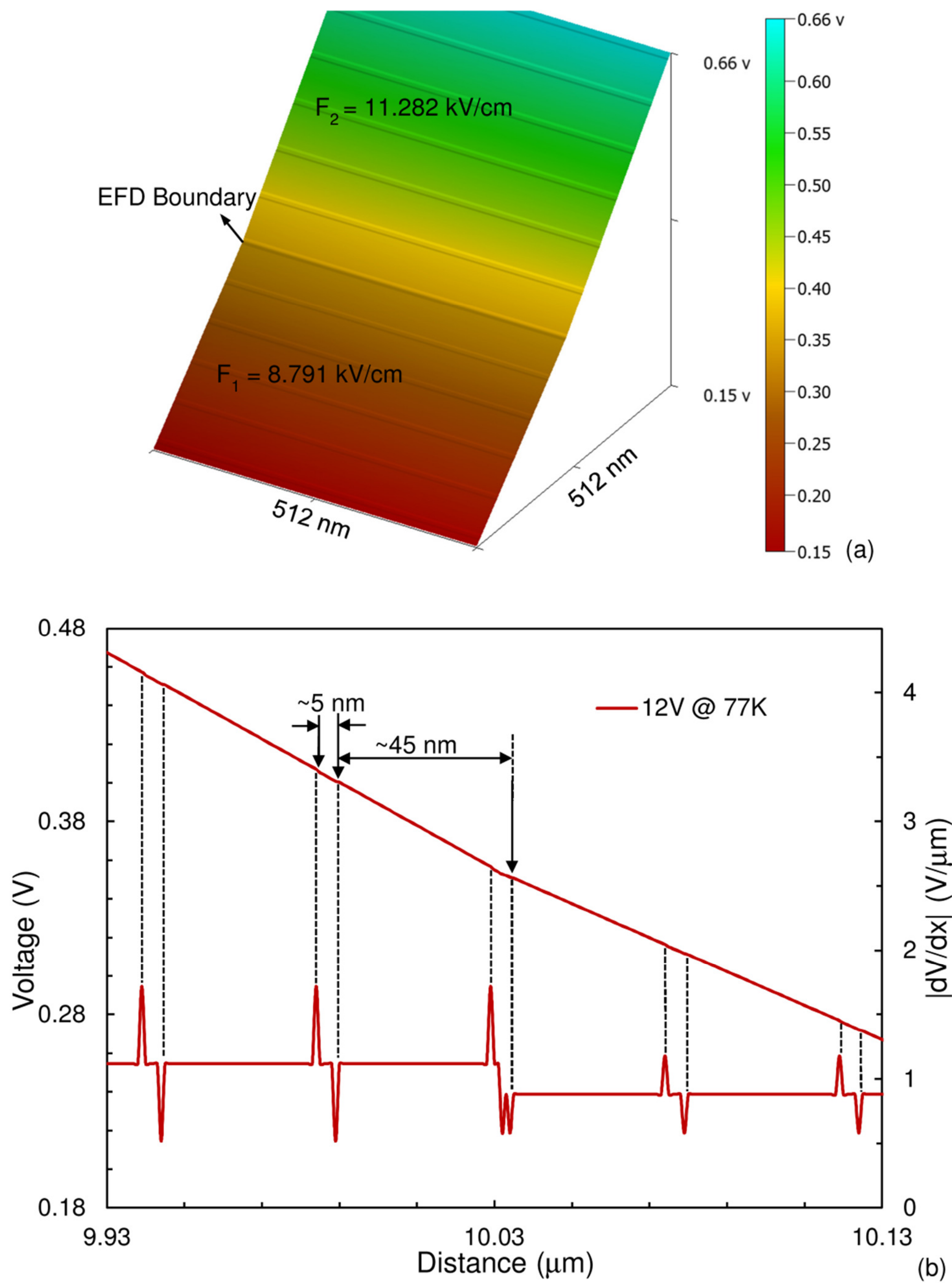

Figure 5.9. (a) 2D SVM scan at the EFD boundary position in the active region distinctly resolves two electric field slope magnitudes F_1= 8.791 kV/cm and F_2 = 11.282 kV/cm at an applied bias of 12 V on top of f-30. (b) Zoomed-in 1D voltage profile across the EFD position along with the |dV/dx|. Voltage drop dips are clearly resolved in all images in the active region portion that occurs at every ~40 nm, which are ~5 nm wide. Dotted lines in (b) mark these drops. The EFD position exists at the center of the doping layer.

Figure 5.7 (a) and (b), and the pair of dotted lines in Figure 5.7 (b) clearly denotes the ~5 nm width for the drop region. It is to be noted that the electric field (-dV/dx) in Figure 5.7 and 5.8 are acquired by averaging 512 line scans voltage profiles for each data point in all SVM measurements, thus indicating accuracy and reliability of the measured parameters. All the line scans resolved identical voltage drops that correspond to spikes in electric field, thus validating the measurement and procedure of data acquisition.

In Figure 5.8 (a) and (b), the EFD boundary position for f-25 is clearly detected as the electric field slope is different, with F_1= 7.763 kV/cm and F_2 = 14.588 kV/cm at an applied device bias of 12 V on top of the device. The change in voltage slope exhibits the EFD boundary, which is perceived to exist in the doping layer for the non-lasing f-25 THz QCL device directly indicating maximum charge carrier accumulation at that interface that creates charge imbalance in the module of the active region. Thus, the effect and existence of dynamic charge carriers are observed. For the lasing f-30 device, SVM scanning is also executed at a 12 V device bias close to the EFD boundary, and the EFD position is directly imaged as shown in Figure 5.9 (a) and (b) where the resolution is based on one data point per nanometer. For the data values obtained from the electric field (-dV/dx) at the spikes are the measured values but the actual values are probably larger since the spot size is ~20 nm. The SVM measurement on lasing f-30 in the EFD boundary position witnessed two electric fields, F_1= 8.791 kV/cm and F_2 = 11.282 kV/cm at an applied bias of 12 V on top of the device, as presented in Figure 5.7 (a) and (b). Due to the presence of a doping layer in each module of the active region, a voltage drop over ~5 nm width every ~45.6 nm is observed in Figure 5.8 (a) and (b) for f-25. A similar drop in voltage is perceived for the f-30 THz QCL device every ~45 nm in the active region in Figure 5.9 (a) and (b); these drops are ~5 nm wide, equivalent to the doping thickness in the phonon well as per the device structure in Figure 5.1 (b). These sudden voltage drops in the voltage profile are ~1 mV and can be probably attributed directly to the doping layer that is present in the phonon well for the f-30 device and directly attributes to maximum charge carrier accumulation (dynamic charge carriers) at EFD boundary interface, which creates charge imbalance inside the module. Both for f-25 and f-30 devices, the SVM images in Figure 5.8 (a), (b) and Figure 5.9 (a), (b), respectively, close to the EFD boundary, identify the exact location of the EFD boundary. The EFD boundary is thus seen to exist in the middle of the phonon well, which is the doping region where this sudden voltage drop occurs. This localization of the EFD boundary in the doping region attributes to maximum

dynamic charge carrier concentration leading to charge imbalance when device under operation, . Thus, the formation of EFDs in operating THz QCLs is detected, and is directly related to the effect of change in dynamic charge carrier concentration across the region.

5.3.2 Direct Observation and Imaging of EFDs in lasing THZ QCLs

The indirect pumping scheme-based THz QCL laser device samples V843 and V962 are under test with uncoated cleaved facets on both ends of a metal-metal waveguide [79, 137]. The conductive cantilever probe of the SVM setup scanned across the device active region, and a 2D voltage profile obtained over a transverse cross section area ($11 \times 11\ \mu m^2$) at 77 K from the front emission facet with 12 V bias in pulse mode for V843 and at 10 V bias for device V962 and is presented in Figure 5.10 (a) and (b) [142], respectively. The figure clearly reveals a monotonic drop in voltage from the top metals, positively biased (12 V for V843 and 10 V for V962), across the intermediate layers, to the grounded bottom metals at 0 V. A sharp voltage drop of ~0.7-0.8 V is observed at the Schottky-like junction in both devices between the top metal (un-annealed) and the top n^+ GaAs contact layer. No significant voltage drop is observed at the interface between the bottom metal and the bottom contact layer due to the Ohmic-like contact [79]. Most strikingly, the image in Figure 5.10 (a) and (b) visualizes the formation of two EFDs across the ~10 μm thick active region at this applied device bias, one close to the top metal layer, which has a higher electric field (greater slope), and one close to the bottom metal layer, which has a lower electric field (smaller slope). The inset image in Figure 5.10 (a) shows the topology of the scanned cross section of the cleaved emission facet. A very small negligible height difference ~900 nm is observed well within limits of AFM (2.5 μm) across the five different layers – the top metal layer, the top n^+ GaAs contact layer, the ~10 μm thick multi-quantum-well active region, the bottom n^+ GaAs contact layer and the bottom metal layer. This topology image confirms that the cross section of the ~10 μm thick multi-quantum-well active region is almost atomically flat.

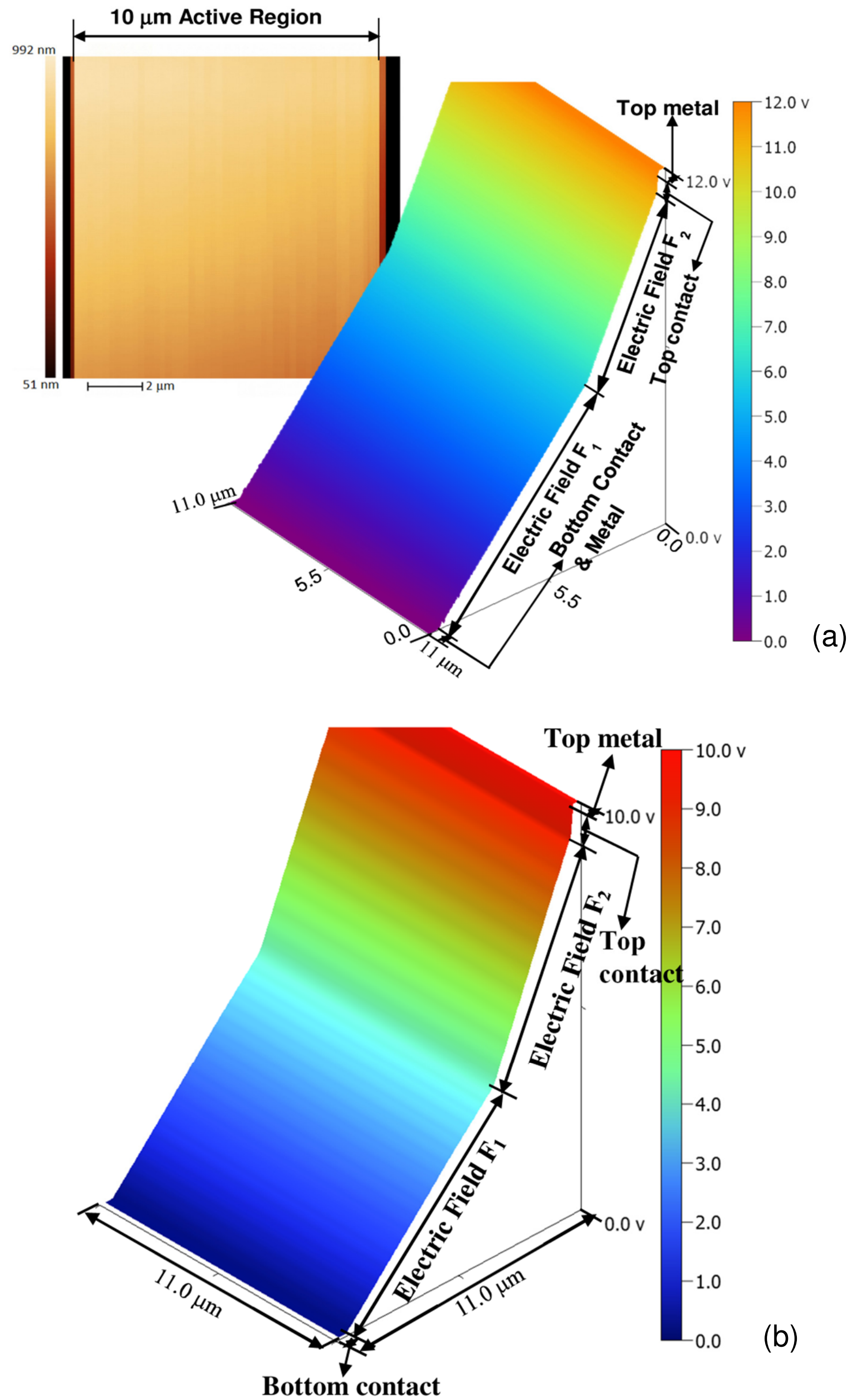

Figure 5.10. Formation and evolution of electric field domains in operating THz QCL. (a) The SVM measured 2D voltage profile across the active region of a THz QCL (device V843, cooled at 77 K) under a forward bias of 12 V. It shows two electric field domains (F_1 and F_2) across the ~10 µm thick multi-

quantum-well active region. The inset of the figure displays a 2D AFM topology image simultaneously acquired over the same area. (b) 2D SVM measured voltage distribution profile at an applied device bias of 10 V for THz QCL device V962. The EFDs (F_1 and F_2) across the ~10 μm thick active region is clearly revealed [142]. For both (a) and (b) the devices were biased in pulsed mode (3.5 μs pulse width, 100 Hz repetition rate).

Similar SVM scans are performed at different applied device biases ranging from 2 V up to 25 V, with steps of 2, 1 or 0.5 V. It is worthy of note that the last few bias points exceed the final device NDR, which is at ~21.8 V for V843 and ~21.5 V for V962. By averaging cross-section line scans that make up the 2D SVM image, similar to the ones shown in Figure 5.10 (a) and (b), one-dimensional SVM measured voltage profile curves are obtained as a function of the distance from the top metal layer, as shown in Figure 5.11 (a) - (c) for V843 and V962. At low biases (2 V to 9 V for V843 and 2 V to 7 V for V962), the electric field is almost uniform across the entire active region (one slope), and the slope of the voltage profile curves over the active region increases proportionally with the increase in applied device bias. Beyond 10 V in V843 and 7 V in V962, however, two slopes due to formation electric field domain start to emerge across the ~10 μm thick active region. As the device bias further increases, the two slopes remain almost unchanged, while the boundary between the higher electric field domain (denoted by dashed-lines) and the lower electric field domain (solid-lines) in Figure 5.11 (a) evenly shifts from the top metal layer to the bottom metal layer. At a device bias between 17 V and 18 V, the higher EFD expands over the entire active region for the V843 THz QCL device. At higher biases of 18 V to 21 V, only one slope can be observed in the voltage curves, as in Figure 5.9 (a), which increases proportionally to the applied device bias in V843. For device biases between 22 V and 25 V in V843, two slopes again emerge, and the higher electric field domain expands from the top metal layer to the bottom metal layer at the expense of the lower electric field domain, as observed in Figure 5.11 (a) and (b). The lasing threshold voltage V843 at 77 K is ~20.4 V, so the SVM results show the formation of EFDs not only below but also above the lasing threshold. A similar observation is obtained from Figure 5.11 (c) for the V962 device, where from 7 V – 15 V, which is the current plateau region, two EFDs are detected, from 16 V – 20 V, a linear drop in voltage attained that increases continuously with increase in applied device bias, and from 21 V – 24 V two slopes of EFDs witnessed which is the NDR region.

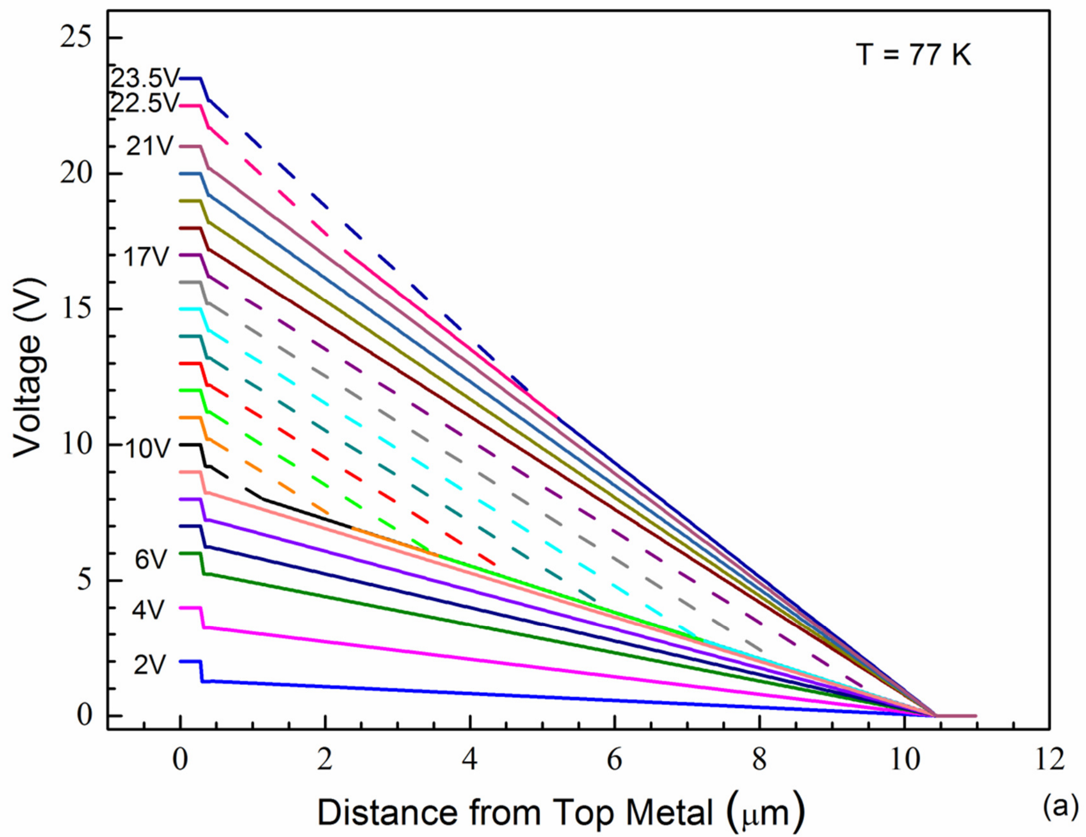
T = 77 K
23.5V
22.5V
21V
17V
10V
6V
4V
2V
Voltage (V)
Distance from Top Metal (μm)
(a)

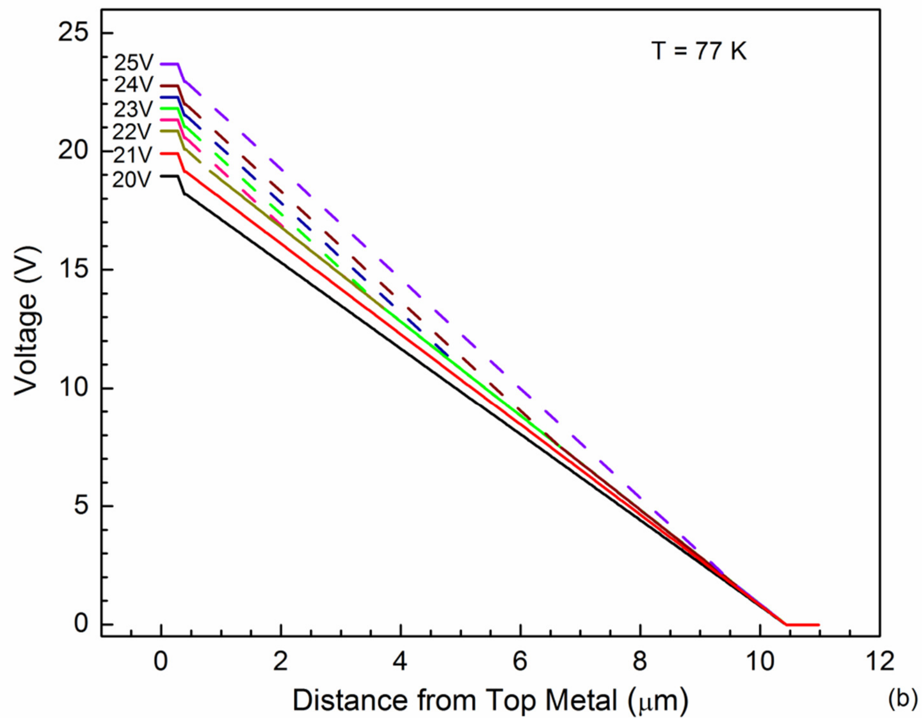
T = 77 K
25V
24V
23V
22V
21V
20V
Voltage (V)
Distance from Top Metal (μm)
(b)

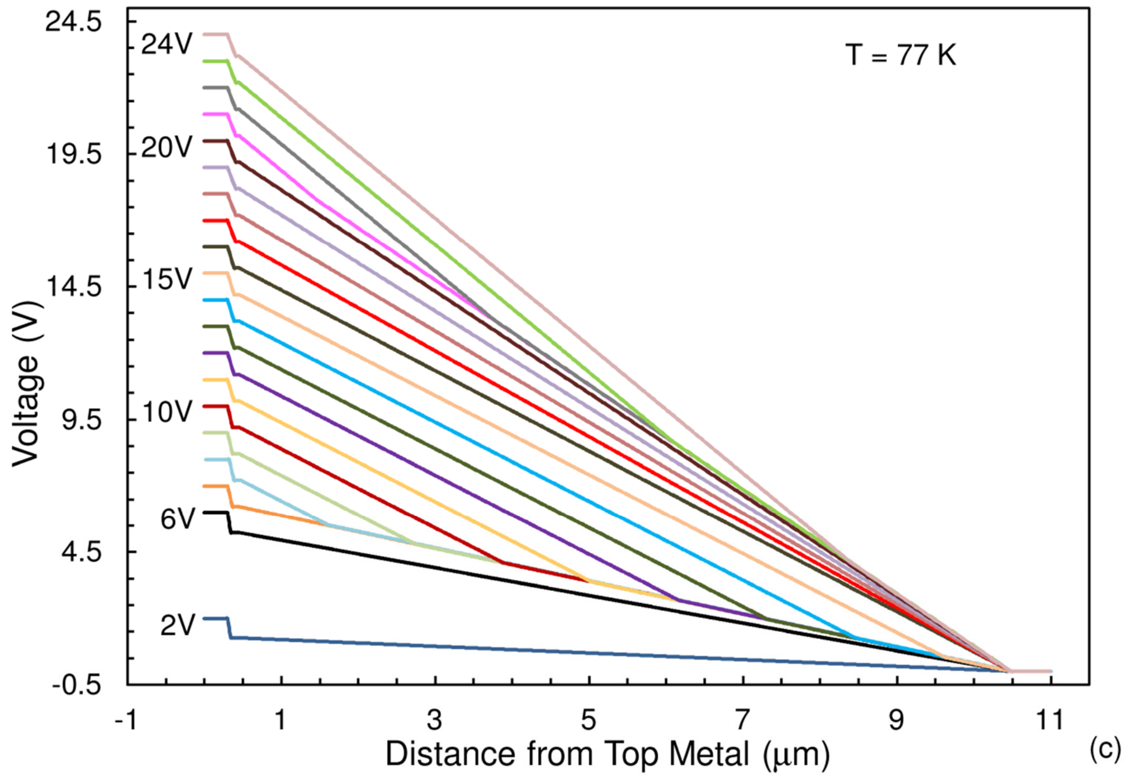

Figure 5.11. (a) One dimensional (1D) section analysis of the SVM voltage profile across the active region of the device at applied device biases spanning 2V – 23.5V for V843. (b) 1D voltage profile curves at higher biases (20 V to 25 V) with a smaller device bias step (0.5 V) between the SVM scans so as to present more detailed EFD evolution in the NDR region for V843. The formation and evolution of two electric field domains over the multi-quantum-well active region is clearly observed in device bias ranges spanning 10 – 17 V and 22– 25 V in (a) and (b). (c) 1D voltage distribution SVM voltage profile across the active region of the V962 device at applied device biases spanning 2V – 24V.

One major advantage of SVM is its quantitative analysis – the electric field magnitude (F) within the observed EFDs can be exactly quantified from the slopes (F = average of ($\Delta V/\Delta d$)) of the voltage profile curves in Figures 5.11 (a) - (c); the derived results are shown in Table 5.1 and Table 5.2 for V843 and V962, respectively. Over pre-threshold device biases on V843, as seen from Table 5.1 spanning 10 to 17 V, two distinct electric fields (F_1 and F_2) are observed. At different device biases, F_1 varies slightly from 8.57 to 8.59 kV/cm, with an average of 8.58 kV/cm, while F_2 varies with an average of 16.77 kV/cm. Two new electric fields (F_3 and F_4)

Table 5.1. SVM measured electric field in each observed electric field domain for V843. The electric field values are obtained by linearly fitting the different sections of the voltage curves. The small variation is attributed to small system errors.

Applied Device Bias (V)	F_1 (kV/cm)	F_2 (kV/cm)	F_3 (kV/cm)	F_4 (kV/cm)
10.0	8.58	16.77	-	-
11.0	8.57	16.77	-	-
12.0	8.58	16.77	-	-
13.0	8.57	16.76	-	-
14.0	8.59	16.76	-	-
15.0	8.58	16.77	-	-
16.0	8.58	16.77	-	-
17.0	8.58	16.77	-	-
….	….	….	….	….
22.0	-	-	20.95	24.35
22.5	-	-	20.96	24.35
23.0	-	-	20.96	24.35
23.5	-	-	20.96	24.35
24.0	-	-	20.96	24.35
25.0	-	-	20.96	24.35
Average	**8.58**	**16.77**	**20.96**	**24.35**

emerge at biases above the lasing threshold, from 22 V to 25 V. At these biases, F_3 and F_4 average 20.96 kV/cm and 24.35 kV/cm, respectively for V843. For the device V962, the electric field F_1 varies from 6.19 to 6.22 kV/cm, with an average of 6.21 kV/cm, while F_2 varies between 14.88 kV/cm and 14.91 kV/cm, with an average of 14.90 kV/cm. At biases of 21 V to 24 V, electric fields F_3 and F_4 average at 19.71 kV/cm and 24.02 kV/cm, respectively for V962. Note that this quantitative measurement of distinctly different EFDs while the semiconductor quantum laser is in operation, illustrating the exclusive potential for cryogenic temperature SVM technique to advance THz QCL research marks a direct development at the beginning of nanotechnology research.

Table 5.2. SVM measured electric field in each observed electric field domain for V962. The electric field values are obtained by linearly fitting the different sections of the voltage curves. The small variation is attributed to small system errors.

Applied Device Bias (V)	F_1 (kV/cm)	F_2 (kV/cm)	F_3 (kV/cm)	F_4 (kV/cm)
7.0	6.21	14.90	-	-
8.0	6.22	14.89	-	-
9.0	6.20	14.90	-	-
10.0	6.22	14.90	-	-
11.0	6.22	14.89	-	-
12.0	6.19	14.88	-	-
13.0	6.20	14.90	-	-
14.0	6.22	14.89	-	-
15.0	6.22	14.91	-	-
….	….	….	….	….
21.0	-	-	19.69	24.05
22.0	-	-	19.72	23.99
23.0	-	-	19.70	24.00
24.0	-	-	19.72	24.02
Average	**6.21**	**14.90**	**19.71**	**24.02**

The experimental and theoretical light–current density–voltage (L-J-V) characteristics of V843 and V962 devices under test are shown in Figure 5.3 (a) and (b), respectively providing useful insights to understand the SVM measured voltage profiles. The simulated current density–electric field (J-F) curve by Dupont et al [79] for the V843 sample reveals three features associated with resonant tunneling processes. In V843, the peak at around F_{e1} = 4.4 kV/cm is related to the alignment of the extraction state (e_{m-1}) with the lower lasing state (1_m) (see Appendix A.2.2 for a detailed band diagram and wave functions). The peak at around F_{e2} = 8.7 kV/cm is related to the alignment of the extraction state (e_{m-1}) with the upper lasing state (2_m), and the peak at around F_{ei} = 21 kV/cm is related to the alignment of the extraction state (e_{m-1}) with the injection state (i_m). The subscript m stands for the index of the modules increasing along the electron flux direction; the subbands in a module are labelled as e (for extraction from lower

lasing state (LLS) by resonant phonon scatting) 1, 2 and i (for injection to upper lasing state (ULS) via resonant phonon scattering). These features tunnelling observed from the simulation are confirmed by the experimental LJV curve by Dupont et al. [79] and correspond to a shoulder structure at around 4.6 kV/cm, a current plateau starting at around 8.7 kV/cm and a final NDR at around 21 kV/cm in the experimental J-F curve for V843 in Figure 5.3 (a). The experimental curve also shows a turning point at $F_{plateau}$= ~16.8 kV/cm, where the plateau comes to an end and the current starts to sharply increase. Clearly a correlation between these electric fields of resonant tunneling features and those of the high field domains obtained from the SVM measurements; i.e., F_1, F_2 and F_3 quite reasonably match to F_{e2}, $F_{plateau}$ and F_{ei} in quantity, from Figure 5.3 (a) and Figure 5.11 (a) and (b), .respectively, in V843.

This electric field correlation in V843 can be understood as follows. When the quantum cascade laser device is biased at ~9.5 V, which corresponds to an electric field of ~8.7 kV/cm across the ~10 μm thick active region after excluding a ~0.8 V Schottky contact drop, all of its 276 cascade modules are uniformly biased at this electric field. The extraction state (e_{m-1}) aligns with the upper lasing state (2_m) of the immediate downstream module, where the current channel due to the e-2 tunneling resonance is at its peak current-carrying capacity (J_{e2} = ~0.5 kA/cm^2). As the applied device bias continues to increase on top of the device, the incremental bias would not be equally distributed among the serially-stacked 276 modules [104]. If it was, the device would experience an NDR due to misalignment of the e-2 resonance, and the device current would substantially drop (as shown in the simulation curve of a single module). To accommodate increases in device bias, some of the modules (starting with those closest to the top contact layer, downstream of electron flux) are enforced to hop to a higher bias point, switching from the e-2 to the e-i tunneling resonance current channel, which has a higher peak current-carrying capacity. The rest of the cascade modules remain at the e-2 resonance (F_{e2}), pinning the device current at threshold current density (J_{e2}), which represents the overall current density through all modules in the active region. The exact bias point (electric field) of the switched modules is determined by drawing a constant current-density line that passes through the peak value of the e-2 resonance and intersects with the e-i resonance curve. This electric field is found to be $F_{plateau}$ = ~16.8 kV/cm, as shown in Figure 5.3 (a). Additional increases in device bias are accommodated as more cascade modules switch from the lower bias point (F_{e2}) to the higher bias point ($F_{plateau}$). This trend continues until all cascade modules switch into the e-i resonance current channel,

which demonstrates the reason of why the electric fields of the two observed EFDs are pinned at F_{e2} and $F_{plateau}$, respectively, in the device bias range between 10 and 17 V for the sample V843 as observed and determined from Figure 5.11 (a) and (b). A similar explanation is valid for V962 device at the two observed EFDs pinned at F_{e2} and $F_{plateau}$, respectively, in the device bias range between 7 and 15 V.

The length (l_k) of each EFD section for V843 is measured directly from the SVM voltage profile curves in Figure 5.11 (a) and (b). As one cascade module period is d = 36.2 nm [79] in thickness, the number (n_k) of the cascade modules in each EFD section can be obtained from $n_k = l_k/d$ (k = 1, 2). These numbers can also be calculated through a second approach using Equation 5.1 and 5.2 that assumes a linear partition of the cascade modules between the two EFDs (F_1 = 8.58 kV/cm and F_2 = 16.77 kV/cm) for V843 that comply with the total applied device bias (V) for N = 276. The numbers of quantum cascade modules in each EFD are obtained through these two approaches (SVM measured and theoretically calculated), exhibiting very good agreement, as presented in Figure 5.12. This finding confirms that the boundary of the electric field domains linearly shifts from the top to the bottom contact layer (opposite to the electron flux direction) as device bias increases and thus accommodates the increased bias.

A similar analysis can be applied to another high field domain transition observed between F_3 and F_4 for V843. From the experimental J-F curve taken at 77 K, the device current density reaches its maximum value of J_{NDR} = ~1.6 kA/cm at F_3, corresponding to the alignment of the e-i resonance. As the device bias further increases, the current first slightly drops and then bounces back to the value of J_{NDR} at F_4 (see Figure 5.11 (b)). F_3 and F_4 thus become observable in the SVM measurements for the same reason F_1 and F_2 do (as described above). However, differences appear in the transition from F_{e1} resonance to F_{e2} resonance Figure 5.3 (a). The SVM results reveal that the electric field across all cascade modules continuously increases from zero up to F_{e2}, without a halt at F_{e1}. This increase could be attributed to the fact that the current density at any intermediate electric field between F_{e1} and F_{e2} might for all time be higher than the peak current density (J_{e1}) of the F_{e1} resonance; considering F_{e1} and F_{e2} are close to each other, it is possible that some broadening mechanisms make their resonant current density peaks broad enough to completely overshadow the valley in between. So the current density through the device can no longer be pinned at J_{e1} when the electric field exceeds F_{e1}. In other words, the device does not experience an NDR region between F_{e1} and F_{e2}, which is different from results

predicted by the theoretical model [79], as shown in Figure 5.3 (a). One possible reason for this discrepancy could be that the broadening due to impurity scattering is likely underestimated in the model. Nevertheless, the experimental curve indeed shows that only a shoulder feature (instead of a current plateau similar to the one between F_{e2} and $F_{plateau}$) is observed at F_{e1}. Hence, no cascade modules are pinned at F_{e1}, and an EFD does not emerge at F_{e1} in the SVM measurements.

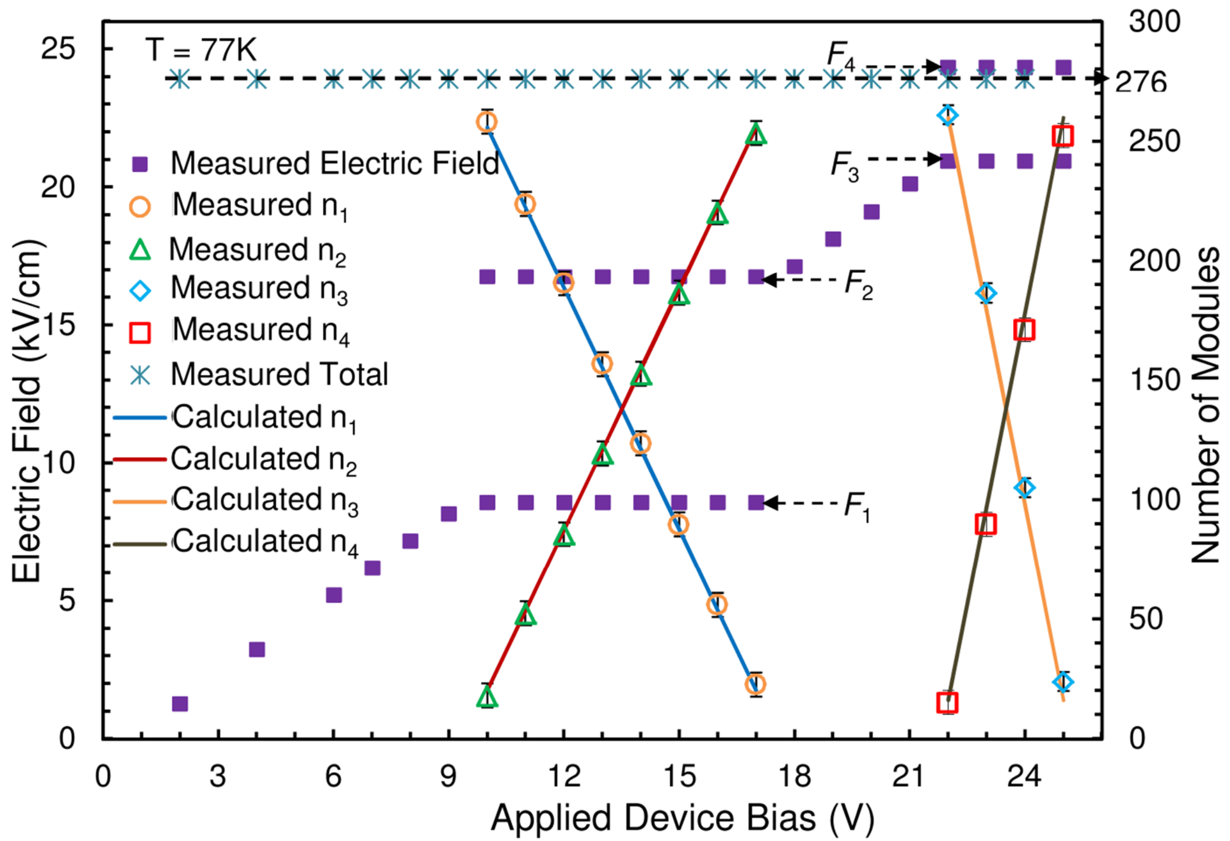

Figure 5.12. The SVM measured electric field across individual cascade modules in the active region of operating V843 device as a function of applied device bias. The electric field increases in direct proportion with the applied device biases over ranges of 2 – 9 V and 18 – 21 V. Two EFDs coexist in bias ranges of 10-17 V and 22 - 25 V. Shown together is the partition number of the cascade modules in each EFD. Discrete symbols (Measured n_k, k = 1, 2, 3, 4) are calculated from the first approach ($n_k = l_k/d$) based on the SVM measurement results of EFD length (l_k) in (Figure 5.11 (a) and (b)). Solid lines (Calculated n_k, k = 1, 2, 3, 4) are calculated from the second approach (see text for details). The sum (Measured total) of the SVM measured module numbers (n_1+ n_2, or n_3+ n_4) is ~276.

Only one uniform electric field domain is observed over the device bias range between 2 V and 9 V, in which the electric field increases proportionately with the device bias. The same behavior is observed over the device bias range from 18 to 21 V, where the device current again increases monotonically with the device bias. Looking at the SVM-measured electric field across individual cascade modules as a function of applied device bias, the two gaps, over which the electric field hops directly from F_1 to F_2 and from F_3 to F_4, as shown in Figure 5.12 are clearly noticed. The SVM measurements also clearly and quantitatively resolve the voltage drop across the Schottky-like junction at the top metal/semiconductor interface in Figure 5.11 (a) – (c), the depletion region of which is mainly in the semiconductor side [143]. The voltage drop across this Schottky-like junction ranges from 0.723 V to 0.812 V at biases of 2 to 25 V, confirming the hypothesis put forward in previous publications that predict a 0.8 V Schottky contact drop [18, 79, 144].

5.3.3 Determination and Evolution of EFD in Operating THz QCLs

Individual quantum cascade modules can be resolved in high-resolution SVM scans by reducing the scan range. In a one-dimensional (1D) rough SVM scan at a device bias of 15 V, the measured voltage profile exhibits two distinct sections over the ~10 μm multi-quantum-well active region and the curve in each section appears smooth and straight, as shown in Figure 5.13 (a). By zooming in on the SVM scans in three 500 × 500 nm^2 regions – one close to the top metal/semiconductor interface, one close to the EFD boundary, and one close to the bottom metal/semiconductor interface is in the insets of Figure 5.13 (a) – it is revealed that every ~36 nm in the multi-quantum-well active region a small voltage dip can be observed in the zoomed-in 1D voltage profile curves, as shown in Figure 5.13 (b) – (d). This small voltage dip (~1.2 mV) is directly attributed to the delta-doping profile ($\eta_{2D} = 3.25 \times 10^{10}$ cm^{-2}) present in the injection barrier, which is the first layer of each cascade module from the upstream of the electron flux as well as the boundary layer between two neighbouring modules. The dV/dx data values are measured and presented for the voltage profiles in Figure 5.13 (b) – (d) and the data values obtained at the spikes are the measured values but the actual values are probably larger since the tip diameter is ~20 nm.

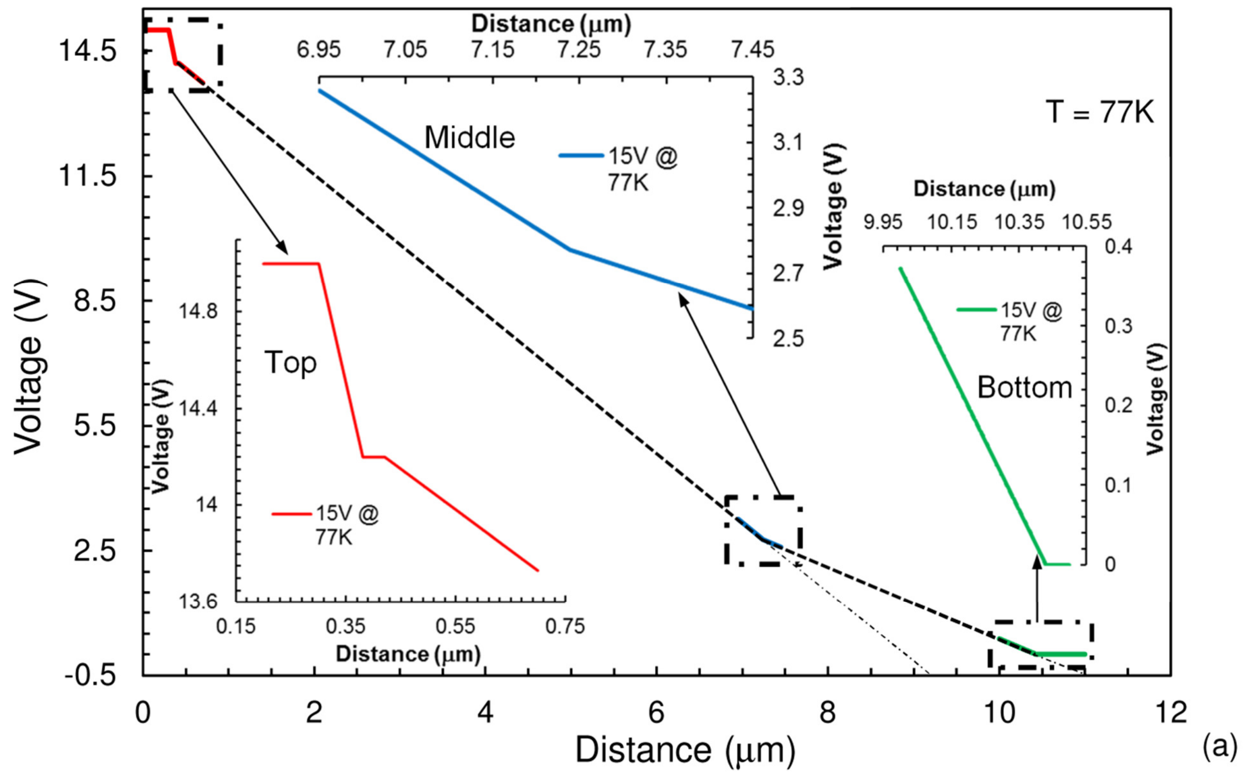
T = 77K
Middle
Top
Bottom
15V @ 77K
Voltage (V)
Distance (μm)
(a)

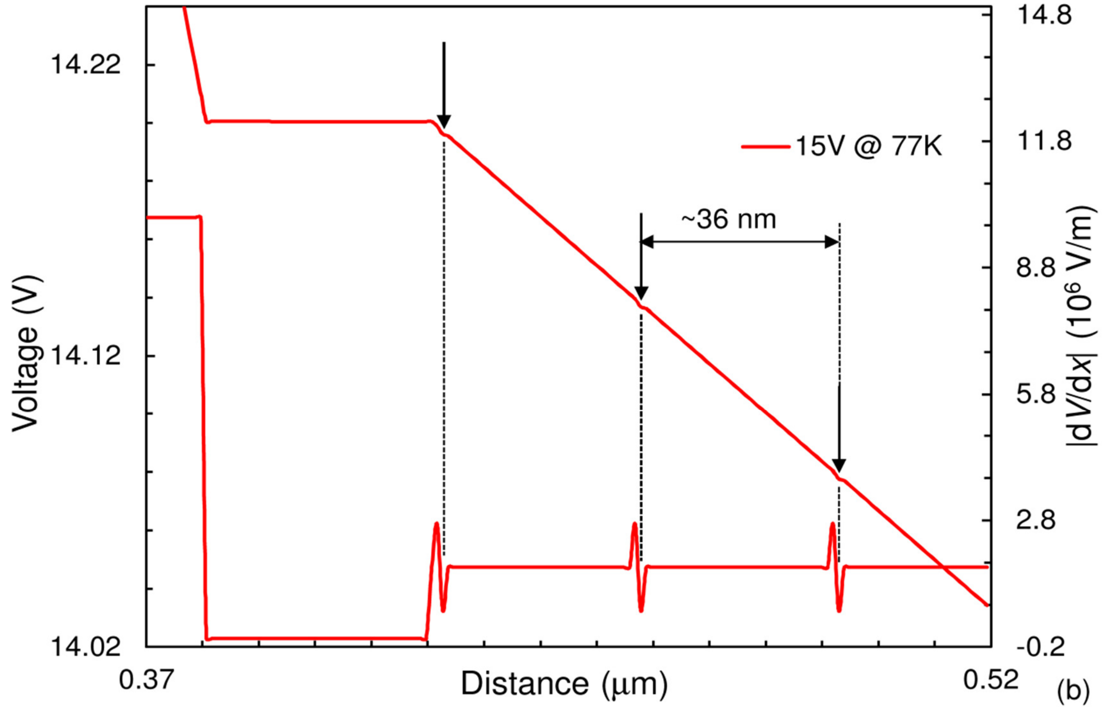
15V @ 77K
~36 nm
Voltage (V)
|dV/dx| (10^6 V/m)
Distance (μm)
(b)

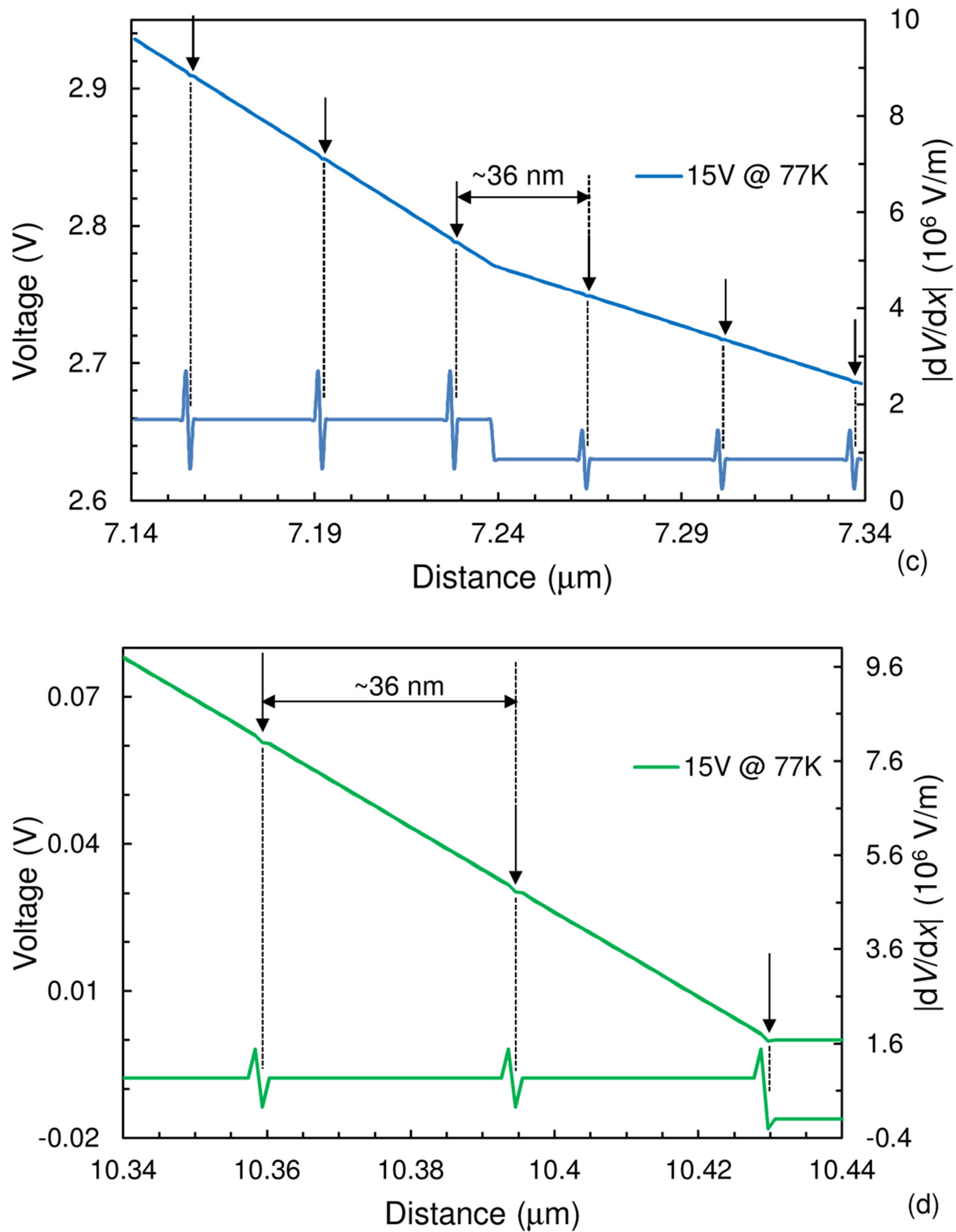

Figure 5.13. Rough and high-resolution SVM scans. (a) The 1D SVM voltage curve cross the active region of the V843 device at a bias of 15 V and at T = 77 K. The rough scan (dashed line) spans 11 μm from the top metal layer to the bottom metal layer, clearly showing the co-existence of two electric field domains. It also shows that the voltage curve is straight and smooth in each section. The three zoomed-in scans (one close to the top metal layer, one at the EFD boundary, one close to the bottom metal layer) spans 500 nm each (solid curves in the insets). (b), (c), (d), The corresponding further zoomed-in curves that show the small voltage dips at the delta-doped injection barriers. The bottom curve in each figure (b,

c, d) is the first order derivative (|dV/dx|) of each corresponding voltage profile curve, for the purpose of identifying the exact location of the voltage dips.

A back-of-the-envelope estimation indicates, at most, an additional potential drop ~5 mV exists between the upstream state e and the delta doping layer. The origin of the sharp dips in potential across the region at such a low doping level is not understood yet – it may be due to some localized oxidation – and will be the subject of further studies. Nevertheless, by high resolution SVM scans in the proximity of the top and bottom contacts, it is certain that the positions of the voltage dips correspond to the nominal coordinates of delta-doping as presented in Figure 5.14. This particularity is very helpful in this study and is used as a “ruler”. The evolution of the EFD position and the observation of the EFD boundary, which is directly attributed to maximum dynamic charge carrier accumulation at the junction, is thus the major advancement of using this cryogenic SVM technique in operating THz QCLs.

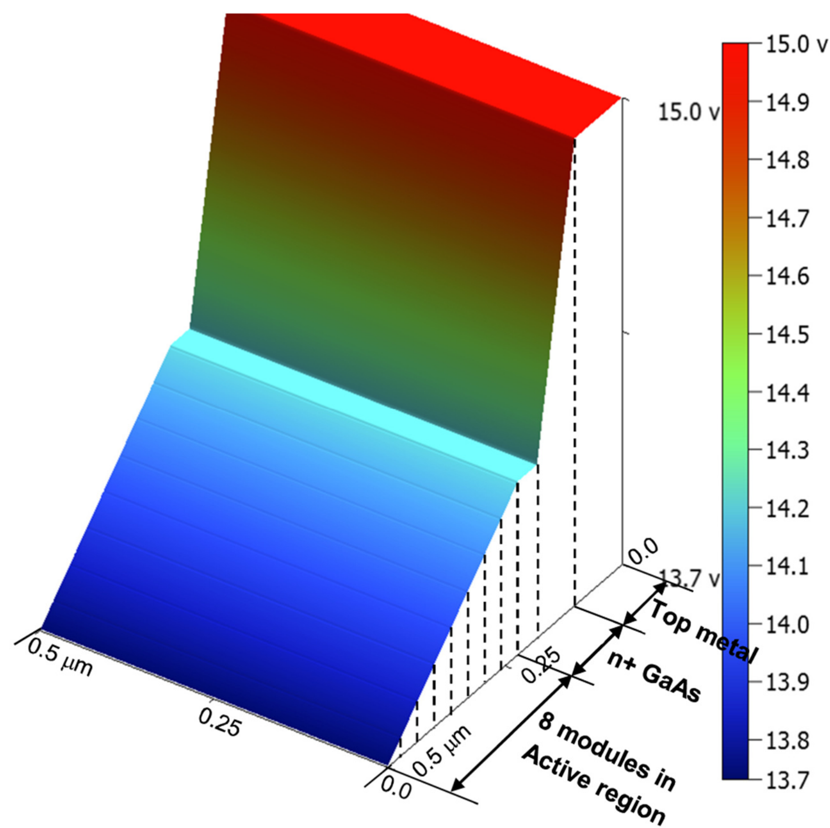

Figure 5.14. High-resolution 2D SVM image near the top metal/semiconductor interface. The 2D SVM voltage image over a 500 × 500 nm^2 scan area starting from the top metal into the active region of the

V843 device at 15 V and 77 K. It clearly resolves the top metal layer, the top GaAs contact layer, and 8 quantum cascade modules, which are separated by small voltage dips in this 2D voltage profile. The period of each individual cascade module is measured from the figure to be ~36.1 nm.

High-resolution SVM scans over the 500×500 nm^2 region close to the EFD boundary region identify the exact location of the EFD boundary and reveal how it evolves in Figure 5.15 and Figure 5.16. Two voltage slopes can easily be distinguished over a span of 14 cascade modules – the boundary of each module is denoted by lines of small voltage dip in Figure 5.15 (a). The periodic spacing is measured from zoomed-in high-resolution scans to be ~36.1 ± 0.1 nm, in excellent agreement with the design value of 36.2 nm (0.3% relative error). Each cascade module consists of four GaAs quantum wells (6.1 to 8.5 nm in thickness) and four $Al_{0.25}Ga_{0.75}As$ barrier layers (0.9 to 4.4 nm). These layers are not individually distinguishable in SVM measurements because of very small (or even zero) voltage contrast (AlGaAs/GaAs are undoped layers) at the interfaces between the wells and the barriers, except the small voltage dip at the delta-doped injection barrier. By further zooming the SVM scan into only three modules, the EFD boundary is disclosed to be ~12 ± 0.5 nm away from the small voltage dip (the injection barrier) towards the upstream direction of the electron flux, as shown in Figure 5.15 (b) [145], where electrons typically pile up at the extraction (*e*) state before tunneling to the injection state (*i*) of the downstream module. The electric field discontinuity across the EFD boundary is attributed to charge imbalance in the transition region, resulting from this electron accumulation on the *e* state. The associated electron sheet density (η_e) can be estimated by Gauss' law, yielding

$$q(\eta_e - \eta_{2D}) = \varepsilon_0 \varepsilon_r (F_2 - F_1) \qquad (5.3)$$

where ε_0 is the vacuum permittivity, ε_r is the relative permittivity of GaAs (12.5 at 80 K), F_1 = 8.58 kV/cm, F_2 = 16.77 kV/cm, q electron charge (1.6×10^{-19} C) and $\eta_{2D} = 3.25 \times 10^{10}$ cm^{-2}, which is the nominal dopant sheet density in the injection barrier. The calculation yields η_e = 8.92×10^{10} cm^{-2}. Note that this is roughly 2.74 times the nominal dopant sheet density in one module.

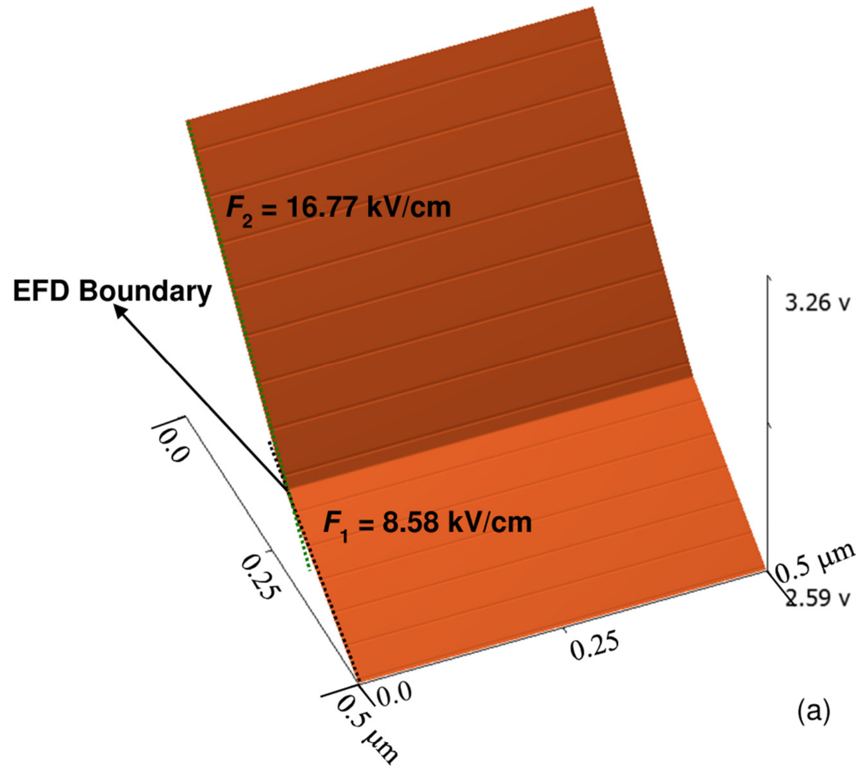

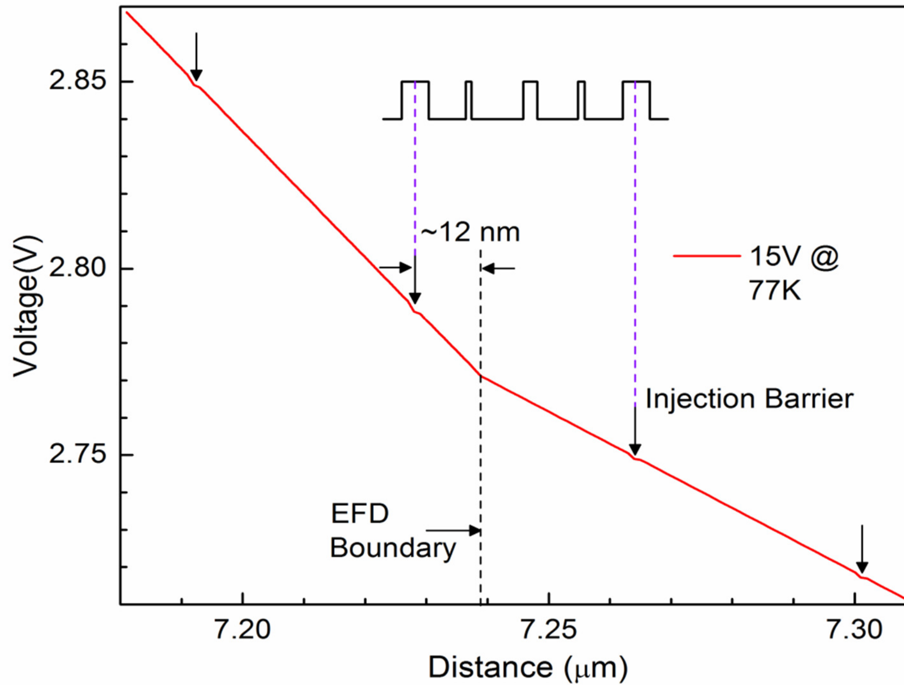

Figure 5.15. Resolution of individual quantum cascade modules and the boundary of EFDs. (a) The 2D SVM voltage image over a 500 × 500 nm^2 scan area near the EFD boundary on the V843 device at 15 V and 77 K. It clearly reveals two electric fields over a span of 14 cascade modules. The period of each individual cascade module is measured from the figure to be ~36.1 ± 0.1 nm. (b) A 1D zoomed-in view of

three consecutive modules near the EFD boundary. The EFD boundary, in other words the turning point of the electric field, locates at ~12 nm ± 0.5 nm (due to 1 nm observable resolution limit of SVM) to the upstream of the delta-doped injection barrier layer of one module [145].

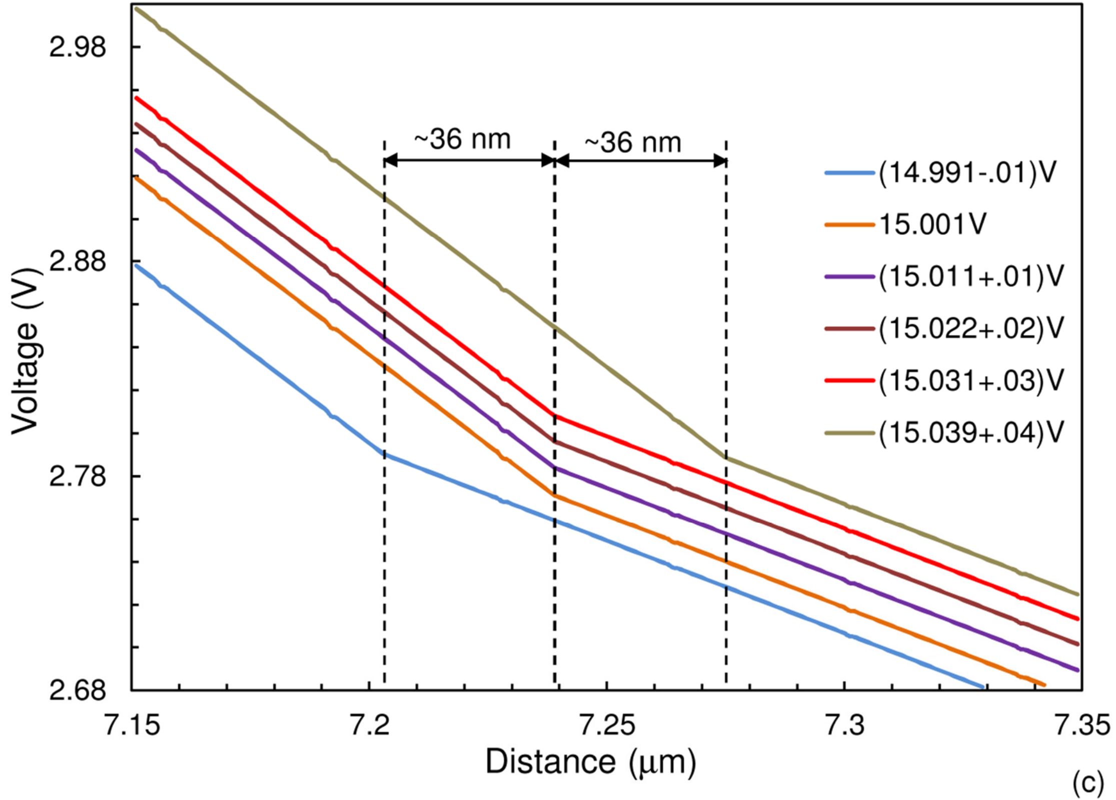

Figure 5.16. Resolution of charge shifting by hopping of EFD boundary. 1D SVM voltage profile curves at a series of device biases with a small incremental bias step (~10 ± 1 mV increase each time). The EFD boundary does not shift if the device bias increase is less than ~30 mV. When it does, the EFD boundary is observed to hop at least one module each time (a phenomenon being termed as *EFD boundary hopping*). All curves (except the one at 15.001 V) are accumulatively shifted by 0.01V vertically for clarity in the figure.

Because the EFD boundary is associated with charge accumulation in the region it occurs, the EFD boundary has to coincide with a quantum well (or wells) in which the presence of electron wavefunction is substantial (i.e., the extraction state in this case). This implies that the EFD boundary does not shift continuously with the gradual increase of the applied device bias, but rather hops discretely, which is confirmed in a series of SVM scans with a much

smaller incremental step (~10 mV each time) in the applied device bias, as shown in Figure 5.16. At a device bias of 14.991 ± 0.001 V, the EFD boundary locates at ~7.203 ± 0.0005 μm. When the device bias increases to 15.001 ± 0.001 V, the EFD boundary jumps to ~7.239 ± 0.0005 μm and remains unchanged at the next three biases of 15.011 ± 0.001, 15.022 ± 0.001, and 15.031 ± 0.001 V. When the device bias further increases to 15.039 ± 0.001 V, the EFD boundary jumps again to ~7.275 ± 0.0005 μm. The EFD boundary hops each time by a distance of ~36 ± 0.5 nm (± 0.5 nm is considered as SVM can acquire a maximum of 1 nm data per scan point, thus observable resolution limit of SVM is 1 nm), which is exactly the thickness of one module. Apparently, the EFD boundary does not shift if the accumulative increases of the applied device bias are smaller than (16.77 kV/cm – 8.58 kV/cm) × 36 nm = ~30 mV, which is the minimum bias increase needed to switch one module from the lower EFD (F_1) to the higher EFD (F_2). This one-module-at-a-time progression of the EFD boundary is determined from the SVM measurements therefore convincingly confirmed to be the nanoscopic origin; this feature of one-module-at-a-time progression of EFD was reported from sawtooth-like current-voltage (I-V) characteristics exhibited by QCLs [146]. If the curves were not vertically shifted in Figure 5.16, the potential curves in the lower field domain would overlay each other almost perfectly, whereas the potential curves in the high field domain are clearly spaced by ~10 mV at the end of the last module (m=276). This means that during a $\leq$ 30 mV increase of applied bias between two hopping events, the additional potential is mainly distributed in the higher field domain; i.e., the electric field "flexes" in the higher field domain before going back to its "rest" value when the EFD boundary has just shifted by one module. So, once the maximum allowable accumulation of the dynamic charge is acquired ~30 mV for the V843 THz QCL device the EFD boundary hops onto the next module. This charge accumulation relates to directly observe the hopping of the EFD boundary on accumulation of the required charge carrier concentrations for that particular module, and as the device is in operating condition, these are the dynamic charge carriers. Thus, the evolution of EFD and the EFD boundary in operating THz QCL is determined by nanoscopic profiling of dynamic charge carriers while mapping and analyzing their effects.

Quantum cascade modules in the close proximity of the EFD boundary are simulated by self-consistently solving coupled Schrödinger-Poisson equations. The lower electric field (F_1), the higher electric field (F_2) and the voltage drop across seven modules around the EFD boundary, which are derived from a high-resolution SVM scan at 12 V – are employed as input

parameters in the simulation. For the sake of simplicity, carriers are assumed at thermal equilibrium (100 K) in each module. The band diagram and the potential profile across the modules are calculated. The simulation results confirm that the transition from the lower electric field domain to the higher electric field domain occurs inside one cascade module, with a fairly-resolvable turning point (Fig. 5.17). The turning point of the potential profile coincides with the part of the wavefunction of the extraction state (*e*) in the widest well of the lower phonon stream, which is ~12.3 nm away from the center of the injection barrier layer. It is worthy to note that the first and second-order derivatives of the potential profile yield electric field profile and charge density profile, respectively. Electron accumulation is indeed observed at the EFD boundary in the simulation curve.

As expected, in the low field domain (the right side in the figure) the levels e_{m+1} and 2_m are almost perfectly anti-crossed (coupling strength Ω_{e2}=0.24 meV), and in the high field domain (the left side) e_m and i_{m+1} start to be coupled, resulting in a positive differential conductivity of this domain (Fig. 5.17). The subscript m stands for the index of the modules increasing from right to left. Across the downstream injection barrier of the transitional module (in which the EFD boundary is located) the levels e_m and 2_{m+1} are fairly detuned and levels e_m and i_{m+1} are still weakly coupled, which puts this short section in negative differential conductivity region and commands extra charge accumulation in e_m to maintain current conservation through this transitional module. Similar argument could be applicable to the levels e_{m-1} and 2_m who just passes their anti-crossing according to the simulation. The impact of the electric field domain boundary on the transport behavior of THz QCLs is profound. The transitional cascade module across the EFD boundary is divided into two sections with different electric fields, so its energy levels are not well aligned. As a result, electron transport across the EFD boundary is nonresonant and may limit the current [21]. Advances in hybrid electron transport, which combines resonant and nonresonant tunnelling to support efficient transport in semiconductor quantum systems such as THz QCLs with multiple EFDs are of great interest and crucial importance. However, additional experimental and theoretical work is needed to fully understand these mechanisms. The evolution and determination of EFD observed from Figure 5.15 for V843 thus clearly revealed to match with the simulated results presented in Figure 5.17. This correlation between simulation and SVM measurements confirms that the EFD boundary where maximum charge accumulation occurs due to charge imbalance in the module is ~12 nm away

from delta-doped layer thus indicating accuracy, reliability and validity of the SVM measured voltage and electric field distributions. This observation and verification of charge accumulation directly confirm the EFD boundary where the dynamic charge carriers accumulate in that particular module, when device under operation. Thus, the evolution of EFD from SVM is endorsed with simulated results in operating THz QCL, and the nanoscopic profiling of dynamic charge carriers is quantified and determined.

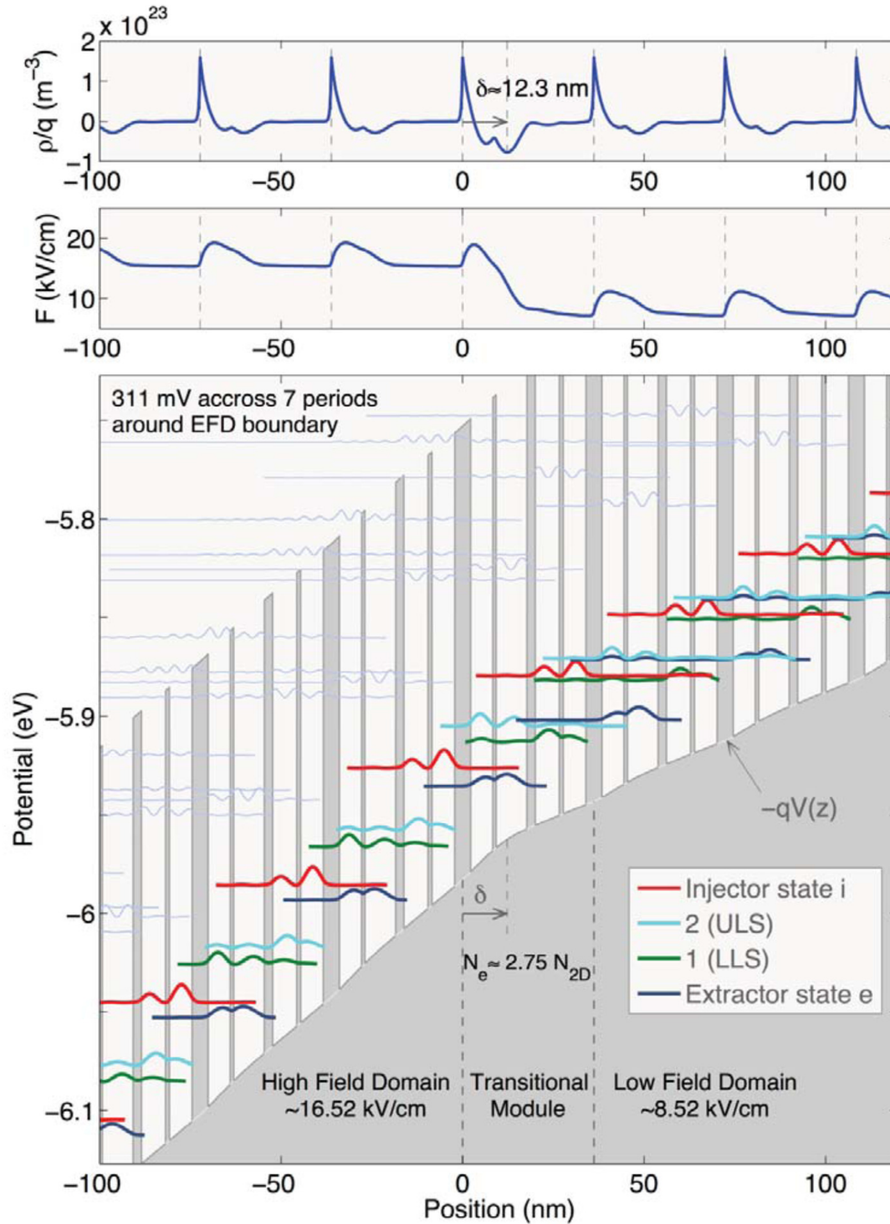

Figure 5.17. Simulation of the EFD boundary. Self-consistently solving the coupled Schrödinger-Poisson equations yields the simulation results of electron wavefunction and band diagram across the EFD

boundary, confirming the EFD boundary is ~12.3 nm away from the delta-doped injection barrier in the transitional module. The delta-doped dopants are assumed to exponentially diffuse (by 48 Ang/decade) to the upstream direction of electron flux due to Si segregation during the molecular beam epitaxy of the QCL structure. The line running at GaAs conduction band edge (in gray and white) is the potential curve V(z) that the SVM tries to measure. The two curves on the top show the simulated charge density profile and electric field profile, respectively. The simulation is performed at a device bias of 12 V.

This new ability to perform cryogenic SVM under pulse bias by probing quantum photonic devices while in operation and on a nano-scale opens up critical new avenues of experimental analysis and enables direct measurement of many fundamental physical parameters. In this way, the nanoscopic origins and macroscopic functions are compellingly connected. The cryogenic temperature SVM and other associated techniques [41, 49, 52, 53, 135] have been employed to measure important inner workings such as the device's voltage profile, dopant profile, charge carrier profile and current profile at nanometric scales and in two dimensions. They also allow visualizing the development and evolution of high electric field domains in operating THz QCLs, and quantitatively determine the electric field and EFD boundary that exist in the current plateau and NDR regions of device operation, which are directly related to the effect of dynamic charge carriers.

5.4 Summary

In this chapter, the evolution and formation of the EFD is directly observed and determined in nanometer scale on operating THz QCL devices. The EFD is observed using the cryogenic-temperature SVM technique by probing the operating nano-device to resolve the inner workings, which results in achieving the voltage profile and electric field distribution across the active region of the device. Nanosurface profiling is executed on both non-lasing and lasing THz QCLs and the EFD boundary position along with its evolution are detected. Quantitative analysis is performed and two slopes indicating existence of two electric fields in the active region of the devices are identified as F_1 and F_2 in the current plateau region while as F_3 and F_4 in NDR region. The EFD boundary localization is distinctly viewed to exist where the charge carrier concentration or accumulation of dynamic charge carriers in the module is highest, thus resulting in the EFD boundary to hop from one module to the next when the required charge accretion

overcomes the bias. The evolution of EFD and the hopping of the EFD boundary are directly related to the effect of dynamic charge carrier's accumulation existing in operating THz QCLs. The hopping of EFDs leading to inter-module carrier transition due to dynamic charge carrier accumulation is thus observed. In particular, the electric potentials profile across quantum cascade modules and the charge carriers that perhaps instigate the evolution of EFDs are directly and experimentally resolved from operating THz QCL devices. Nevertheless, the demonstration of resolving the charge carrier potentials in an operating optoelectronic laser device is unprecedented and could possibly open the door to many future applications in probing and identifying underlying mechanisms for many puzzling sub-par performance and degradations in nanoelectronic devices, quantum devices and optoelectronic devices.

Chapter 6: Conclusion and Future Work

6.1 Summary and Conclusion

The internal dynamics of operating nanophotonic devices (THz QCL and ICL) have been nanoscopically profiled, imaged and observed by mapping the electric field distribution across the active region. The quantitative analysis of the charge carrier in individual modules is achieved from ICL devices, while nonlinear electric field leading to evolution of electric field domain observed in THz QCL devices in nanometer scale.

The nonlinearity of the electric field distribution and formation of EFDs in operating THz QCL devices are some of the aspects that may pose to hinder the device performance. These EFDs are major concerns in device operation that leads to non-uniformity of the active region due to internal dynamics leading to accumulation of dynamic charge carriers forming EFD boundaries. The charge carrier density and the carrier transport due to quantum hopping can instigate in the formation of EFDs in the region. A quantitative measurement analysis of potential profiles and electric field distribution resolving of EFDs are performed to present an in-depth understanding that may drive the external measures in THz QCL and in some cases may deprive the device to operate at its best. AFM-based cryogenic temperature scanning voltage microscopy (SVM), a non-destructive carrier measurement technique has been established to bridge a connection and relate internal mechanisms with external measures allowing observation of these effects which can be minimized while designing future devices.

In the process of experimentally observing the electric field distribution and the effect of charge carrier variations on operating laser devices by quantitatively studying the inner workings; on the basis of electric potentials, the AFM-based nanoscopic probing technique is developed and established. This new ability of nanoscopic probing is applied on the ICL and on the THz QCL. The probing of the ICL device using the nanoscopic SVM measurement technique while operating on a nanoscale regime opens new possibilities of experimental analysis enabling

direct measurement of many physical parameters. This bridges the gap between external measures of lasing operation of the device and the internal mechanisms in nanophotonic devices. The results obtained from the nanoscopic voltage measurements on a lasing mid-IR ICL device provide the first experimental evidence that the electric field across the interband cascade regions of ICL devices are not uniform. The substantial variation of electric field over the active region in each cascade stage suggests considerable charge transfer and accumulation in type-II QW layers, resulting in a strong internal electric field in the region. This electric field strength refers to the charge density across the InAs/GaInSb/InAs interface layers for all the ICL devices measured. The dynamic sheet charge carrier density is estimated from the electric field distribution for electron and hole concentrations as σ_e and σ_h, for different devices at varied applied biases in each individual module at the interface junctions of the type-II QW layers. The quantification of the overall 2D dynamic charge carrier density across the cascade stages due to positive and negative charges signifies the behaviour of carrier transport in the device. This sheet charge carrier density instigates the need for evaluation of the device's potential performance. With the establishment of this SVM technique for nanoscopic charge carrier analysis of both at cryogenic temperature and room temperatures can be executed, thus the gap between external and internal performances is being bridged presenting the internal dynamics of the device in nanometer scale. This clearly displays the non-uniformity of electric field distribution in the active region of the device and the dynamic charge carrier density in the modules.

This cryogenic SVM measurement technique is employed to study the THz QCL devices and the evolution and formation of the EFD is directly observed and determined in nanometer scale on operating THz QCL devices. In both non-lasing and lasing THz QCLs the EFD boundary position and its evolution are detected. The mechanisms responsible for sub-par device performance of THz QCLs that have been the subject of speculation are thus identified and determined quantitatively. The nanoscale electric potential distribution inside operating QCLs is experimentally observed and as per the EFD hypothesis, the quantum-well-barrier active region is divided into multiple sections having distinctly different electric fields. Quantitative analysis resolved two slopes indicating the existence of two electric fields in the active region of the devices in the current plateau region and NDR region; however, the lasing region of operation in the devices are smooth with no sign of the existence of any EFDs. The electric field across these serially-stacked quantum cascade modules hops between discrete

values that are related to tunneling resonances. The EFD boundary localization is distinctly viewed to exist where the concentration of dynamic carriers in the module is highest, thus resulting in the EFD boundary when the required charge accretion overcomes the bias, leading to a hopping-style shift in the EFD boundary. The findings specify the significance of quantum active regions designed for intrinsically more uniform and stable electric field profiles. The nonlinearity of the electric field distribution and formation of EFDs are identified in operating devices through the variation observed for charge carrier concentration by this nanoscopic SVM measurement technique. The resolving of the EFDs (due to maximum dynamic charge carrier accumulation) is of utmost importance which presents an understanding of the internal mechanisms or dynamic behaviour of the device and bridges the external measures with these internal measurements. In particular, direct and quantitative electric potentials profiles across quantum cascade modules and conclusive identification of the underlying mechanisms from the inner workings of the device are achieved, which relates the effect of dynamic charge carriers that causes to develop EFDs that are experimentally resolved. Thus, the electric field distribution profile achieved from this SVM measurement technique bridges the external device performance to the inner workings in operating THz QCLs.

The extent of the development and establishment of this cryogenic SVM technique can relate internal dynamics to the external measures by mapping electric field potential and in some cases quantify dynamic charge carrier density in the nanoscale regime in operating nano-devices. However, additional experimental and theoretical work is needed to fully understand these mechanisms. This work and continued study are expected to help further the understanding and development of THz QCLs and ICLs. All these new insights will be of critical importance in designing superior mid-IR ICLs and THz QCLs. Major fundamental concerns in device operation such as non-uniformity of the electric field, dynamic charge carrier accumulation, formation of EFDs and quantum hopping phenomenon can be analyzed. This nanoscopic probing technique can characterize and analyse voltage and current related behaviour in operating nano-devices; consequently, the establishment is a formidable advancement in this area of nanotechnology.

6.2 Future Work

The new ability to probe quantum photonic devices while in operation on a nano-scale has opened critical new avenues of experimental analysis enabling direct measurement of many fundamental physical parameters. In this way, the nanoscopic origins and macroscopic functions are being compellingly connected. The underlying mechanisms responsible for device failures and sub-par performance will be identified with clarity, which will accelerate device design and optimization processes. The cryogenic temperature SVM and other associated techniques [17, 41, 49, 52, 147] can be employed to measure important inner workings such as the device's voltage profile, dopant profile, charge carrier profile and current profile at nanometric scales in two dimensions. SVM can probably be used to visualize the development and evolution of electric field domains not only THz QCLs, but also in semiconductor superlattices and other resonant-tunneling based quantum structures. SVM can also permit study of the extra voltage drop across THz QCLs without the top n^+ GaAs contact layer, while examine the alignment of the electron injection from the bulk contact layer into the first quantum cascade module. If the spatial resolution and voltage sensitivity are further improved, this technique may reveal subtle information such as electron cloud distribution inside a module, the observation of which would shed light into thermal backfilling issues. The technique may also help in understanding how stimulated emission reconfigures the electric field inside a module, as the radiative wells should become more conductive upon the ignition of stimulated emission. All these new insights will be of critical importance in designing THz QCLs with better performance. The SVM cryogenic temperature technique that has been presented is not limited to QCLs or ICLs, but is applicable to many other active quantum and nanoelectronic devices, such as quantum-well infrared photodetectors (QWIP), semiconductor quantum-well optical amplifiers, semiconductor modulators, single electron transistors, spintronic devices, and oscillators based on resonant tunneling and the Gunn effect, to name but a few. The domain boundary in the measured QCLs looks stable with a sharp transition from one domain to another, but the SVM technique could probe domain instability in weakly coupled semiconductor superlattices [148], which so far have been addressed extensively in theory [149, 150] but transfer without experimental confirmation of the predicted complex dynamics of electric field domains.

Appendix A: THz QCL Device Fabrication and Performance Measurement

A.1 THz QCL Device Fabrication

The THz QCL device fabrication starts from the substrate wafer, usually GaAs. The multiple quantum well (MQW) structure forming the active region of the device is grown on a semi-insulating (SI) (100) oriented GaAs substrate using molecular beam epitaxy (MBE) with GaAs/$Al_{0.15}Ga_{0.85}As$. It is necessary to grow the epitaxial layers as thickly as possible, but due to uncertainty and non-uniformity during long-term growth (MBE growth rate ~0.5 – 1.0 µm/hr), to avoid degradation, the overall thickness of the epitaxial layers is characteristically controlled within 10-15 µm [16, 151]. Especially, in structures with very thin barriers (2 monolayers), experience indicates that the sharpness of the barriers is critical, and as the growths tend to be long term (up to 10 µm) process, stability of growth is necessary to prevent non-uniformities among modules [149]. The THz QCL device can be restricted in two major waveguide structures: semi-insulating surface-plasmon (SISP) [11, 61] and metal-metal (MM) [152] waveguide structures. Between the top metal contact layer and the bottom n^+ surface plasmon, the active region mode is sandwiched, forming the SI-SP structure. This structure has very low waveguide loss, so in turn, can be used to achieve high power THz QCLs [16]. The structure that sandwiches the mode between the top and bottom metal contacts poses very high confinement factor and very high waveguide loss in the MM structure. This MM structure is used to achieve high temperature operation for THz QCLs [16, 151].

A.1.1 Metal-Metal Waveguide

Williams et al. [151] proposed for the first time the MM waveguide structure that had enhancement in maximum operating temperature (T_{max}) and threshold current density (J_{th}). In

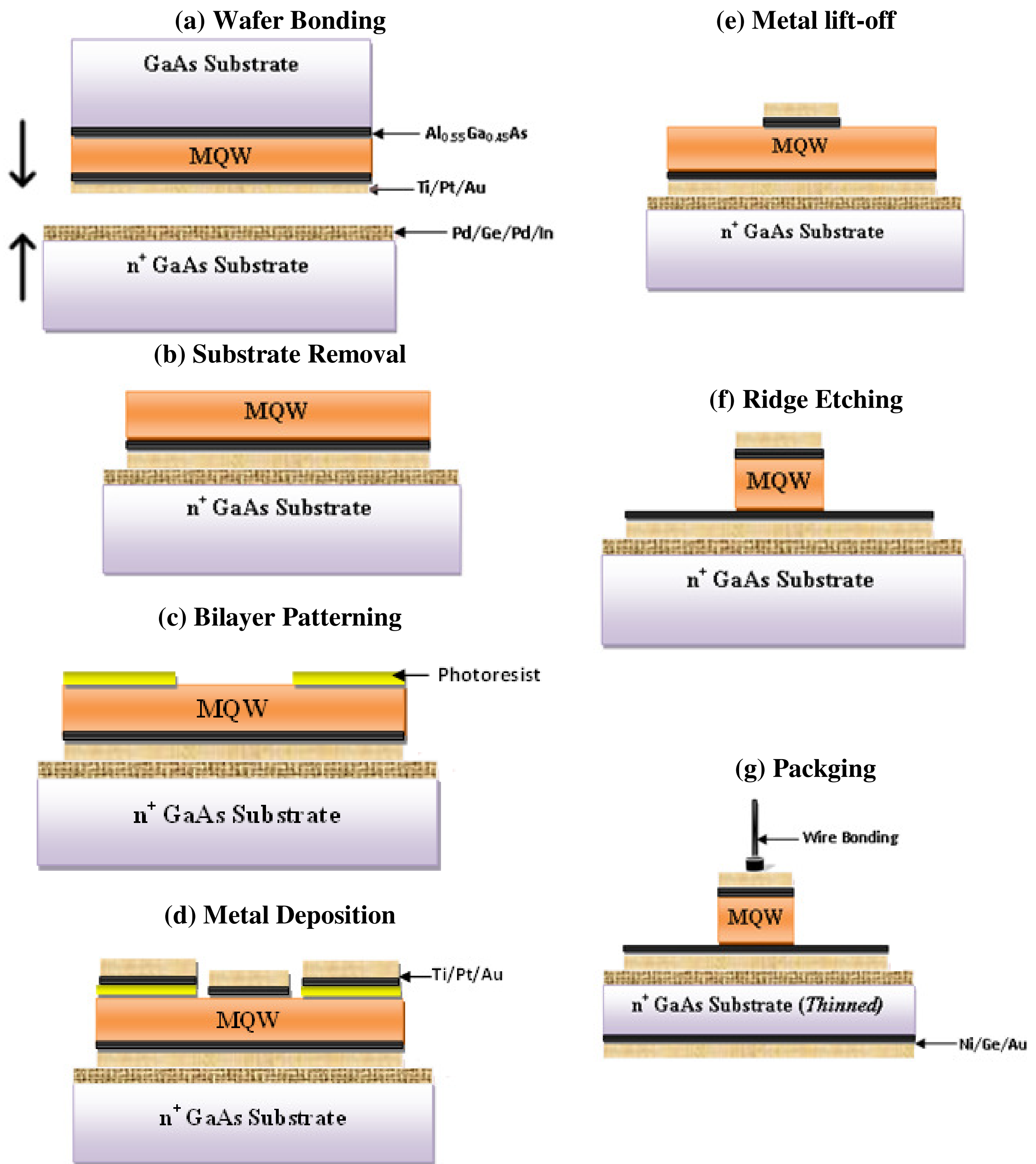

Figure A.1. Schematic of the Metal-Metal fabrication process steps for the THz QCL device.

this structure the modes are confined and sandwiched between the top and bottom metal contacts. The threshold gain is very low, thus the device is used to accomplish high temperature operations. The process called "substrate removal" is a part of MM waveguide fabrication in

THz QCL devices and is the most difficult part. Following MBE growth, the wafers were cut and cleaned in ultrasonic cleaner and then oxygen plasma descum treatment was applied to remove organic contaminants and native oxide [11]. The next step was to deposit the metallic non-alloyed ohmic contacts on the epitaxial layers because of delicacy of the LTG-grown epilayer. Then Ti/Pt/Au (250/550/1000 Å) metal layers deposited via electron-beam evaporation, followed by patterning via lift-off in acetone on top of the 10 µm thick epi-layer. On the other hand, a silicon doped n^+ ($\sim 1\times10^{18}$ cm^{-3}) GaAs substrate is encrusted with a Pd/Ge/Pd/In (250/100/250/10000 Å) metal heap. This becomes the receptor substrate after the wafers are bonded [11, 16]. Then these two wafer pieces are placed on a hot plate face to face and aligned along their crystal axes. A glass slide is then placed on top of the stack so that pressure can be applied evenly. This is followed by a process called wafer bonding whereby both wafers are reactively bonded (In-Au bonding) under 0.5 MPa pressure at 200 ºC for 90 minutes, as shown in Figure A.1 (a).

The next step after wafer bonding is to remove the substrate of the device wafer via a process called lapping and selective etching as shown in Figure A.1 (b). In order to protect the back of the receptor wafer and the sides of the device wafer during the substrate removal etch, firstly, low temperature plasma-enhanced chemical vapour deposition (PECVD) is used to coat the front and back of the bonded wafers with ~2000 Å of SiO_2. The oxide is removed from the top of the wafer automatically by lapping of the substrate on application of oxide early in the process, but the oxide is left behind on the sides as desired [16]. The bonded wafer is then mounted on a glass holder using wax and a mechanical lapping process is used to remove around 550 µm of the GaAs substrate. Thereafter, citric acid : H_2O (4:1) solution (etch rate ~ 0.3 µm/min) is used to chemically etch the remaining (~ 50 µm) of the GaAs substrate. As shown in Figure A.1 (b), the sample is dismounted from the holder, cleaned and made ready for photolithography and metallization steps.

Then the waveguide ridge pattern on top of the sample using conventional photolithography techniques were defined as shown in Figure A.1 (c). To ensure the ridge pattern is parallel to the major flat (crystallographic orientation) of the wafer immense care to be taken. The light emission surfaces are cleaved perpendicular to the laser ridges at the end of fabrication leading to two photolithograph masks being used in the process. A metal lift-off process takes place using Mask 1 to pattern a bi-layer photoresist coating, then after Ti/Pt/Au

(250/550/3000 Å) is deposited on top of the patterned bi-layer photoresist, and lifted-off using NMP at 80 ºC shown in Figure A.1 (steps c to e). To form the waveguide ridges, etching of the MQW layers are performed in regions that are not covered by the top metal. The window openings are then defined by Mask 2 for etching. $NH_4OH:H_2O_2:H_2O$ (2:1:10) is used as wet etchant on the MQWs of GaAs/AlGaAs structure etching 10 µm in vertical direction and yielding 10 µm undercut from sidewalls [11, 16]. To minimize this undercut effect only 5 µm in vertical direction etch is performed as shown in Figure A.1 (f). Figure A.2 (a) and (b) show scanning electron microscope (SEM) images of fabricated QCL devices with a ridge width of 200 µm and 30 µm, respectively.

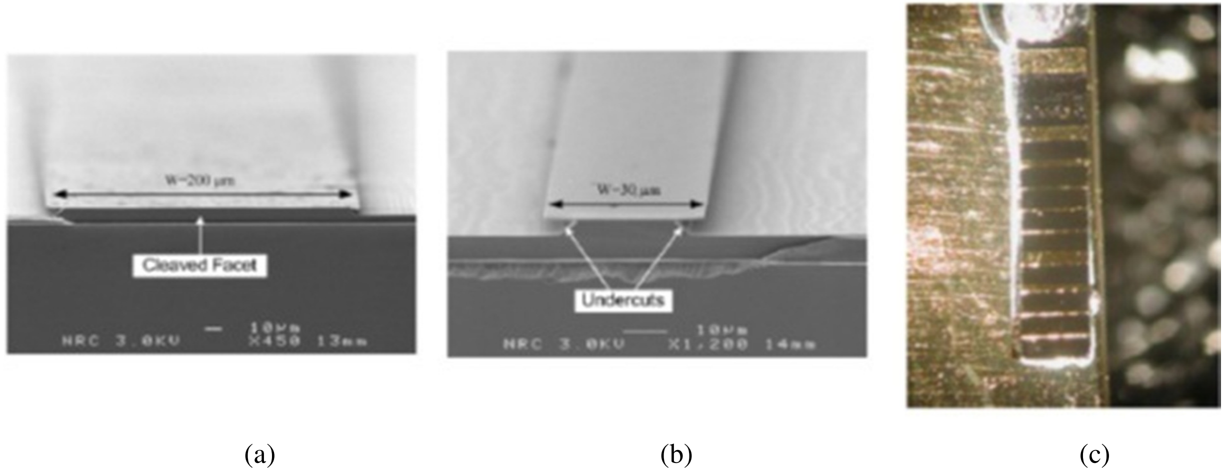

Figure A.2. SEM micrograph for fabricated (a) 200 µm and (b) 30 µm QCL after cleaving, and (c) image of packaged devices. [16].

The last step of the fabrication is device packaging where the device is made ready for usage by making the contacts as shown in Figure A.1 (g). To facilitate the heat dissipation through the substrate, firstly, the n^+ GaAs substrate is thinned down to ~ 150 µm and then at the bottom of the wafer the ground contact is implemented while a very small contact resistance is expected from the heavily doped n-type GaAs receptor substrate [11]. Onto the back of the substrate a pile of Ni/Ge/Au (250/550/3000 Å) metal was then deposited. Then after, the sample piece is sliced into ~1 mm long Fabry-Perot resonator laser bars and is In soldered (epi-layer side up) on an Oxygen-free copper package, as shown in Figure A.2 (c) [16]. Very careful considerations are taken to mount the emission facet of laser ridges as close as possible to the

edge and thin Au wires are used to connect the top metal contact on the ridge of each device to different electrical pins of a 16-pin package which is then placed on a cryostat cold finger for low-temperature measurements.

A.1.2 Semi Insulating Surface Plasmon Waveguide

The SISP waveguides have very low surface reflectivity of 0.33, compared to that of MM waveguide that has a reflectivity of 0.7, this result in higher mirror loss in the device. This device has a low confinement factor of $\Gamma \approx 0.3$ inside the active region. So as expected, with low confinement factor and high mirror loss, the loss in SISP waveguide increases leading to a higher threshold gain compared to the MM waveguide. This effect consequently, work for a lower T_{max} in the SISP THz QCL. Due to its high mirror loss, the SISP waveguide structure emits high power, thus making it suitable for high power applications. The fabrication steps related to the SISP structure is detailed below.

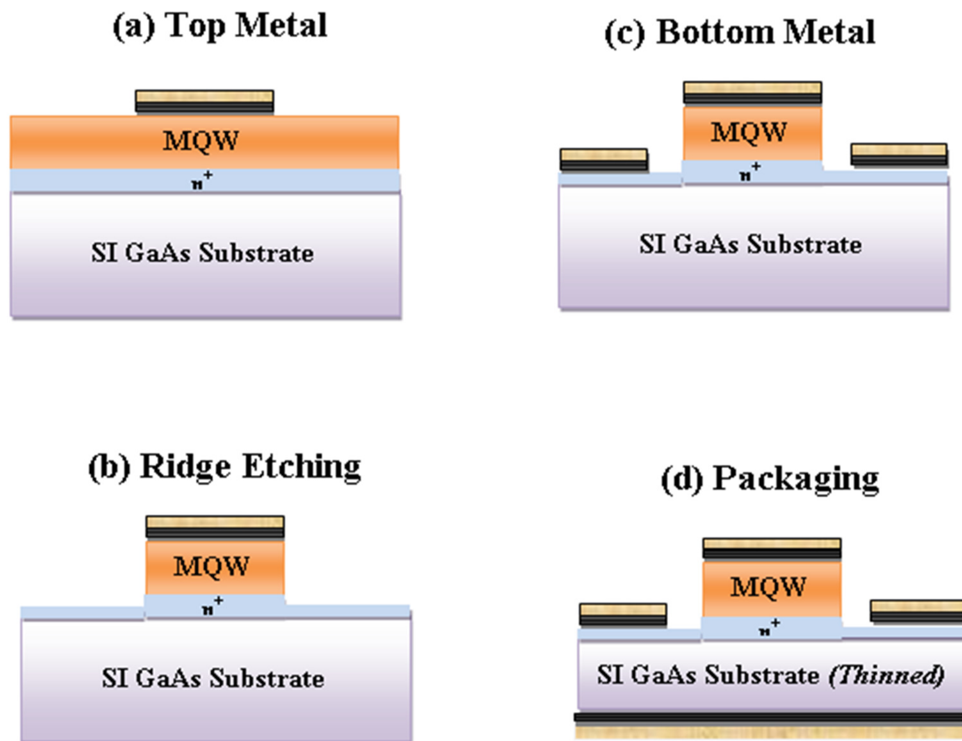

Figure A.3. Schematic of fabrication for the SISP THz QCL with metal-metal structure.

Metal-metal bonding is not required for the fabrication of the SISP THz QCL device, so the device is processed on the as-grown SI-GaAs wafers. The wafer is first cleaned by standard

Isopropanol (IPA) / Acetone / deionized (DI) water in an ultrasonic cleaner. Then the organic contaminations and native oxide are removed by an oxygen plasma descum treatment and HCl : H_2O (1 : 10) dip. For a metal lift-off process, mask 1 is used to pattern a bi-layer photoresist coating, after which, a pile of Ti/Pt/Au (250/550/10000 Å) metals (unless otherwise noted) is deposited on top, as seen in Figure A.3 (a). Then, to alloy the top metals for an Ohmic contact, the sample is annealed at 350 °C for 15 seconds in N_2 ambient in an RTA process [16]. The MQW layers from the part that are not covered by the top metal in the active region of the device are then etched off using dry etch process, exposing the bottom n^+ GaAs layer for electrical contact as shown in Figure A.3 (b). Using both RIE (50 W) and ICP (400 W) powers, this dry etching is performed on cooled substrate (10 °C) at low pressure (4 mTorr) in BCl_3 environment, then at the bottom metal contact etch is stopped by an end point detection system [16]. To rule out the ambiguity in the end-point detection of the dry etch process, a practically thick n^+ layer is required that also makes sure that the bottom contact does not finish. Mask 2 is used to define the opening windows for the side contacts after exposing the bottom contact n^+ layer [16]. As shown in Figure A.3 (c), a stack of Ni/Ge/Au (250/550/3000 Å) metals is then deposited, to form the bottom contacts, after which, the substrate thinning and device packing steps are the same as in MM device fabrication and shown in Figure A.3 (d). Figure A.4 shows the SEM image of the cleaved and wire-bonded SISP THz QCL is ready for characterisation. The package is then placed on a cryostat cold finger for low-temperature measurements.

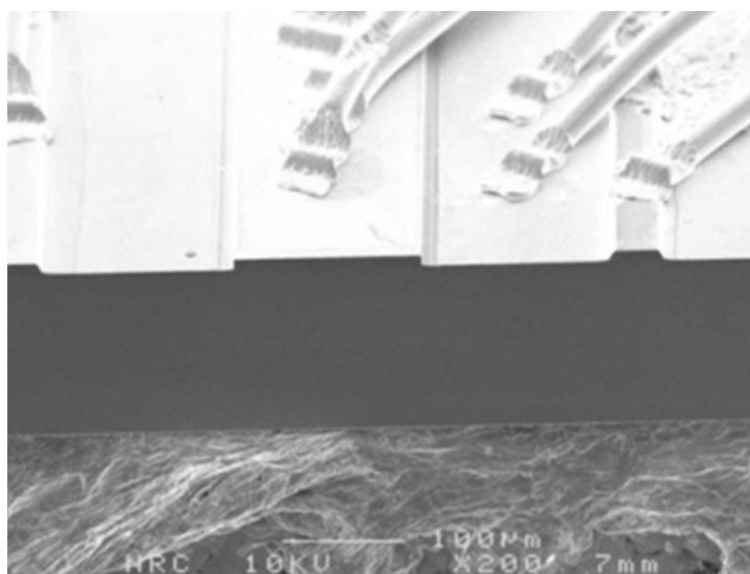

Figure A.4. SEM image of a fabricated SISP THz QCL [16].

A.2 External Performance on THz QCL devices

A.2.1 Experimental setup and Measurements

The THz QCL devices operate at low temperature. Engineering the band structure of the multiple-quantum-well active region of the THz QCL, the maximum lasing temperature have increased recently to 199.5K (pulsed) and 117 K (CW) [15, 57]. The most basic and important measurement techniques for the THz QCL devices are the light-current-voltage (LIV) and Spectra measurement. The LIV measurement determines how the current varies with increase in voltage and estimates the current profile, while the light intensity is also measured at different temperatures signifying the THz QCL device power. This gives an assessment of the highest temperature the specific device can lase. The spectra measurement gives a view of the wide or narrow range the specific device can lase along with temperature. For the purpose of LIV measurement on the THz QCL device, the device bars are mounted on the package and are placed in a closed cycle liquid Helium cooled cryostat. The cryostat has a polyethylene window

Figure A.5. Schematic of the LIV measurement set up for THz QCL and ICL devices [151].

that is ~80% transparent to THz light. The THz light emit from the device passes through the window when device under operation. The device mounted on the cryostat is kept very close to its window opening so that maximum amount of light is transmitted outside. The cryostat is cooled down to low temperatures and a far-infrared detector is placed in the vicinity to collect the light for LIV measurements. A liquid-He cooled silicon bolometer (IR Lab Inc, Model HDL-5) or a Golay Cell detector is used as a detector for detecting the light intensity of the THz signals. The silicon bolometer is the most preferred option due to its high sensitivity for the THz frequency domain. The bolometer also has a polyethylene window that passes the THz signal, being ~80% transparent, from the device to the Winston cone, placed inside the bolometer dewar and the beam is focused onto the silicon detector part.

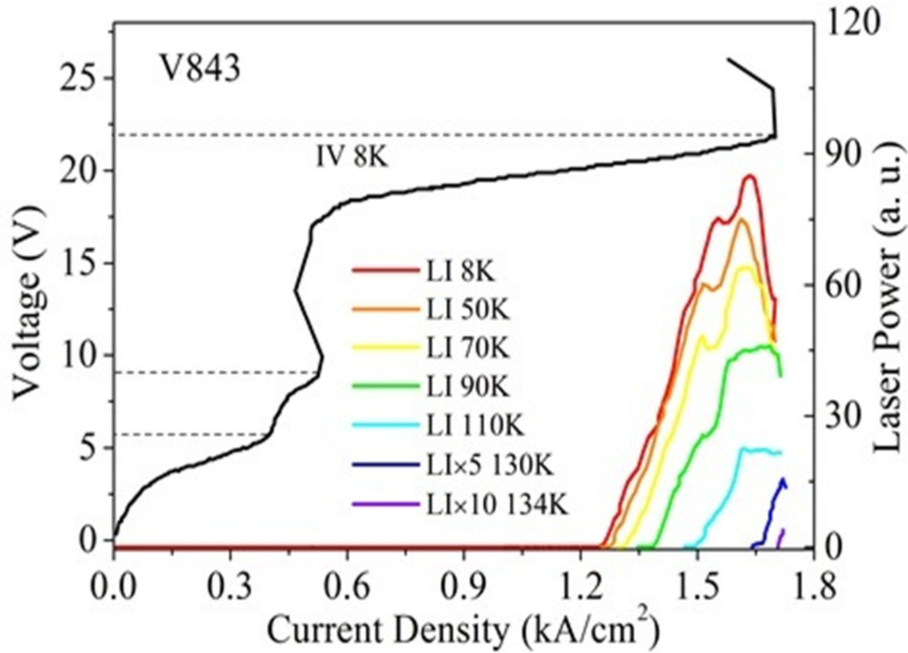

Figure A.6. LIV Measurement of THz QCL for sample V843 [79].

The Schematic block diagram for the THz QCL LIV measurement is shown in Figure A.5 [153]. The required threshold input power (electric bias) of THz QCLs is provided from an avtech high voltage pulse generator. For pulsed mode operation, pulses of less than 1 KHz frequency are generally applied at around a ~0.03% duty cycle. Higher frequency operation is limited by the response time of the silicon bolometer, which is in the range of milliseconds. A current probe simultaneously measures the externally applied electric bias. Pulsed voltage and

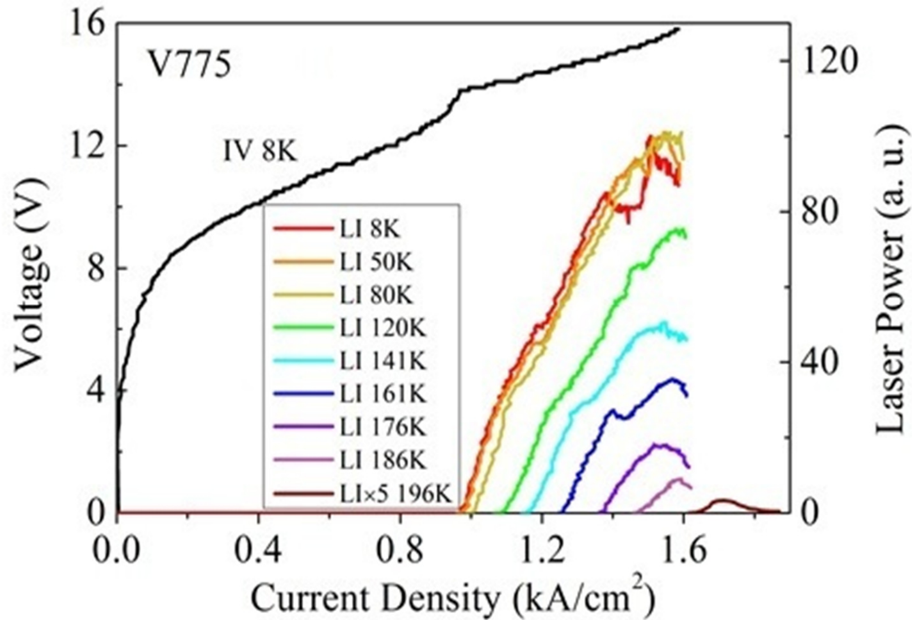

Figure A.7. LIV Measurement of THz QCL for sample V775 [15].

current signals are averaged for 200 periods in the pulse region using a Tektronix 420 Oscilloscope. The light signal detected by the silicon bolometer is then fed to a Lock-in amplifier that already has the pulse signal applied as the reference signal for the measurement, as shown in Figure A.6. Thus, the measured voltage and current signals from the oscilloscope are collected directly by the Labview program on the computer while the light signal coming from the Si bolometer is fed to the lock-in amplifier and is then collected by the computer. All the data are acquired using a Labview program. The responsivity of the Si bolometer is calibrated to be 9 kV/W multiplied by 200 or 1000, depending on the gain filter used in the measurement and considering the transparencies of the polyethylene window. IV measurement data is then collected from the oscilloscope and, similarly, LI measurements are also obtained while the light intensity data is collected from the Lock-in amplifier as the device operates in pulsed mode at different temperatures by sweeping the voltage of the pulse generator. Samples V843 and V775 were tested in the lab using the above measurement setup, and the LIV curves were plotted as shown in Figures A.6 and A.7, which match the published data of Dupont et al. [79] and Fatheloloumi et al. [15], respectively. The spectra measurement was also performed in our lab

and the set up was modified by placing the spectrometer from Bruker (model no. IFS 66V/s) in between the cryostat and the bolometer and the spectroscopy was measured for the devices.

A.2.2 Device Design and Simulation

The THz QCL devices with an indirect pumping scheme such as the V843 are fabricated on a $GaAs/Al_{0.25}Ga_{0.75}As$ layer structure [79]. The active region of the THz QCL consists of 276 cascade modules, each 36.2 nm long. The band structure of quantum cascade modules (under three different applied electric fields at *Ee1*, *Ee2*, and *Eei*) is shown in Figure A.8. Each module consists of four wells and four barriers with nominal layer thicknesses of 62.5/**10.9**/66.5/**22.8**/84.8/**9.1**/61/**44** Å — the barriers are indicated in bold fonts. The injection barrier (44 Å) is delta-doped with Si to $\eta_{2D}= 3.25 \times 10^{10}$ cm^{-2} at the center. The laser devices are processed into metal-metal waveguide ridges 150 μm wide and ~1 mm long. The device emits at 3.2 THz and operates up to a heat-sink temperature of 138 K in pulsed mode. Figure A.9 shows a temperature-dependent light-current density (L-J, 10 to 138 K) and voltage – current density (V-J, 10 to 250 K) characterizations [79]. All parameters refer to pulsed operation at a repetition rate of 1 kHz and a pulse width of 250 ns for L-J-V measurements.

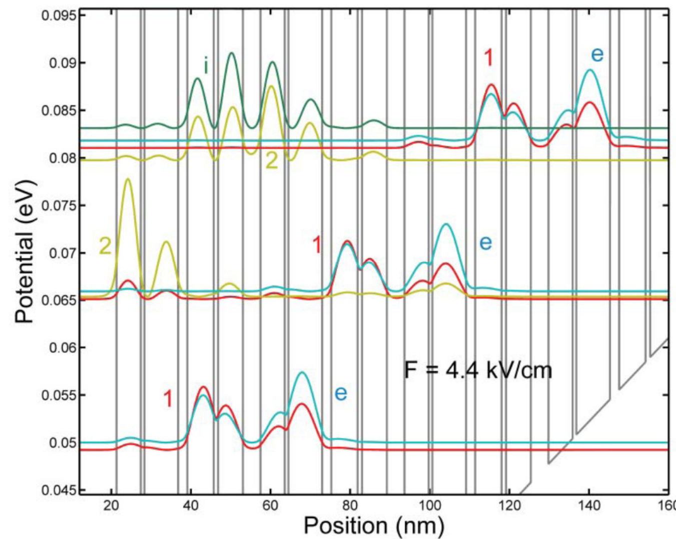

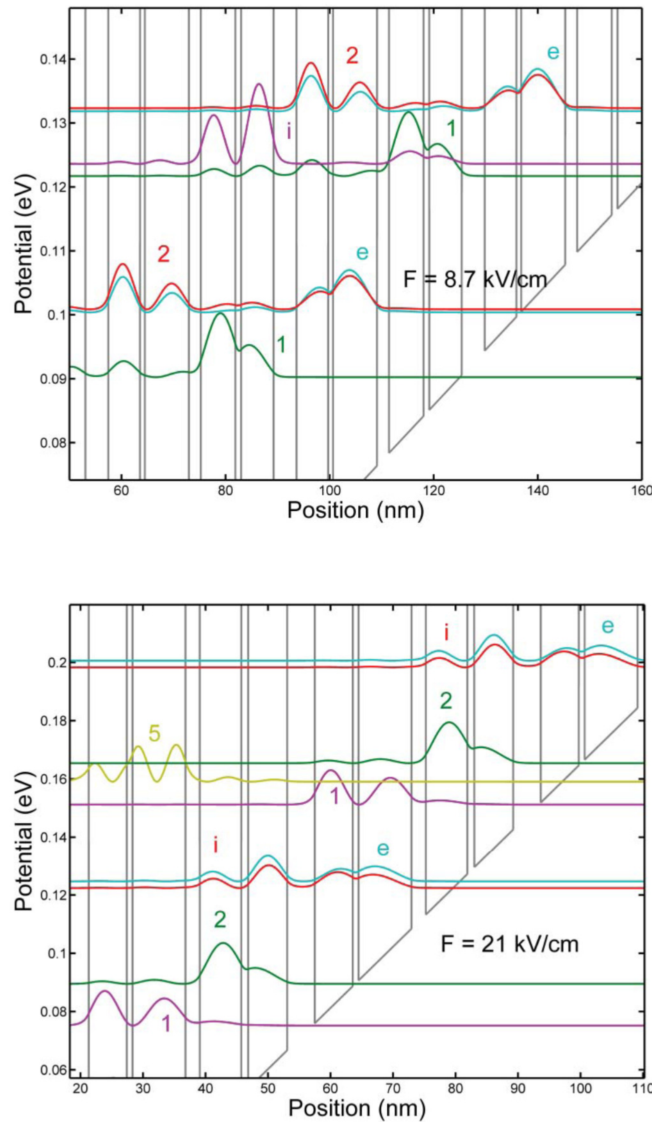

Figure A.8. Three electron tunneling resonances. Band diagram of cascade modules of the THz QCL (V843) active region with the moduli squared of the main electron wave functions. The cascade module of the THz QCL consists of four GaAs (Wells) and four $Al_{0.25}Ga_{0.75}As$ (barriers) layers. The energy separation between the upper (*2*) and lower (*1*) lasing states is ~13 meV at 77 K at an electric field of 21 kV/cm, corresponding to a lasing frequency of ~3.2 THz. It shows that at F = ~4.4 kV/cm (a), the extraction level (*e*) aligns with the lower lasing level (*1*), at F = ~8.7 kV/cm (b), the extraction level (*e*) aligns with the upper lasing level (*2*), and at F = ~21 kV/cm (c), the extraction level (*e*) aligns with the injection level (*i*). The energy levels (*e*, *1*, *2*, *i*) are named in ascending energy order at threshold. Note that the level *2* may not be always higher than the level *1* even though it is conventionally named as the upper lasing state.

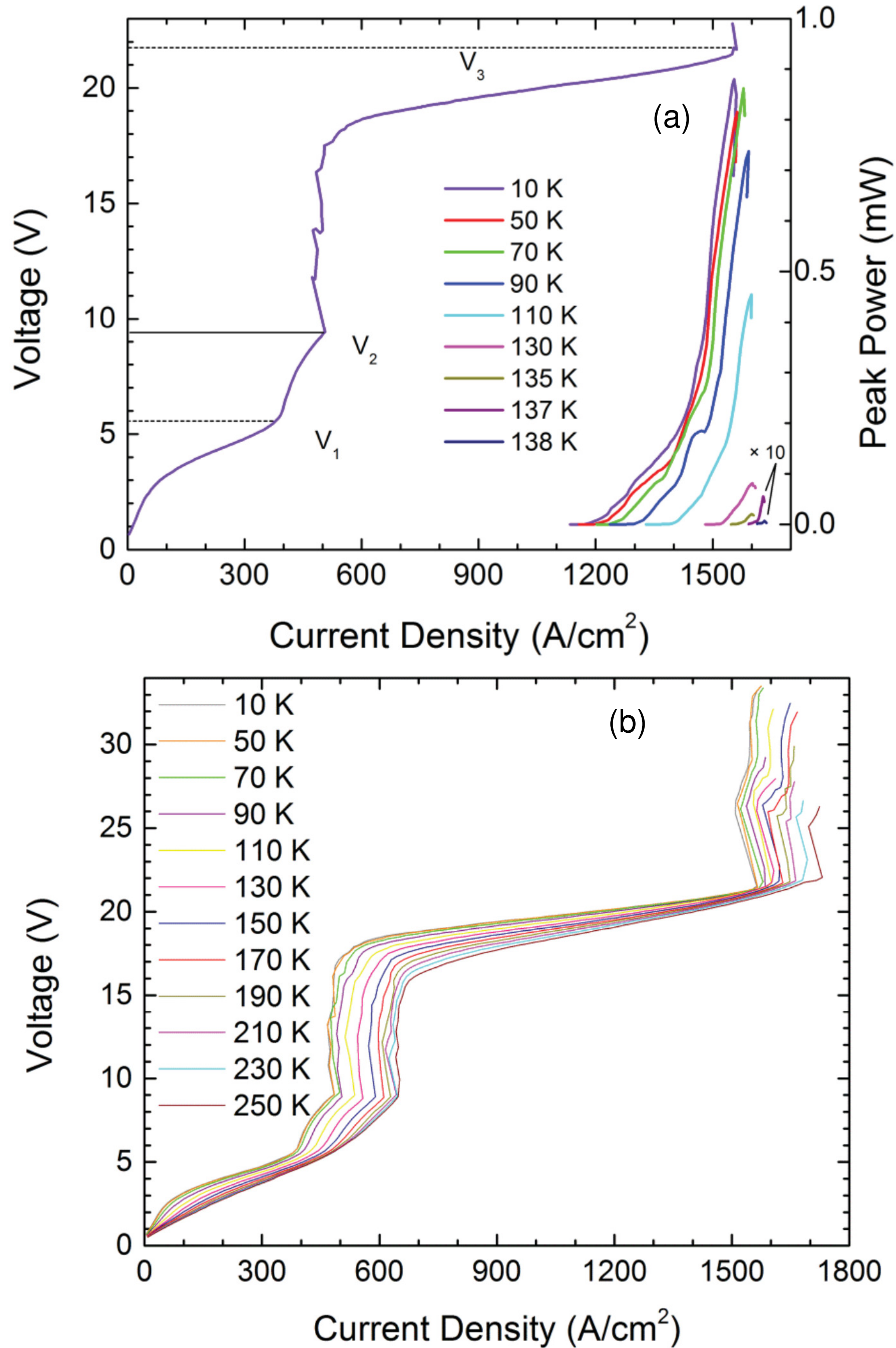

Figure A.9. Light-current density-voltage (*L-J-V*) characteristics of the THz QCL (V843). The *J-V* curve in (a) is measured at 10 K. At V_1 = ~5.5 V, the *J-V* curve shows a shoulder, corresponding to the *e-1*tunneling resonance. At V_2 = ~9.4 V, the *J-V* curve shows another shoulder, corresponding to the *e-2* tunneling resonance. At V_3 = ~21.8 V, the *J-V* curve shows negative differential resistance (NDR), corresponding to the misalignment of the *e-i* tunneling resonance. The device lases up to 138 K in pulsed mode. The pulse width is 250 ns and the pulse repetition rate is 1 kHz in the measurements. No perceptible difference on device performance is observed before and after the SVM scans [79].

The rate equation (RE) model used in the simulation is based on density matrix formalism and it is computationally efficient. The RE model does not solve self-consistently the electronic temperature and the coupled Schrödinger-Poisson equations unless otherwise stated. Second order tunneling model [88] is employed to calculate the current channels between all pairs of states of two neighboring modules. The band non-parabolicity is included in energy state and wavefunction calculation while it is ignored in the calculation of inter-subband scattering times (LO-phonon, Interface roughness, and ion-impurity scattering times) for simplicity. The dephasing time between the resonant states (0.2 ps) is calculated based on the approach presented in [144]. For more details of the RE model, please refer to [144].

References

[1] P. Rodgers, “Nanoelectronics: Single file”, Nature Nanotechnology, Jun. 2006.

[2] J. Simmons, and V. Klimov, “Nanophotonics/Nanoelectronics”, Centre for Integrated nanotechnologies, Science Themes, 2002.

[3] R. Czajka, L. Jurczyszyn, and H. Rafh-Tabar, “Surface Physics at the Nano-Scale via Scanning Probe Microscopy and Molecular Dynamics Simulations”, Prog. Surf. Scie., vol. 59, pp. 13-23, Sep. 1998.

[4] S. John, “Strong Localization of Photons in Certain Disordered Dielectric Supperlattices”, Phy. Rev. Lett., vol. 58, pp. 2486, 1987.

[5] J. Faist, F. Capasso, D. L. Sivco, C. Sirtori, A. L. Hutchinson, and A. Y. Cho, “Quantum Cascade Laser”, Science Reports, vol. 264, pp. 553-556, Apr 1994.

[6] L. Pavesi, “Porous Silicon: a Route Towards a Si Based Photonics?”, Microelec. Journal, vol. 27, pp. 437-448, 1996.

[7] P. Jiang, S. He, D. Shi, H. Zhang, and H. Gao, “Progress in Single-Electron Tunneling Device”, Vacuum Sci and Tech. vol. 21, pp. 303-310, Apr. 2001.

[8] S. Heinze, J. Tersoff, R. Martel, V. Derycke, J. Appenzeller, and P. Avouris, “Carbon nanotubes as Schottky Barrier Transistors”, Phy. Rev. Lett., vol. 89, pp. 106801, 2002.

[9] G. Binnig, and H. Rohrer, “Scanning Tunneling Microscopy”, Helvetica Physica Acta, vol. 55, pp. 726-735, Jul.1982.

[10] G. Binnig, C. F. Quate, Ch. Gerber, “Atomic Force Microscope”, Phys. Rev. Lett., vol. 56, pp.930-933, Mar. 1986.

[11] R. Köhler, A. Tredicucci, F. Beltram, H. E. Beere, E. H. Linfield, A. G. Davies, D. A. Ritchie, R. C. Iotti, and F. Rossi, “Terahertz semiconductor heterostructure laser”, Nature, vol.417, pp.156-159, May 2002.

[12] S. Fathololoumi, E. Dupont, D. Ban, M. Graf, S. R. Laframboise, Z. R. Wasilewski, and H. C. Liu, “Time-Resolved Thermal Quenching of THz Quantum Cascade Lasers”, IEEE J. Quantum Electron., vol.46, 396-404, Mar. 2010.

[13] S. Fathololoumi, E. Dupont, S. G. Razavipour, S. R. Laframboise, A.Delage, Z. R. Wasilewski, A. Bezinger, G. Z. Rafi, S. Safavi-Naeini, D. Ban, and H. C. Liu, “Electrically switching transverse modes in high power THz quantum cascade lasers”, Opt. Express, vol. 18, pp.1036-1048, Apr 2010.

[14] S. Fathololoumi, E. Dupont, S. G. Razavipour, S. R. Laframboise, G. Parent, Z. R. Wasilewski, H. C. Liu, and D. Ban, "On metal contacts of terahertz quantum cascade lasers with a metal–metal waveguide", IOP Semicon. Sci. Tech., vol. 26, pp.105021-1-5, Sep. 2011.

[15] S. Fathololoumi, E. Dupont, C.W.I. Chan, Z. R. Wasilewski, S. R. Laframboise, D. Ban, A. M´aty´as, C. Jirauschek, Q. Hu, and H. C. Liu, "Terahertz quantum cascade lasers operating up to ∼ 200 K with optimized oscillator strength and improved injection tunneling", Opt. Express, vol.20, pp.3866-3876, Feb.2012.

[16] S. Fathololoumi, "Terahertz Quantum Cascade Lasers: towards high performance operation", PhD thesis, University of Waterloo, Department of Electrical and Computer Engineering, 2010.

[17] R. S. Dhar, and D. Ban, "Two-dimensional profiling of carriers in terahertz quantum cascade lasers using calibrated scanning spreading resistance microscopy and scanning capacitance microscopy", J. Microscopy, vol. 251, pp.35-44, Jul. 2013.

[18] S. Fathololoumi, E. Dupont, Z. R. Wasilewski, C. W. I. Chan, S. G. Razavipour, S. R. Laframboise, Shengxi Huang, Q. Hu, D. Ban, and H. C. Liu, "Effect of Oscillator Strength and Intermediate Resonance on the Performance of Resonant Phonon-based Terahertz Quantum Cascade Lasers," J. Appl. Phys., vol. 113, pp.113109-1-17, Mar. 2013.

[19] K. K. Choi, B. F. Levine, R. J. Malik, J. Walker, and C. G. Bethea, "Periodic negative conductance by sequential resonant tunneling through an expanding high-field superlattice domain," Phys. Rev. B, vol. 35, pp.4172–4175, Mar. 1987.

[20] H. T. Grahn, H. Schneider, and K. V. Klitzing, "Optical detection of high field domains in GaAs/AlAs superlattices," Appl. Phys. Lett., vol. 54, pp.1757–1759, Feb. 1989.

[21] H. T. Grahn, R. J. Haug, W. Muller, and K. Ploog, "Electric-field domains in semiconductor superlattices: A novel System for tunneling between 2D Systems," Phys. Rev. Lett., vol. 67, pp.1618–1621, Sep. 1991.

[22] C. Shafai, D. J. Thomson, M. Simard-Normandin, G. Mattiussi, and P. J. Scanlon, "Delineation of semiconductor doping by scanning resistance microscopy", Appl. Phys. Lett., vol. 64, pp.342-344, Jan. 1994.

[23] P. De Wolf , T. Clarysse and W. Vandervorst, "Quantification of nanospreading resistance profiling data", J. Vac. Sci. Technol. B, vol.16, pp.320-326, Jan. 1998.

[24] J. J. Kopanski, “Scanning Capacitance Microscopy for Electrical Characterization of Semiconductors and Dielectrics**”,** edited by S. Kalinin and A. Gruverman, in “Scanning Probe Microscopy”, Vol. 1, Springer, New York, Chapter I.3, pp.88-112, 2007.

[25] H. Yin, T. Li, W. Wang, W. Hu, L. Lin, and W. Lu, “Scanning capacitance microscopy investigation on InGaAs/InP avalanche photodiode structures: Light-induced polarity reversal”, Appl. Phys. Lett., Vol. 95, pp.093506-1-3, Sep. 2009.

[26] C. R. Blanchard, “Atomic Force Microscopy”, The Chemical Educator, Springer New York, vol. 1, pp.1-8, 1996.

[27] A. Trache, and G. A. Meininger, “Atomic Force Microscopy (AFM)”, in *Current Protocols in Microbiology,* R. Coico, T. Kowalik, J. M. Quarles, B. Stevenson and R. K. Taylor eds., Wiley & Sons Inc., vol. 2C, 2.1-2.17., Feb. 2008.

[28] N. A. Geisse, “AFM and Combined Optical Techniques”, Materials Today, vol. 12, pp.40–45, Aug. 2009.

[29] W. Vandervorst, and M. Meuris, “Method for resistance measurements on a semiconductor element with controlled probe pressure”, EP-466274, Jan. 1992.

[30] W. Vandervorst, and M. Meuris, “Method for resistance measurements on a semiconductor element with controlled probe pressure”, US-5369372, Nov. 1994.

[31] P. Eyben, W. Vandervorst, D. Alvarex, M. Xu, and M. Fouchier, “Probing Semiconductor Technology and Devices with Scanning Spreading Resistance Microscopy”, edited by S. Kalinin and A. Gruverman, in “Scanning Probe Microscopy”, Vol. 1, Springer, New York, Chapter I.2, pp.31-87, 2007.

[32] D. Ban, E. H. Sargent, St. J. Dixon-Warren, I. Calder, T. Grevatt, G. Knight, and J. K. White, “Two-dimensional profiling of carriers in a buried heterostructure multi-quantum-well laser: Calibrated scanning spreading resistance microscopy and scanning capacitance microscopy,” J. Vac. Sci. Technol. B, vol. 20, pp.2126-2132, Oct.2002.

[33] D. Ban, E. H. Sargent, St. J. Dixon-Warren, I. Calder, T. Grevatt, G. Knight, and J. K. White, “Two-dimensional transverse cross-section nanopotentiometry of actively driven buried-heterostructure multiple-quantum-well lasers”, J. Vac. Sci. Technol. B, vol. 20, pp.2401-2407, Dec.2002.

[34] P. Eyben, M. Xu, N. Duhayon, T. Clarysse, S. Callewaert and W. Vandervorst, “Scanning spreading resistance microscopy and spectroscopy for routine and quantitative two-dimensional carrier profiling”, J. Vac. Sci. Technol. B, vol. 20, pp.471-478, Jan. 2002.

[35] J. R. Matey and J. Blanc, “Scanning capacitance microscopy”, J. Appl. Phys. Vol.57, pp.1437–1444, Mar. 1985.

[36] J. R. Matey, “Scanning Microscopy Technologies and Applications”, Proc. Of SPIE, vol. 897, pp.110–117, May 1988.

[37] J. K. Clemens, “Capacitive Pickup and the Buried Subcarrier Encoding System for the RCA VideoDisc”, RCA Review, vol. 39, pp.33–59, Mar. 1978.

[38] J. A. Slinkman, H. K. Wickramasinghe, and C. C. Williams, “Scanning capacitance voltage microscopy,” U. S. Patent No. 5065103, Nov. 1991.

[39] J. J. Kopanski, J. F. Marchiando, and J. R. Lowney in Semiconductor Characterization: Present Status and Future Needs, W. M. Bullis, D. G. Seiler, and A. C. Diebold, Eds. AIP, New York, pp. 308–312, 1996.

[40] J. J. Kopanski, J. F. Marchiando, and J. R. Lowney, “Scanning capacitance microscopy measurements and modeling: Progress towards dopant profiling of silicon”, J. Vac. Sci. Technol. B, vol. 14, pp.242–247, Jan. 1996.

[41] S. B. Kuntze, D. Ban, E. H. Sargent, St. J. Dixon-Warren, J. K. White, and K. Hinzer, “Scanning Voltage Microscopy”, edited by S. Kalinin and A. Gruverman, in “Scanning Probe Microscopy”, Vol. 1, Springer, New York, Chapter III.1, pp. 561-600, 2007.

[42] S. B. Kuntze, D. Ban, E. H. Sargent, St. J. Dixon-Warren, J. K. White, and K. Hinzer, “Electrical Scanning Probe Microscopy: Investigating the Inner Workings of Electronic and Optoelectronic Devices”, Solid State Mat. Sci., B, vol.30, pp.71-124, Jun.2005.

[43] T. Tanbun-ek, R. A. Logan, and J. P. van der Ziel, “High frequency buried heterostructure 1.5 µm GaInAsP/InP lasers, grown entirely by metalorganic vapour phase epitaxy in two epitaxial growth steps”, Electron. Lett., Vol. 24, pp.1483-1485, 1988.

[44] T. Kallstenius, U. Smith, and B. Stoltz, “Studies of Internal Structure in InGaAsP/InP-Based Lasers Using Atomic Force Microscopy in Combination with Selective Etching”, J. Electrochem. Soc., vol.146, pp. 749-754, Feb. 1999.

[45] R. S. Dhar, and D. Ban, “SSRM and SCM study for doping concentration of THZ QCL devices”, Photonics North 2012 Conference, Montreal, Canada, June 6-8, 2012, Proc. of SPIE, Vol. 8412, Sep. 2012.

[46] L. Held, “Implantation isolation in AlGaAs/GaAs structures”, Master of Science thesis, KTH, Sweden, Mar. 2011.

[47] C. D. Nardi, R. Desplats, P. Perdu, C. Guérin, J. L. Gauffier, and T. B. Amundsen, “EEPROM Failure Analysis Methodology: Can Programmed Charges Be Measured Directly by

Electrical Techniques of Scanning Probe Microscopy?", Proc. 31st ISTFA, pp. 256-261, Nov. 2005.

[48] C. D. Nardi, R. Desplats, P. Perdu, C. Guérin, J. L. Gauffier, and T. B. Amundsen, "Direct Measurements of Charge in Floating Gate Transistor Channels of Flash Memories Using Scanning Capacitance Microscopy" Proc. 32nd ISTFA, pp. 86-93, Nov. 2006.

[49] D. Ban, E. H. Sargent, St. J. Dixon-Warren, I. Calder, A. J. SpringThorpe, R. Dworschak, G. Este, and J. K. White, "Direct imaging of the depletion region of an InP p –n junction under bias using scanning voltage microscopy", Appl. Phys. Lett., Vol.81, pp.5057-5059, Dec.2002.

[50] T. Trenkler, R. Stephenson, P. Jansen, W. Vandervorst, and L. Hellemans, "New aspects of nanopotentiometry for complementary metal–oxide–semiconductor transistors", J. Vac. Sci. Technol. B, vol. 18, pp.586-594, Jan. 2000.

[51] W. W. Chow, "Physics and Simulation of Optoelectronic Devices III", Proc. SPIE., vol. 2399, pp.445, 1995.

[52] D. Ban, E. H. Sargent, K. Hinzer, St. J. Dixon-Warren, A. J. SpringThorpe, and J. K. White, "Direct observation of lateral current spreading in ridge waveguide lasers using scanning voltage microscopy", Appl. Phys. Lett., vol. 82, pp.4166–4168, Jun. 2003.

[53] D. Ban, E. H. Sargent, St. J. Dixon-Warren, K. Hinzer, J. K. White, and A. J. SpringThorpe, "Scanning Voltage Microscopy on Active Semiconductor Lasers: The Impact of Doping Profile Near an Epitaxial Growth Interface on Series Resistance", IEEE J. Quantum Electron., vol. 40, pp.651-654, Jun. 2004.

[54] Veeco Metrology Group, "Application Modules: Dimension and Multimode Manual. Software Version 5.12r4. Revision B.", May 2003.

[55] Attocube technology Group, http://www.attocube.com/nanoSCOPY/afmI.html, Attocube Instruments, January 2012.

[56] B. Ferguson, and X. C. Zhang, "Materials for terahertz science and technology", Nature Mater., vol.1, pp.26-33, Sep.2002.

[57] B. S. Williams, S. Kumar, H. Callebaut, Q. Hua, and J. L. Reno, "Terahertz quantum-cascade laser operating up to 137 K", Appl. Phys. Lett., vol. 83, pp.5142-5144,Dec.2003.

[58] D. Ban, M. Wächter, H. C. Liu, Z. R. Wasilewski, M. Buchanan, and G. C. Aers, Terahertz quantum cascade lasers: Fabrication, characterization, and doping effect, J. Vac. Sci. Technol. A, vol. 24, pp.778-782, Jun.2006.

[59] B. S. Williams, "Terahertz quantum-cascade lasers", Nat. Photon., Vol. 1, pp.517-525, Sep.2007.

[60] S. Fathololoumi, E. Dupont, S. G. Razavipour, S. R. Laframboise, A. Delage, Z. R. Wasilewski, A. Bezinger, G. Z. Rafi, S. Safavi-Naeini, D. Ban, and H. C. Liu, "Electrically switching transverse modes in high power THz quantum cascade lasers", Opt. Express, vol. 18, pp. 1036-1048, Apr. 2010.
[61] B. S. Williams, S. Kumar, Q. Hu, and J. L. Reno, "Operation of terahertz quantum-cascade lasers at 164 K in pulsed mode and at117 K in continuous-wave mode", Opt. Express, vol. 13, pp.3331 -3339, May 2005.
[62] H. C. Liu, M. Wächter, D. Ban, Z. R. Wasilewski, M. Buchanan, G. C. Aers, J. C. Cao, S. L. Feng, B. S. Williams, and Q. Hu, "Effect of doping concentration on the performance of terahertz quantum-cascade lasers", Appl. Phys. Lett., vol. 87, pp.141102-1-3, Sept. 2005.
[63] L. Ajili, G. Scalari, M. Giovannini, N. Hoyler, and J. Faist, "Doping in quantum cascade lasers.II. GaAs/Al0.15Ga0.85As terahertz devices", J. Appl. Phys., vol. 100, pp.043102-1-3, Aug. 2006.
[64] A. Benz, G. Fasching, A. M. Andrews, M. Martl, K. Unterrainer, T. Roch, W. Schrenk, S. Golka, and G. Strasser, "Influence of doping on the performance of terahertz quantum-cascade lasers", Appl. Phys. Lett., vol. 90, pp.101107-1-3, Mar. 2007.
[65] S. Höfling, R. Kallweit, J. Seufert, J. Koeth, J. P. Reithmaier, and A. Forchel, "Reduction of the threshold current density of GaAs/AlGaAs quantum cascade lasers by optimized injector doping and growth conditions", J. Cryst. Growth., vol. 278, pp.775-779, May 2005.
[66] E. Mujagić, M. Austerer, S. Schartner, M. Nobile, L. K. Hoffmann, W. Schrenk, G. Strasser, M. P. Semtsiv, I. Bayrakli, M. Wienold, and W. T. Masselink, "Impact of doping on the performance of short-wavelength InP-based quantum-cascade lasers", J. App. Phy., vol. 103, pp.033104-1-4, Feb. 2008.
[67] V. D. Jovanović, S. Höfling, D. Indjin, N. Vukmirović, Z. Ikonić, P. Harrison, J. P. Reithmaier, and A. Forchel, "Influence of doping density on electron dynamics in GaAs/AlGaAs quantum cascade lasers", J. App. Phy., vol. 99, pp.103106-1-9, May 2006.
[68] V. Spagnolo, G. Scamarcio, W. Schrenk, and G. Strasser, "Influence of the band-offset on the electronic temperature of GaAs/Al(Ga)As superlattice quantum cascade lasers", Semicon. Sci. Technol., vol. 19, pp. s110-s112, Apr. 2004.
[69] M. S. Vitiello, G. Scamarcio, V. Spagnolo, C. Worrall, H. E. Beere, D. A. Ritchie, C. Sirtori, J. Alton, and S. Barbieri, "Subband electronic temperatures and electron-lattice energy relaxation in terahertz quantum cascade lasers with different conduction band offsets", Appl. Phys. Lett., vol. 89, pp.131114-1-3, Sep. 2006.

[70] T. Clarysse, G. Brammertz, D. Vanhaeren, P. Eyben, J. Goossens, F. Clemente, M. Meuris, W. Vandervorst, R. Srnanek, R. Kinder, B. Sciana, D. Radziewicz, Z. Li, "Accurate carrier profiling of n-type GaAs junctions", Mat. Sci. Semi. Process, vol. 11, pp.259-266, Jun. 2008.

[71] R. P. Lu, K. L. Kavanagh, St. J. Dixon-Warren, A. J. SpringThorpe, G. Hillier, D. Macquistan, and E. Griswold, "Calibrated scanning spreading resistance microscopy profiling of carriers in III–V structures", J. Vac. Sci. Technol. B, vol. 19, pp.1662-1670, Jun. 2001.

[72] P. De Wolf, T. Clarysse, W. Vandervorst, J. Snauwaert, and L. Hellemans, "One- and two-dimensional carrier profiling in semiconductors by nanospreading resistance profiling", J. Vac. Sci. Technol. B, vol. 14, pp.380-385, Jan. 1996.

[73] Y. Huang, C. C. Williams, and M. A. Wendman, "Quantitative two-dimensional dopant profiling of abrupt dopant profiles by cross-sectional scanning capacitance microscopy", J. Vac. Sci. Technol. A, vol. 14, pp.1168-1171, Jun. 1996.

[74] R. S. Dhar, St. J. Dixon-Warren, M. A. Kawaliye, J. Campbell, M. Green and D. Ban, "Direct Charge Measurements to Read Back Stored Data in Non Volatile Memory Devices using Scanning Capacitance Microscopy", J. Vac. Sci. Technol. B, vol. 31, pp.061801-1-7, Dec. 2013.

[75] St. J. Dixon-Warren, R. P. Lu, S. Ingrey, D. Macquistan, T. Bryskiewicz, G. Smith, and B. Bryskiewicz, "Scanning spreading resistance microscopy study of a metal organic chemical vapor deposited grown InP optoelectronic structure", J. Vac. Sci. Technol. B, vol. 19, pp.1752-1757, Aug. 2001.

[76] W. Brezna, and J. Smoliner, "Investigation of contact-force dependent effects in conductive atomic force microscopy on Si and GaAs", J. Appl. Phys., Vol. 104, pp.044309-1-5, Aug. 2008.

[77] C. Eckhardt, W. Brezna, O. Bethge, E. Bertagnolli, and J. Smoliner, "Tip geometry effects in scanning capacitance microscopy on GaAs Schottky and metal-oxide-semiconductor-type junctions", J. Appl. Phys.,Vol. 105, pp.113709-1-5, Jun. 2009.

[78] CED magic. (2013) Available at: http://cedmagic.com/history/firstsuccessful-ced.html.

[79] E. Dupont, S. Fathololoumi, Z. R. Wasilewski, G. Aers, S. R. Laframboise, M. Lindskog, S. G. Razavipour, A. Wacker, D. Ban, and H. C. Liu, "A phonon scattering assisted injection and extraction based terahertz quantum cascade laser", J. Appl. Phys., vol. 111, pp.073111-1-10, Apr. 2012.

[80] R. Stephenson, A. Verhulst, P. De. Wolf, M. Caymax, and W. Vandervorst, "Contrast reversal in scanning capacitance microscopy imaging", Appl. Phys. Lett., vol. 73, pp.2597-2599, Nov. 1998.

[81] E.-S. Kang, J.-W.Kang, and H.-J. Hwang, J.-H.Lee, Nondestructive one-dimensional scanning capacitance microscope dopant profile determination method and its application to three-dimensional dopant profiles", J. Vac. Sci. Technol. A, vol. 18, pp.1338-1344, Aug. 2000.

[82] V. V. Zavyalov, J. S. McMurray, and C. C. Williams, "Scanning capacitance microscope methodology for quantitative analysis of p-n junctions", J. Appl. Phys., Vol. 85, pp.7774-7783, Jun. 1999.

[83] J. F. Marchiando, J. J. Kopanski, and J. Albers, "Carrier concentration dependence of the scanning capacitance microscopy signal in the vicinity of p–n junctions", J. Vac. Sci. Technol. B, vol. 18, pp.409-413, Feb. 2000.

[84] G. P. Agrawal and N. K. Dutta, "Long wavelength semiconductor lasers", Van Nostrand Reinhold New York, 1986.

[85] P. Werle, F. Slemr, K. Maurer, R. Kormann, R. Mucke, and B. Janker, "Near- and mid-infrared laser-optical sensors for gas analysis", Opt. Lasers Eng., vol. 37, pp.101–114, Feb. 2002.

[86] I. P. Kaminow, T. Li, A. E. Willner, "Optical fiber telecommunications VIA components and subsystems", Academic Press Wiley, 2013.

[87] Y. Yao, A. J. Hoffman and C. F. Gmachl, "Mid-infrared quantum cascade lasers", Nature Photon., vol. 6, pp.432 – 439, Jun. 2012.

[88] G. Scalari, C. Walther, M. Fischer, R. Terazzi, H. Beere, D. Ritchie, and J. Faist, "THz and sub-THz quantum cascade lasers", Laser Photon. Rev., vol. 3, pp.45–66, Feb. 2009.

[89] Ed Murphy, "The semiconductor laser: enabling optical communication", Nature Photon., vol. 4, pp.287, May 2010.

[90] Y. Chassagneux, R. Colombelli, W. Maineult, S. Barbieri, H. E. Beere, D. A. Ritchie, S. P. Khanna, E. H. Linfield, and A. G. Davies, "Electrically pumped photonic-crystal terahertz lasers controlled by boundary conditions", Nature, vol. 457, pp.174-178, Jan. 2009.

[91] J. Kohoutek, A. Bonakdar, R. Gelfand, D. Dey, I. Hassani Nia, V. Fathipour, O. G. Memis, and H. Mohseni, "Integrated All-Optical Infrared Switchable Plasmonic Quantum Cascade Laser", Nano Lett., vol. 12, pp.2537−2541, Apr. 2012.

[92] D. Costantini, L. Greusard, A. Bousseksou, R. Rungsawang, T. P. Zhang, S. Callard, J. Decobert, F. Lelarge, G.-H. Duan, Y. De Wilde, and R. Colombelli, "In Situ Generation of Surface Plasmon Polaritons Using a Near-Infrared Laser Diode", Nano Lett., vol. 12, pp.4693−4697, Aug. 2012.

[93] I. Vurgaftman, W. W. Bewley, C. L. Canedy, C. Soo Kim, M. Kim, J. R. Lindle, C. D. Merritt, J. Abell, and J. R. Meyer, "Mid-IR type-II interband cascade lasers", IEEE J. Sel.. Topics Quantum Electron., vo. 17, pp.1435-1444, Sep. 2011.

[94] R. Q. Yang, J. L. Bradshaw, J. D. Bruno, J. T. Pham, and D. E. Wortman, "Mid-infrared type-II interband cascade lasers," IEEE J. Quantum Electron., vol. 38, pp.559–568, Jun. 2002.

[95] R. Q. Yang, L. Li, L. Zhao, Y. Jiang, Z. Tian, H. Ye, R. T. Hinkey, C. Niu, T. D. Mishima, M. B. Santos, J. C. Keay, M. B. Johnson, and K. Mansour, "Recent progress in development of InAs-based interband cascade lasers", Proc. of SPIE, vol. 8640, pp.86400Q-1-10, 2013.

[96] R. Q. Yang, Z. Tian, J. F. Klem, T. D. Mishima, M. B. Santos, and M. B. Johnson, "Interband cascade photovoltaic devices", Appl. Phys. Lett., vol. 96, pp.063504-1-3, Feb. 2010.

[97] J. R. Meyer, C. A. Hoffman, F. J. Bartoli, and L. R. Ram-Mohan, "Type-II quantum well lasers for the mid-wavelength infrared," Appl. Phys. Lett., vol. 67, pp.757-759, May 1995.

[98] R. Q. Yang, C. J. Hill, K. Mansour, Y. Qiu, A. Soibel, R. Muller, and P. Echternach, "Distributed feedback midinfrared interband cascade lasers at thermoelectric cooler temperatures," IEEE J. Sel.. Topics Quantum Electron., vol. 13, pp.1074-1078, Sep. 2007.

[99] I. Vurgaftman, W. W. Bewley, C. L. Canedy, C. S. Kim, M. Kim, J. R. Lindle, C. D. Merritt, J. Abell, and J. R Meyer, "Rebalancing of internally generated carriers for mid-infrared interband cascade lasers with very low power consumption," Nature Commun., vol. 2, pp.585-1-7, Dec. 2011.

[100] W. W. Bewley, C. L. Canedy, C. S. Kim, M. Kim, J. R. Lindle, C. D. Merritt, J. Abell, J. R. Meyer, "High power room-temperature continuous-wave mid-infrared interband cascade lasers", Opt. Express, vol. 20, pp.20894-20901, Aug. 2012.

[101] E. Dupont, S. Fathololoumi, and H. C. Liu, "Simplified density matrix model applied to three-well terahertz quantum cascade lasers," Phys. Rev. B, vol. 81, pp. 205311-1-18, May 2010.

[102] S. C. Lee and A. Wacker, "Nonequilibrium Greens function theory for transport and gain properties of quantum cascade structures," Phys. Rev. B, vol. 66, pp.245314-1-18, Dec. 2002.

[103] H. Callebaut, S. Kumar, B. S. Williams, Q. Hu, and J. L. Reno, "Analysis of transport properties of terahertz quantum cascade lasers," Appl. Phys. Lett., vol. 83, pp.207–209 Jul. 2003.

[104] C. Jirauschek and P. Lugli, "Monte-Carlo-based spectral gain analysis for terahertz quantum cascade lasers", J. Appl. Phys., vol. 105, pp.123102-1-5, Jun. 2009.

[105] M. A. Eriksson, R. G. Beck, M. Topinka, J. A. Katine, R. M. Westervelt, K. L. Campman, and A. C. Gossard, "Cryogenic scanning probe characterization of semiconductor nanostructures", Appl. Phys. Lett., vol. 69, pp.671-673, Jul. 1996.

[106] Z. Tian, C. Chen, R. Q. Yang, T. D. Mishima, M. B. Santos, J. C. Keay, M. B. Johnson and J. F. Klem, "InAs-based Plasmon-waveguide Interband Cascade Lasers", Proc. of SPIE, vol. 7616, pp.76161B-1-9, 2010.

[107] J. R. Meyer, C. A. Hoffman, F. J. Bartoli, and L. R. Ram-Mohan, "Type-II quantum well lasers for the mid wavelength infrared," Appl. Phys. Lett., vol. 67, pp.757–759, Aug. 1995.

[108] Z. Tian, Y. Jiang, L. Li, R. T. Hinkey, Z. Yin, R. Q. Yang, T. D. Mishima, M. B. Santos, and M. B. Johnson, "InAs based interband cascade lasers near 5.3 µm" , IEEE J. Quantum Electron., vol. 48, pp.915-921, Jul. 2012.

[109] J. Faist, D. Hofstetter, M. Beck, T. Aellen, M. Rochat, and S. Blaser, "Bound-to-continum and two-phonon resonance quantum cascade lasers for high duty cycle, high-temperature operation", IEEE J. Quantum Electron., vol. 38, pp.533-546, Jun. 2002.

[110] R. S. Dhar, C. Xu, D. Ban, L. Li, H. Ye, R. Q. Yang, M. B. Johnson, T. D. Mishima and M. B. Santos, "Direct Observation of Non-uniform Electric Field in the Active Regions of an Interband Cascade Laser", CLEO 2014 Conference, San Jose, USA, June 8-13, 2014.

[111] D. A. Neamen, "Semiconductor physics and devices basic principles", Mc Graw Hill higher education, 3rd Edition, New York, 2003.

[112] W. W. Bewley, J. R. Lindle, C. L. Canedy, M. Kim, C. S. Kim, D. C. Larrabee, I. Vurgaftman, and J. R. Meyer, "Gain, loss, and internal efficiency in interband cascade lasers emitting at λ=3.6 - 4.1 µm," J. Appl. Phys., vol. 103, pp.013114-1-4, Jan. 2008.

[113] A. Soibel, K. Mansour, Y. Qiu, C. J. Hill, and R. Q. Yang, "Optical gain, loss, and transparency current in high performance mid-infrared interband cascade lasers," J. Appl. Phys., vol. 101, pp.093104-1-4, May 2007.

[114] C. Sirtori, S. Barbieri and R. Colombelli, "Wave engineering with THz quantum cascade lasers", Nature Photon., vol. 7, pp.691-701, Aug. 2013.

[115] T. Kubis, S. R. Mehrotra, and G. Klimeck, "Design concepts of terahertz quantum cascade lasers: Proposal for terahertz laser efficiency improvements," Appl. Phys. Lett., vol. 97, pp.261106 -1-3, Dec. 2010.

[116] C. Walther, M. Fischer, G. Scalari, R. Terazzi, N. Hoyler, and J. Faist, “Quantum cascade lasers operating from 1.2 to 1.6 THz,” Appl. Phys. Lett., vol. 91, pp.131122-1-3, Sep. 2007.

[117] C. W. I. Chan, Q. Hu, and J. L. Reno, “Ground state terahertz quantum cascade lasers,” Appl. Phys. Lett., vol. 101, pp.151108-1-3, Oct. 2012.

[118] G. Scalari, M. I. Amanti, C. Walther, R. Terazzi, M. Beck, and J. Faist, “Broadband THz lasing from a photon-phonon quantum cascade structure,” Opt. Express, vol. 8, pp.8043–805, Mar. 2010.

[119] Q. Qin, B. S. Williams, S. Kumar, J. L. Reno, and Q. Hu, “Tuning a terahertz wire laser,” Nature Photon., vol. 3, pp.732–737, Jan. 2009.

[120] H. Luo, S. R. Laframboise, Z. R. Wasilewski, G. C. Aers, H. C. Liu, and J. C. Cao, “Terahertz quantum-cascade lasers based on a three-well active module,” Appl. Phys. Lett., vol. 90, pp.041112-1-3, Jan. 2007.

[121] M. A. Belkin, J. A. Fan, S. Hormoz, F. Capasso, S. P. Khanna, Md. Lachab, A. G. Davies, and E. H. Linfield, “Terahertz quantum cascade lasers with copper metalmetal waveguides operating up to 178 K,” Opt. Express, vol. 16, pp.3242-3248, Mar. 2008.

[122] S. Kumar, Q. Hu, and J. L. Reno, “186 K operation of terahertz quantum cascade lasers based on a diagonal design,” Appl. Phys. Lett., vol. 94, pp.131105-1-3, Apr. 2009.

[123] A. Wade, G. Fedorov, D. Smirnov, S. Kumar, B. S. Williams, Q. Hu, and J. L. Reno, “Magnetic field-assisted terahertz quantum cascade laser operating up to 225 K,” Nature Photon., vol. 3, pp.41–45, Jan. 2009.

[124] M. Brandstetter, C. Deutsch, M. Krall, H. Detz, D. C. MacFarland, T. Zederbauer, A. M. Andrews, W. Schrenk, G. Strasser, K. Unterrainer, “High power terahertz quantum cascade lasers with wafer bonded symmetric active regions,” Appl. Phys. Lett., vol. 103, pp.171113-1-3, Oct. 2013.

[125] J. R. Freeman, J. Maysonnave, N. Jukam, P. Cavalié, K. Maussang, H. E. Beere, D. A. Ritchie, J. Mangeney, S. S. Dhillon, and J. Tignon, “Direct intensity sampling of a mode locked terahertz quantum cascade laser,” Appl. Phys. Lett., vol. 101, pp.181115-1-3, Nov. 2012.

[126] M. S. Vitiello, G. Scamarcio, V. Spagnolo, S. S. Dhillon, C. Sirtori, “Terahertz quantum cascade lasers with large wall-plug efficiency,” Appl. Phys. Lett., vol. 90, pp.191115-1-3, May 2007.

[127] M. I. Amanti, M. Fischer, G. Scalari, M. Beck, and J. Faist, “Low-divergence single-mode terahertz quantum cascade laser,” Nature Photon., vol. 3, pp.586–590, Sep. 2009.

[128] N. Yu, J. Fan, Q. J. Wang, C. Pflüg, L. Diehl, T. Edamura, M. Yamanishi, H. Kan, and F. Capasso, "Small-divergence semiconductor lasers by plasmonic collimation," Nature Photon., vol. 2, pp.564-570, Jul. 2008.

[129] K. Vijayraghavan, Y. Jiang, M. Jang, A. Jiang, K. Choutagunta, A. Vizbaras, F. Demmerle, G. Boehm, M. C. Amman, and M. A. Belkin, "Broadly tunable terahertz generation in mid-infrared quantum cascade lasers," Nature Commun., vol. 4, pp.2021, Jun. 2013.

[130] S. Kumar, C. W. I. Chan, Q. Hu, and J. L. Reno, "A 1.8-THz quantum cascade laser operating significantly above the temperature of ħω/kB," Nature Phys., vol. 7, pp.166–171, Feb. 2011.

[131] J. Kröll, J. Darmo, S. S. Dhillon, X. Marcadet, M. Calligaro, C. Sirtori, and K. Unterrainer, "Phase resolved measurements of stimulated emission in a laser," Nature, vol. 449, pp.698-702, Oct. 2007.

[132] D. Burghoff, T.-Y. Kao, D. Ban, A. W. M. Lee, J. Reno, and Q. Hu, "A terahertz pulse emitter monolithically-integrated with a quantum cascade laser," Appl. Phys. Lett., vol. 98, pp.061112-1-3, Feb. 2011.

[133] M. S. Vitiello, L. Consolino, S. Bartalini, A. Taschin, A. Tredicucci, M. Inguscio, and P. De Natale, "Quantum-limited frequency fluctuations in a terahertz laser," Nature Photon., vol. 6, pp.525–528, Jul. 2012.

[134] F. Lopez, M. R. Wood, M. Weimer, C. F. Gmachl, C. G. Caneau, "Direct Measurement of Interface Roughness in QCL Materials Grown by MOCVD" The 12th International Conference on Intersubband Transitions in Quantum Wells, Sept. 16 – 20th, 2013, Sagamore Resort, Lake George, Bolton Landing, New York. Conference Program, pages 57-58.

[135] D. Ban, E. H. Sargent, St. J. Dixon-Warren, G. Letal, K. Hinzer, A. J. SpringThorpe, G. Knight, and J. K. White, "Scanning Voltage Microscopy on Buried Heterostructure Multi-Quantum-Well Lasers: Identification of a Diode Current Leakage Path," IEEE J. Quantum Electron., vol. 40, pp.118-122, Feb. 2004.

[136] H. T. Grahn, H. Schneider, K. Von Klitzing, "Optical studies of electric field domains in GaAs-AlxGa1-xAs superlattices," Phys. Rev. B, vol. 41, pp.2890-2899, Feb. 1990.

[137] S. G. Razavipour, E. Dupont, C. W. I. Chan, C. Xu, Z. R. Wasilewski, S. R. Laframboise, Q. Hu, and D. Ban, "A high carrier injection terahertz quantum cascade laser based on indirectly pumped scheme", Appl. Phys. Lett., vol. 104, pp.0411111-1-3, Jan. 2014.

[138] L. L. Chang, L. Esaki and R. Tsu, "Resonant Tunneling in Semiconductor Double Barriers", Appl. Phys. Lett., vol. 24, pp. 593-595, Jun. 1974.

[139] R. Terrazi and J. Faist, “A density matrix model of transport and radiation in quantum cascade lasers,” New Journal of Physics, vol. 12, pp.033045-1-10, Mar. 2010.

[140] S. C. Lee and A. Wacker, “Nonequilibrium Greens function theory for transport and gain properties of quantum cascade structures,” Phys. Rev. B, vol. 66, pp.245314-1-18, Dec. 2002.

[141] Y. J. Han, W. Feng, J. C. Cao, “Optimization of radiative recombination in terahertz quantum cascade lasers for high temperature operation,” J. Appl. Phys., vol. 111, pp.113111-1-4, Jun. 2012.

[142] R. S. Dhar, Z. R. Wasilewski, and D. Ban, “Cryogenic Temperature Voltage Profiling of Operating Laser Devices”, TechnConnect World 2014 Conference, USA, June15-19, 2014.

[143] S. L. Chuang, Physics of Photonic Devices, Wiley, second edition, 2009.

[144] S. G. Razavipour, E. Dupont, S. Fathololoumi, C.W.I. Chan, M. Lindskog, Z. R. Wasilewski, G. Aers, S. R. Laframboise, A. Wacker, Q. Hu, D. Ban, and H. C. Liu, “An indirectly pumped Terahertz Quantum Cascade Laser with low injection coupling strength operating above 150 K,” J. Appl. Phys., vol. 113, pp.203107-1-13, May 2013.

[145] R. S. Dhar, S. G. Razavipour, E. Dupont, C. Xu, S. Laframboise, Z. Wasilewski, Q. Hu, and D. Ban, “Direct Observation of Electric Field Domain in the Active Region of Terahertz Quantum Cascade Laser”, IQCLSW 2014 Conference, Italy, Sept. 2014 accepted.

[146] M. Wienold, L. Schrottke, M. Giehler, R. Hey, and H. T. Grahn, “Nonlinear transport in quantum cascade lasers: The role of electric-field domain formation for the laser characteristics,” J. Appl. Phys., vol. 109, pp.073112-1-6, Apr. 2011.

[147] D. Ban, E. H. Sargent, St. J. Dixon-Warren, “Scanning Differential Spreading Resistance Microscopy on an Actively Driven Buried Heterostructure Multi-Quantum-Well Laser,” IEEE J. Quantum Electron., vol. 40, pp.865-870, Jul. 2004.

[148] G. K. Rasulova, P. N. Brunkov, A. Yu. Egorov, and A. E. Zhukov, “Self-oscillations in weakly coupled GaAs/AlGaAs superlattices at 77.3 K,” J. Appl. Phys., vol. 105, pp.033711-1-7, Feb. 2009.

[149] A. Wacker, M. Moscoso, M. Kindelan, and L. L. Bonilla, “Current-voltage characteristic and stability in resonant-tunneling *n*-doped semiconductor superlattices,” Phy. Rev. B, vol. 55, pp.2466-2475, Jan. 1997.

[150] L. L. Bonilla, J. Galan, J. A. Cuesta, F. C. Martinez, and J. M. Molera, “Dynamics of electric-field domains and oscillations of the photocurrent in a simple superlattice model,” Phy. Rev. B, vol. 50, pp.8644-8657, Sep. 1994.

[151] B. S. Williams, “Terahertz Quantum Cascade Lasers”, PhD thesis, Massachusetts Institute of Technology, Department of Electrical and Computer Science, 2003.

[152] Q. Hu, B. S. Williams, S. Kumar, H. Callebaut, S. Kohen, and J. L. Reno, “Resonant phonon-assisted thz quantum-cascade lasers with metalmetal waveguides”, Semicond. Sci. Technol., Vol.20, pp.S228-S236, 2005.

[153] S. G. Razavipour, “Design, Analysis, and Characterization of Indirectly-pumped Terahertz Quantum Cascade Lasers”, PhD thesis, University of Waterloo, Department of Electrical and Computer Engineering, 2013.